Research Programme of the Research Fund for Coal and Steel

FIre and Seismic performances of Hybrid fire WALLs in case of single-storey industrial and commercial steel buildings (FISHWALL)

Development and Validation of FE numerical models

Christophe Renaud – CTICM

WP3: Fire behaviour of a hybrid fire wall solution associated with unprotected steel structure

Deliverable: D3.4

Contributing partners		
	CVUT	Czech Republic

Grant agreement No: 101034083

Version	Issue	Purpose	Author	Reviewer	Approved
A	D3.4	01/04/2025	C. Renaud	All partners	
B	D3.4	15/05/2025 (Comments from partners considered)	C. Renaud	B. Zhao	C. Renaud

TABLE OF CONTENTS

ABSTRACT

It is well known that the intrinsic fire resistance of single-storey unprotected steel-framed buildings is largely sufficient to guarantee the evacuation of occupants in the event of fire. In consequence, for this type of building, the main concern of national fire regulations in Europe is how to prevent the spread of fire to the whole building. To achieve this objective, two performances shall be usually satisfied, namely, the appropriateness of constructive systems to ensure that there is no progressive collapse between fire compartments, and the efficiency of fire walls to stop the fire inside the initial compartment regardless of the state of structures exposed to fire. In practice, many constructional solutions can be implemented in order to preserve the integrity of the fire walls, while accepting that the fire exposed part of the structure may collapse. One of the most common solutions is to place a non-load bearing wall between two independent steel structures and to connect it to them by means of "fusible" links. In fire situation, these fusible links have to allow the wall to be disconnected from the structure affected by fire without endangering the separating function of the wall, which shall remain fixed to the steel structure on the other side of the wall and therefore not exposed to fire. However, due to the lack of corresponding scientific evidence, questions are being very often raised about the real efficiency of such systems in fire situation, which, in certain cases, have also to provide an adequate seismic resistance, if they are used in seismic areas.

Today, concrete or masonry wall solutions are frequently used for the compartmentation of buildings, predominately for low-rise commercial and industrial steel buildings. However, as an alternative, lightweight sandwich panels (comprising two thin flat metal faces and an insulated core) could become an appropriate steel fire wall solution, offering numerous benefits in comparison to other solutions, including fire resistance, durability, flexibility, easy dismounting and fast construction times. But, there is an evident lack of technical information about the adequate fire performance of such type of wall solutions when they are implemented in single-storey buildings with unprotected steel structure, which constitutes a major obstacle for their large use.

In this context, the overall goal of the FISHWALL project is to develop a design guidance and recommendations for an innovative hybrid fire wall solution based on lightweight steel-faced sandwich panels associated with unprotected steel structure under both fire and seismic actions, but considered individually. This will be achieved through the following specific tasks: i) Establishing of a full range of experimental evidence about the fire and seismic behaviour of the investigated hybrid fire wall solution by carrying out a number of tests; ii) Investigating intensively the fire and seismic performances of the above hybrid fire wall solution in combination with unprotected single-storey steel structures through a variety of parametric numerical studies by means of validated FE numerical models; iii) Developing both cost-effective and innovative “fusible” connection systems for fire walls to be used in combination with unprotected steel structures of single-storey buildings; and iv) Developing a design guidance and practical recommendations for the studied hybrid fire wall and fusible links solutions, on the basis of above studies, from which engineers can carry out very efficient design.

The present report aims to report on the comparison study conducted between the results of the fire tests carried out on steel purlins crossing through a fire wall (detailed in Deliverable 4.1 [9]) and a fire wall connected to steel portal frames by means of fusible links (detailed in Deliverable [1]) and the results of FE models developed in the scope of the task 3.4 to analyse in detail the structural behaviour of the tested elements. The results of a comparative study carried out to compare several FE models developed with different FE codes (ANSYS, Ls-dyna and ABAQUS) that could be used to investigate the fire resistance of the fusible link solutions investigated in the project are also summarised.

1 INTRODUCTION

The aim of the project FISHWALL is to provide a hybrid steel-based fire wall solution using sandwich panels for single-storey buildings with unprotected steel structure.

The investigated fire partition solution can be placed between two independent building structures and connected to them by means of "fusible" systems. In this case, it is necessary to ensure that in the event of a fire, the fire wall does not fail together with the steel structure exposed to the fire. The fusible links must therefore be designed to withstand the pushing phase due to the thermal expansion of the structure exposed to the fire and to fail on the fire side, so that when the structure collapses, the wall can be separated from this structure without jeopardising the separating function of the wall, which must remain attached to the steel structure on the other side of the wall and therefore not exposed to the fire. The partition fire wall may also be fixed to the supporting steel structure of the building, which remains continuous at the location of the walls. In this situation, appropriate measures must be taken to prevent the collapse of fire walls because of significant fire-induced movement of the steel structure. These measures mainly concern the fire protection of the steel members (columns, portal frames) supporting the fire walls. In addition, the positioning of fire walls throughout the building means that roof members such as purlins and rafters pass through the tops of the walls. Consequently, structural members that penetrate the walls must also be partially fire protected. This protection must allow the fire-induced plastic hinges in the members to form away from the walls, thus preventing damage to the walls from the collapse of the heated steel members.

To ensure the appropriateness of the design recommendations proposed for the partition wall solutions under consideration, two fire tests were carried out in the PAVUS testing laboratory. The first test involved a fire wall made of sandwich panels connected to an unprotected steel structure by two fusible link solutions based on conventional steel connections with aluminium bolts as the fusible component. The second test involved a fire wall made of steel-faced sandwich panels fixed to an unprotected steel structure and penetrated by two steel purlins supporting an insulated steel roof. The results from the tests, presented in Deliverable D3.2 [2] and D3.3 [1] respectively, were used to check the ability of the 3D FE models developed in a pre-modelling work to simulate as accurately as possible the structural behaviour of the tested elements. This deliverable aims to report on the comparison results and the developed FE models.

The results of a comparative study carried out to compare several 3D numerical models developed with different FE codes (ANSYS, Ls-dyna and ABAQUS) that could be used to investigate the fire resistance of the fusible link solutions investigated in the project are also summarised. This allows to make sure of the relevance of numerical results obtained with different models.

2 RESULTS OF PRELIMENARY COMPARATIVE STUDY

This section summarises the result of a comparative study was performed to compare several 3D detailed models developed with different FE codes (ANSYS, Ls-dyna and ABAQUS) that could be used to investigate the fire resistance of the fusible link solutions instigated in the scope of the project FISHWALL and to check their capability to simulate the structural behaviour of the studied fusible links. The comparative study is based on three benchmark cases with increasing level of complexity, dealing with the same fusible link solution. The aim of the first study case is to calculate the shear resistance of the considered fusible system at ambient temperature. The aim of the second study case is to calculate the shear resistance of the fusible system at elevated temperature. The aim of this last study case is to calculate the fire resistance of the fusible system exposed to standard fire conditions, requiring a two steps analysis. The first step comprises the determination of temperature fields in the fusible system. The second step consists of calculating the fire resistance of the fusible system considering the temperatures previously determined.

2.1 Selected fusible system

The Figure 2.1 gives the schematic of the selected fusible system on which the three case studies are based. It consists of a Z-shaped steel profile and a steel channel arranged back to back and linked together with two M12 aluminium bolts. Figure 2.2 presents the geometry of the steel profiles composing the fusible link.

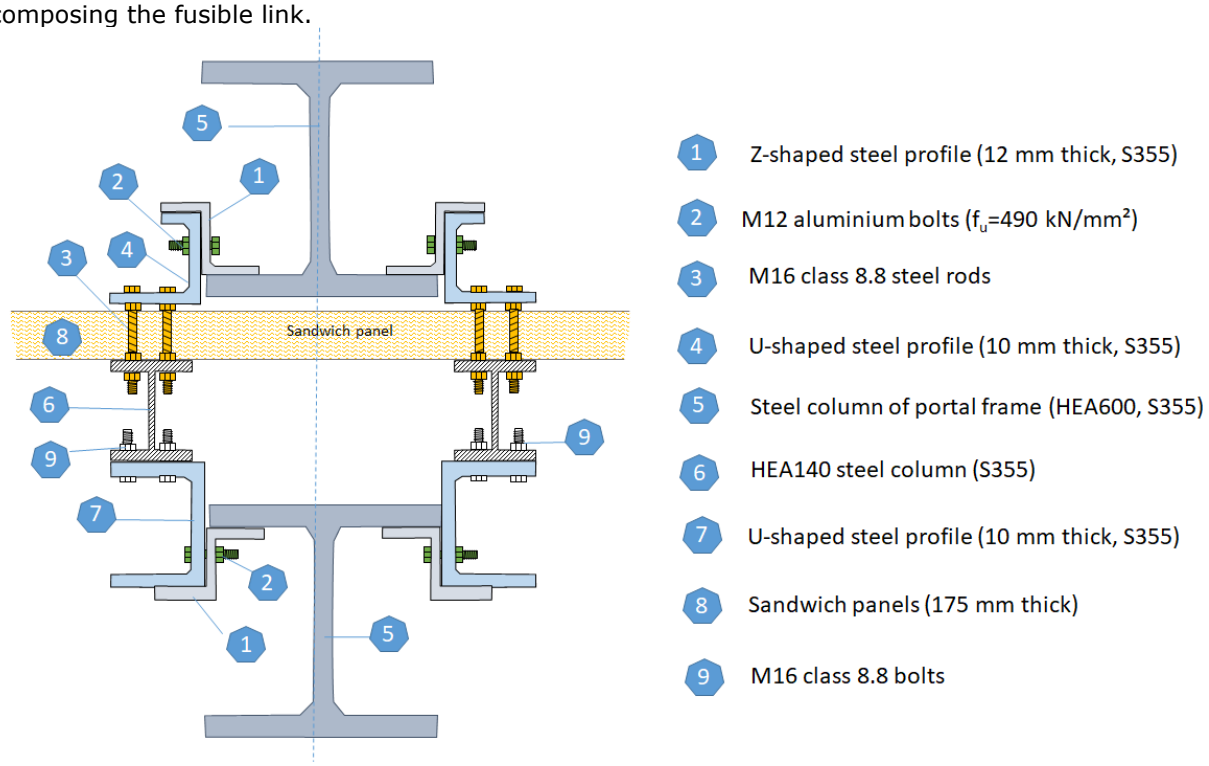

Figure 2.1: Shematic of the investigated fusible system

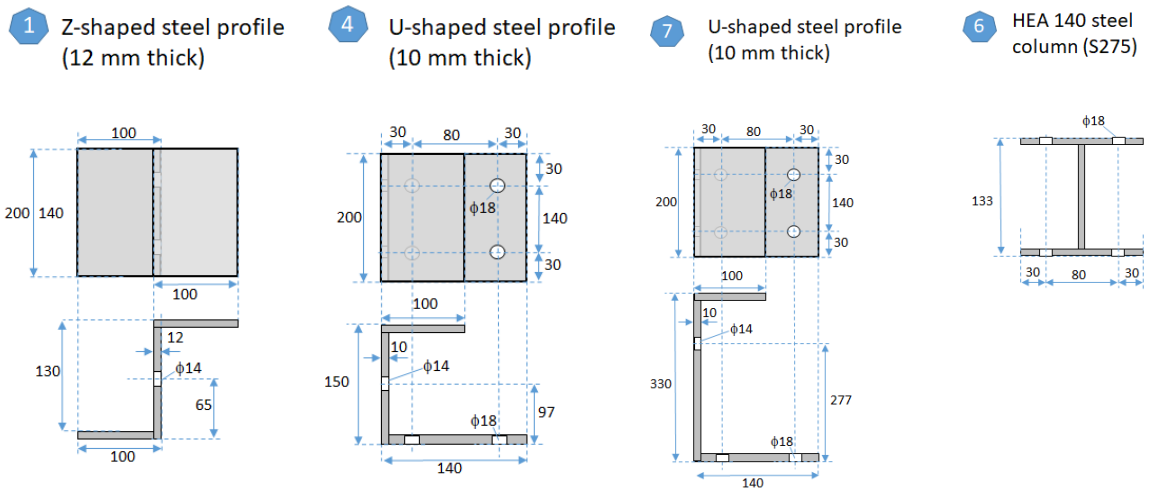

Figure 2.2: Dimensions of steel profiles composing the fusible link

2.2 Case study n°1: Shear resistance of the fusible system at normal temperature

The aim of this first case study was to calculate the shear resistance of the fusible system at normal temperature.

2.2.1 Geometrical details and loading conditions

The first case study deals only with the part of fusible link showed in Figure 2.1. The steel rods passing through the fire wall made of sandwich panels are not considered here. Displacements UY and UZ of the lower surface of the largest flange of the steel channel are assumed to be restrained (on the whole surface), while a shear force V (uniformly distributed) is applied on the steel plate (corresponding to the lower flange of the steel column of a portal frame) on which the Z-shaped steel profile is welded. The displacement Ux at the end of the lower flange of the Z-shaped steel profile as well as the end of the steel plate is assumed to be restrained (on the whole width).

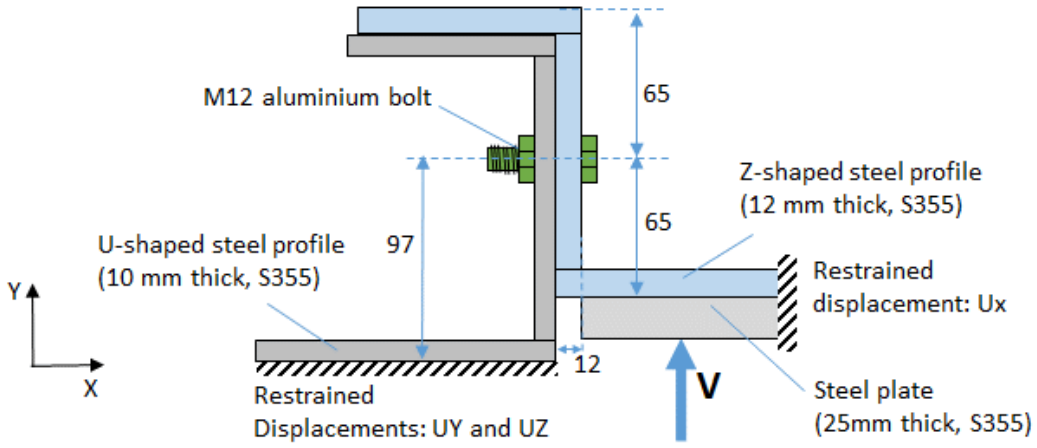

Figure 2.3: Geometrical details for case study n°1

2.2.2 Numerical analyses

The mechanical behaviour of the fusible system is analysed using FE codes ANSYS, Ls-dyna and ABAQUS. Several simplifications in modelling were considered to reach an adequate compromise between the model accuracy and the computational cost associated to the calculations.

2.2.2.1 Modelling assumptions

The following assumptions were adopted:

- The fusible system is meshed with brick finite elements, marked as C3D8R in ABAQUS code and solid185 in ANSYS code. A minimum of three elements is used for modelling correctly the thickness in steel profiles.
- Due to symmetry, only half of the fusible system is modelled and meshed. Appropriate boundary conditions (restraining UZ displacement) are applied to the plane of symmetry.
- Bolts are modelled as detailed as possible. Nevertheless, some features of the geometry that are assumed to have insignificant effect on the response of the joints are ignored. First, threaded parts of the bolts and nuts (fillets) are omitted and the bolt–nut assembly is modelled as a simple component, assuming that relative motion between bolts and nuts, or loosening, does not take place during loading. Moreover, the bolt head and the nut were modelled as being cylindrical rather than hexagonal in ABAQUS. Lastly, no washers are modelled.
- Aluminium bolts were modelled with either nominal (i.e. 12mm) or effective diameter (approximately 10.4mm).
- Bolt-hole clearances are either considered (bolt holes are 2mm larger in diameter than the bolts) or neglected in the analyses.
- Interaction between all link components was modelled using surface-to-surface contact, neglecting friction phenomenon. This includes the contact between the steel profiles, the bolt heads and shanks, and the upper surface and holes of the steel profiles. Aluminium bolts are less resistant and rigid than steel members. Hence, they are denoted as the master surfaces in contact parts and meshed coarser than the slave surfaces to increase the contact convergence rate. Penalty function was chosen as the contact algorithm. Default values were adopted for most of the contact-related parameters.
- The fusible system is subjected to a gradually increasing shear load V until failure occurs (see Figure 2.3).
- A quad-linear material model with strain hardening represents the constitutive behaviour of steel profiles, while based on test results given in the project deliverable D3.1 [3], a trilinear stress-strain relationship defines the constitutive behaviour of aluminium bolts (see Figure 2.4), considering the nominal characteristics reported in Table 1.

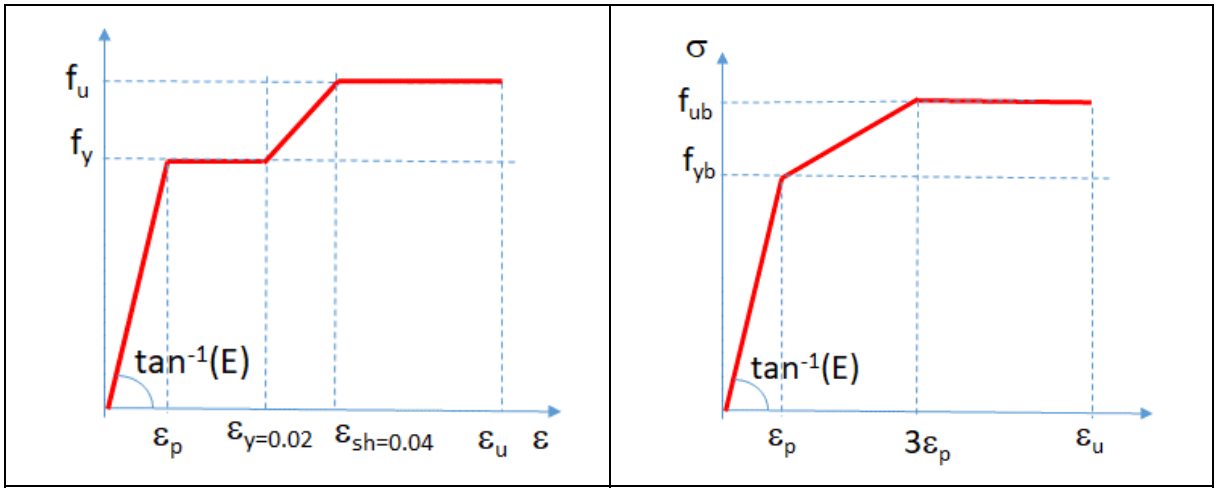

a) Steel profiles b) bolts

Figure 2.4: Strain-stress relationships for steel profiles and bolts

Table 1: Materials properties for steel profiles and aluminium bolts

Properties	Steel profile S355	Aluminum bolts
Young's modulus E (N/mm^2)	210000	70000

Yield strength f_y (N/mm^2)	355	420
ultimate strength f_u (N/mm^2)	1.25×f_y	490
Ultimate strain ε_u	0.2	0.05
Poisson's ratio	0.3	0.3
Density (kg/m^3)	7850	2700

Figure 2.5 presents the meshing adopted in modelling of the investigated fusible system.

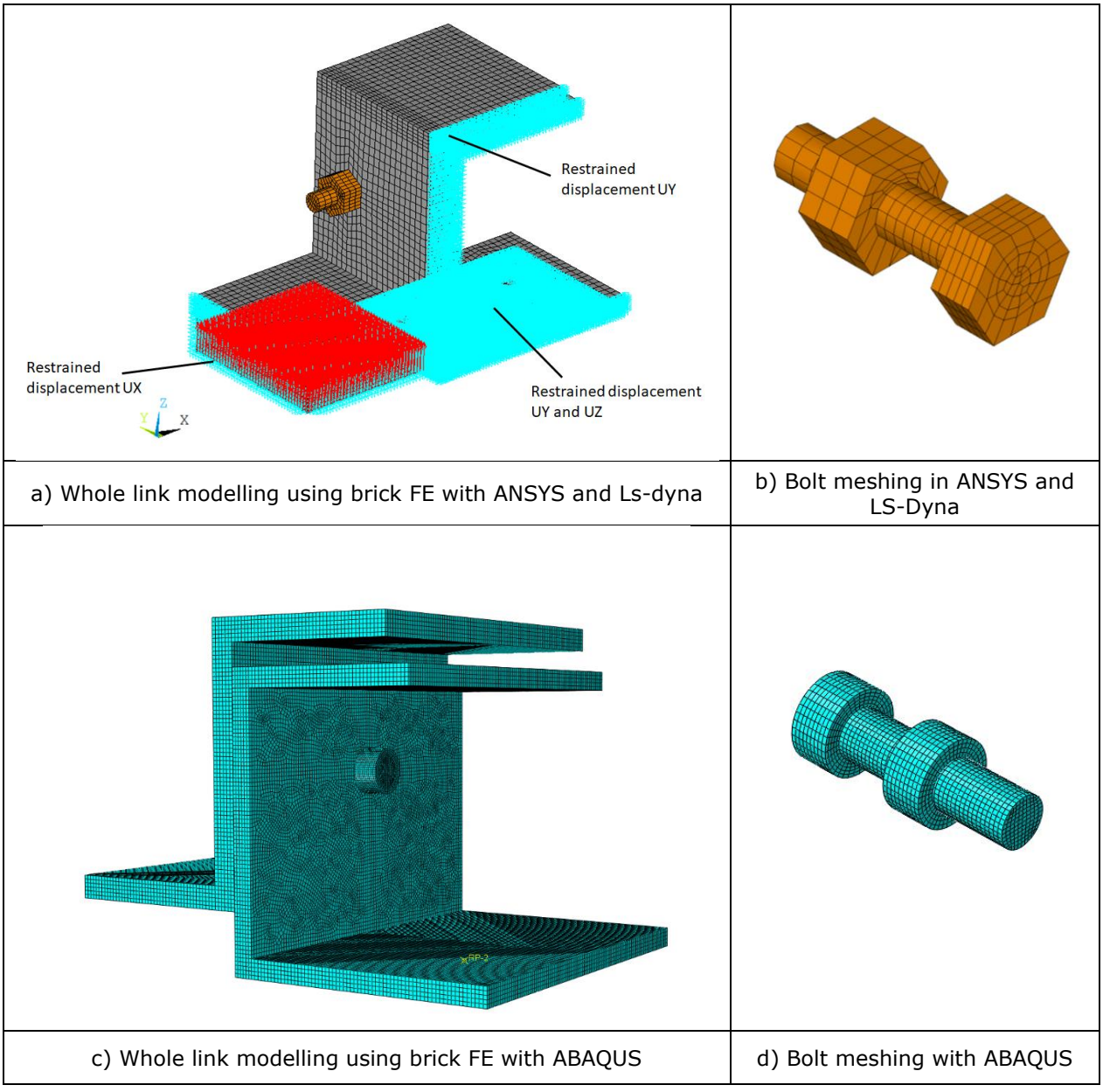

a) Whole link modelling using brick FE with ANSYS and Ls-dyna

b) Bolt meshing in ANSYS and LS-Dyna

c) Whole link modelling using brick FE with ABAQUS

d) Bolt meshing with ABAQUS

Figure 2.5: 3D finite element model for the mechanical analysis of the investigated fusible link

2.2.2.2 Main results

The main results of the FE analyses are presented below. Figure 2.6 gives the evolution of the vertical displacement of the Z-shaped steel profile as a function of the applied load calculated from the

different codes used. Figure 2.7 shows the deformed shape and corresponding Von Mises plastic strain distributions predicted by the ANSYS model in the meshed components of the fusible system.

Regarding results, all models predict a failure of the fusible system by bolt shear, as expected. The comparison to the analytical model clearly shows the satisfactory accuracy of developed models in predicting the shear resistance of the considered fusible system (calculated from the ultimate strength and the modelled diameter of bolts).

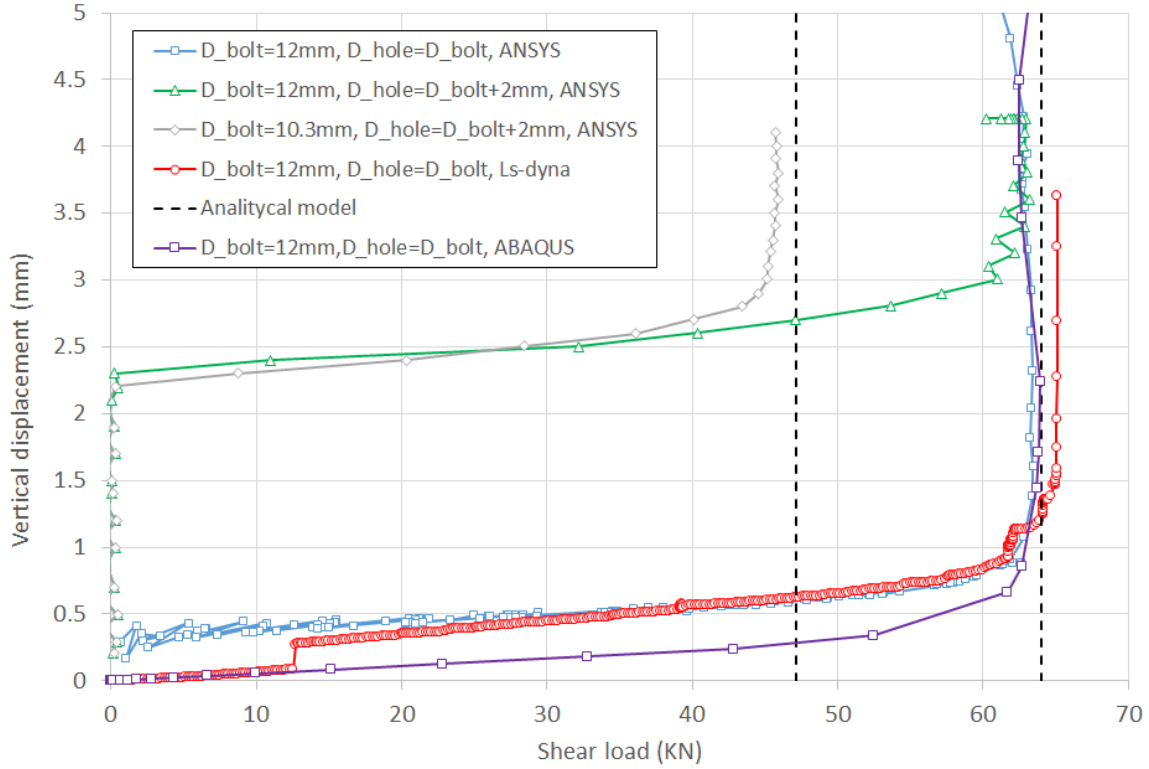

Figure 2.6: Displacement-load curve calculated for the modelled fusible link modelled - Comparison between numerical and analytical models

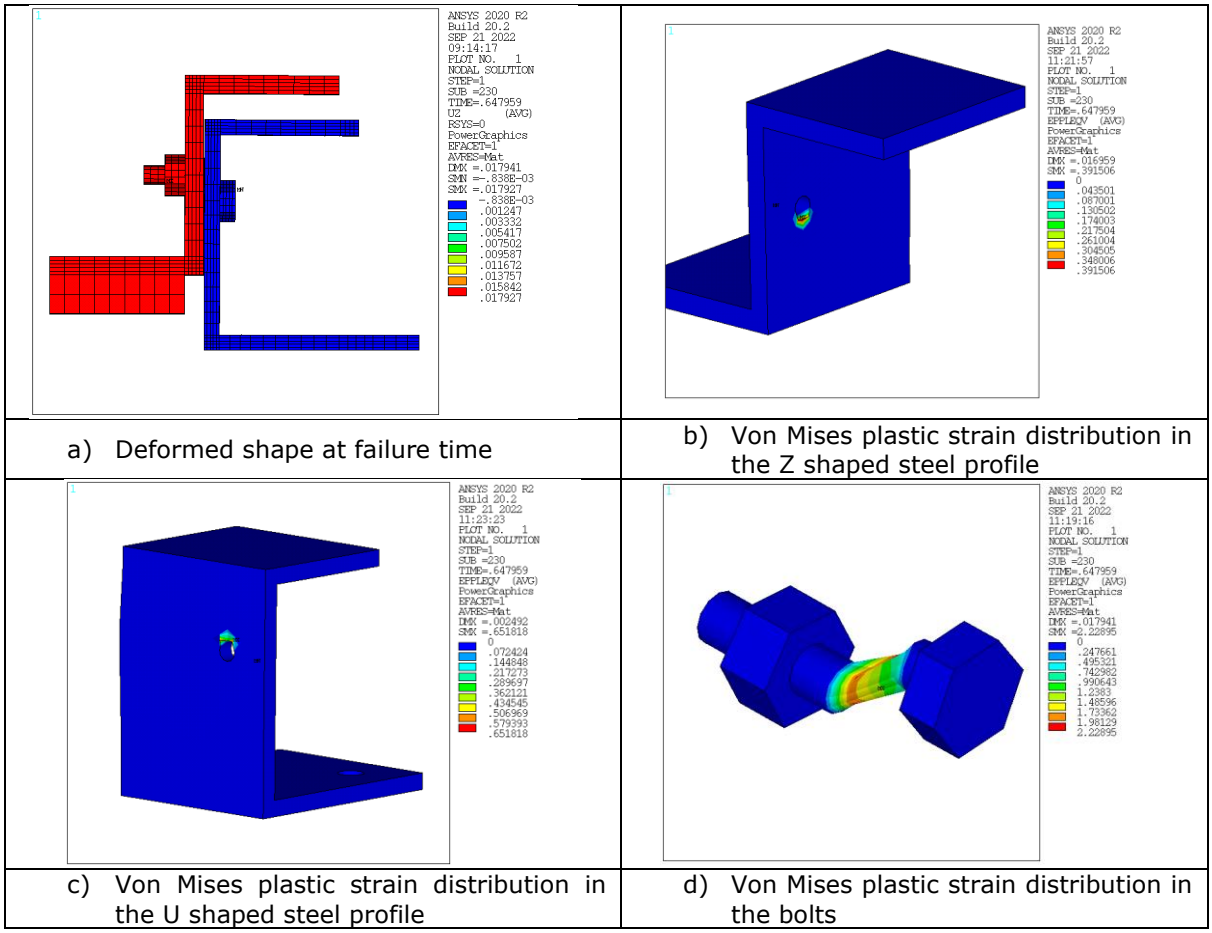

a) Deformed shape at failure time

b) Von Mises plastic strain distribution in the Z shaped steel profile

c) Von Mises plastic strain distribution in the U shaped steel profile

d) Von Mises plastic strain distribution in the bolts

Figure 2.7: Deformed shape and Von Mises plastic strain distributions in components of the fusible system at failure time - ANSYS

2.2.3 Case study n°2: Shear resistance of the fusible system at elevated temperature

The aim of this second case study is to calculate the shear resistance of the fusible link system at elevated temperature, assuming a uniform temperature distribution across all components (steel profiles and aluminium bolts).

2.2.4 Geometrical details and loading conditions

The geometric details are the same as those in the first case study. However, the fusible link is now subjected to a constant shear force of 20 kN and a gradually increasing uniform temperature until failure.

2.2.5 Numerical analyses

2.2.5.1 Modelling assumptions

As the fusible link is the same as that considered in the first case study, the numerical modelling is based on that developed previously, introducing relevant modifications for the temperature dependence of the material properties.

The mechanical properties of steel sections at elevated temperatures were taken from EN 1993-1-2, taking into account both the yielding plateau and work hardening and the nominal properties given in Table 2.

The mechanical properties of aluminium bolts were defined from the stress-strain relationship given in Figure 2.8, taking into account the nominal properties given in Table 1. As data from the Task 3.1 tests were not yet available, strength reduction factors at elevated temperatures were taken from EN 1999-1-2 (see Table 2).

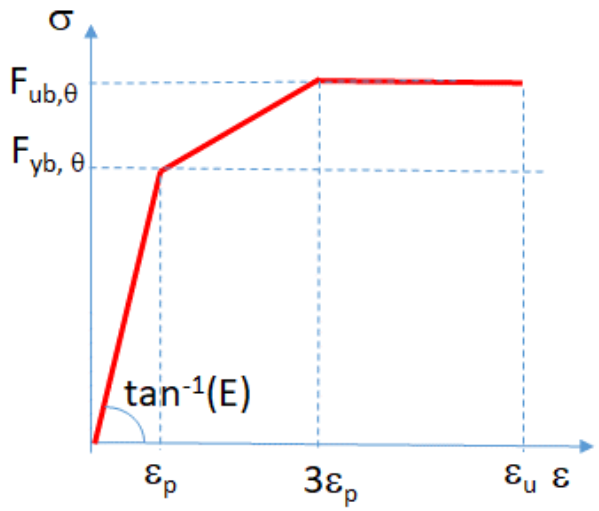

Figure 2.8: Strain-stress relationship for aluminium bolts at elevated temperature

Table 2: Reduction factors k_θ for aluminium bolts at elevated temperature

Temperature θ_a [°C]	$k_{E.\theta} = \frac{E_\theta}{E}$	$k_{y.\theta} = \frac{f_{yb.\theta}}{f_{yb}}$	$k_{u.\theta} = \frac{f_{ub.\theta}}{f_{yb}}$
20	1.0	1.0	1.0
100	0.97	0.9	0.9
150	0.93	0.75	0.75
200	0.86	0.5	0.5
250	0.78	0.23	0.23
300	0.68	0.11	0.11
350	0.54	0.06	0.06
400	0.4	0.045	0.045
550	0	0	0

2.2.6 Main results

The main results of the FE analyses are summarized in the following figures. The time-vertical displacement curve of the Z-shaped steel section is shown in Figure 97. The deformed shape of the fusible link at the time of failure is shown in Figure 98. It should be noted that all models predict failure of the fusible link by bolt shear as expected. The failure temperature calculated from the numerical models, in the range 236-244°C, is very close to the theoretical value calculated from the analytical model with the nominal shear resistance of the bolts at elevated temperature (calculated from the ultimate strength at elevated temperature and the modelled diameter of the bolts).

.

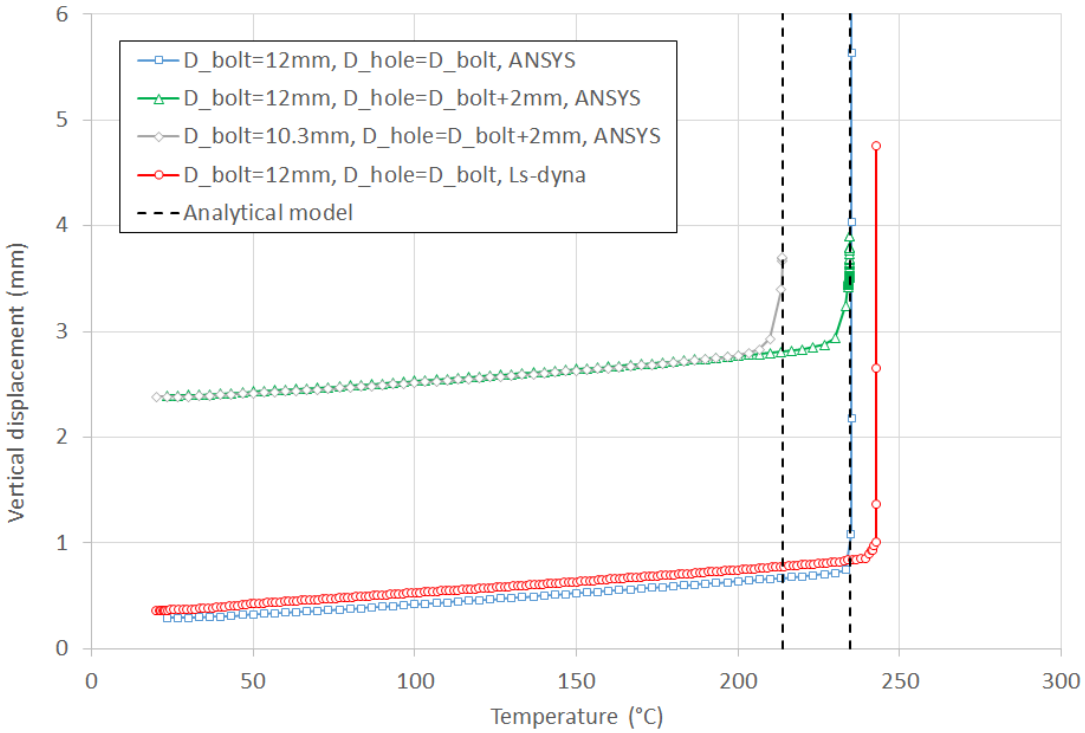

Figure 2.9: Displacement-temperature curve calculated for the modelled fusible link - Comparison between numerical and analytical models

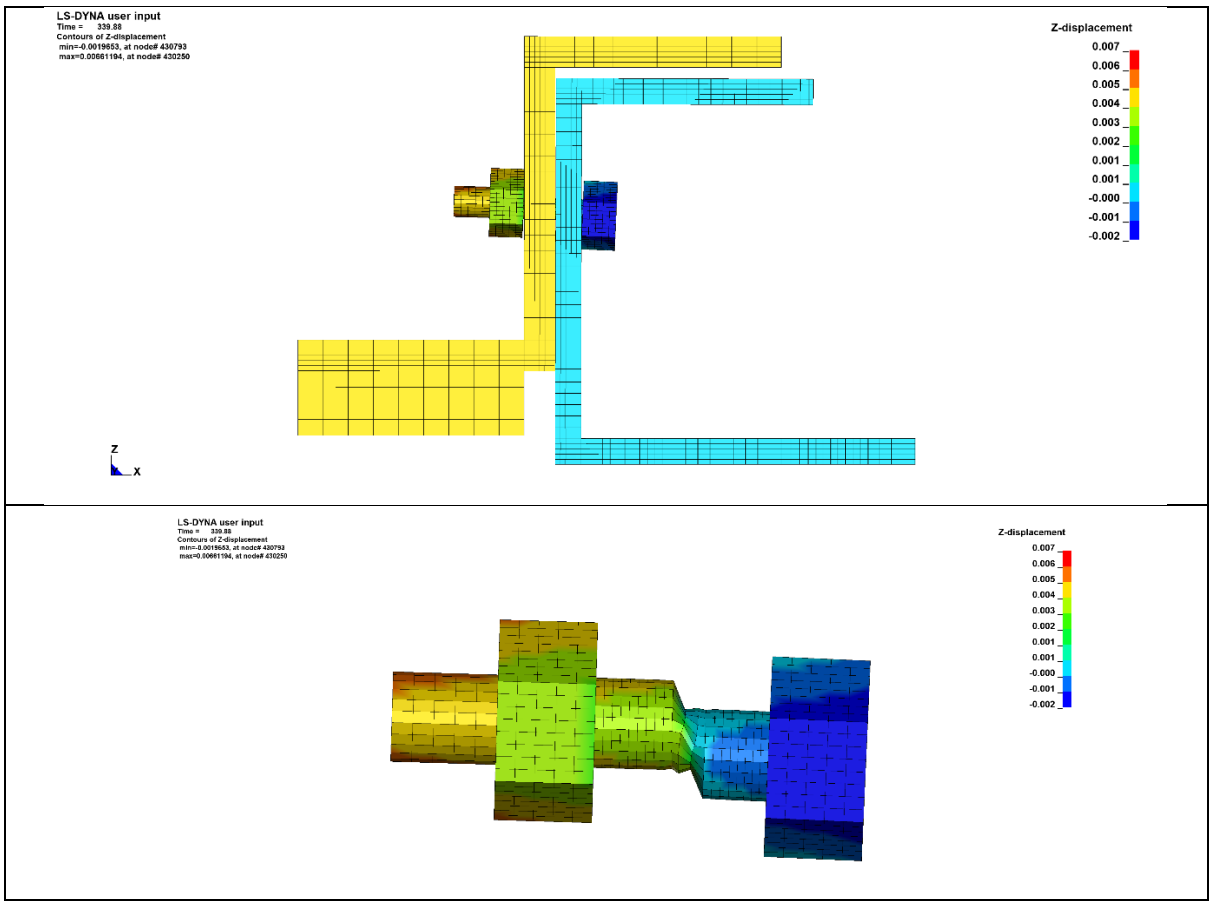

Figure 2.10: Deformed shape of the fusible system at failure time – Ls-dyna

2.3 Case study n°3: Fire resistance of the fusible link exposed to standard fire

The objective of this third case study was to determine the standard fire resistance of the fusible link when subjected to shear loading. This involved conducting a sequentially coupled three-dimensional thermal-mechanical analysis. The fusible system was modelled using solid elements.

2.3.1 Geometric details and loading conditions

The geometric details of the case study are reported in Figure 3.11. The sizes of the steel profiles are the same as those in the first case study. A part of the steel column supporting the sandwich panels (i.e. the flange in contact with the wall) and the steel rods passing through the wall are now considered. The column flange is assumed to be fully restrained.

The fusible link is subjected to the nominal standard fire curve up to 120 min and is loaded: first with the steel rods under compression with a shear force V=50 kN, and then with aluminium bolts under shear force V=20 KN.

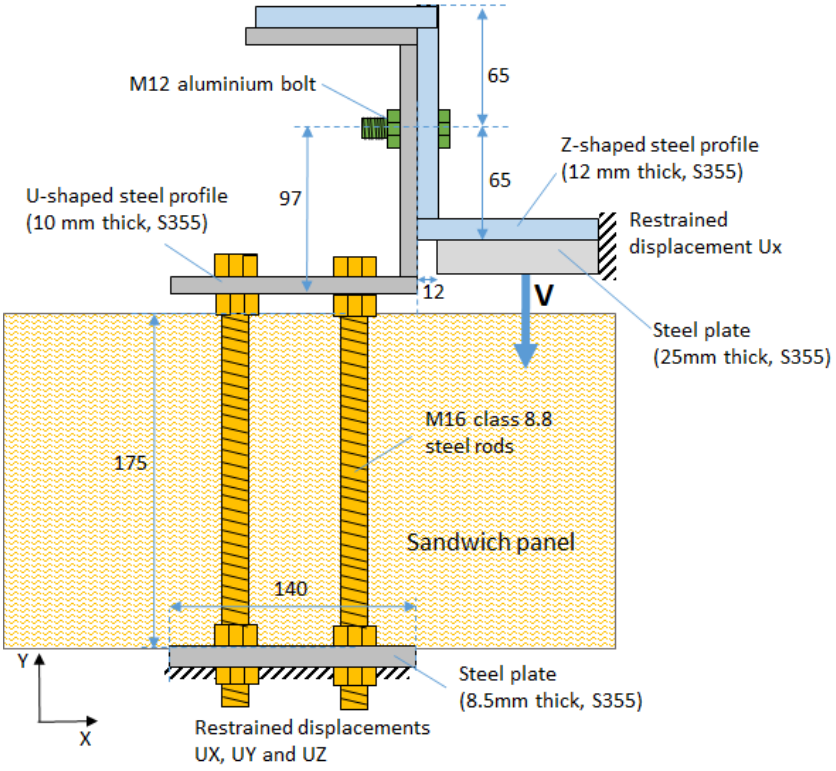

Figure 2.11: Geometrical details for case study n°3

2.3.2 Numerical analyses

2.3.2.1 Modelling assumptions

Since the fusible link is the same as that considered in the previous study cases, the numerical models are based on those developed previously, with appropriate modifications to take into account thethe following considerations :

- The heat flows transferred to the fire exposed and unexposed surfaces of the fusible link system are calculated according to EN 1991-1-2, using a convective heat transfer coefficient of αc = 25 W/m²K, a surface emissivity of 0.7 and a fire emissivity of 1.0 on the fire exposed side. The convective heat transfer coefficient is set to 4 W/m²K on the unexposed side. Direct heat transfer is assumed between all components, no gaps due to differential thermal expansion of materials and no shadow effect are considered.
- Perfect contact between all elements is assumed.
- The thermal properties of carbon steel and aluminium bolts are according to EN 1993-1-2 and EN 1999-1-2 respectively.

- The thermal properties of the mineral wool of sandwich panels (considered as independent of the temperature) are the following: density: 120 kg/m^3, specific heat: 1000 J/kg.K and thermal conductivity: 0,045 W/m.K;
- The mechanical properties of steel rods are defined from the stress-strain relationship given in Figure 2.12: Strain-stress relationship for steel rods, considering the parameters given in Table 3;
- Influence of the sandwich panel on the mechanical behaviour of the fusible link is neglected.

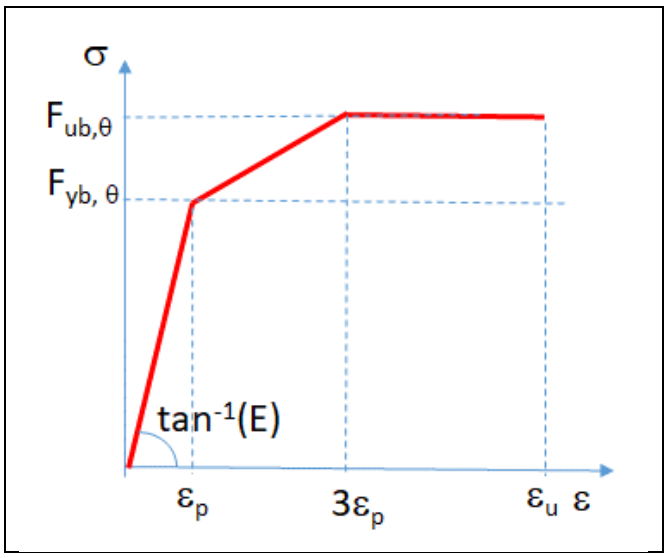

Figure 2.12: Strain-stress relationship for steel rods

Table 3: Reduction factors k_θ for steel rods

Temperature θ_a [°C]	$k_{E.\theta} = \frac{E_\theta}{E}$	$k_{y.\theta} = \frac{f_{yb.\theta}}{f_{yb}}$	$k_{u.\theta} = \frac{f_{ub.\theta}}{f_{yb}}$
20	1,000	1,000	1,000
100	1,000	0,968	0,968
150	0,950	0,952	0,952
200	0,900	0,935	0,935
300	0,800	0,903	0,903
400	0,700	0,775	0,775
500	0,600	0,550	0,550
600	0,310	0,220	0,220
700	0,130	0,100	0,100
800	0,090	0,067	0,067
900	0,0675	0,033	0,033
1000	0,0450	0,000	0,000

For information purposes, the following figures show the three-dimensional models developed with ANSYS for both thermal and mechanical analyses of the fusible link under consideration.

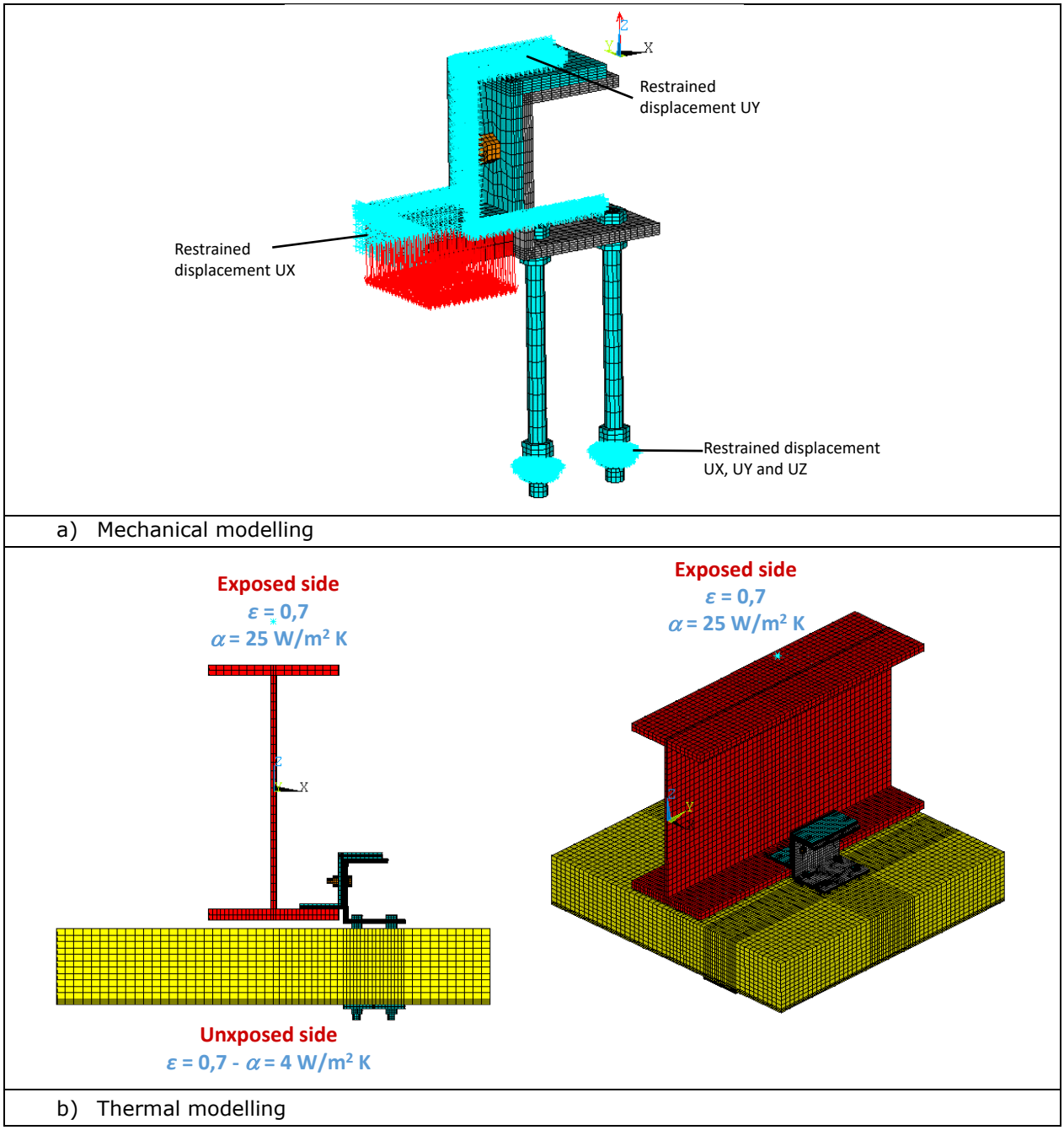

Figure 2.13: FE models developed with ANSYS for the thermal and mechanical analyses of the considered fusible link

2.3.2.2 Main results

The main results of the FE analyses are presented below. The calculated temperature curves at major points along the fusible system are shown in Figure 2.14 and Figure 2.15. Figure 2.16 and Figure 2.15 give the vertical displacement-time curves calculated at the middle of the lower flange of the Z-shaped profile while Figure 2.18 to Figure 2.20 show the deformed shape of the fusible link at failure time obtained for both loading situations. It can be noted that the results obtained with the three models are very similar in terms of displacements and failure modes. Regarding the calculation of temperature rise, it should be noted that the temperatures calculated in certain parts of the fastener under consideration are slightly higher with ABAQUS than with the ANSYS model, with no obvious explanation for this difference.

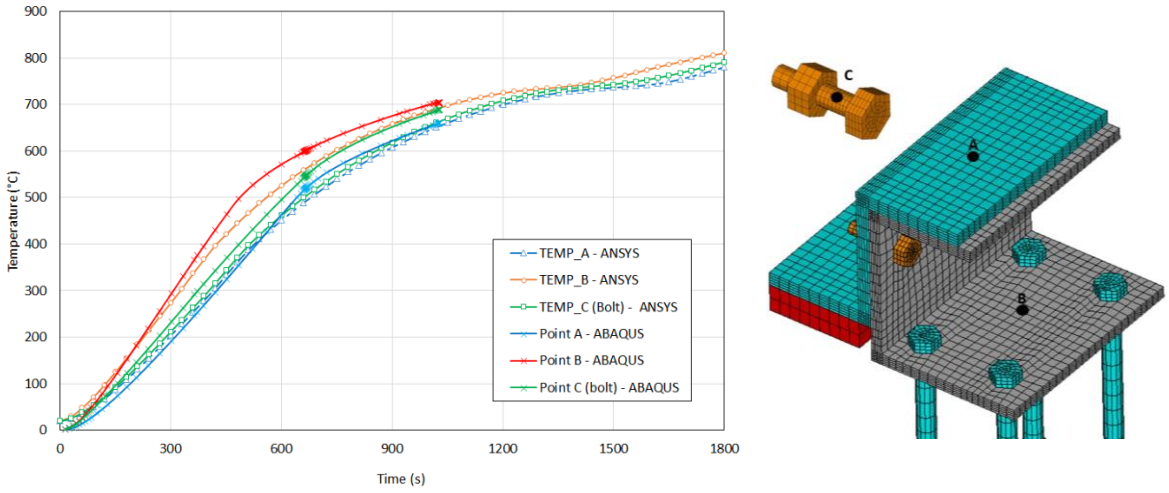

Figure 2.14: Time-temperature curves calculated in some points in the fusible system

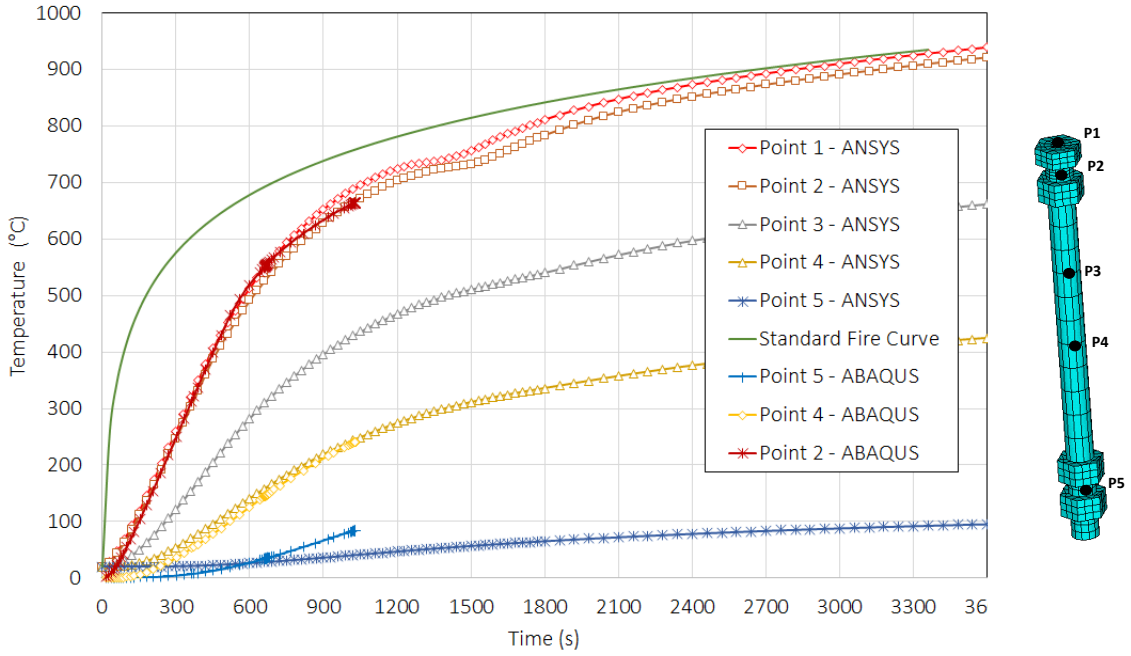

Figure 2.15: Time-temperature curves calculated in some points along the steel rods

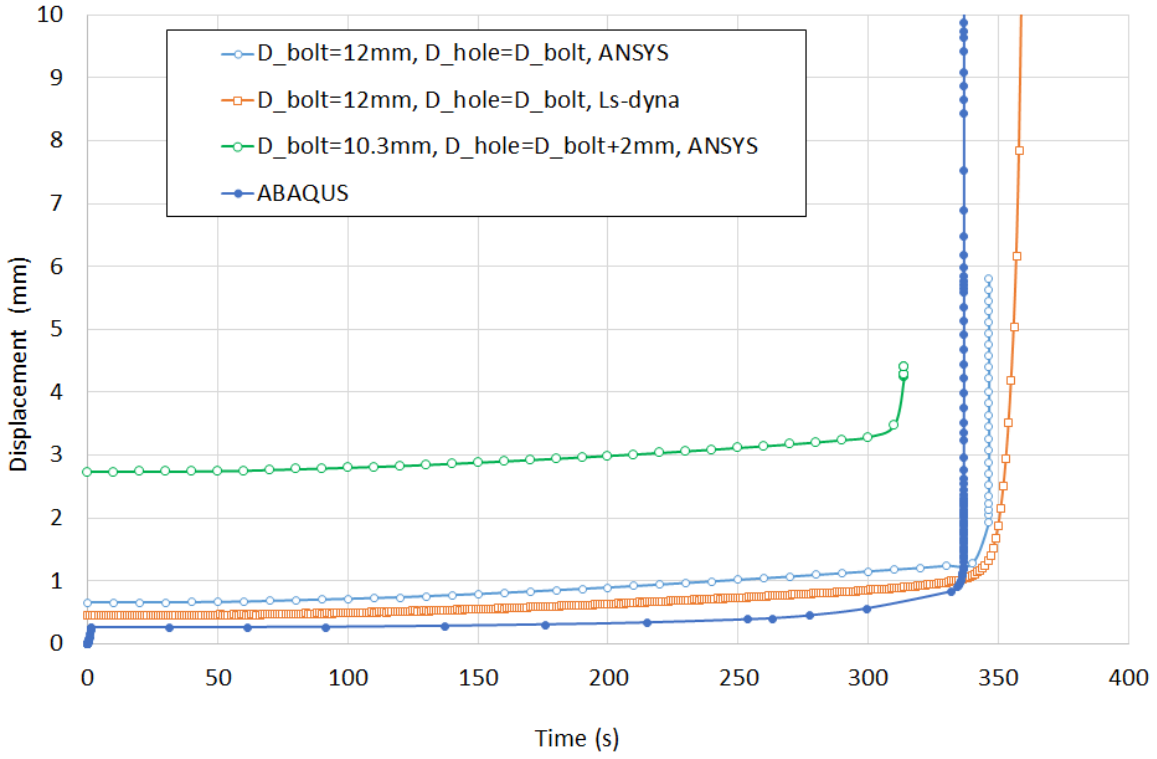

Figure 2.16: Vertical displacement-time curves calculated for the fusible link – Aluminium bolts in shear

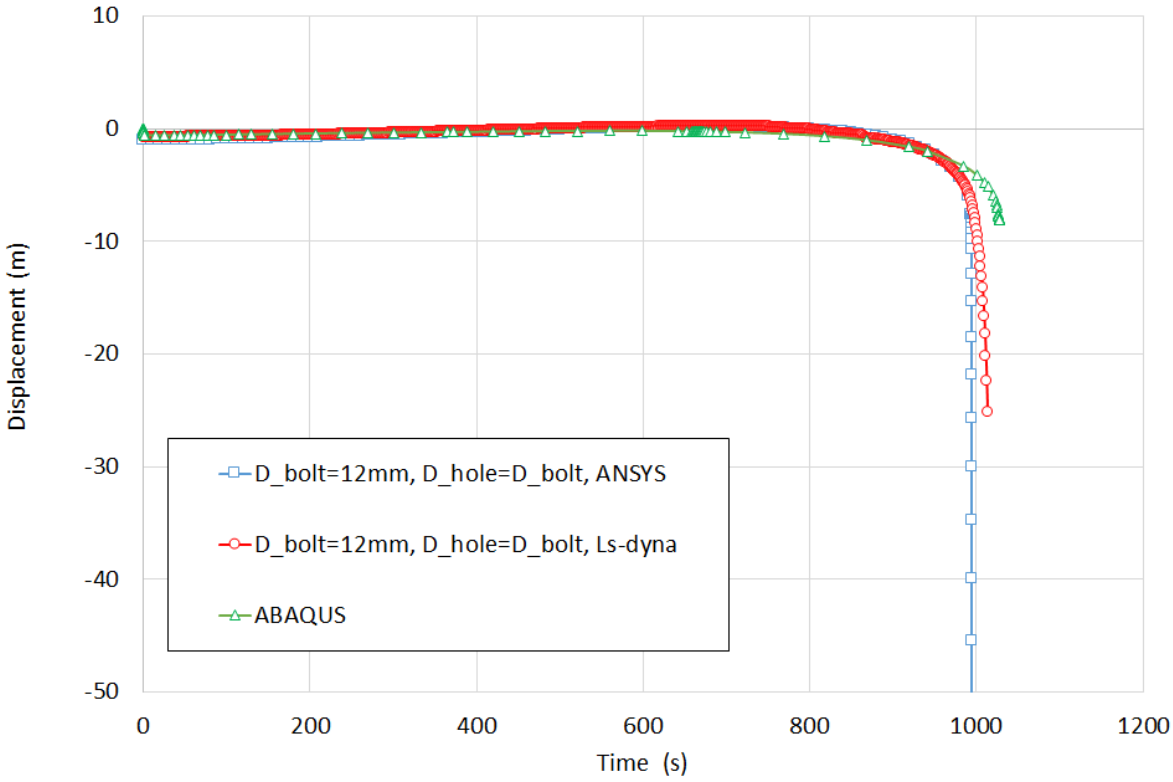

Figure 2.17: Vertical displacement-time curves calculated for the fusible link – steel rods under compression

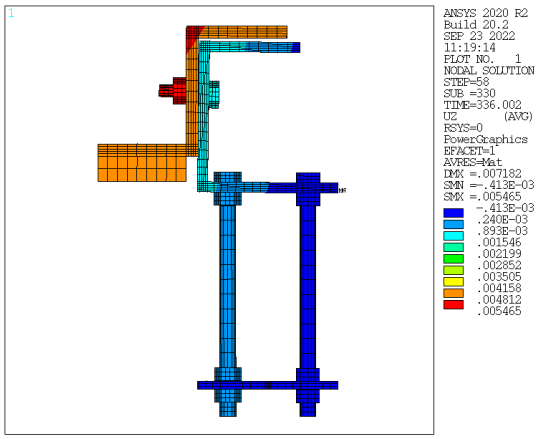

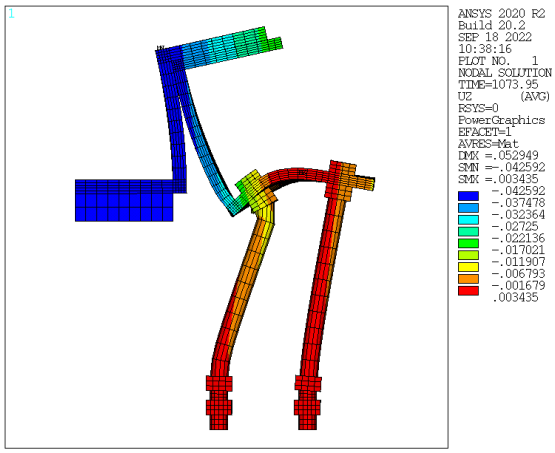

Aluminum bolts under a shear force V=20 KN

Steel rods under compression with a shear force V=50 kN

Figure 2.18: Deformed shape of the fusible link predicted by the ANSYS model at failure time

Figure 2.18Figure 2.20

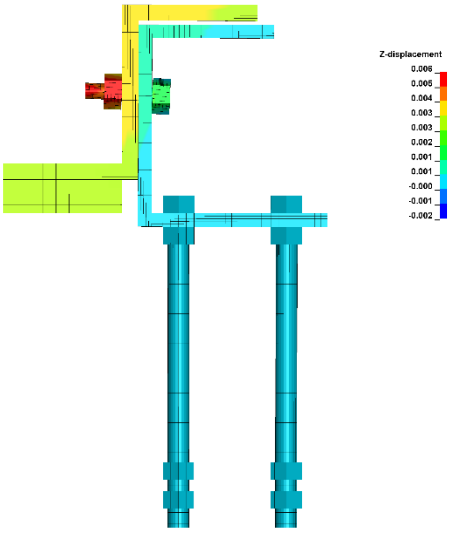

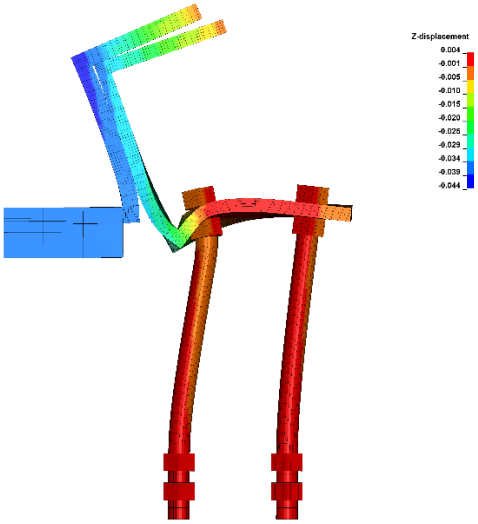

Aluminum bolts under shear force V=20 KN

Steel rods under compression with a shear force V=50 kN

Figure 2.19: Deformed shape of the fusible link predicted by the Ls-dyna model at failure time

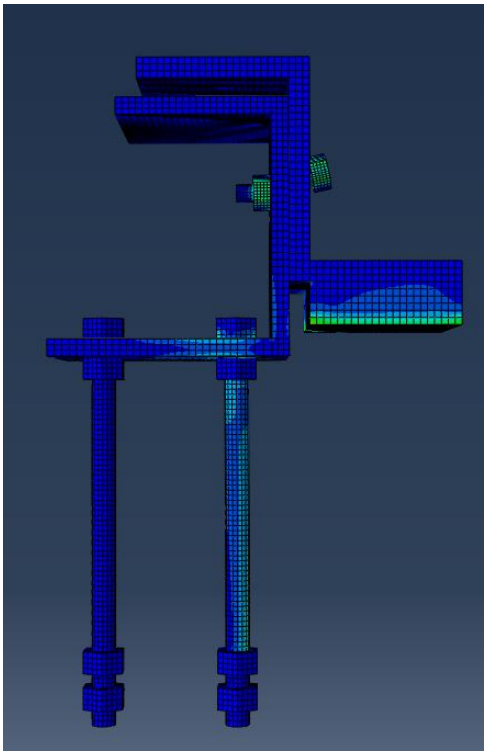

Aluminum bolts under shear force V=20 KN

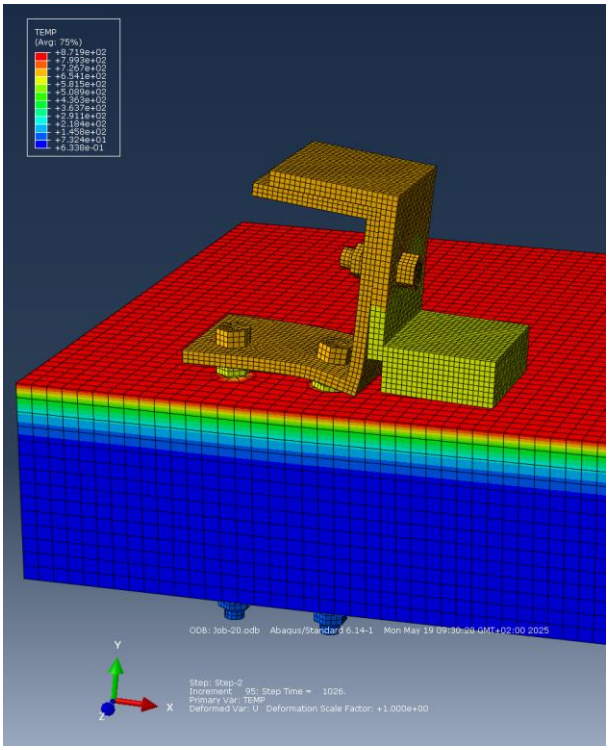

Steel rods under compression with a shear force V=50 kN

Figure 2.20: Deformed shape of the fusible link predicted by the ABAQUS model at failure time

3 VALIDATION OF NUMERICAL MODELS DEVELOPPED FOR STEEL PORTAL FRAMES ASSOCIATED TO FUSIBLE LINKS

Numerical analyses of the test performed in Task 3.5 were carried out to better understand the behaviour of the tested specimen, to provide a scientific interpretation of the test and to explain the observed behaviour. This work also validated the ability of the detailed 3D numerical models developed in Task 3.4 to simulate the thermo-mechanical behaviour of the fusible links tested.

The results of the FE model compared with the results of the test carried out in Task 3.5 are presented below.

3.1 Brief description of the fire test

3.1.1 Tested specimen

A detailed description of the test setup and test measurements is given in the deliverable D3.3 of the FISHWALL project [1]. Therefore, only a brief overview is given here.

Figure 3.1 shows a schematic of the test arrangement. The test specimen consisted of a non-load bearing fire wall measuring 3m wide × 3.2m high × 0.175 m thick, made of lightweight sandwich panels spanning horizontally between two fire-unexposed steel columns (HEA320) connected to steel structures, either semi-portal frames on the fire-exposed side or either single steel columns (HEA 140) on the other side, using two different "fusible" systems.

Each semi-portal frame consisted of a single steel column (HEA 320) connected by a moment resisting bolted connection to a steel beam (IPE 360) supported at its free end by means of a forked support fixed to a fire protected steel beam (HEB500) as part of a horizontal support frame placed around the furnace. The fork support was designed to allow a free axial thermal expansion of the beams along 50 mm. Steel base plates were welded to the bottom of the columns and bolted to 10 mm thick steel plates placed on the ground floor of the furnace. The bottom end of the columns located on the fire exposed side were fire protected.

With regard to the "fusible" systems, the following solutions were tested:

- The first link solution (see Figure 3.2) consists of an L-shaped folded plate welded to a 10 mm thick gusset plate and a U-shaped steel profile (with 10 mm thick) reinforced by a 12 mm thick stiffener placed back to back. They are assembled using two M12 aluminum bolts. The gusset steel plate is welded between the flanges of the portal frame column, while the U-profile is bolted to the column supporting the sandwich panels by means of four M16 threaded steel rods passing through the firewall.
- The second fusible link solution (see Figure 3.3) consists of an L-shaped steel profile (with 10 mm thickness) assembled with two M12 aluminum bolts to a UPN 240 steel channel spanning horizontally between the portal frame columns, each end of the UPN profile being bolted with three M20 bolts of grade 8.8 to a 10mm thick steel stiffener welded between the flanges of the portal frame columns. Slotted holes were made to allow the free longitudinal thermal expansion of the UPN 240. The L-shaped profiles are attached to the wall steel column by means of four threaded steel rods passing through the fire wall on the wall side and four steel bolts on the other side.

A vertical loading of 25 kN was applied at the beam's mid-span using dead weights. In terms of heating conditions, the test specimen was exposed to hot gas temperatures as close as possible to the ISO standard fire curve.

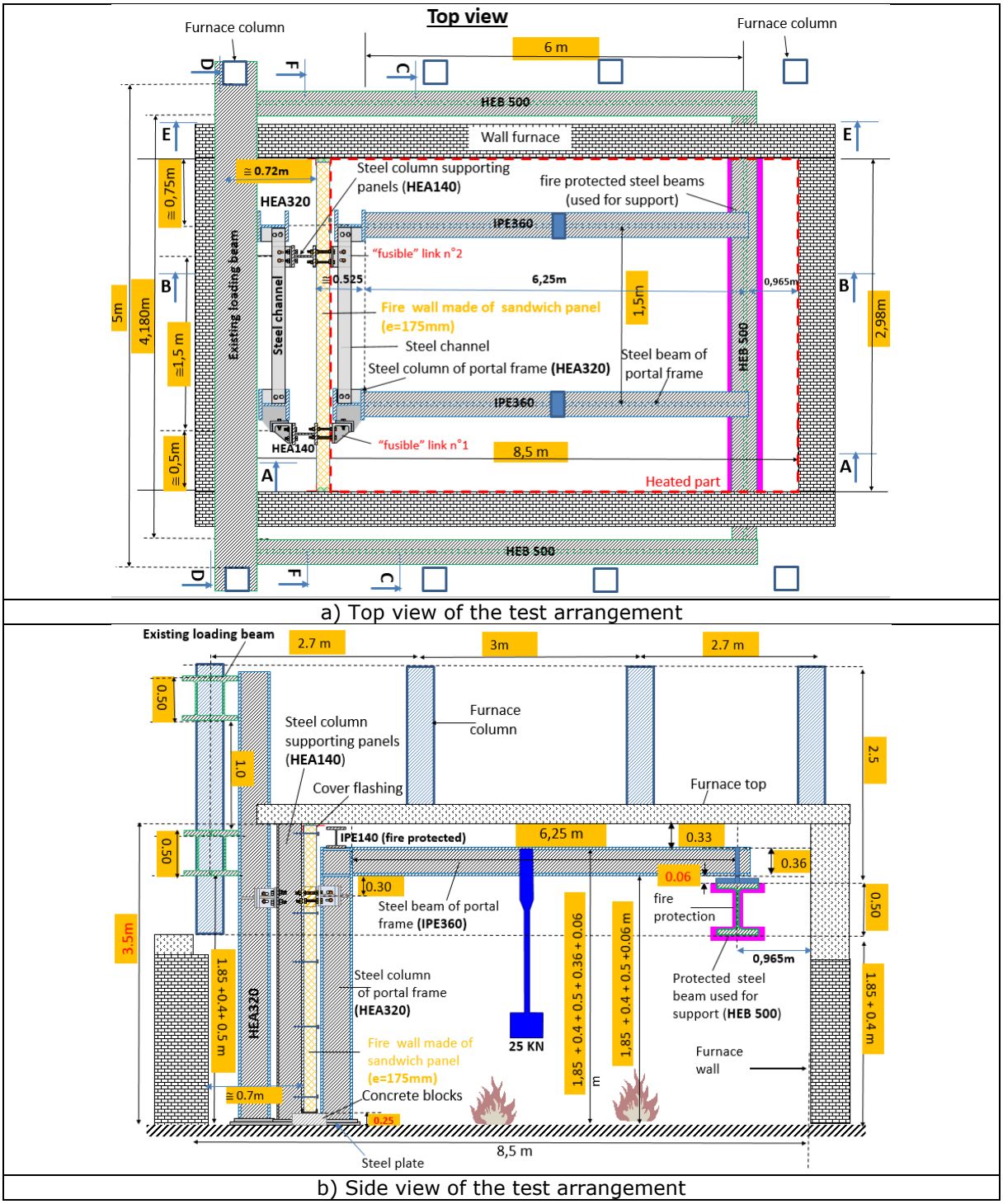

a) Top view of the test arrangement

b) Side view of the test arrangement

Figure 3.1: Schematic of the test arrangement

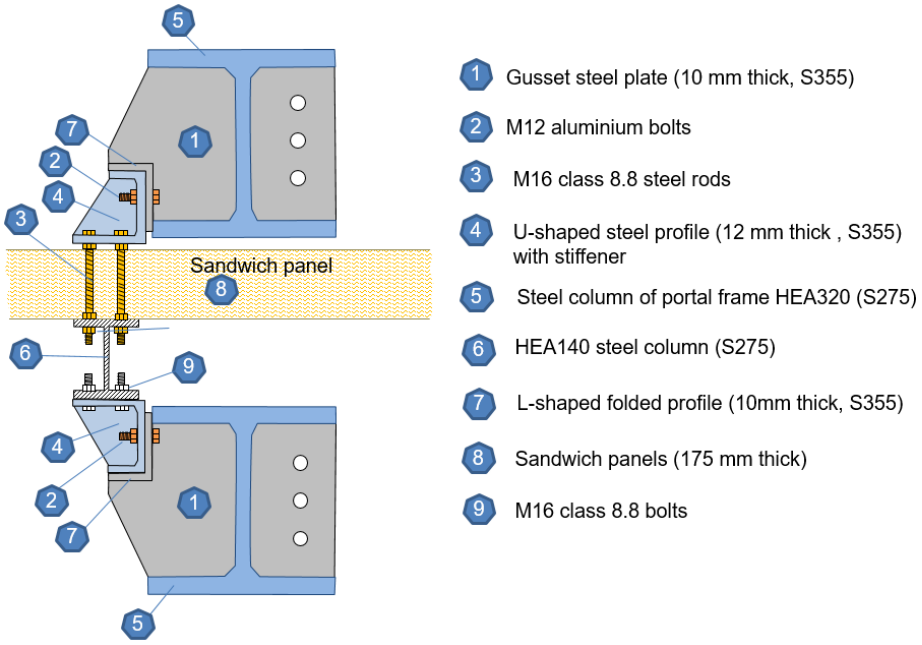

Figure 3.2: Geometrical details of the first fusible link configuration

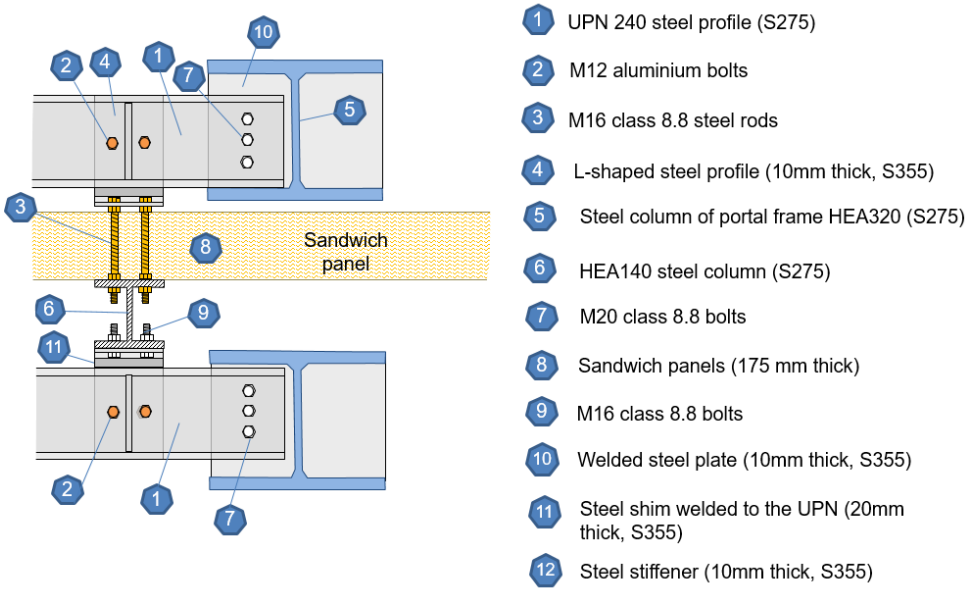

Figure 3.3: Geometrical details of the second fusible link configuration

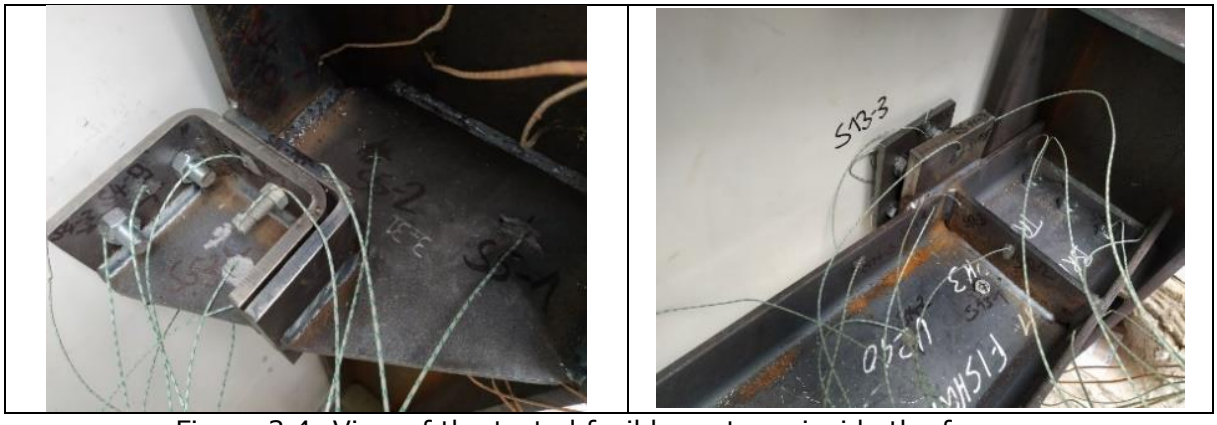

Figure 3.4: View of the tested fusible systems inside the furnace

3.1.2 Main experimental results

Figure 3.5 and Figure 3.6 show the evolution of the furnace temperature measured around the semi-portal frame n°1 (P1 to P6) and semi-portal frame n°2 (P7 to P12). They clearly show that the hot gas temperature distribution in the furnace is not uniform. The temperature curves measured around the semi-portal frame n°2 are generally higher than the ISO fire curve, while those around the semi-portal frame n°1 are lower. The maximum difference in temperature measured between the two portal frames can be as much as 160°C. Furthermore, the temperatures measured near the columns of the semi-portal frames (P1 and P4 for semi-portal frame n°1; P7 and P10 for semi-portal frame n°2) are similar and much lower than those measured in the centre of the furnace.

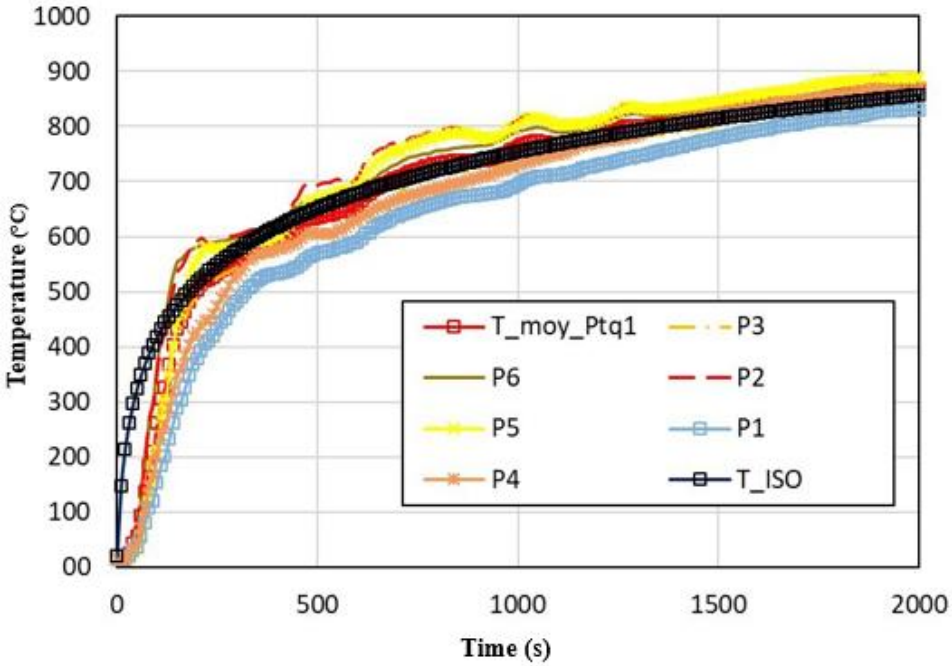

Figure 3.5: Hot gas temperature-time curves recorded around the semi-portal frame n°1

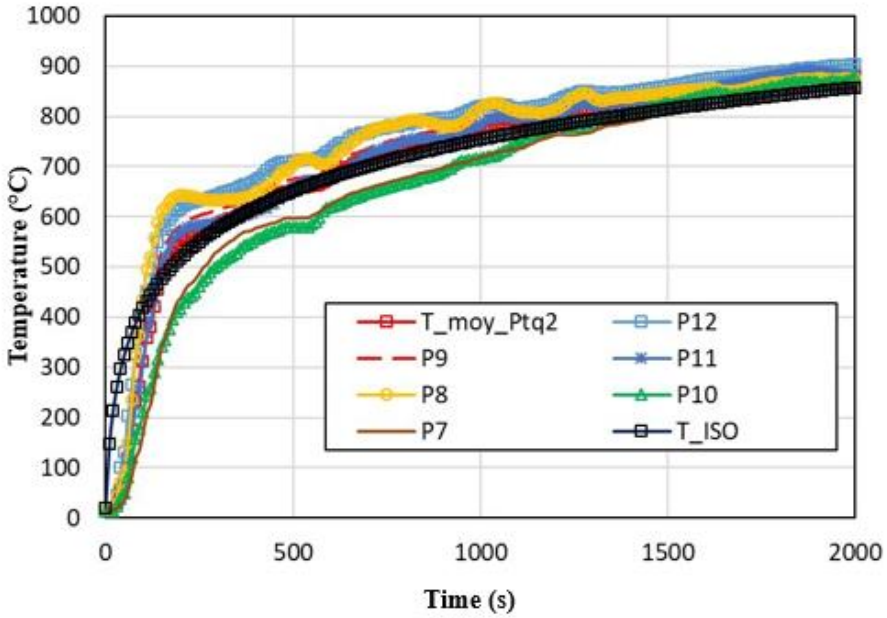

Figure 3.6: Hot gas temperature-time curves recorded around the semi-portal frame n°2

Figure 3.7 and Figure 3.8 show the temperature-time curves of the cross-sections located along the beams of the semi-portal frames (sections S1 and S7 are 0.25 m from the column; sections

S2 and S8 are 2.25 m from the column). They show a significant longitudinal temperature gradient along the length of each beam. In fact, the cross-sections closest to the columns (sections S1 and S7) heat up less quickly than sections S2 and S8, and the difference between the maximum and minimum temperatures of each part considered (web, top and bottom flanges) is approximately 150°C at 15 minutes for the two semi-portal frames. This difference is consistent with the temperature distribution of the hot gases in the furnace. Figure 3.9 shows a comparison of cross-sections temperatures of the two semi-portal frames. It shows that the heating of the beam cross-sections of semi-portal frame n°2 is greater than that of the corresponding beam cross-sections of the semi-portal frame n°1. This observation is consistent with the measured temperature distribution in the furnace. In fact, most of the temperature curves measured around semi-portal frame n°2 are above the ISO fire curve, while those measured around the semi-portal frame n°1 are below it. Regarding the heating of the columns, the temperature rises on sections S3 and S9 show a significant temperature gradient across the cross-section of the columns (see Figure 3.10 and Figure 3.11). In fact, the temperature of the flange furthest away from the fire wall (P1, P2) is almost like that of the web column (P3), and they are much higher than that of the flange closest to the fire wall (P4, P5), with a maximum difference of about 150°C at 1200 seconds, for the two semi-portal frames. It should be noted that the space between the column flange and the wall is only about 40 mm, which could have the effect of greatly reducing the heat flow of hot gases in this space. In addition, Figure 3.12 also shows the comparison of the average temperature between the two columns for the flange directly exposed to the fire (expo), the web (web) and the flange next to the fire wall (unexpo). Like the observations made for the heating of the beams, the temperature of section S9 of the column of semi-portal frame No. 2 is slightly higher than that of section S3 of the other column, with a maximum difference of approximately 22°C at 1000 seconds.

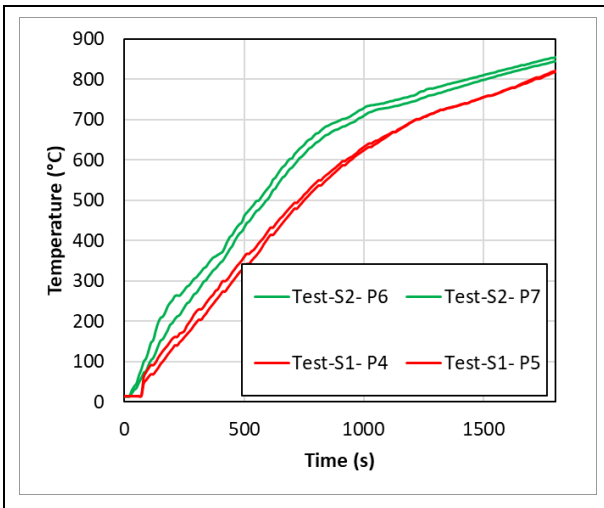

a) Bottom flange

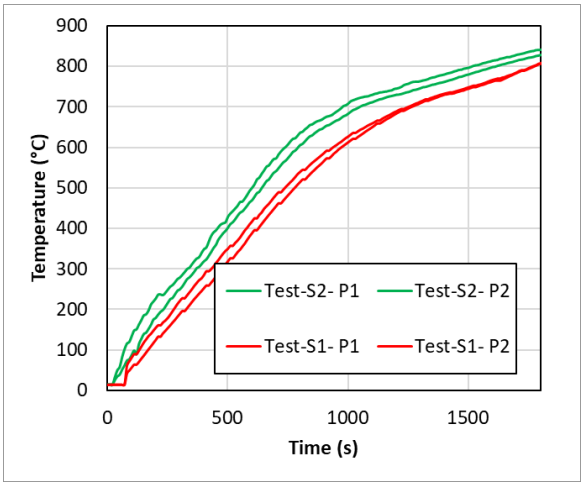

b) Upper flange

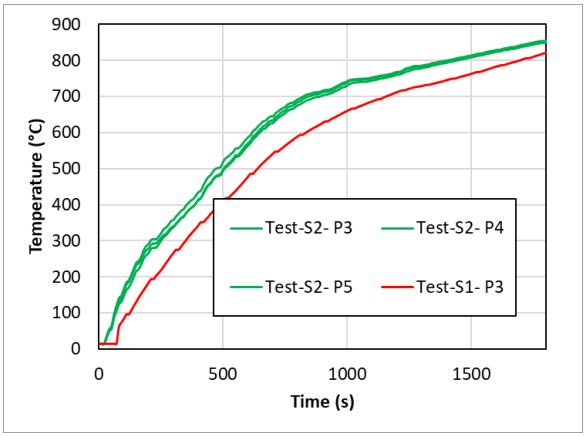

c) Web

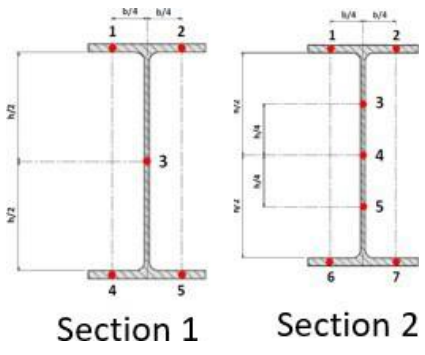

d) Temperature-measured points

Figure 3.7:Temperature-time curves recorded on beam cross-sections S1 and S2 of semi-portal portal n°1

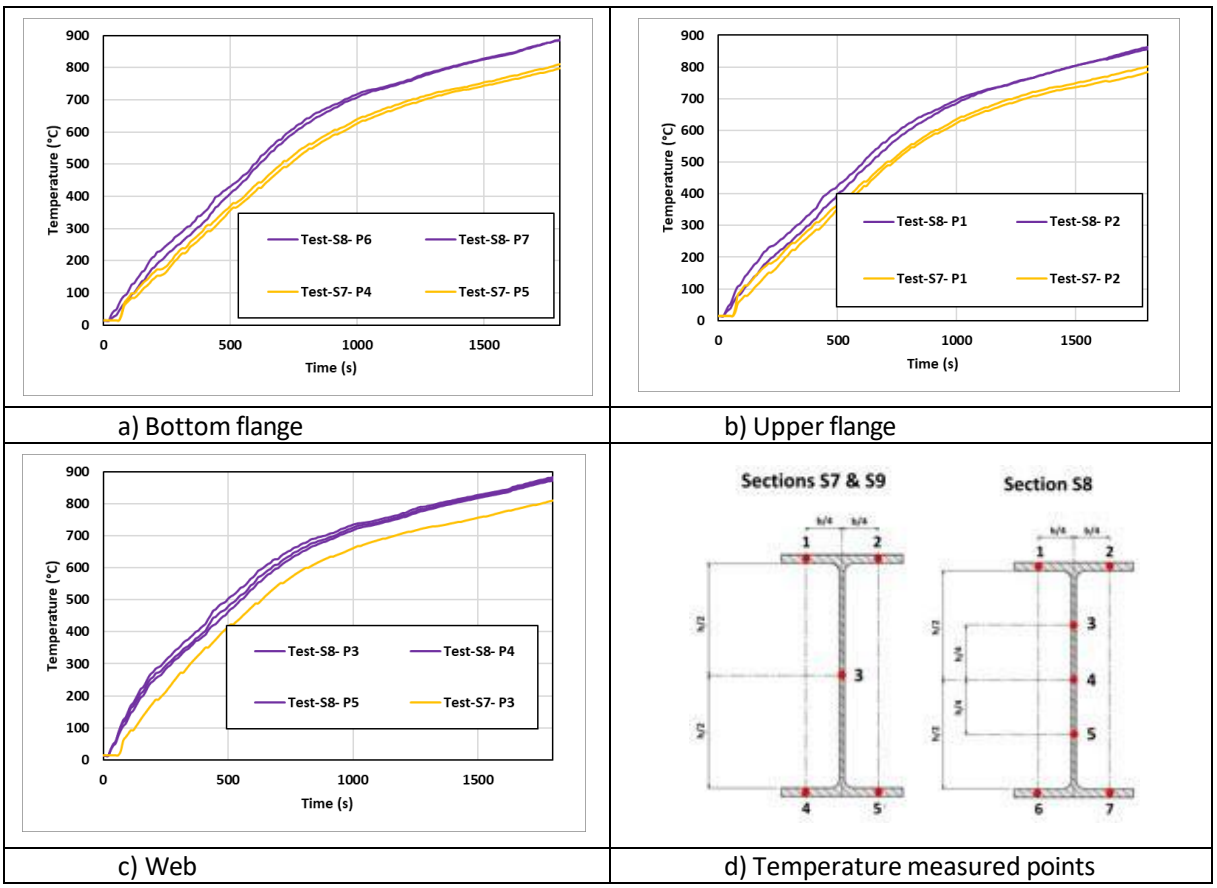

a) Bottom flange | b) Upper flange

c) Web | d) Temperature measured points

Figure 3.8:Temperature-time curves recorded on beam cross-sections S7 and S8 of semi-portal frame n°2

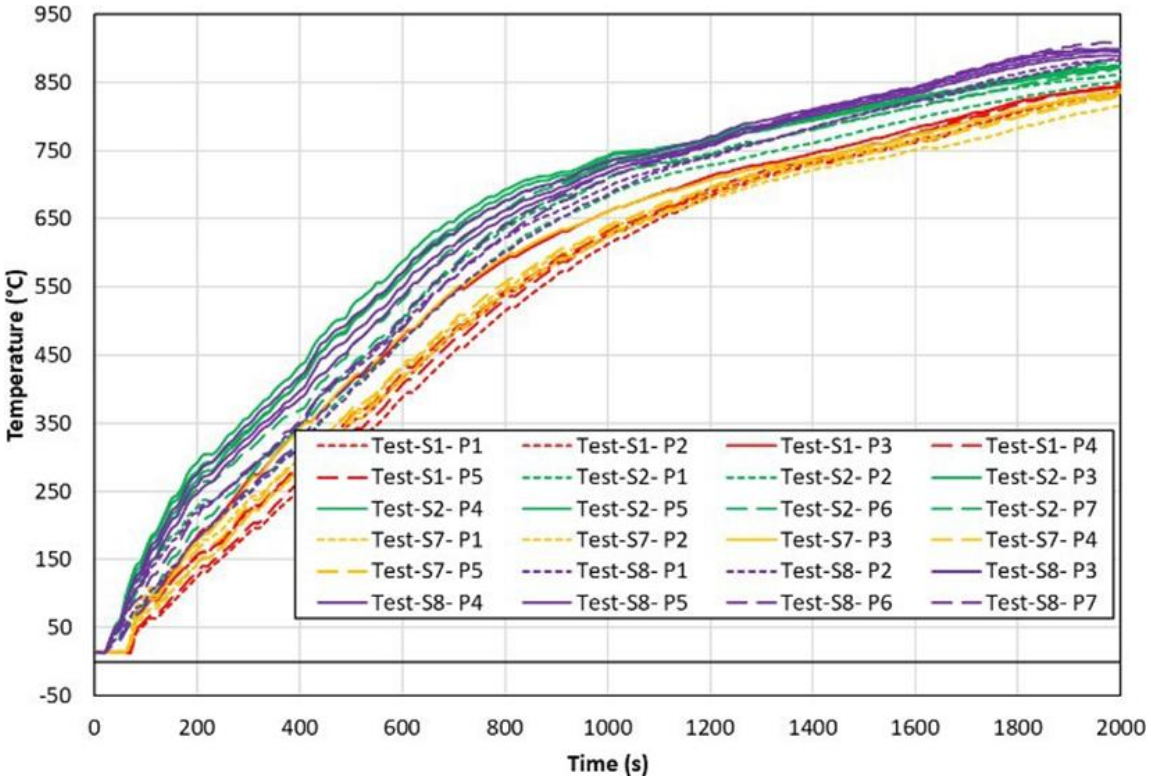

Figure 3.9:Comparison of temperatures measured along the crossbeams of the semi-portal frames

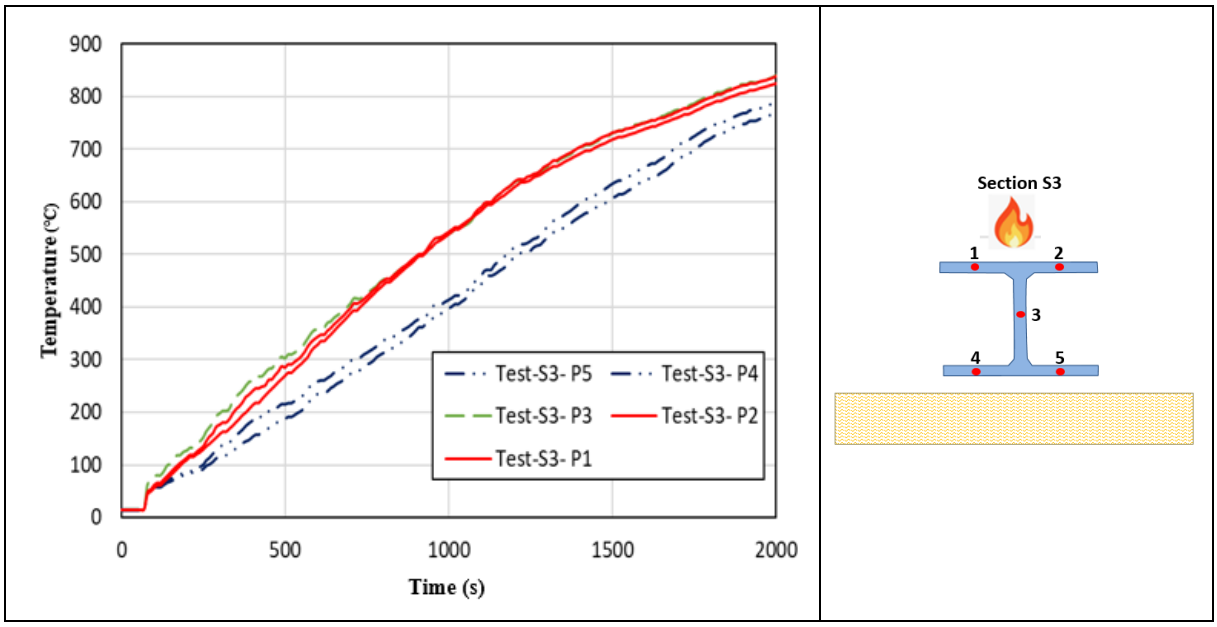

Figure 3.10*:*Temperature-time curves recorded on column cross-section S3 of semi-portal frame n°1

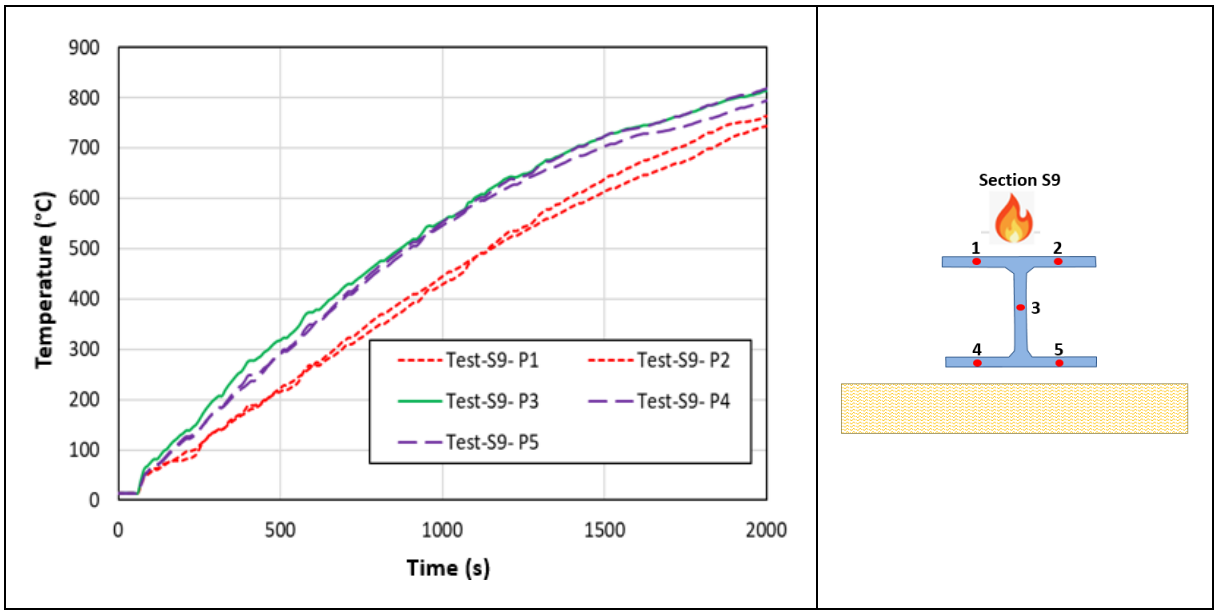

Figure 3.11*:*Temperature-time curves recorded on column cross-section S9 of semi-portal frame n°2

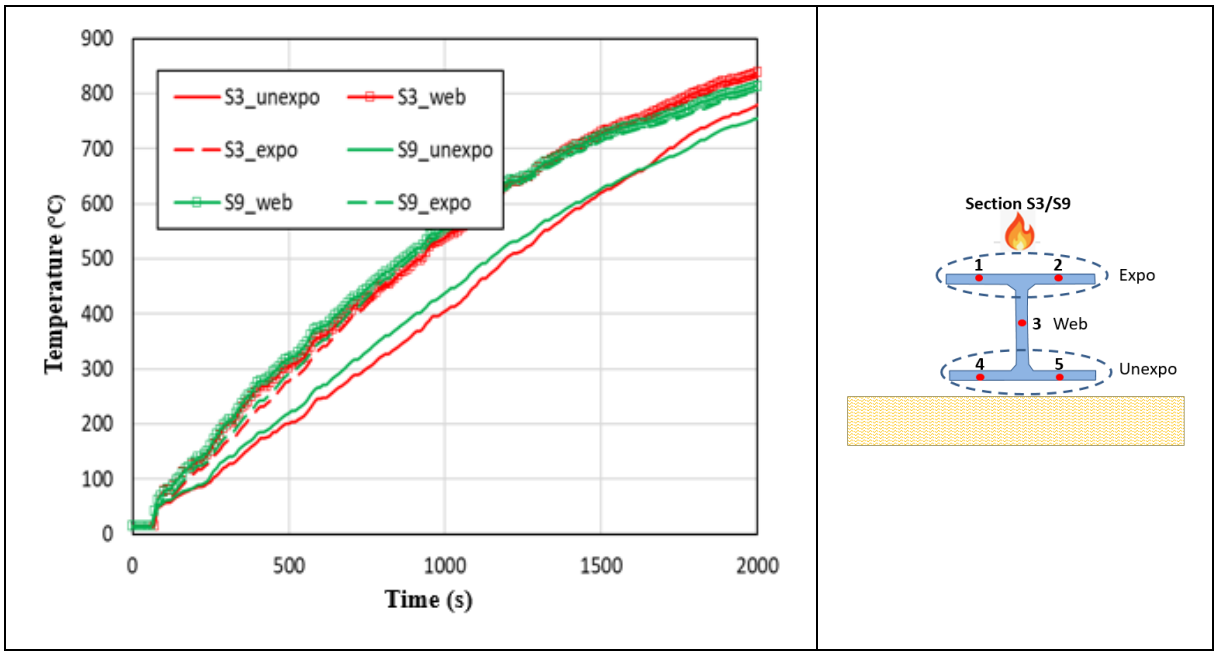

Figure 3.12*:*Comparison of the average temperature of the column cross-sections of two semi-Portal frames

Figure 3.13 to Figure 3.16 show photographs of the test specimen taken during and after the test: the deformed shape of the semi-portal frames during the test (see Figure 3.13), the deformed shape of the fusible links and fire wall (see Figure 3.15), and the deformed shape of the column-beam connections (see Figure 3.16). As expected, the failure of the semi-portal frames was characterized by the lateral torsional buckling of beams, which was not simultaneous. In fact, one of the semi-portal frames failed before the other, with a failure observed at 1620 seconds, corresponding to a temperature increase of approximately 829°C in the web and the lower flange, and 820°C in the upper flange of the beam (at mid-span) of semi-portal frame n°1 (see Figure 3.7). The failure of the other occurred at 1780 seconds, corresponding to a temperature rise of approximately 880°C in the web and the lower flange, and 860°C in the upper flange of the beam (at mid-span) of semi-portal frame n° 2 (see Figure 3.8). In addition, a slight local buckling of the lower flange of the beam at the beam to column junction was observed after the test, together with a flexural buckling of the stiffeners welded to the beams and an elongation of the bolts in the upper row of the bolted column-beam connection of semi-portal frame n°2 (see Figure 3.16).

As expected, the fusible links tested successfully allowed the disconnection of the steel semi-portal frames located inside the furnace without compromising the separation function of the fire wall, which remained attached to the steel columns on the fire-unexposed side of the wall (see Figure 3.15). In addition, the fusible links on the unexposed side were not damaged.

a) After 1420 s

b) After 1560 s

Figure 3.13*:*Deformed shape of semi-portal frames during the test

Figure 3.14*:*View of the specimen after testing

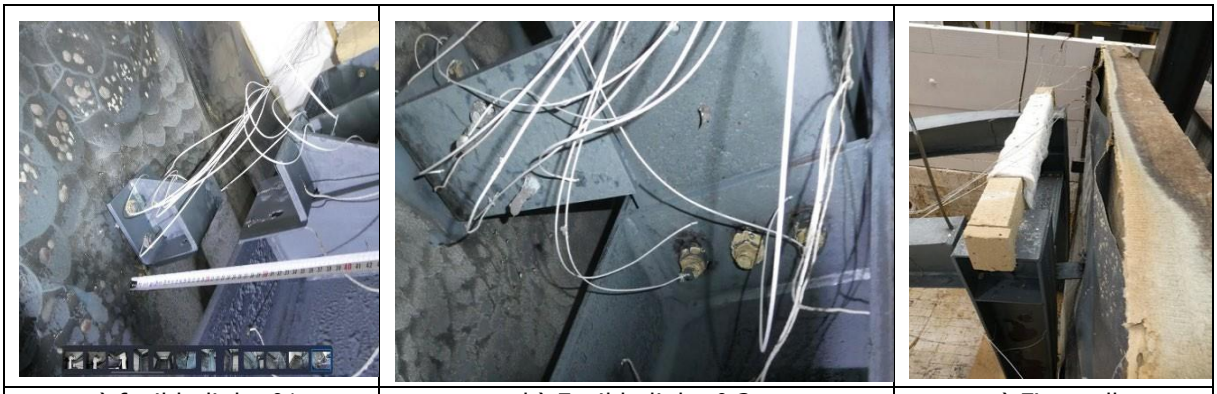

a) fusible link n°1	b) Fusible link n° 2	c) Fire wall

Figure 3.15*:*Condition of fusible links and wall after the test

a) semi-portal frame n°1	b) semi-portal frame n°2

Figure 3.16*:*Deformed shape at the column to beam connection after the test

3.2 Numerical analyses

A sequentially coupled three-dimensional thermal-mechanical analysis procedure has been adopted to simulate the fire behaviour of the tested specimen, consisting of first performing a heat transfer analysis to obtain the temperature fields on the fire-exposed fusible systems and the semi-portal frames and then performing a mechanical analysis using the previously calculated temperature fields to assess the fire behaviour of each semi-portal frame and its associated link in the test. A static-dynamic procedure is used to simulate the progressive failure mechanism of the test specimens. The same meshing is used for both thermal and mechanical models, but with appropriate finite element formulations for each type of analysis.

3.2.1 Thermal analyses

In order to determine the temperature field in the steel portal frames, the associated fusible links and the sandwich panel fire wall, a specific three-dimensional finite element model was developed using ANSYS [8].

3.2.1.1 Modelling considerations

Several modelling simplifications were considered in order to find an appropriate compromise between the accuracy of the FE model and its computational cost. The main assumptions finally adopted are the following:

- Only a part of the test specimen, namely a steel portal frame and its fusible link located on the fire exposed side and a reduced part of the fire wall and a part of the columns supporting the sandwich panels on the unexposed side are meshed (see Figure 3.18 and Figure 3.19). Preliminary analyses has shown that modelling a wall of 1m width and height at level of the fusible links, and columns with a 1m length, is sufficiently representative to accurately

account for the shadow effect and to provide sufficiently accurate results for the heating of the links. Consequently, the fire wall is meshed with a minimum size of 1m x 1.2m (width x height). Both the column and the beam of the portal frame are also meshed with a length of only 1m;

- The steel profiles, aluminium bolts, steel bolts, threaded rods, fusible links and parts of the beam and the columns, as well as the fire wall are modelled using twenty-node brick elements (SOLID90);
- The three modes of heat transfer, namely conduction, convection and radiation, are considered. Four-node surface elements (SURF152) are used to apply convective and radiative exchanges on the outer sides, including a view factor calculation to account for the shadow effect in the radiative heat exchanges. A special feature of the ANSYS code has been used in the purpose. In addition, a surface-to-surface radiation model is used to account for radiation exchanges between all the surfaces exposed to the fire.
- Steel faces of sandwich panels, which are assumed to have an insignificant effect on the thermal response of the panels, have been ignored.
- Perfect thermal continuity is assumed between all contact surfaces (no thermal resistance);
- Bolts and steel rods are modelled as detailed as possible. However, some features of the geometry which are assumed to have a negligible effect on the behaviour of the fusible links are ignored. Firstly, threaded parts of the bolts, rods and nuts are omitted and the bolt–nut assembly is modelled as a single component, assuming that there is no relative motion between bolts and nuts or loosening during loading. Secondly, no washers are modelled and the bolt holes are slightly larger than the bolt diameter. The bolt characteristics have been modified to account for the reduced shear resistance of the threaded part of the bolt.
- Since that the temperature of the hot gases in the furnace is not homogeneous, in order to calculate more accurately the temperature distribution in the modelled link and semi-portal frame, the modelled members are exposed to one of the hot gas temperature curves shown in Figure 3.20. These curves correspond to the average temperatures of hot gas temperatures measured from plate thermometers near the column of each semi-portal frame during the test, i.e. the average of the temperatures recorded by the plate thermometers PT1 and PT4 for the first portal frame and the average of the temperatures measured by PT7 and PT10 for the second portal frame.
- The thermal-physical properties (thermal conductivity, specific heat, density) of steel and aluminum are those given in the EN 1993-1-2 [6] and EN 1999-1-2 [7] respectively.
- An important requirement for accurate numerical heat transfer modelling is the accuracy of the thermal properties of the input materials. Unfortunately, the thermal properties of insulation materials at high temperatures are usually not available because they are difficult to measure. Therefore, the thermal properties of the sandwich panels were calibrated from another FE thermal study. Since it is intended to use the same sandwich panels for all tests, the calibration was made from the results of standard fire resistance tests carried out on walls as part of Task 2.1. The values used in the FE thermal models are then 'apparent' values rather than 'real' physically based material properties. For this study, a simpler thermal model of a simple panel exposed to fire on one side was built. As a first approximation, the same temperature dependent variations in conductivity and specific heat capacity were assumed as presented by some early researchers. The material properties were then modified (density of 120 kg/m3, specific heat of 3000 J/kg.K and thermal conductivity of 0.2 W/m.K) to obtain temperature rises as close as possible to those recorded in reference tests [2]. The Figure 3.17 summarises the results of the calibration analysis by comparing the temperatures calculated with the experimental temperatures. As standard fire tests only record temperatures on the fire-exposed and unexposed sides of the wall, it was not possible to compare temperatures across the full thickness of the wall. The average temperatures recorded on the fire-exposed surface of panels were used for comparison, as thermocouples at the same locations recorded very similar temperature values. On the unexposed surface, the temperatures recorded at different locations showed relatively large variations due to some thermocouples being close to the joints between panels (hot spots). Therefore, only the temperatures recorded on the unexposed side by the thermocouples far enough away from the panel joints were used.
- For the fire-exposed parts, a convective heat transfer coefficient of 25 W/m^2 K is used. On the fire-unexposed side of the fire wall and the column, the convective heat transfer coefficient is 4 W/m^2 K. In addition, the fire emissivity is assumed to be 1 and the surface emissivity of the materials is set to 0.7, in accordance with EN 1991-1-2 [4].

- During the test, it is likely that the flow of hot gases was reduced at the 40 mm gap between the column of the semi-portal frames and the fire wall. As a result, in the numerical model, the convective exchanges on the surfaces of the wall in front of the column flanges of the semi-portal frames, as well as on the corresponding surfaces of the column flanges, were assumed to be negligible.

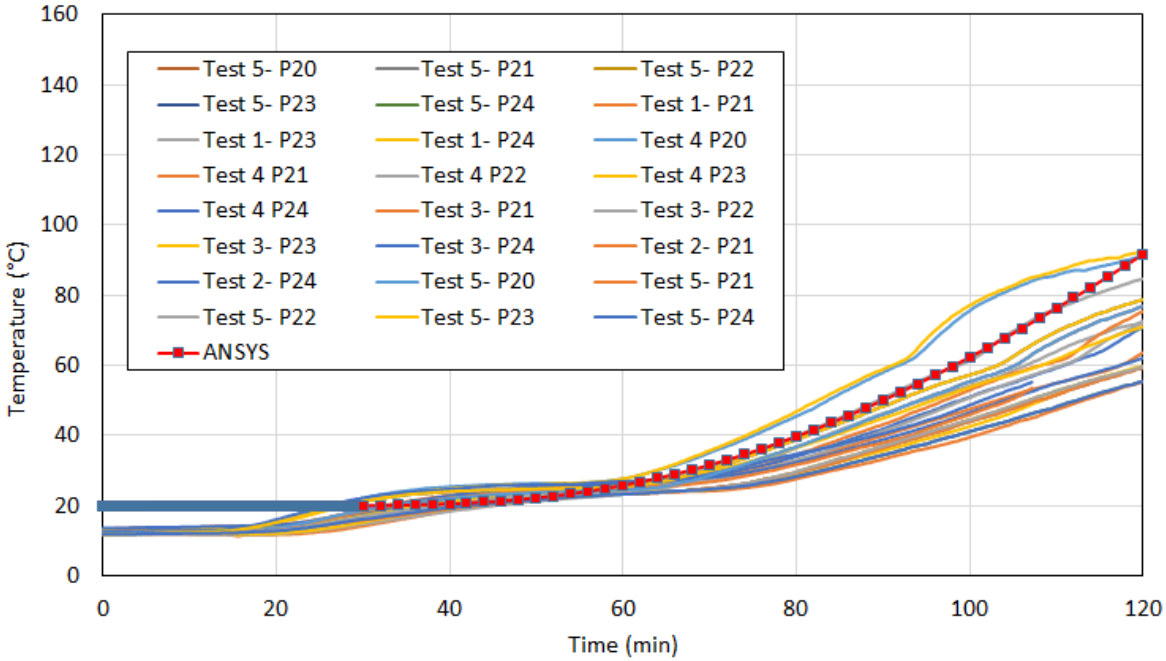

Figure 3.17: Comparison of fire-unexposed panel surface temperatures

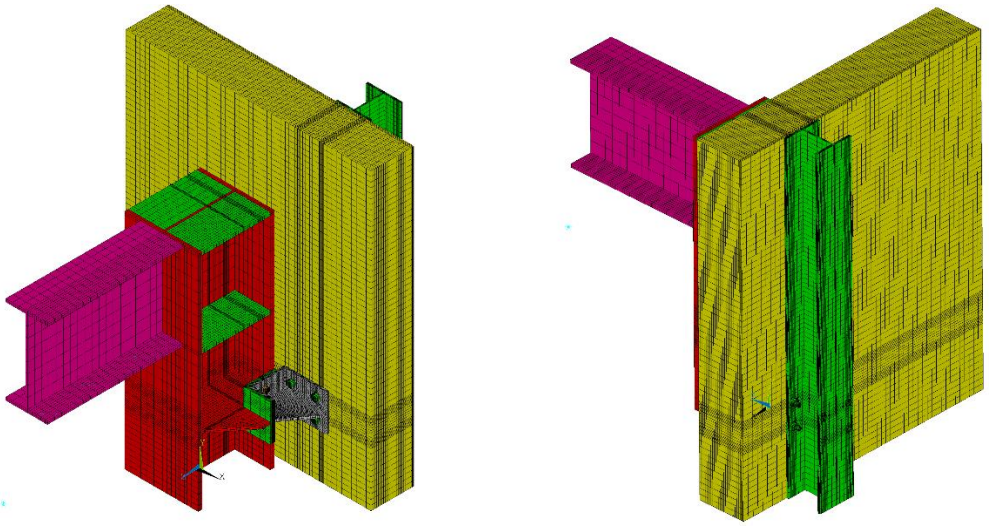

a) View from the fire exposed side

b) View from the fire unexposed side

Figure 3.18: Thermal model for the portal frame n°1 and the associated fusible link

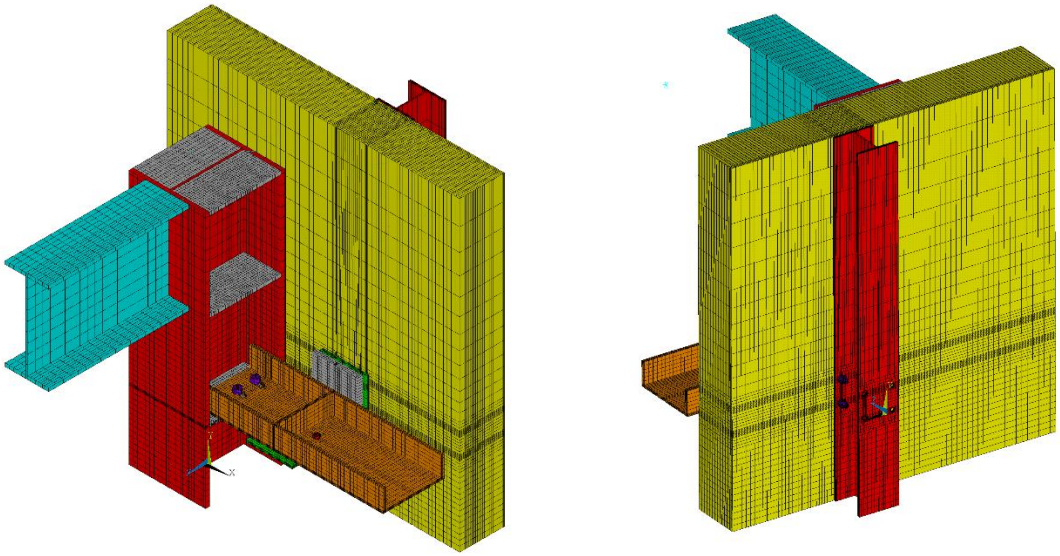

a) View from the fire exposed side

b) View from the fire unexposed side

Figure 3.19: Thermal model for portal frame n°2 and the associated fusible link

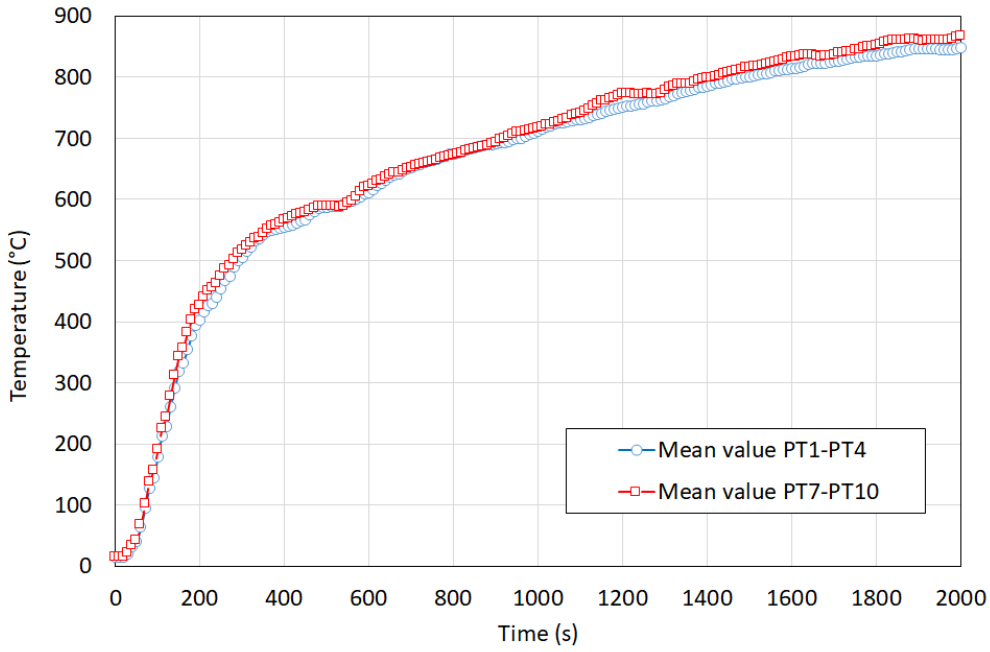

Figure 3.20: Temperature-times curves of hot gas applied in numerical modelling.

3.2.1.2 Analysis results

The main results of the thermal analyses are presented below. A comparison with test data is systematically given to assess the reliability of the thermal model in predicting the heating of the investigated steel portal frames with fusible links.

The results of the comparisons for the steel portal frame n°1 are shown from Figure 3.21 to Figure 3.25, where the temperatures measured during the test are compared with those calculated at the same location, namely the beam cross-section S1, the column cross-section S3 and the fusible link cross-section S4. The Figure 3.26 shows the predicted temperature fields at different times of fire exposure. From these figures, it can be seen that the numerical model accurately predicts the heating of the beam, the column, and the threaded rods. For the beam cross-section S1 (see Figure 3.21), the temperature is slightly underestimated up to 7-8 minutes of fire-exposure, after which the calculated temperatures are very close to the measured ones. The maximum temperature difference is less than 10°C, representing about 2-3% errors. The heating of the column parts directly exposed to fire (web and the flange furthest from the wall) calculated from the model agrees with that measured during the test (see Figure 3.22). Furthermore, the calculated heating curve of the column

flange next to the wall is slightly higher than the experimental one, with an acceptable maximum deviation of about 15% on the safe side. This confirms that the assumption of no convective exchanges in the space between the column and the wall is quite suitable for simulating the heating of the column. Regarding the fusible link (see Figure 3.35), it should be noted that the numerical model adequately predicts the temperature gradient along the threaded rods up to 24 minutes, although the temperature on the fire unexposed side is slightly underestimated. Thereafter, the calculated temperatures increase more rapidly inside the wall, with a maximum difference of about 95°C after 30 minutes. This difference could be explained by the fact that, during the test, a gap appeared around the rods in the wall, whereas the model assumes perfect contact between these elements. This difference could also be explained by the uncertainty about the exact location of the thermocouple in question, given the difficulty of mounting the threaded rods through the fire wall. It should be noted that steel rods and steel bolts maintain at least 90% of their resistance at temperatures below 300°C. Finally, as shown on Figure 3.25, the heating of both the steel profiles and the aluminium bolts forming the fusible link are calculated with relatively good accuracy. However, the calculated heatings are slightly higher than those measured during the test. A maximum difference of about 100°C between the numerical and experimental temperatures can be observed for the aluminium bolts and the steel profiles.

The main results of the temperature comparisons for the steel portal frame n°2 are presented from Figure 3.27 to Figure 3.33. The Figure 3.33 shows the predicted temperature fields at different times of fire exposure. Like the observations given for the first steel portal frame, all comparisons show that the numerical model accurately predicts the heating of the beam, the column, and the threaded rods. In fact, for the beam cross-section S7, it can be noted that the heating of the web (point P3) is correctly predicted after 8 minutes of fire exposure. The maximum temperature is then less than 15°C until the failure of the portal frame. The temperatures of the beam flanges are slightly underestimated, with a maximum temperature difference of 50°C after 8 minutes (see Figure 3.27). With regard to the heating of the column cross-section S9 (see Figure 3.28), the temperature curves of the flanges converge after 650 seconds of fire exposure, both for the flange directly exposed to fire and for the flange closest to the wall. In addition, the temperature calculated at the centre of the web is slightly higher than that measured during the test, until the portal frame fails, with a maximum difference of approximately 50°C. Once again, the comparison shows that the assumption of reduced convective exchanges between the column and the wall is appropriate for modelling the heating of the column. Regarding the heating of the threaded rods (see Figure 3.29), a significant deviation between the experimental measurements can be observed. A noticeable deviation can be observed between the temperatures measured at similar points during the test, for example in the part directly exposed to fire or at the mid-height, where the experimental curves show differences of up to 150°C. However, by considering only the test curves that appear the most consistent with the temperature rise recorded for the first fusible link, the numerical model predicts the temperature gradient along the rods with sufficient accurately. It should be also noted that steel rods and steel bolts maintain at least 90% of their resistance at temperatures below 300°C. Furthermore, the heating of the aluminum bolts is adequately predicted by the model up to 17 minutes, when their temperature reaches approximately 500°C (see Figure 3.29). Beyond this point, a significant temperature deviation can be observed, which can be explained by the fact that, in the test, the aluminium bolts started to melt, making the temperature measurement inaccurate. Finally, the heating of the L shaped profile and the UPN profile (see Figure 3.31 and Figure 3.32) shows that the calculated temperatures for points further from the wall (P1 and P2 at section S11 of the L-profile and P1 and P2 at section S14 of the UPN) are very close to the measured ones. However, for points closer to the wall, significant discrepancies on the safe side are observed between the numerical and experimental results, reaching approximately 100°C, at point P8 on section S11 (on the L-profile) and points P7 and P8 on section S13 (on the UPN profile), where the flow of hot gases could have been limited during the test.

In conclusion, the thermal model accurately predicts the heating of all modelled parts of the test specimen, with most of the calculated temperatures being on the safe side up to the failure time of the semi-portal frames.

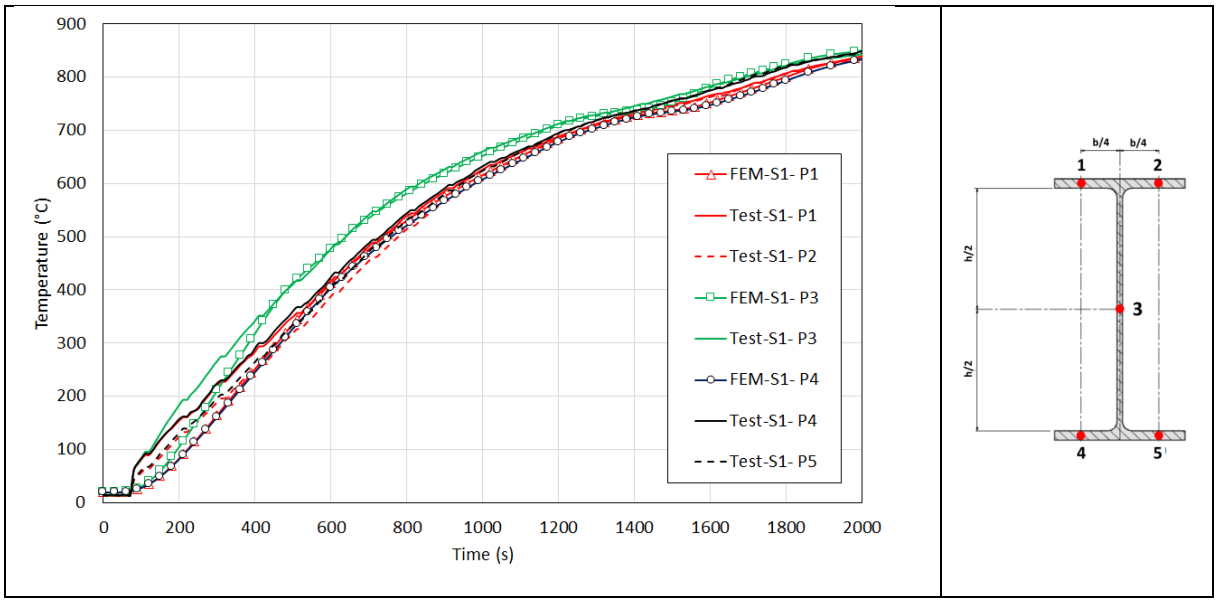

Figure 3.21: Comparison between numerical and experimental temperatures for the beam cross-section S1 of the portal frame n°1

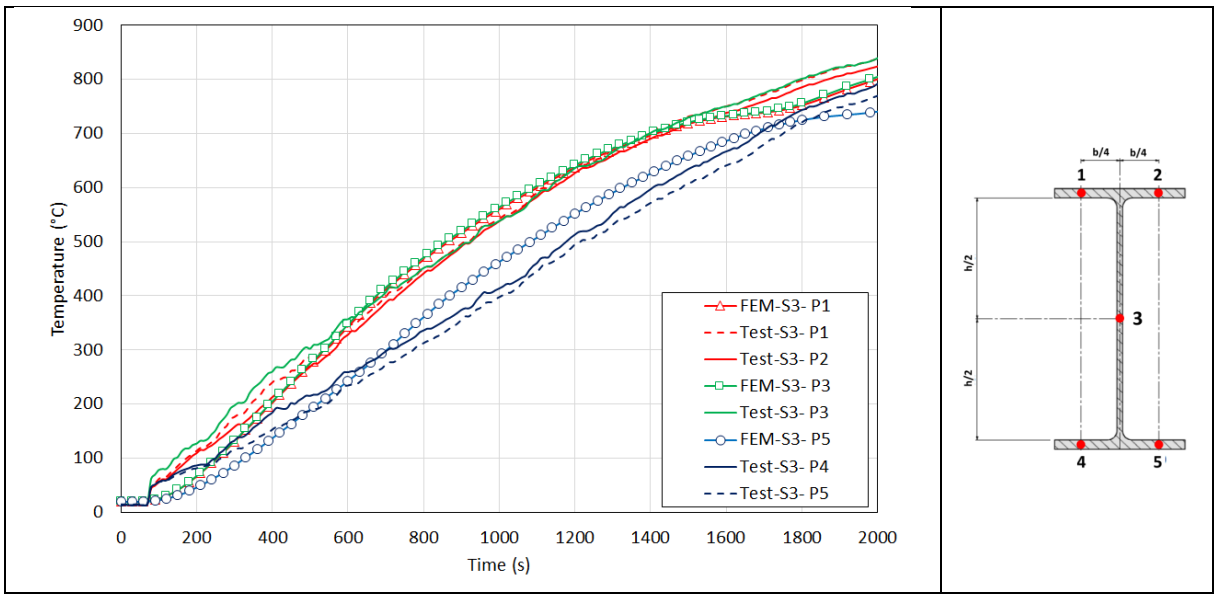

Figure 3.22: Comparison between numerical and experimental temperatures for the column cross-section S3 of the portal frame n°1

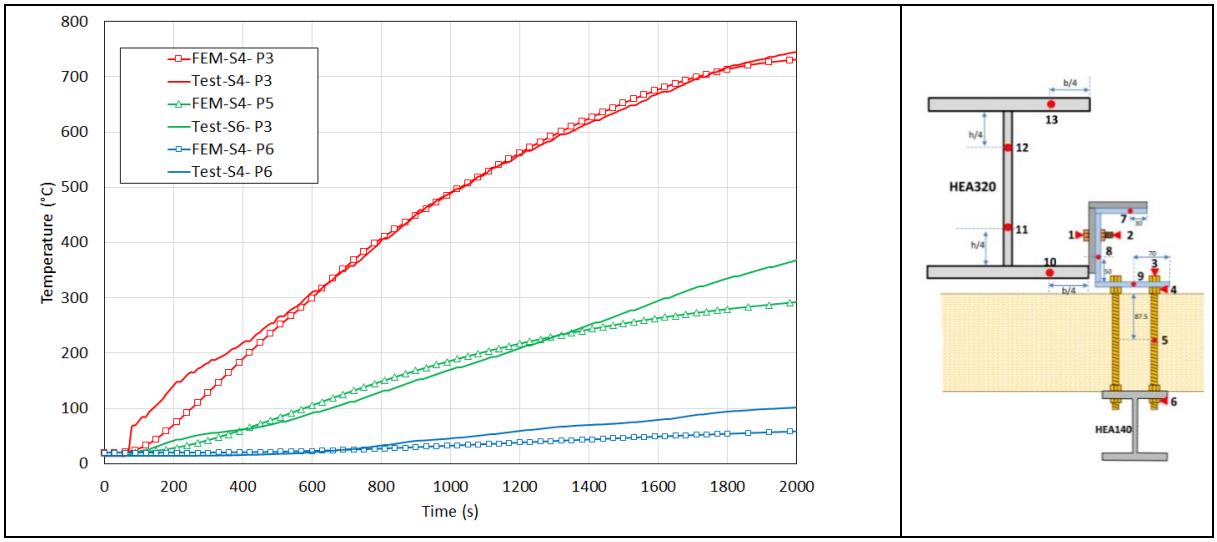

Figure 3.23: Comparison between numerical and experimental temperatures in the steel rods of the fusible link n°1

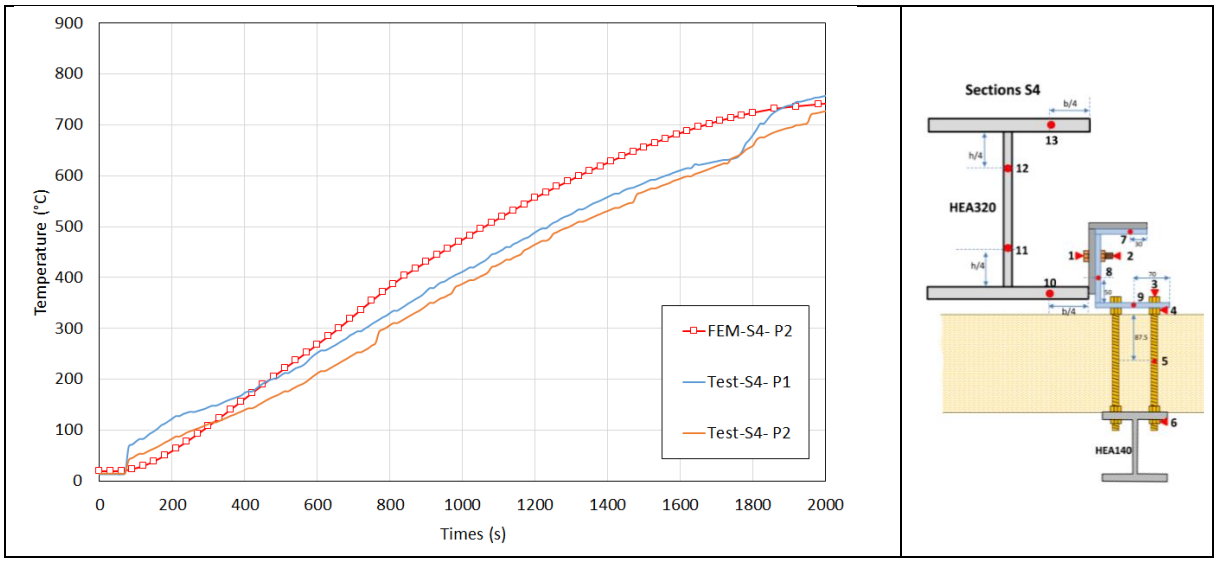

Figure 3.24: Comparison between numerical and experimental temperatures for the aluminium bolts of the fusible link n°1

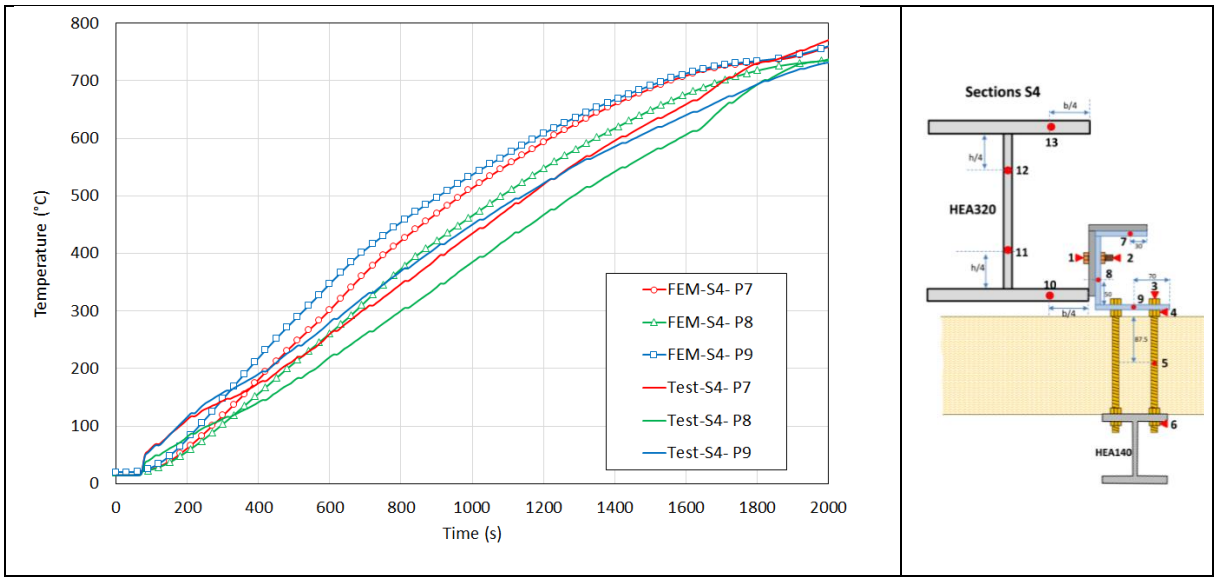

Figure 3.25: Comparison between numerical and experimental temperatures for the steel profiles constituting the fusible link n°1

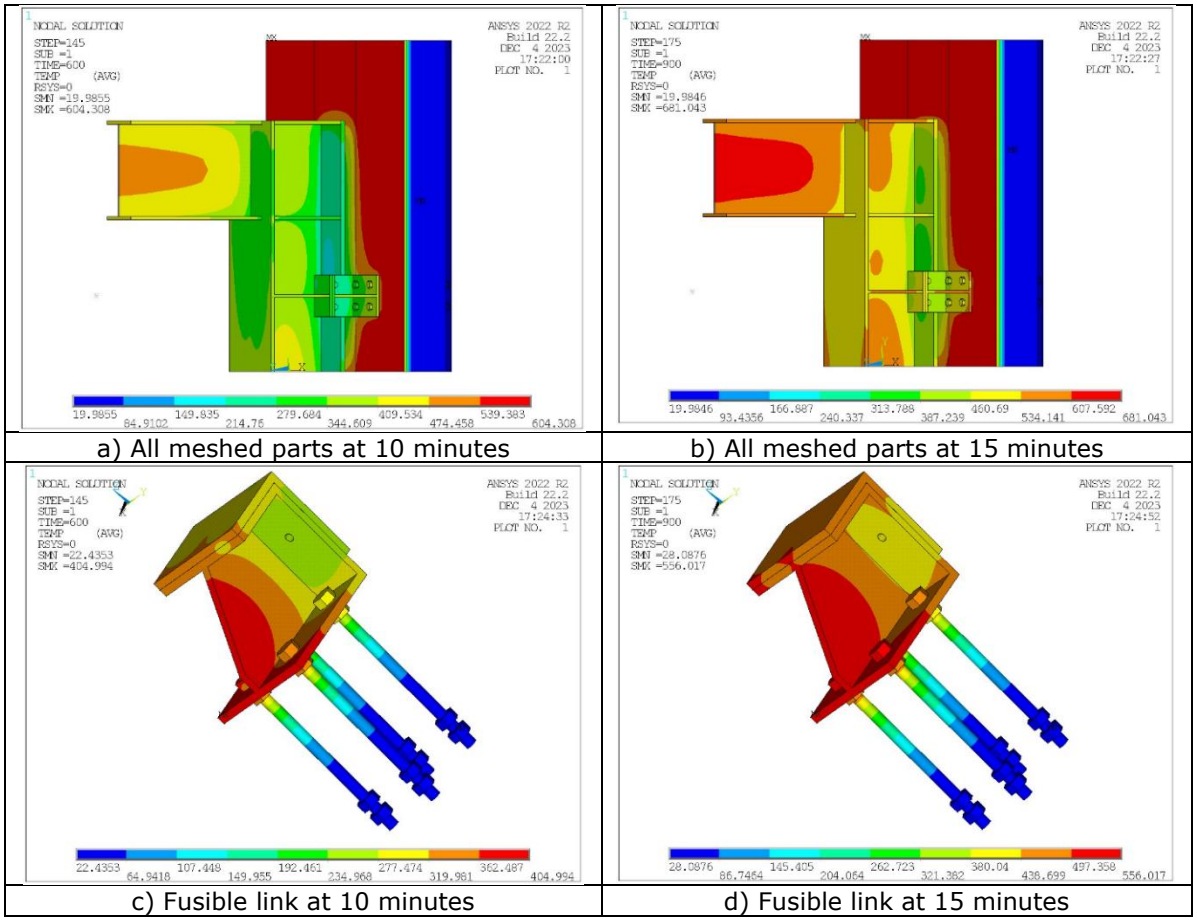

Figure 3.26: Temperature fields calculated on meshed members of steel portal frame n°1 and the associated fusible link after different durations of fire exposure

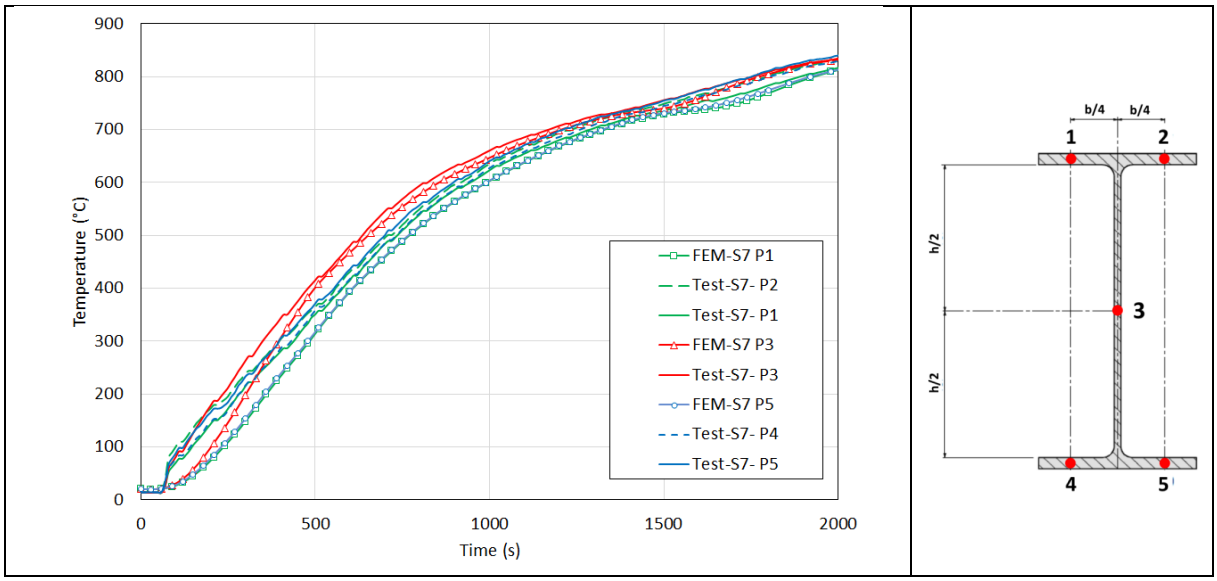

Figure 3.27: Comparison between numerical and experimental temperatures for the beam cross-section S7 of the portal frame n°2

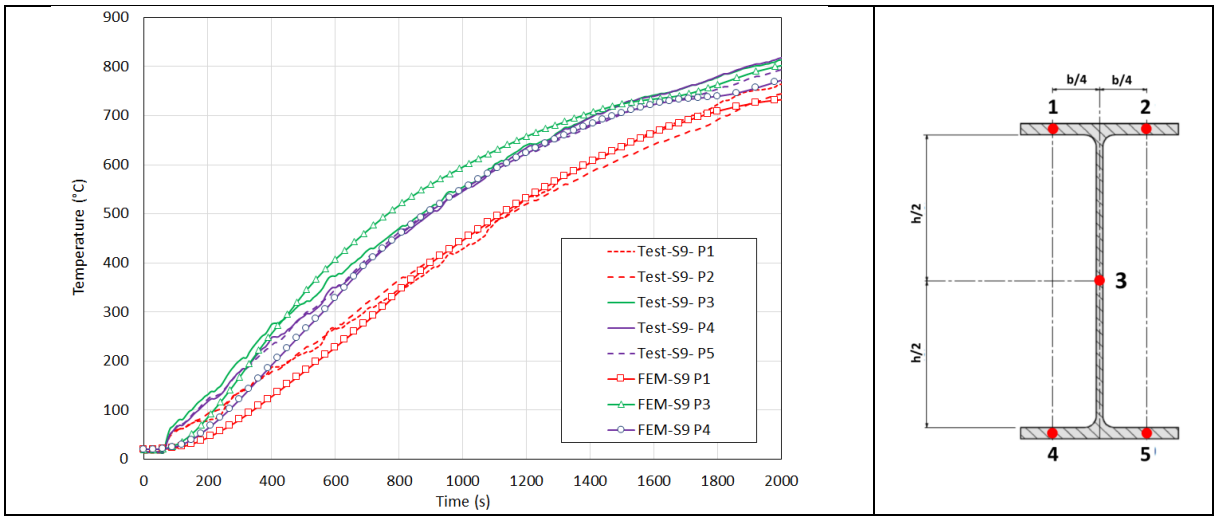

Figure 3.28: Comparison between numerical and experimental temperatures for the column cross-section S9 of the portal frame n°2

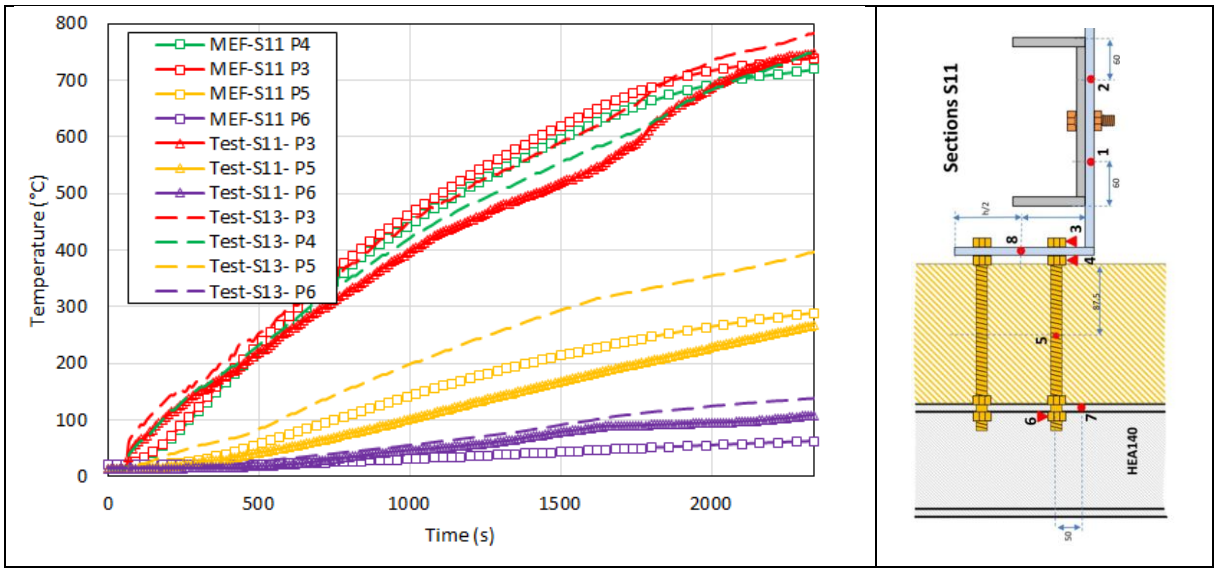

Figure 3.29: Comparison between numerical and experimental temperatures in the steel rods of the fusible link n°2

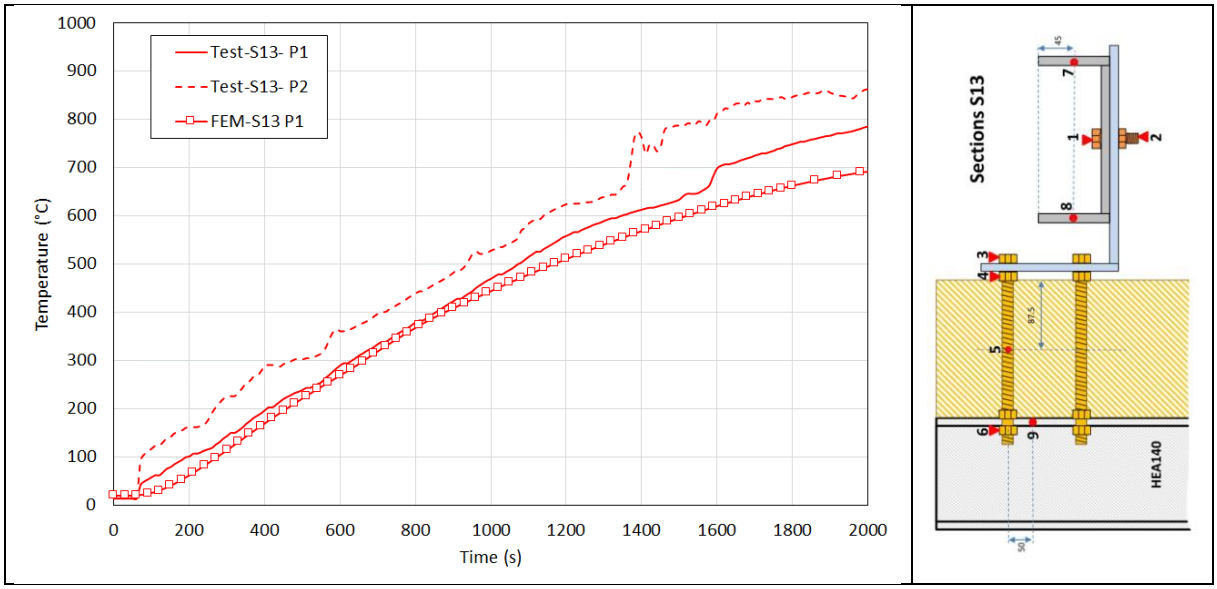

Figure 3.30: Comparison between numerical and experimental temperatures for the aluminium bolts of the fusible link n°2

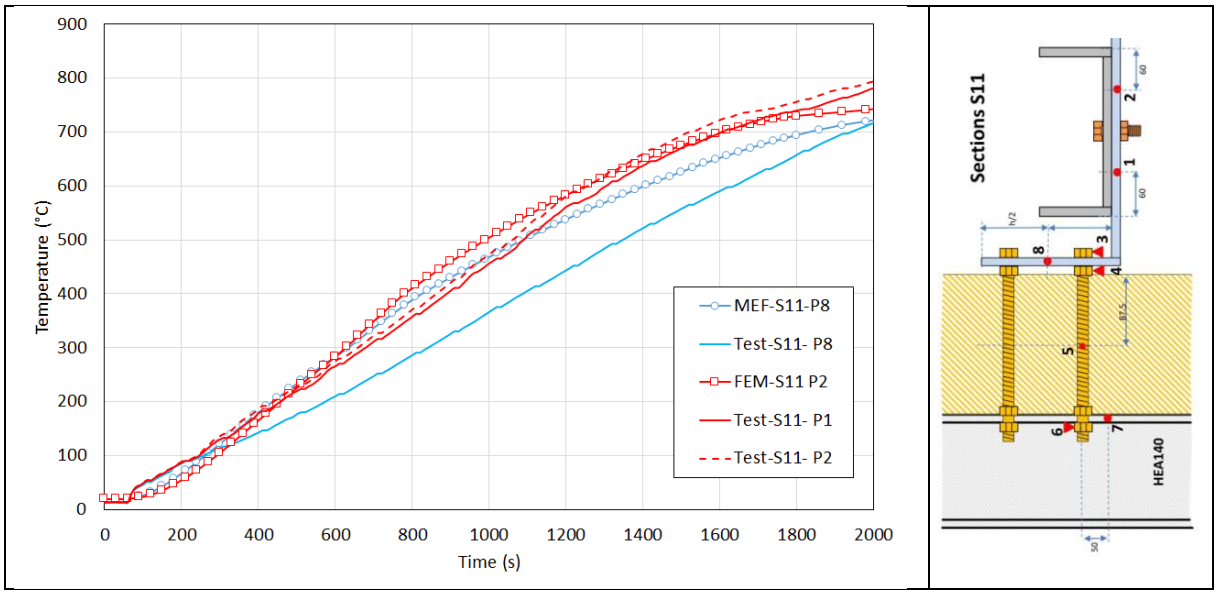

Figure 3.31: Comparison between numerical and experimental temperatures for the L-shaped profile of the fusible link n°2

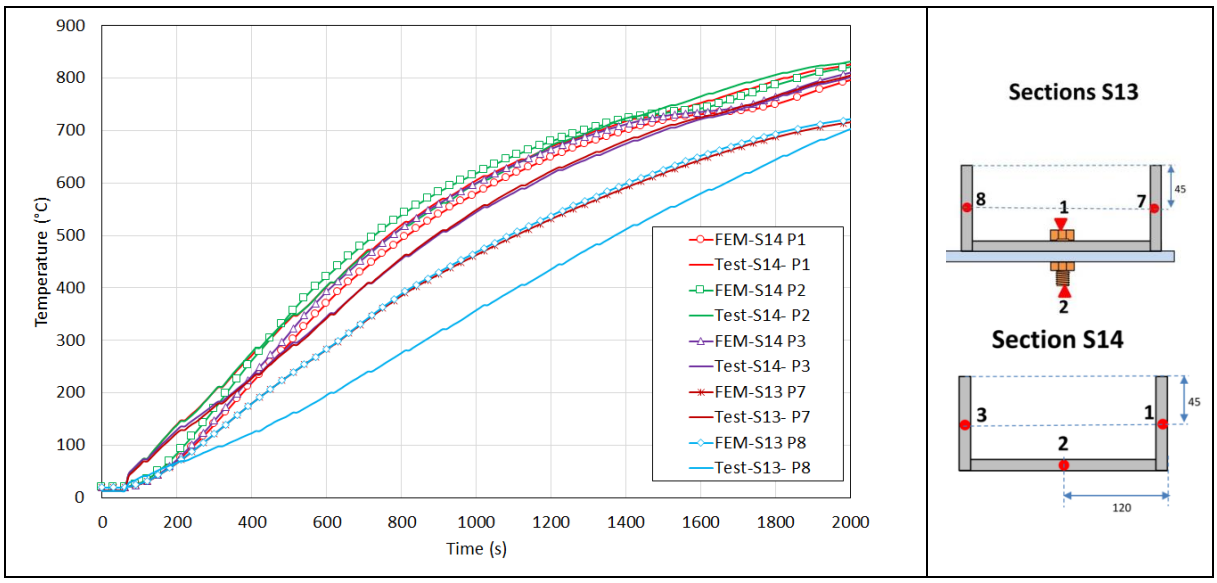

Figure 3.32: Comparison between numerical and experimental temperatures for the UPN profile of the fusible link n°2

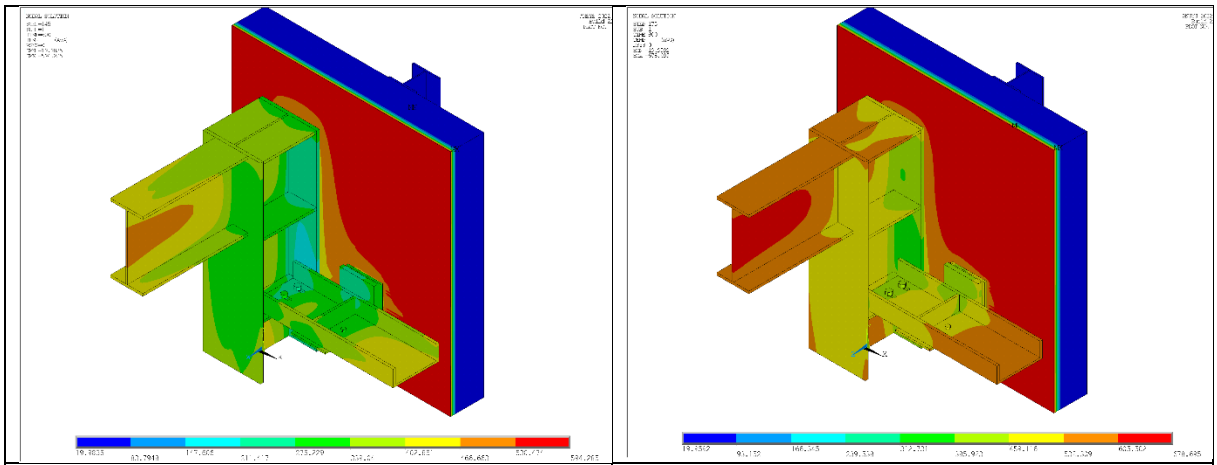

a) All meshed parts at 10 minutes

b) All meshed parts at 15 minutes

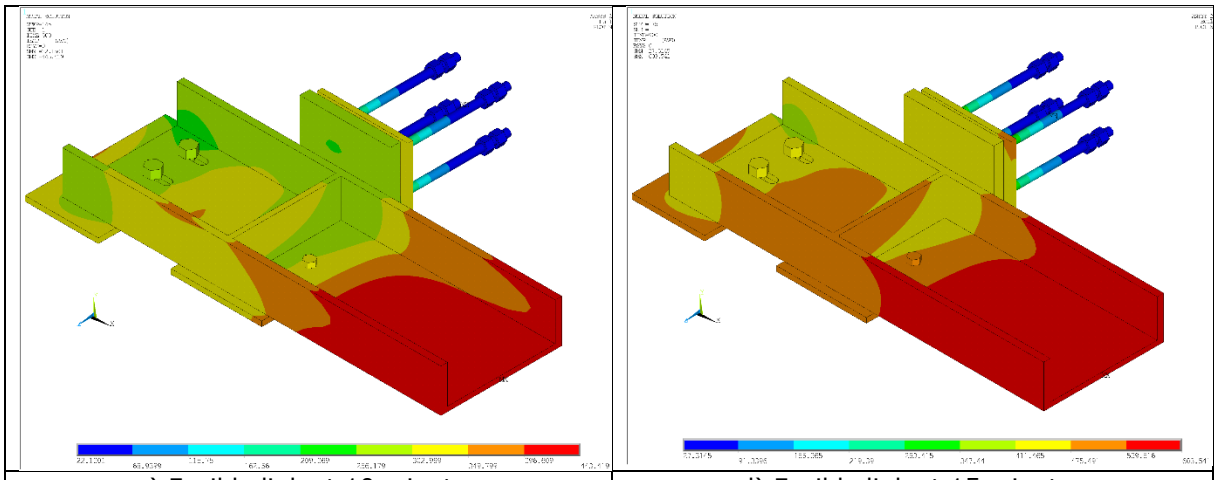

c) Fusible link at 10 minutes | d) Fusible link at 15 minutes

Figure 3.33: Temperature fields calculated on meshed members of steel portal frame n°2 and the associated fusible link after different durations of fire exposure

3.2.2 Mechanical analyses

The mechanical analyses were carried out using a three-dimensional finite element model developed using the ANSYS code [8].

3.2.2.1 Modelling considerations

The following assumptions were made when modelling the test specimen:

- Given the configurations studied, only the fusible links (steel profiles, aluminium bolts and steel rods) exposed to fire and the steel portal frames were modelled and meshed. A part of the portal frame and the associated fusible link (corresponding to the parts meshed in the thermal models) are meshed using 20-node brick FEs (SOLID186), adopting the same meshes as in the thermal models. Other parts of the beam and the column of portal frames are modelled using shell elements (Shell281) to save CPU time.
- Support and restraint conditions coming from the non-modelled parts of the test specimen are considered by introducing appropriate boundary conditions into the models, restraining the relevant degrees of freedom (displacements and rotations). These conditions are assumed to remain unchanged during the fire exposure. Thus, the four threaded rods were assumed to be fully restrained at the level of the steel column supporting the sandwich panels and their lateral restraint by the sandwich panels was ignored. The support system (stop system) at the end of the beam of the portal frames was modelled using a uniaxial spring element with a stiffness equal to the flexural stiffness of the HEB 500 support beam with respect to its weak axis. The spring behavior allows the beam of the semi-portal frame to expand freely over 50 mm (zero stiffness), after which, the stiffness of the spring becomes equal to the flexural stiffness of the support beam. In fact, when the beam expands to the stop, it pushes against the support beam out of the plane. The flexural stiffness considered is that of an HEB 500 isostatic beam on two simple supports, along its weak axis (i.e. 9575374 N/m). All boundary conditions are shown in Figure 3.35 and Figure 3.37.
- The column of the semi-portal frame is fixed at the base.
- The mechanical properties of steel profiles at elevated temperatures are taken from EN 1993-1-2, taking into account the yielding plateau and strain hardening. In the absence of test data, a tri-linear model is also used to model the material behaviour of steel bolts and rods, considering the strength reduction factors given in Annex D of EN 1993-1-2 and the young modulus reduction factors for steel. The mechanical properties of aluminium bolts were defined from the test results given the project deliverable D3.1 [3]. The stress-strain curves considered for steel members and aluminium bolts at elevated temperature are illustrated in Figure 3.39.
- The grades are respectively S275 for the steel components and 8.8 for the steel bolts and rods. The material properties considered at ambient temperature are reported in Table 4, with a Poisson's ratio of 0.3.
- The melting temperature of aluminium is currently around 500°C. In the pushing phase, the aluminium bolts break before the system fails: either by shear failure due to the thermal expansion of the connected components or by their loss of resistance at the melting

temperature. Consequently, the aluminium bolts are deactivated at the failure times determined by the mechanical analyses.

- In addition to the self-weight of steel members: a vertical load of 25 kN (uniformly distributed) is applied to the top flange of the beam of the semi-portal frame, over a length of 0.25 m, to represent the suspended mass attached to the semi-portal frame in the test. This load remains constant throughout the duration of the fire exposure.
- In terms of thermal loading, analysis of the test results indicates that a significant temperature gradient occurred along the length of the beams due to the non-uniform temperature distribution of the hot gases inside the furnace. To best represent this thermal gradient, it would be necessary to adopt different hot gas curves in the numerical model corresponding to the observed temperature field in the furnace. However, although the developed thermal models can accurately predict the heating of the different parts of the test specimen, taking into account the relevant hot gas temperature curves, the thermal loading is applied to the mechanical models as follows to reduce the number of computations:
    - It should be noted that the temperature distribution of the fusible link profiles, in particular the significant temperature gradient along the threaded rods, has an important influence on the fire behaviour of the link. However, the experimental data are not sufficient to accurately describe the heating of these elements. Therefore, at level of the fusible link (including the U-profile, L-profile, aluminium bolts and threaded rods), the temperature fields obtained from the thermal analysis by considering the hot gases temperature recorded near to the beam-to-column connection of portal frames are directly assigned into the mechanical models for all the components of the fusible links.
    - The temperature curves collected during the test on the beam-cross sections S1 and S2 are applied directly to the beam, by considering the temperature distributions along the beam length, as shown in Figure 3.36 and an average temperature for the different parts of the beam cross section, by distinguishing the bottom flange, the top flange and the web.
    - The temperature curves collected during the test on the column cross-section S3 are applied directly to the column, by considering uniform temperature distributions along the column height and an average temperature for the different parts of the column cross section, by distinguishing the bottom flange, the top flange and the web.
    - The fire-protected parts of the considered semi-portal frame, 300 mm at the base of the column and 500 mm at the free end of the beam, are assumed to remain cold (temperature equal to 20°C) during the test.

Table 4: Materials properties of steel components and aluminium bolts

Properties	Steel profile	Steel bolts and rods	Aluminum bolts
Young's modulus E (N/mm^2)	210000	210000	70000
Yield strength f_y (N/mm^2)	334	640	400
ultimate strength f_u (N/mm^2)	443	800	505

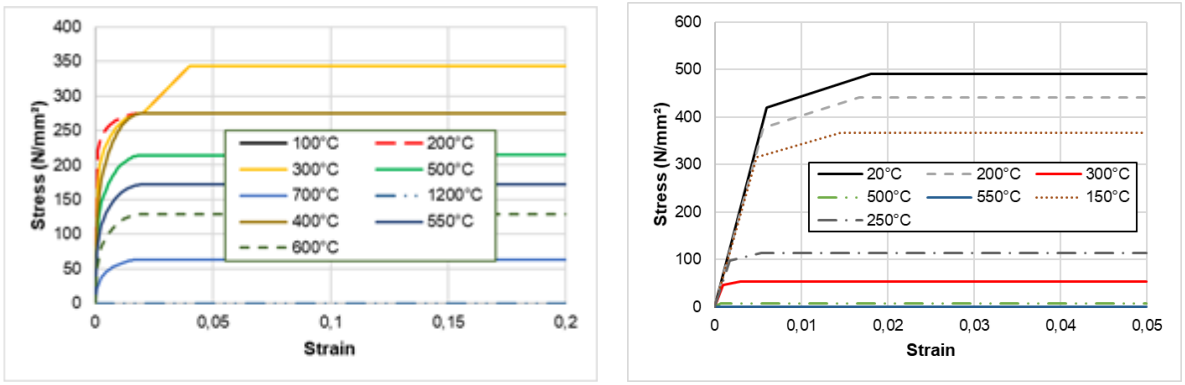

a) Steel profiles b) Aluminium bolts

Figure 3.34: Stress-strain curves of studied materials at elevated temperature

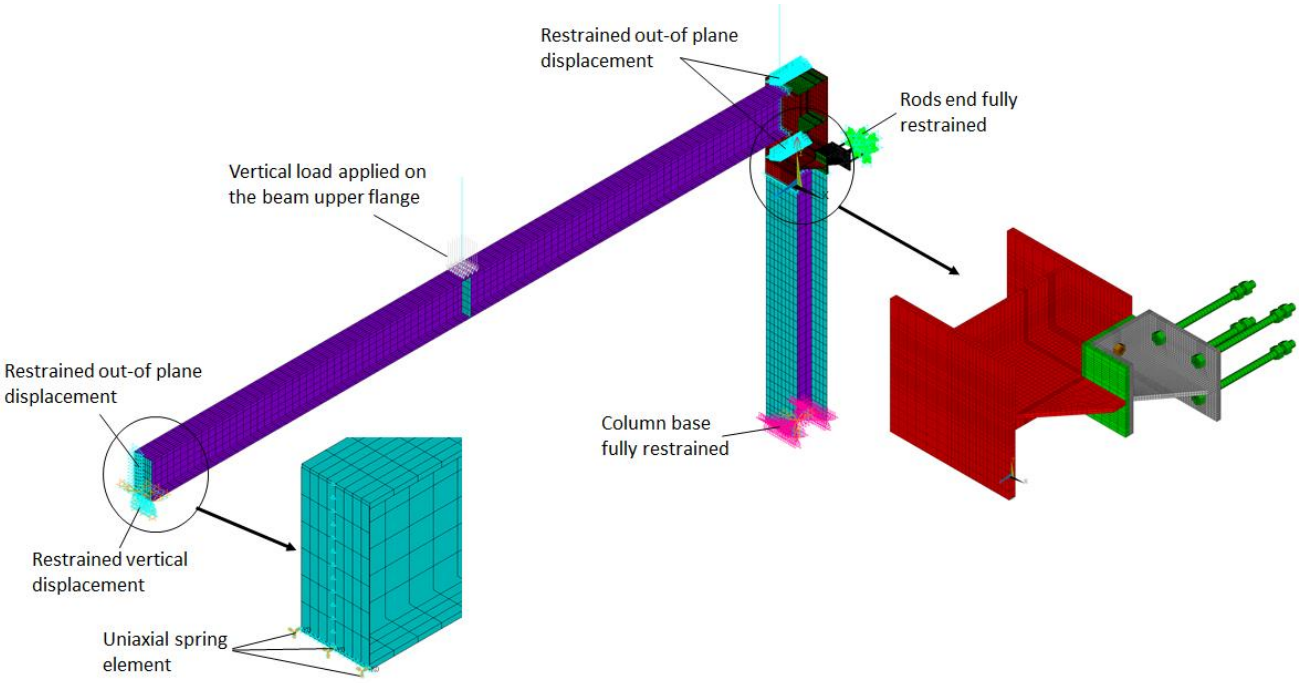

Figure 3.35: Mechanical model developed for the portal frame with fusible link n°1

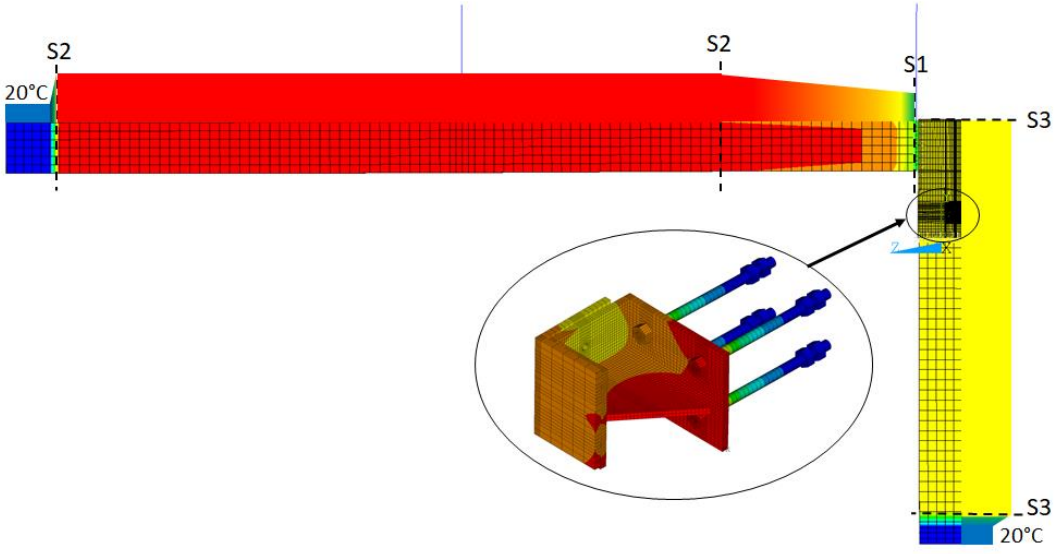

Figure 3.36: Temperature field applied in modeling of portal frame with fusible link n°1

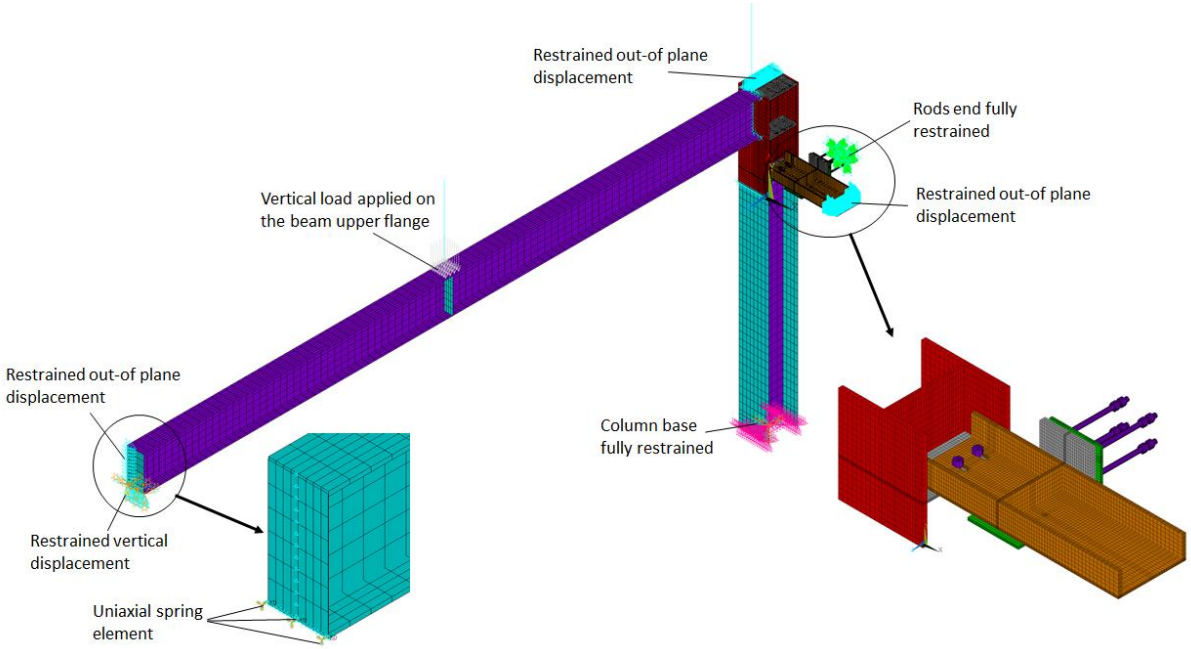

Figure 3.37: Mechanical model developed for the portal frame with fusible link n°2

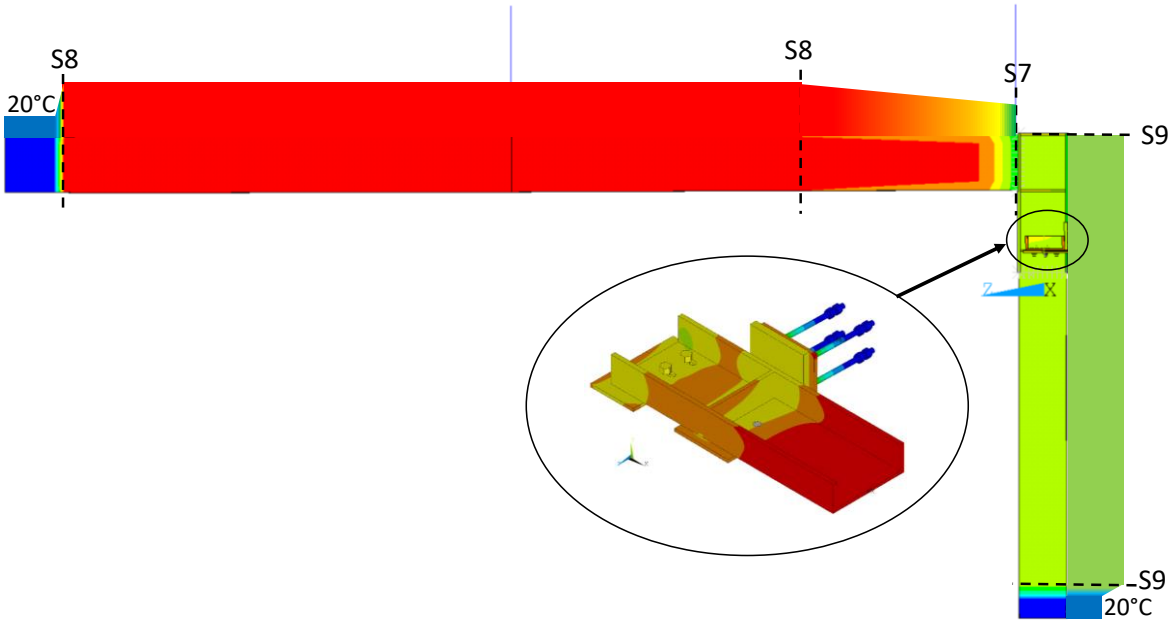

Figure 3.38: Temperature field applied in modeling of portal frame with fusible link n°2

3.2.2.2 Analysis results

The main results of the mechanical analyses are presented hereafter. Are given:

- The deformed shapes of the semi-portal frames (see Figure 3.39 and Figure 3.40) and the fusible links at failure times (see Figure 3.41 and Figure 3.42)
- The temperature fields in the semi-portal frames at failure times (see Figure 3.43)
- The distribution of von Mises equivalent plastic strain in components of fusible links at failure time (see Figure 3.44 and Figure 3.47).
- The time-displacement curves at the beam mid-span and at the beam-to-column connection of the two semi-portal frames (See Figure 3.50 and Figure 3.51 for the steel portal frame n°1 and see Figure 3.55 and Figure 3.56 for the steel portal frame n°2).

- The time–support reaction curves of the two semi-portal frames (see Figure 49 and Figure 55);
- The time-axial reaction curves calculated at the restrained end of steel rods of the two fusible links (see Figure 52 and Figure 56);
- The main results of an additional calculation in which the lateral-torsional buckling of the beam of the semi-portal frame n°1 is prevented.

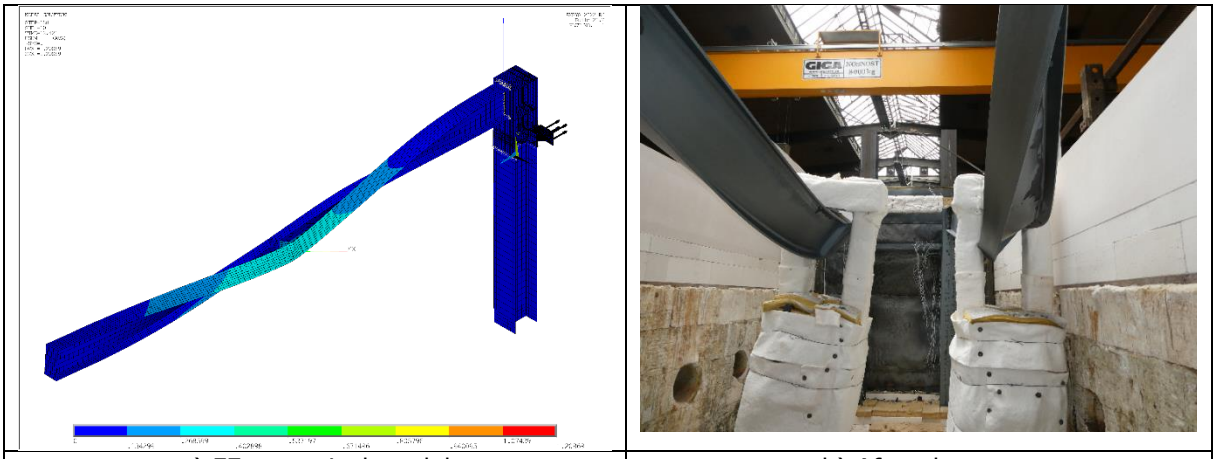

a) FE numerical model | b) After the test

Figure 3.39: Deformed shape at failure time of the first semi-portal frame

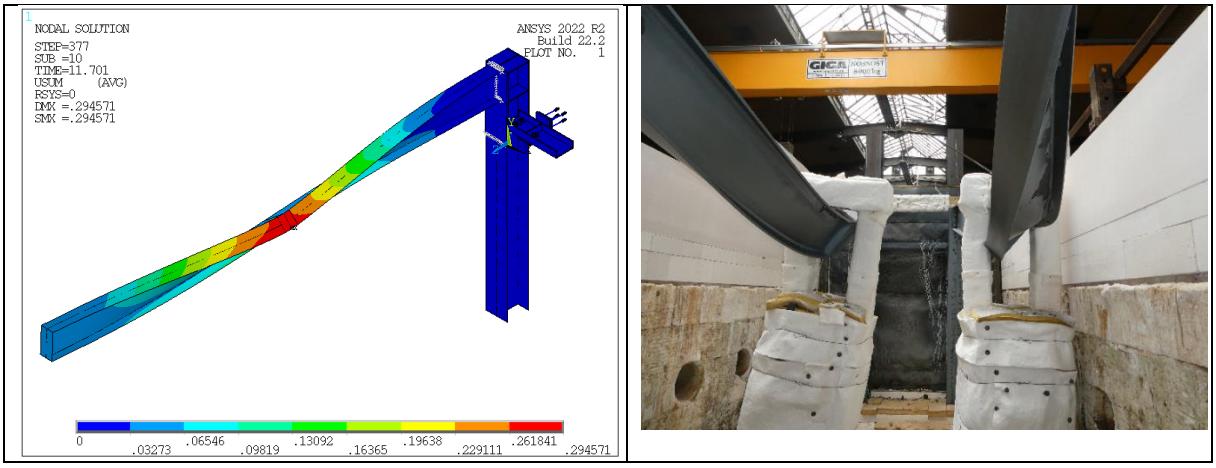

a) FE numerical model | b) After the test

Figure 3.40: Deformed shape at failure time of the second semi-portal frame

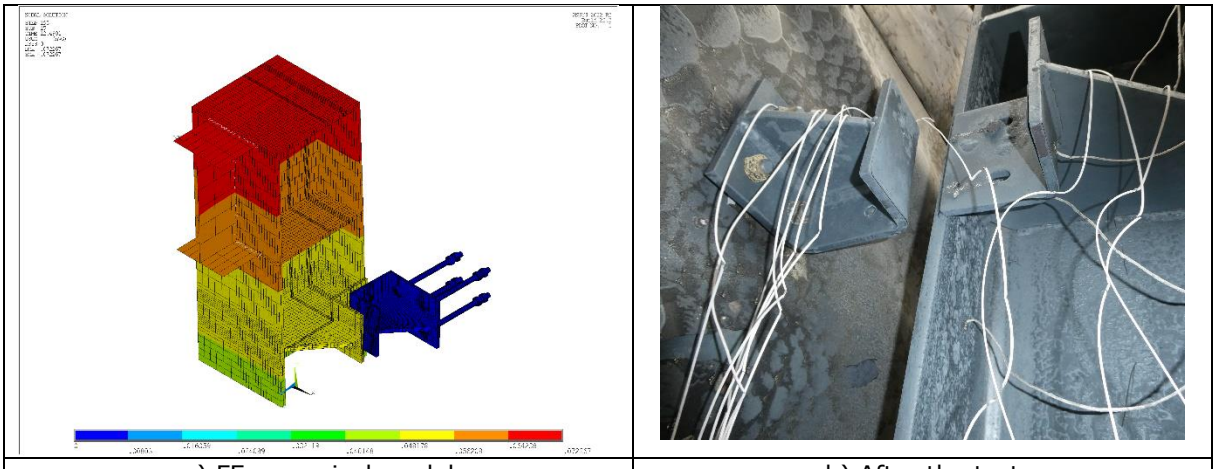

a) FE numerical model | b) After the test

Figure 3.41: Deformed shape of fusible link n°1 predicted by the numerical model and that observed after the test

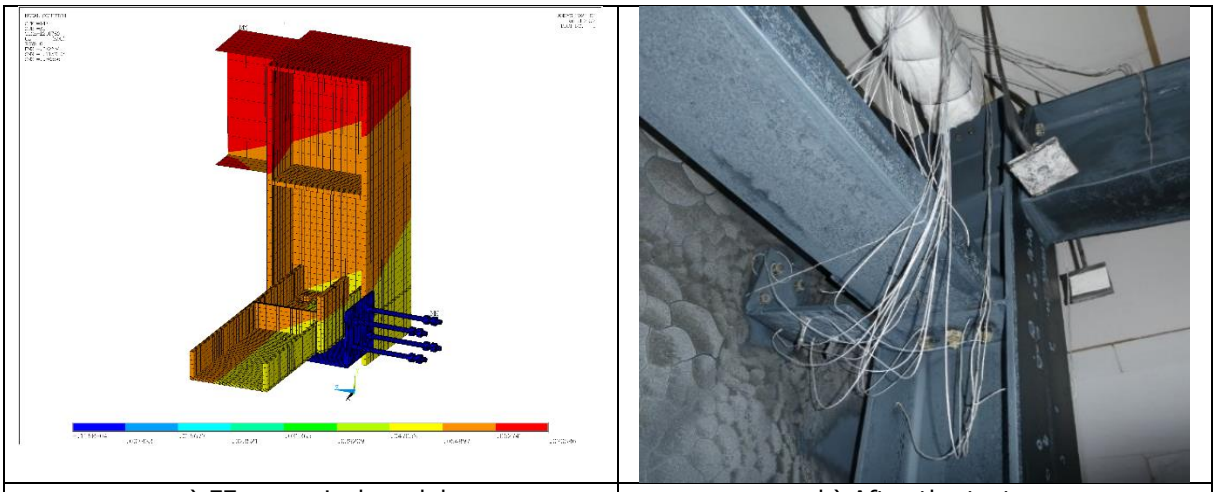

a) FE numerical model | b) After the test

Figure 3.42: Deformed shape of fusible link n°2 predicted by the numerical model and that observed after the test

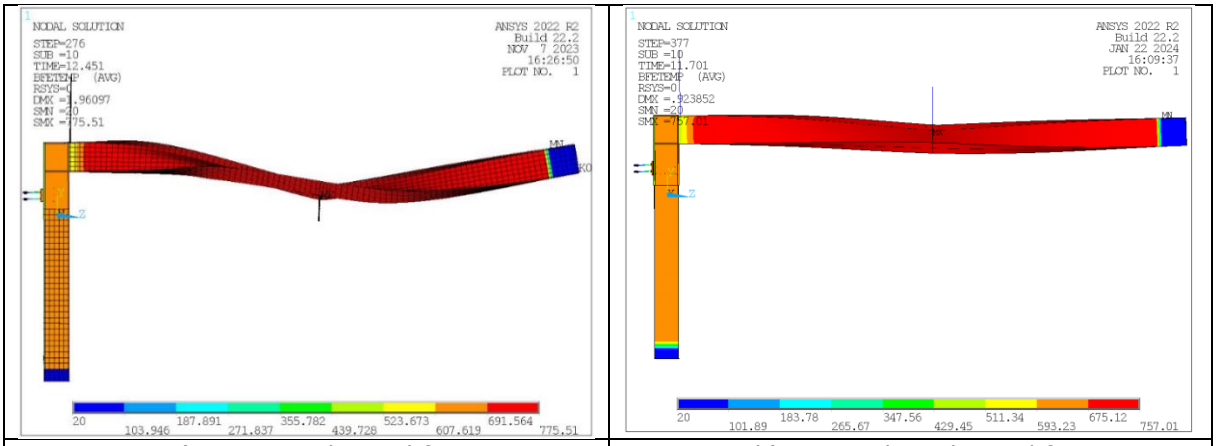

a) First steel portal frame | b) Second steel portal frame

Figure 3.43: Temperature fields in semi-portal-frames at failure times

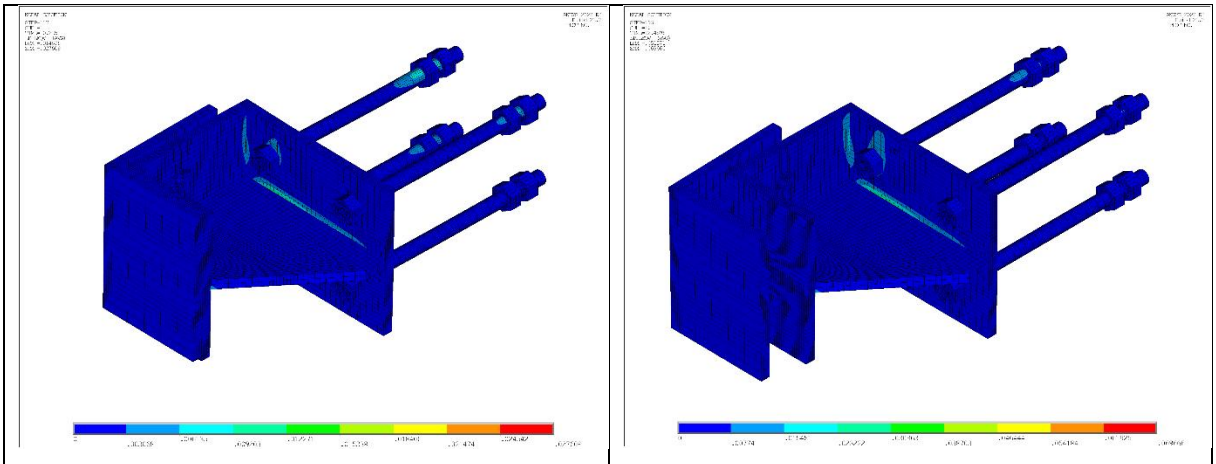

a) At 1045 seconds of fire exposure | b) At failure time of associated portal frame

Figure 3.44: Distribution of Von Mises equivalent plastic strain in the first fusible link

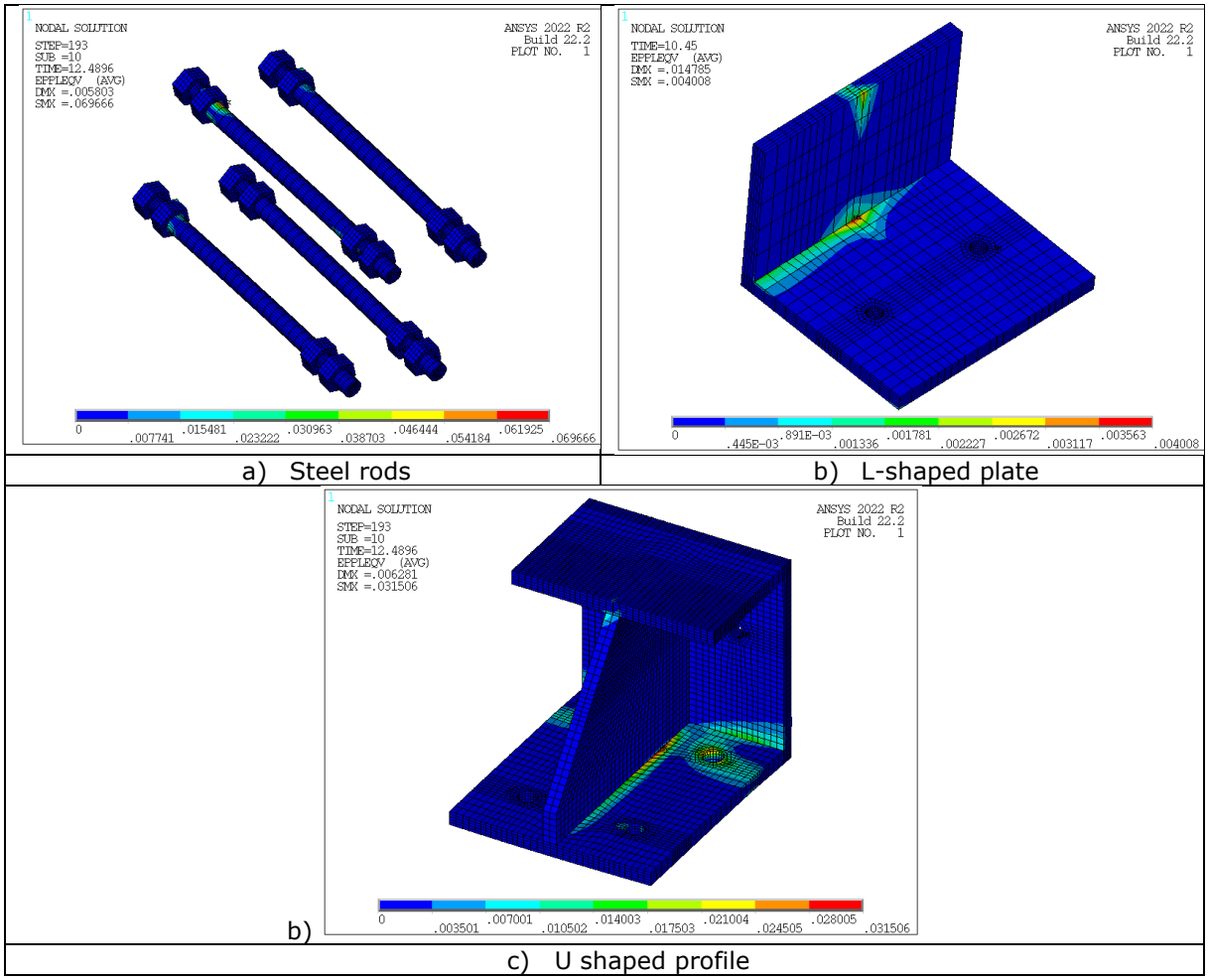

Figure 3.45: Distribution of Von Mises equivalent plastic strain in components of the first fusible link at failure time of the semi-portal frame n°1

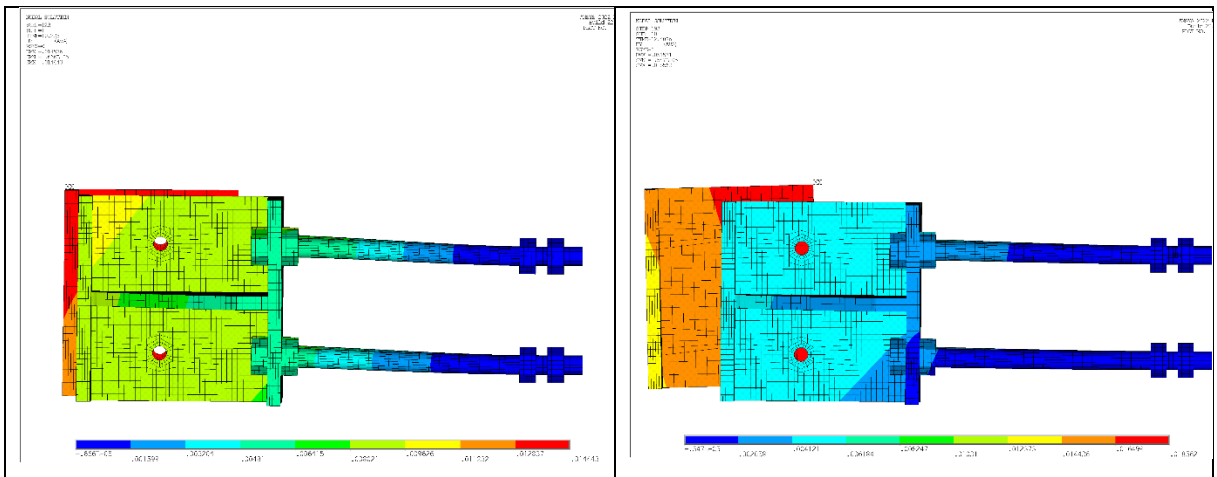

Figure 3.46: Vertical displacement fields in the first fusible link

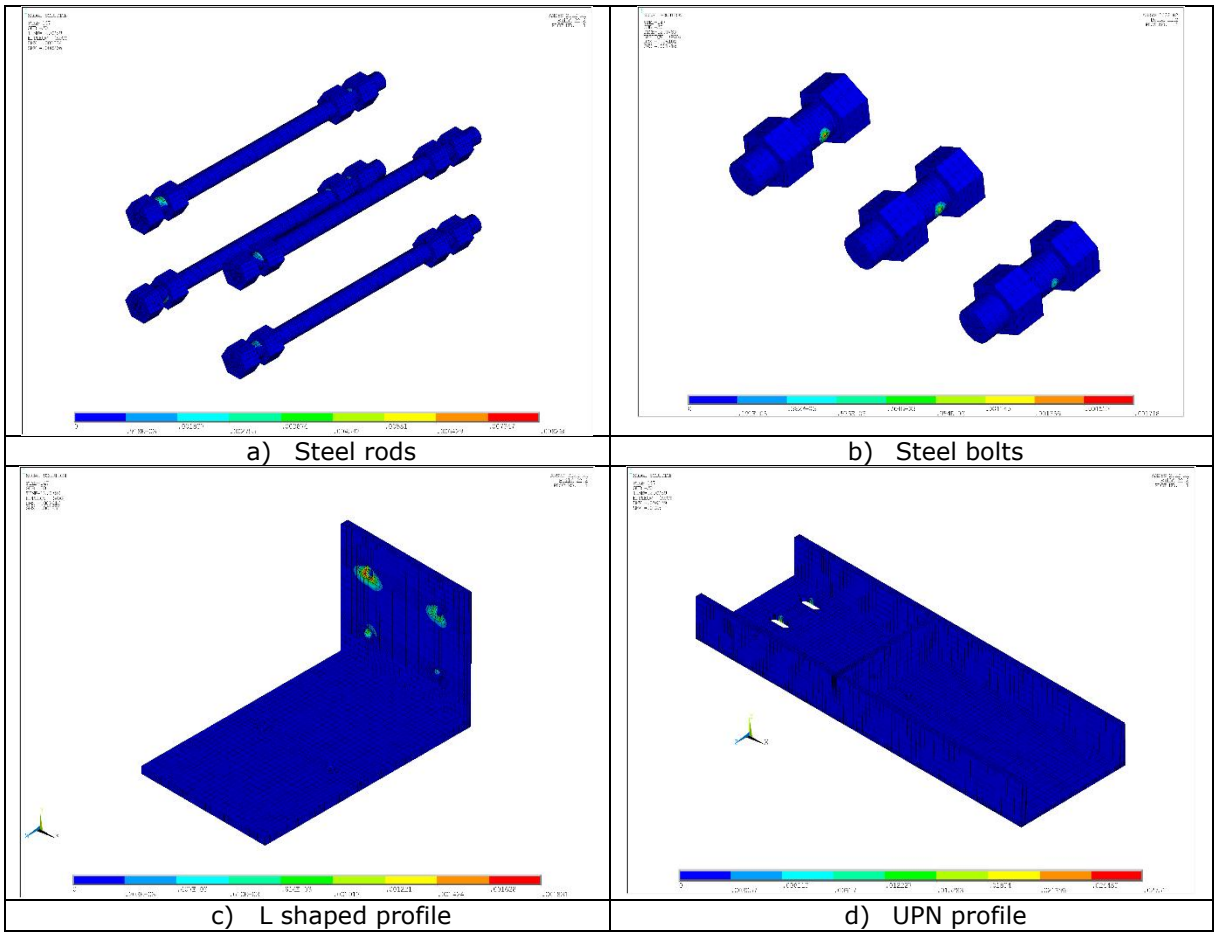

a) Steel rods

b) Steel bolts

c) L shaped profile

d) UPN profile

Figure 3.47: Distribution of Von Mises equivalent plastic strain in components of the second fusible link at failure time of the steel portal frame n°2

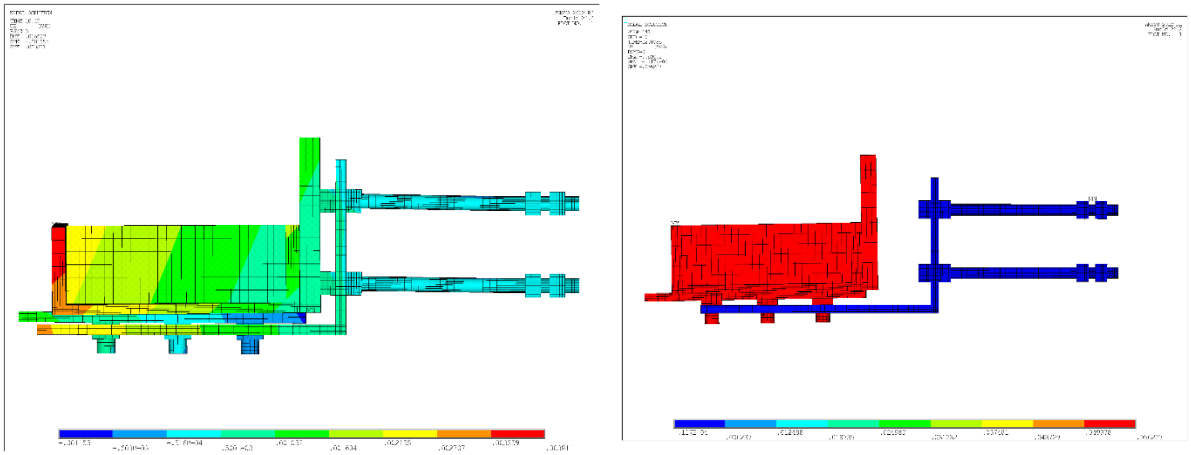

a) At 1045 seconds of fire exposure

b) At failure time of the semi-portal frame n°2

Figure 3.48: Vertical displacement fields in the second fusible link

The results obtained from the numerical model indicate that, as expected, both steel frames failed due to the lateral torsional buckling of the beams under the combined effect of the mechanical loading and the temperature rise. The collapse of the steel frames was not simultaneous, with one frame failing before the other: after approximately 1240 and 1170 seconds of fire exposure when the temperature of the beam reached approximately 765°C and 770°C for semi-portal frame n° 1 and semi-portal frame n° 2, respectively. Unfortunately, during the test, it was not possible to measure displacements at the level of the fusible links exposed to fire. Only their overall behaviour could be visually observed. The developed FE models predict that both portal frames break away from the wall during the collapsing stage, with no noticeable damage or deformation of the fusible links during both the pushing and collapsing stages, except for the loss of aluminium bolts. The U-profile bolted to the threaded rods is detached from the L-profile welded to the portal frame column n°1, as shown in Figure 3.39. Similarly, the L shaped profile bolted to the threaded rods is detached from UPN profile bolted to the portal frame column n°2 (see Figure 3.42). The results of numerical models clearly show that a gap occurs between the parts of the fusible links initially bolted with aluminium bolts (see Figure 3.46 and Figure 3.48). Furthermore, the equivalent plastic strain distributions on the fusible link components indicate that no significant plastic deformation of the profiles or threaded rods is observed until the failure of the portal frames (see Figure 3.45 and Figure 3.47).

Figure 3.50 and Figure 3.51 show the time-displacement curves calculated for the portal frame n°1, at mid-span of the beam and at the beam-to-column connection. It should be noted that the displacements calculated with the numerical model correspond to the relative values compared to those obtained immediately after the application of the mechanical load. Figure 3.49 illustrates the orientation of the displacements, where the positive direction of the horizontal and vertical displacements is from the outside to the inside of the furnace and from the top to the bottom, respectively. It should also be noted that the positive signs of both the horizontal and vertical displacements recorded during the test correspond to displacements of the beam towards the inside of the furnace. The predicted displacement curves are compared with the experimental measurements. The vertical displacement curves Uy (see Figure 3.50a and Figure 3.51a) show an overlap between the test and the numerical model. They increase progressively from the beginning of the test until the failure time. This corresponds to the free thermal expansion of the column with the increase in temperature combined with the deformation due to the vertical load. The horizontal displacement curves then clearly show three distinct phases. From the beginning of the test to about 780 seconds, the displacement Uz at mid-span of the beam gradually increases. This corresponds to the thermal expansion phase of the beam until the displacement at its free end reaches the value of 50 mm, which corresponds to the end stop. The second phase is then characterized by a plateau in the horizontal displacement H3, from 780 seconds to 1240 seconds. The horizontal displacement no longer evolves, and a stop force is generated in the beam until the semi-portal frame fails. Finally, the asymptotes of the curves occur at approximately 1240 seconds (for the numerical model) and 1620 seconds (for the test), corresponding to the failure times of the beam of the semi-portal frame. At the time of failure, it can be seen that the calculated and measured horizontal displacements do not evolve in the same direction, one being positive and the other being negative. This could be explained by the location of the plastic hinge that occurs in the loading area of the beam, which does not occur exactly at exactly the same location between the numerical simulation and the test, thus leading thus to a rotation in two opposite directions of the rod used to measure the displacement at the beam mid-span. Is should also be noted that, experimentally, the abutment phase (which starts at around 900 seconds) and the failure occur later than predicted by the numerical model.

Therefore, the comparison results indicate that the developed numerical models correctly estimate the fire behaviour of steel portal frames and their failure mode. The observed phenomenon in the fusible links also appears to be well represented. However, the fire resistance rating obtained by modelling for both steel frames is shorter than that observed during the test. This can be explained by the fact that some assumptions made in the models do not allow for a perfect representation of all the test conditions:

- The evolution of the vertical displacement at the mid-span of the beams (see Figure 3.50a) shows that significant deformations start to occur at about 1240 seconds and progressively increase until the complete failure at about 1600 seconds. However, in the numerical simulations, the portal frame fails more abruptly. This difference in behaviour could be explained by the loading conditions applied to the portal frame in the modelling, where the vertical loads are applied consistently to the top flange of the beams throughout all the fire exposure. However, during the lateral torsional buckling of the beams, it was observed that the lower flange of the beam came into contact with the vertical steel profiles of the loading system (surrounding the beam cross-section) used to suspend the dead weight. This contact can have a favourable effect and bring partial restraint to the lateral torsional buckling of the beams.

- The fire resistance of a steel portal frame depends also on material properties and heating conditions. In simulations, there are uncertainties in the values of the mechanical properties considered for the steel (yield and ultimate strengths) and in the thermal gradients introduced in the models along the steel members. In fact, the material properties of the steel considered at ambient temperature are derived only from the values indicated in the steel certificates supplied, which are not necessarily the actual values for the steel profiles of the portal frames. In addition, the number of experimental temperature curves recorded during the test is not sufficient to have an accurate idea about the temperature gradients that could have occurred along the portal frames, in particular at the level of the fire-protected areas (column base, loaded beam area and beam ends).
- With regard to the support conditions at the free end of the beams, the actual clearance could be slightly greater than the theoretical value considered, i.e. 50 mm. Furthermore, the value of the spring stiffness assigned to take account of the stop system could be overestimated.

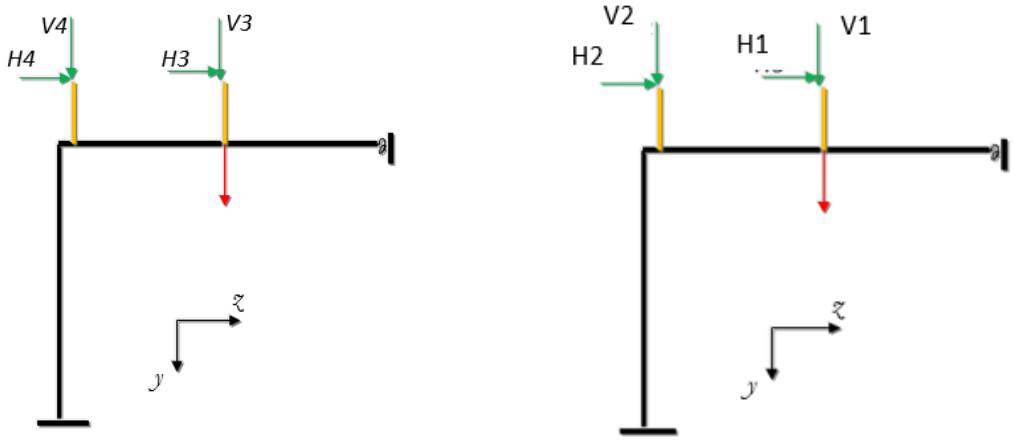

a) Portal frame n°1 a) Portal frame n°2

Figure 3.49: Schematic of recorded displacements during the test

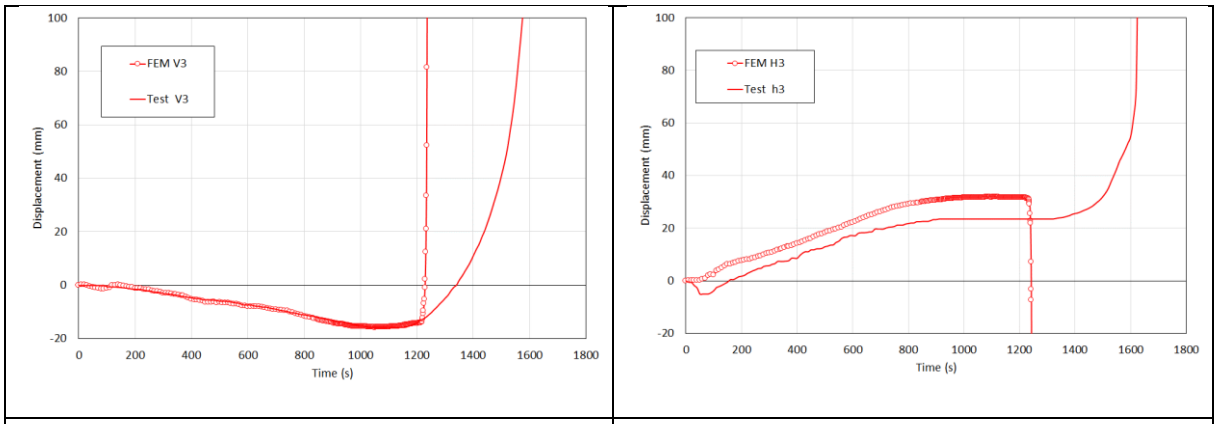

a) Vertical displacement b) Horizontal displacement

Figure 3.50: Time-displacement curves at the mid-beam of portal frame n°1

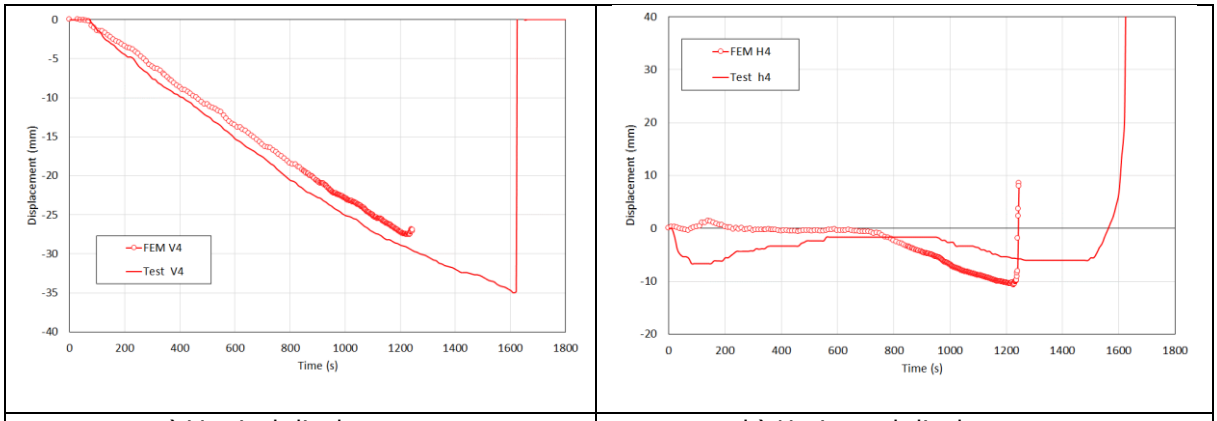

a) Vertical displacement | b) Horizontal displacement

Figure 3.51: Time-displacement curves at the beam-to-column connection of portal frame n°1

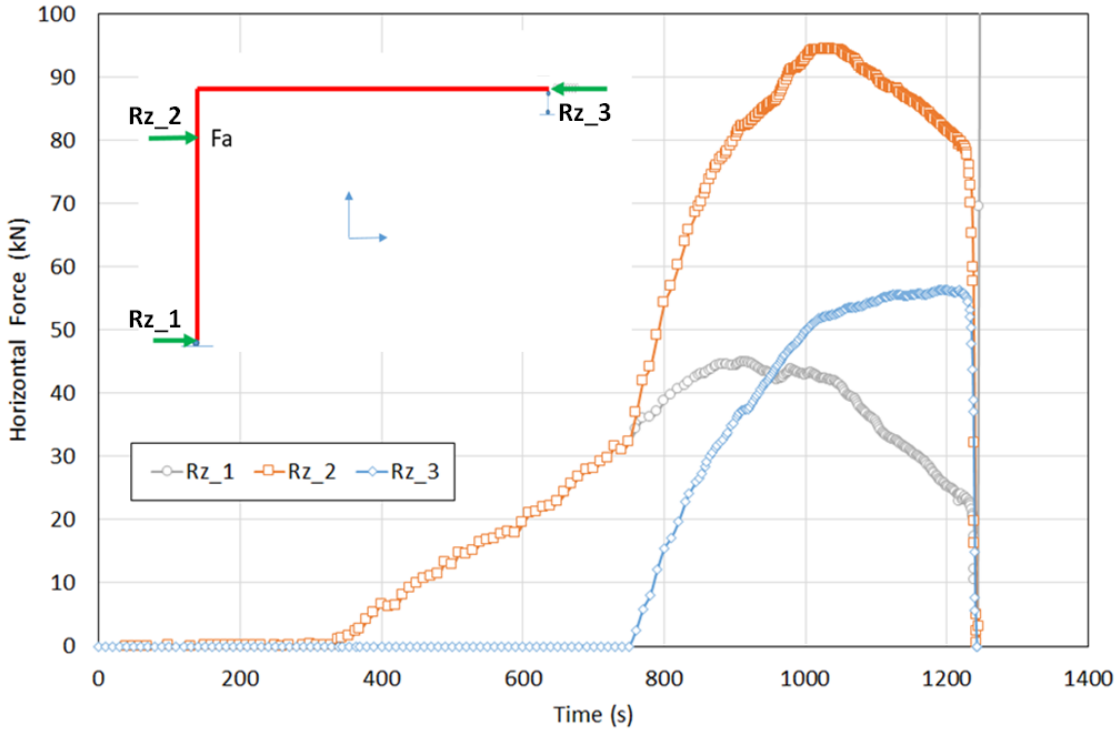

Figure 3.52: Horizontal reaction forces calculated for the portal frame n°1

In better understand the fire behaviour of the fusible links during the fire exposure, the Figure 3.52 shows the evolution of the support reactions of portal frame n°1: at the column base (RZ_1), at the spring end (Rz_3) and at the fusible link level (Rz_2) where the positive values correspond to the arrows shown in the diagram in Figure 3.52. To facilitate comparison, the absolute value of the reaction forces at the supports is presented. It can be seen that the abutment generates a reaction in the spring element (Rz_3), which results in a significant increase in the reaction at the fusible link (Rz_2). This additional force also explains the slope of the horizontal displacement curve H4 at the beam-to-column connection, which changes abruptly after 780 seconds when the system is pushed towards the wall (see Figure 3.51b). Furthermore, during this phase, the force transmitted to the fusible link reaches a peak of approximately 95 kN after 1020 seconds of fire exposure and then decreases. Finally, under the combined effect of the compression force induced by the contact, the load applied to the top flange at the mid-span of the beam, and the reduction in steel strength with the temperature rise, the failure of the semi-portal frame occurs at approximately 1240 seconds. This failure is associated with a combination of bending and lateral-torsional buckling of a beam under compression and bending.

With regard to the behaviour of the fusible link n°1, the evolution over time of the calculated support reactions shows that up to 280 seconds of fire exposure, no force is transmitted to the fusible link

due to free thermal expansion (see Figure 3.52). An initial increase in the force on the fusible link (noted as Rz_2) can be observed from 280s. This increase occurs when the beam has not yet expanded sufficiently to generate a pushing force. This first part of the force is induced by the temperature gradient in the cross-section of the column. As the model considers a temperature gradient between the column flanges (see Figure 3.22), a thermal deflection occurs in the column which tends to generate an initial pushing force on the link. This force is balanced by the reaction at the base of the column (see Figure 3.52). In this second phase, the beam is still in a state of free thermal expansion until 780 seconds. From this moment, the accelerated increase in pushing force generated on the fusible link coincides with reaching of the end-stop and continues until failure due to lateral-torsional buckling. Finally, after the failure of the semi-portal frame, no more force is transmitted to the link where the U-profile bolted to the rods has separated from the L-section welded to the portal column. In fact, it can be noted that the pushing force curve on the fusible link decreases towards 0 (see Figure 3.52). Figure 3.54 also shows the evolution of the displacements of several points on the contact surfaces between the U-profile and the L-profile (points 1, 2, 6 on the U-profile: curves in green; points 3, 4, 5 on the L-profile: curves in red). Initially, the increase in the Ux displacement curves shows a slight rotation around the Uy axis of the column cross-section as a function of time. Furthermore, from 0 to 280 seconds of fire exposure, when there is no contact between the two profiles, the Uy displacements (vertical displacement) of the U-shaped section do not change, whereas those of the L-shaped section increase with the thermal expansion of the column. Then, when they come into contact again at 280 seconds, the Uy displacements of the L-profile cause those of the U-section to also increase due to contact friction. The same phenomenon is observed for the Uz displacements. In particular, the difference in the displacement Uz of corresponding points on the 2 profiles shows that the contact between the two profiles is no longer maintained on all their surfaces that were initially in contact during the fire exposure.

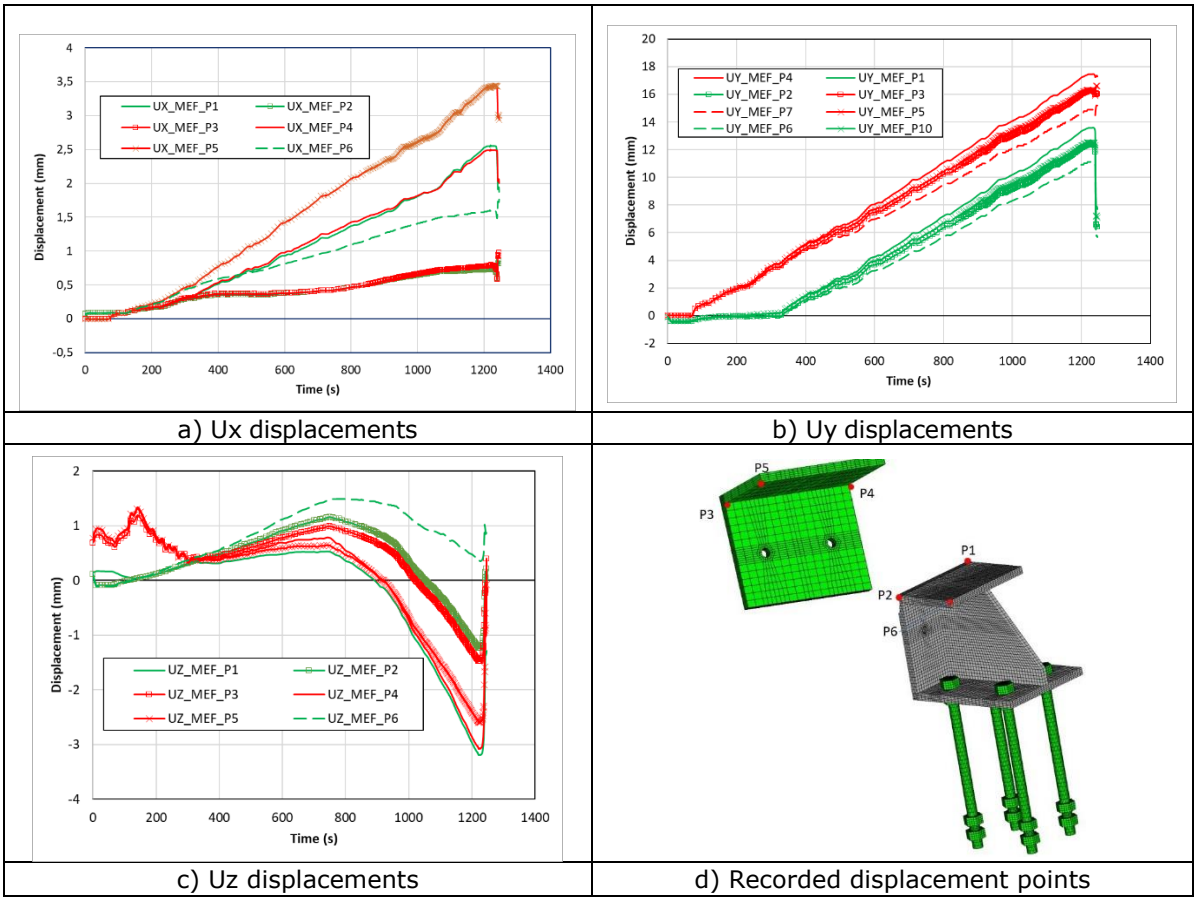

a) Ux displacements | b) Uy displacements

c) Uz displacements | d) Recorded displacement points

Figure 3.53: Time-displacement curves predicted at the contact surfaces between the two steel profiles of the fusible link n°1

The Figure 3.54 illustrates the time–axial reaction curves calculated at the restrained end of the steel rods of fusible link no. 1. From 280 seconds, the four rods are in compression and take up forces with quite different values. In fact, the two rods closest to the U-section web (rods no. 1 and no. 2 in Figure 3.54) take up greater compressive forces than the other two rods, with a maximum value of 43 kN (1st rod) and 33 kN (2^{2nd} rod) at around 1000 seconds. This difference between the forces acting on the rods and their evolution as a function of the time to fire exposure can be explained by the displacement of the contact surface between the upper flange of the U-shaped profile and that of the L-shaped profile along the Y axis as a result of the thermal induced longitudinal expansion of

the column, and the thermal bending combined with the torsion of the column during the fire exposure.

In conclusion, the maximum horizontal force transmitted from the n°1 semi-portal frame to the fusible link n°1 is approximately 95 kN.

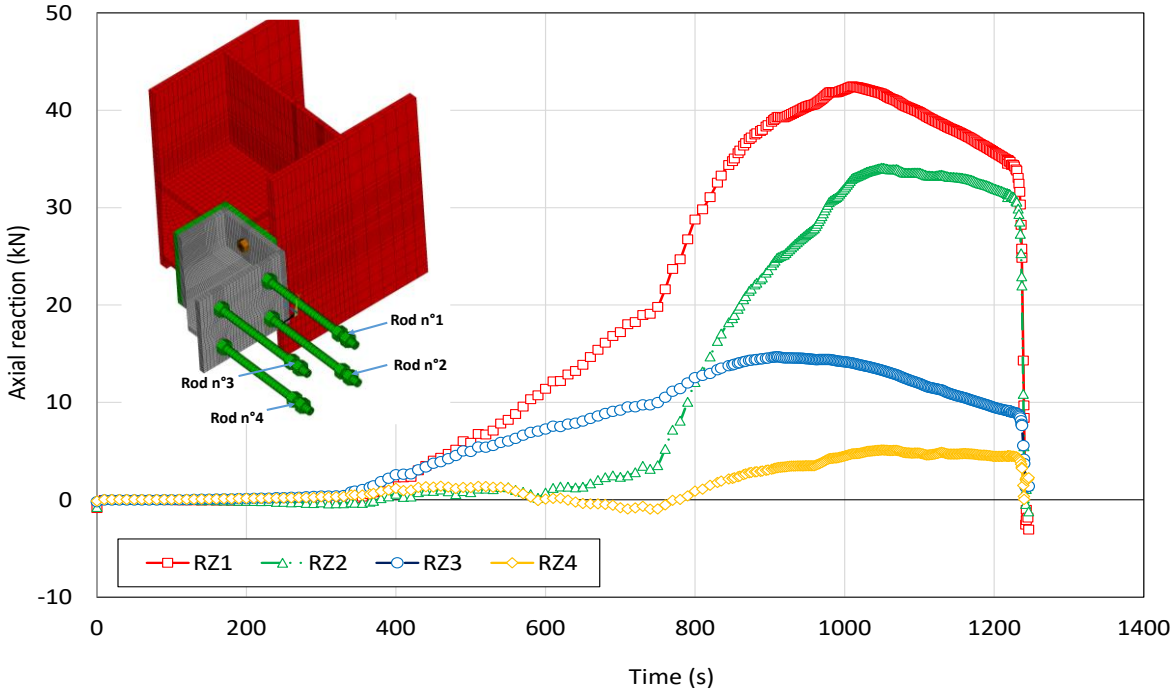

Figure 3.54: Time axial reaction curves calculated at the restrained end of steel rods of fusible link n°1

The overall behavior of the steel portal frame n°2 predicted by the numerical model is shown in Figure 3.55 to Figure 3.57. In general, the numerically predicted behavior of the portal frame n°2 is similar to that predicted for the portal frame n°1. In general, the mechanical behaviour of the two semi-portal frames is similar and shows three distinct phases. However, the calculated fire resistance duration of the portal frame n°2 is slightly shorter than that of the other. It can also be seen that the shape of the horizontal displacement curve at the beam-to-column connection is different between the two semi-portal frames, from the beginning to the abutment of each semi-portal frame. In addition to the thermal gradients on the columns, this could be due to the different arrangement of the fusible links associated with the semi-portal frames and their flexural stiffness. In addition, the onset of the plateau in the second phase and the failure of semi-portal frame no. 2 occurred earlier than those calculated for the semi-portal frame n°1. This can be explained by the difference in temperatures affected on the beam of the semi-portal frames. In fact, the temperatures affecting the beam of semi-portal frame n°2 (sections S7 and S8) are higher than those of the corresponding sections on semi-portal frame n°1 (sections S1 and S2). It is therefore quite logical that the lateral-torsional buckling of the beam should occur when the temperature in the beam mid-span reaches the same level (approximately 760-770°C) in both cases. The Figure 3.57 shows the time-horizontal reaction curves calculated at supports of the steel portal frame n°2. It should be noted that the pushing force transmitted from the portal frame n°2 to the corresponding fusible link peaks at around 60 kN at 1020 seconds. This maximum force is therefore lower than the force supported by the first fusible link. Figure 3.58 shows the temporal evolution of the support reactions calculated at the level of the threaded rods of fusible link n°2. This trend is consistent with the overall behaviour of the semi-portal frame. In fact, it is clear that from 275 seconds, as observed on fusible link n°1, the 4 rods are in compression and take up forces of different values. The rod closest to the column and the UPN-web (rod n°3) bears a higher compression force than the other rods, with a maximum value of 38 kN at about 1050 seconds. This difference between the axial forces acting on the rods can be explained by the eccentricity between the load transmitted from the column to the UPN profile via the steel bolts to the stiffener plan and the support of the threaded rods along the y and x axes. When the semi-portal frame fails, at approximately 1170 seconds, the axial reactions decrease abruptly, corresponding to the stage when the UPN profile is detached from the fire wall and the heads of the threaded rods.

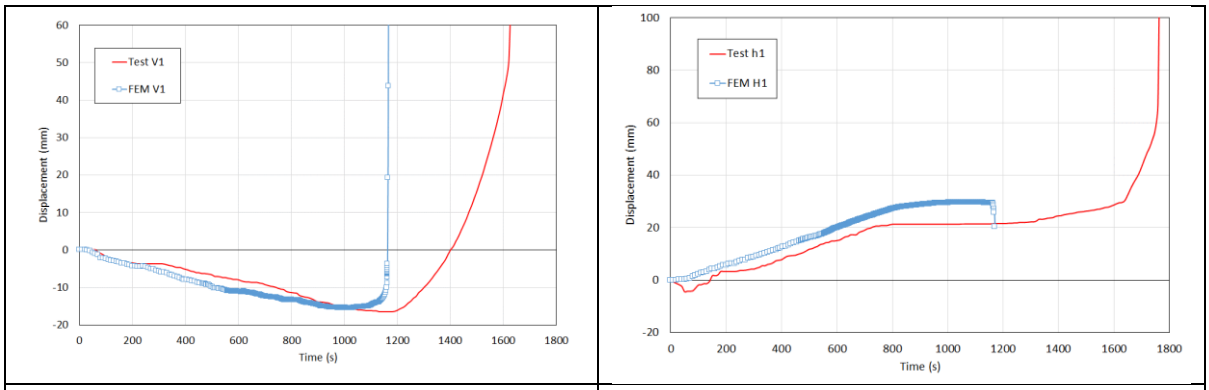

a) Vertical displacement Uy | b) Horizontal displacement Uz

Figure 3.55: Time-displacement curves at the mid-beam of portal frame n°2

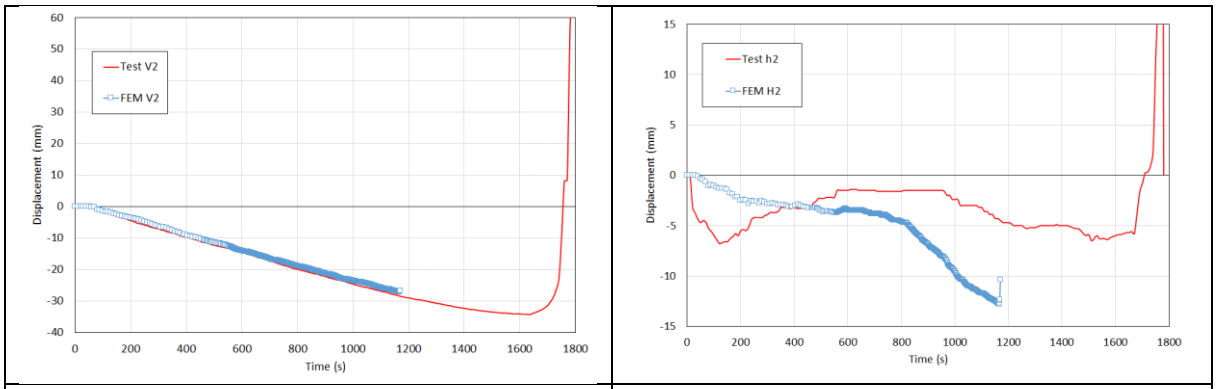

a) Vertical displacement Uy | b) Horizontal displacement Uz

Figure 3.56: Time-displacement curves at the beam-to-column connection of portal frame n°2

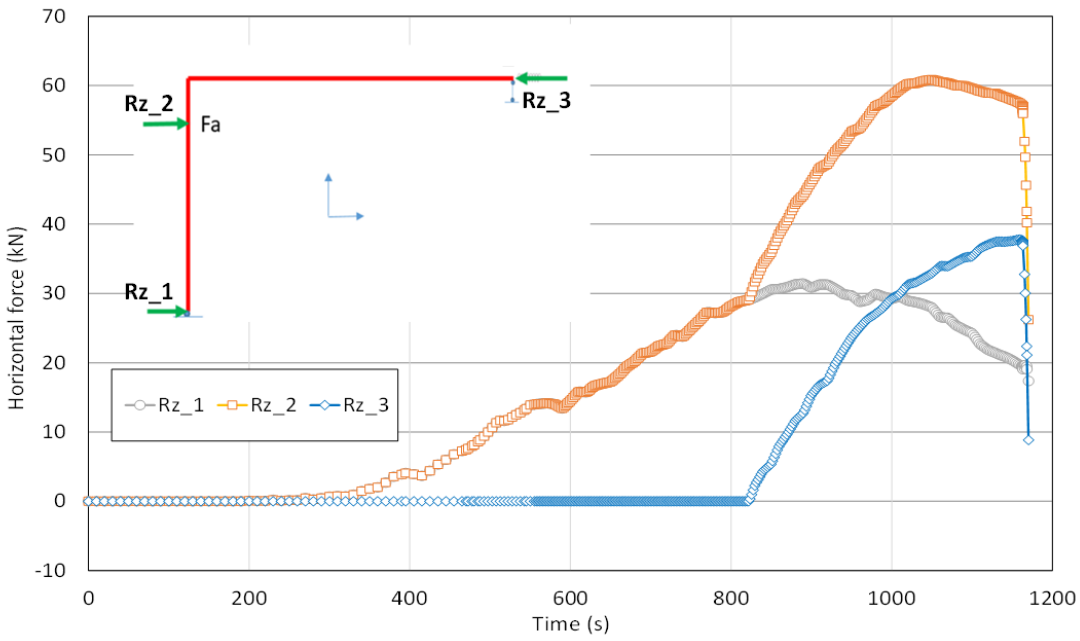

Figure 3.57: Horizontal reaction forces calculated for the portal frame n°2

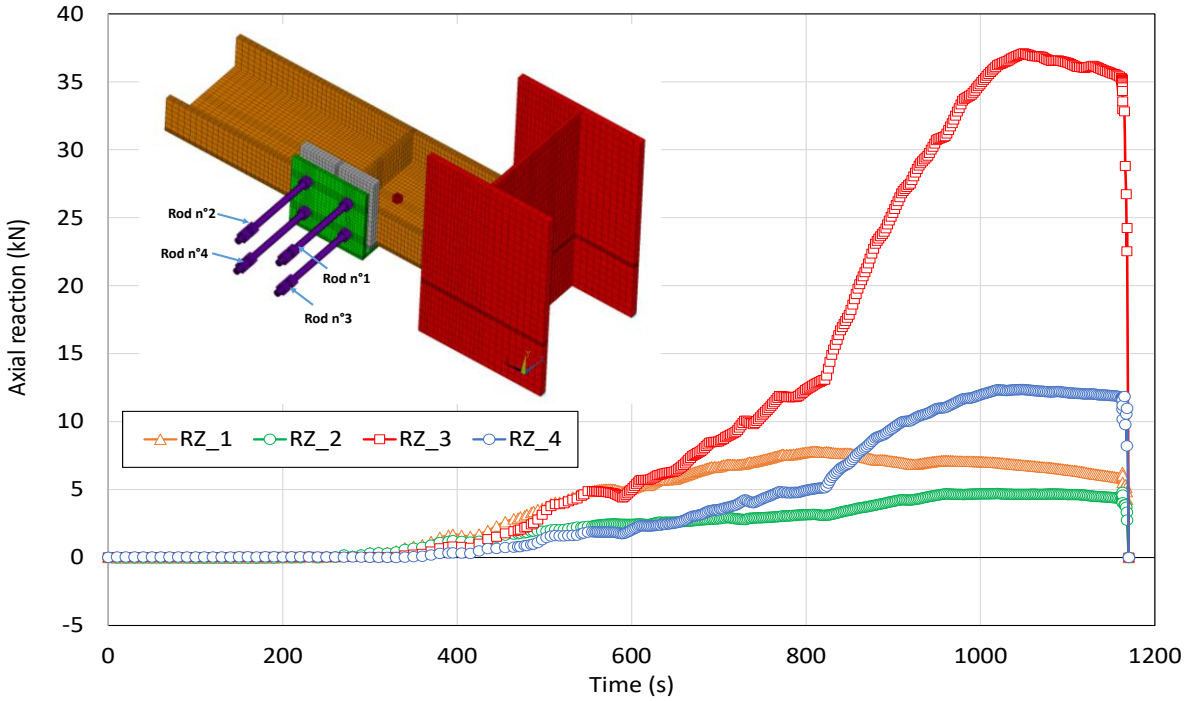

Figure 3.58: Time axial reaction curves calculated at the restrained end of steel rods of fusible link n°2

In order to confirm the fact that the loading system used in the test may have had a favourable effect on the fire behaviour of the semi-portal frames, an additional FE analysis was carried out on the semi-portal frame n°1. Here, it is assumed that the beam of the semi-portal frame is laterally restrained along its entire length to prevent lateral-torsional buckling. All the other boundary conditions and loading conditions remain unchanged. (see Figure 3.59). The deformed shape of the semi-portal frame at failure is shown in Figure 3.60, which indicates that the failure mode is the plastification of the profile cross-section at the beam mid-span (at load level) at approximately 1779 seconds. The new displacement curves obtained are shown in Figure 3.61 and Figure 3.62, and are compared with the experimental curves. They clearly show that the calculated fire resistance time of the semi-portal frame is now greater than that observed during the test. The evolution of the axial reaction at the level of the threaded rods and that of the calculated support reactions of the semi-portal frame as a function of the time to fire exposure are shown in Figure 3.63 and Figure 3.64, respectively. They show that the calculated curves for the support reactions of the semi-portal frame and the axial reactions at the threaded rods are similar to those obtained with the initial FE model. In particular, the peak of the horizontal force acting on the fusible link appears to occur at the same time, after approximately 1000 seconds. However, the force calculated by considering that the lateral-torsional buckling is prevented (RZ_2 equal to 93 kN) is slightly lower than that calculated by the initial model (RZ_2 equal to 95 kN). This small difference could be explained by the fact that, in the case where all the out-of-plane displacements of the beam are prevented, there is a lower pushing force on the fusible link than in the other case. The results obtained with the model where the lateral-torsional buckling of the beam is restrained confirm that, during the test, the out-of-plane displacements of the beam were probably limited by the load suspension elements, providing partial restraint against buckling, which had a favourable effect on the fire resistance of the semi-portal frame. As a result, the portal frame failed later than the numerically calculated fire resistance time for a laterally unrestrained beam.

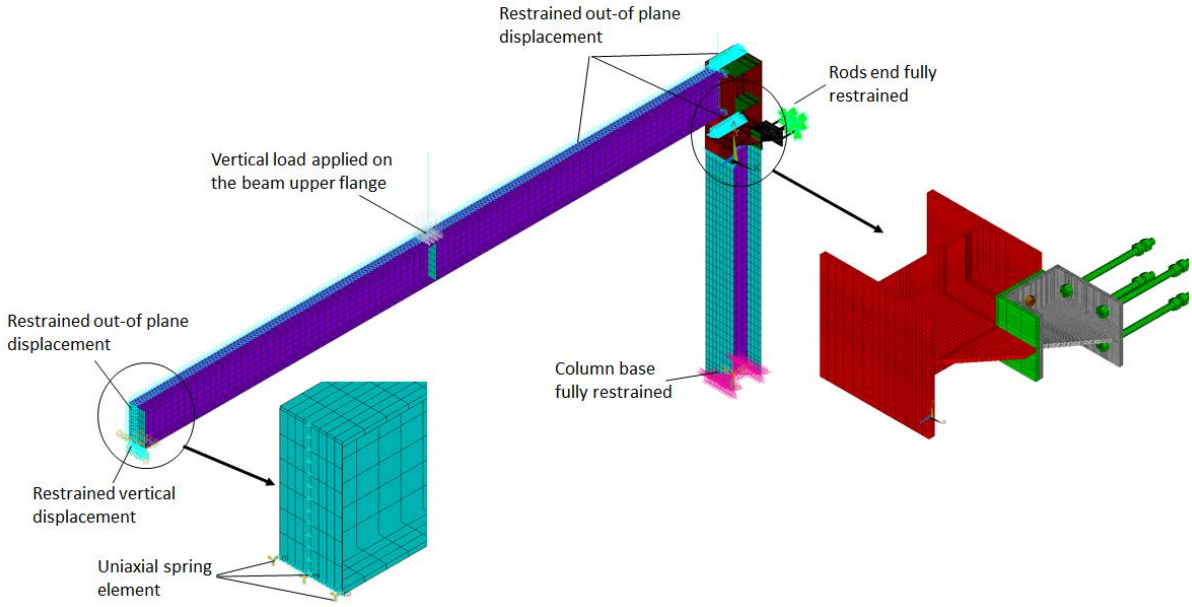

Figure 3.59: Mechanical model developed for the portal frame n°1 with restrained lateral displacement conditions

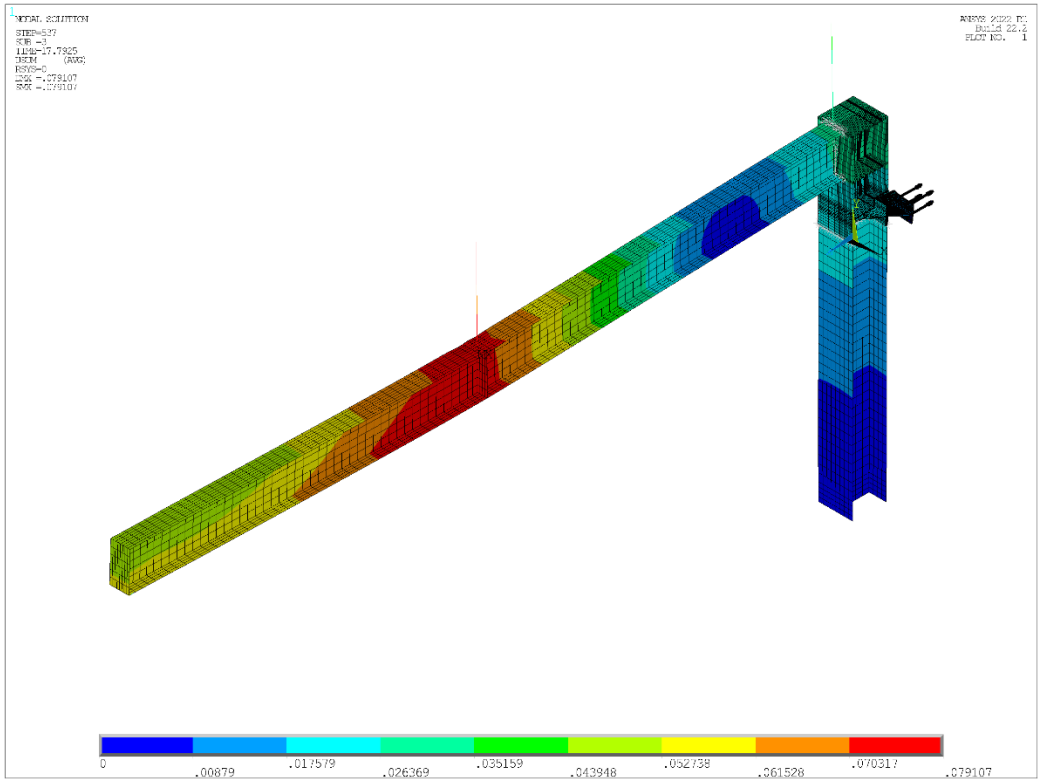

Figure 3.60: Deformed shape at failure time of the steel portal frame n°1 with restrained lateral displacement conditions

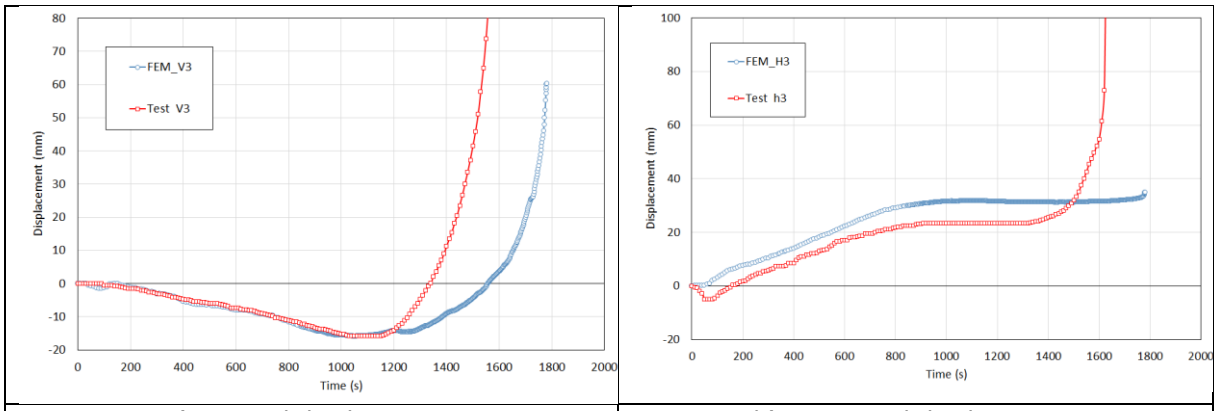

a) Vertical displacement | b) Horizontal displacement

Figure 3.61: Time-displacement curves at the mid-beam of portal frame n°1 with restrained lateral displacement conditions

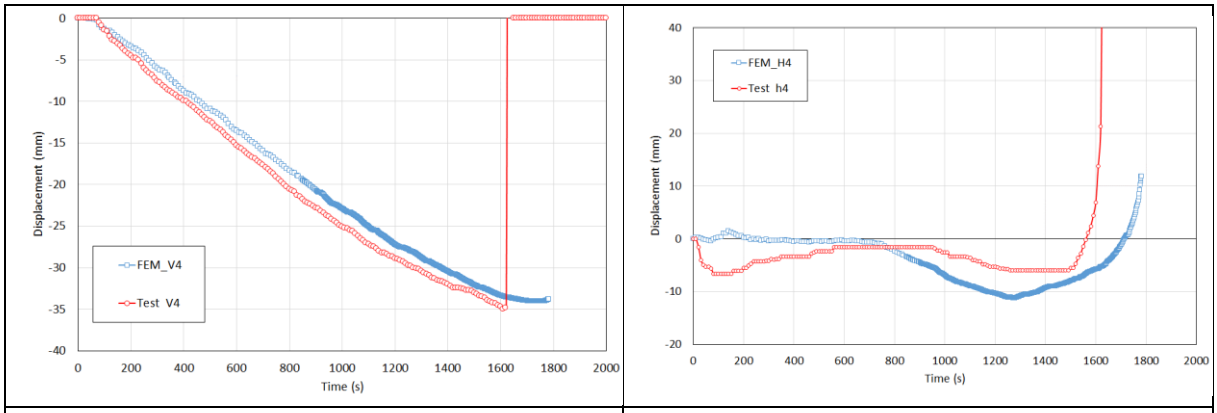

a) Vertical displacement | b) Horizontal displacement

Figure 3.62: Time-displacement curves at the beam-to-column connection of portal frame n°1 with restrained lateral displacement conditions

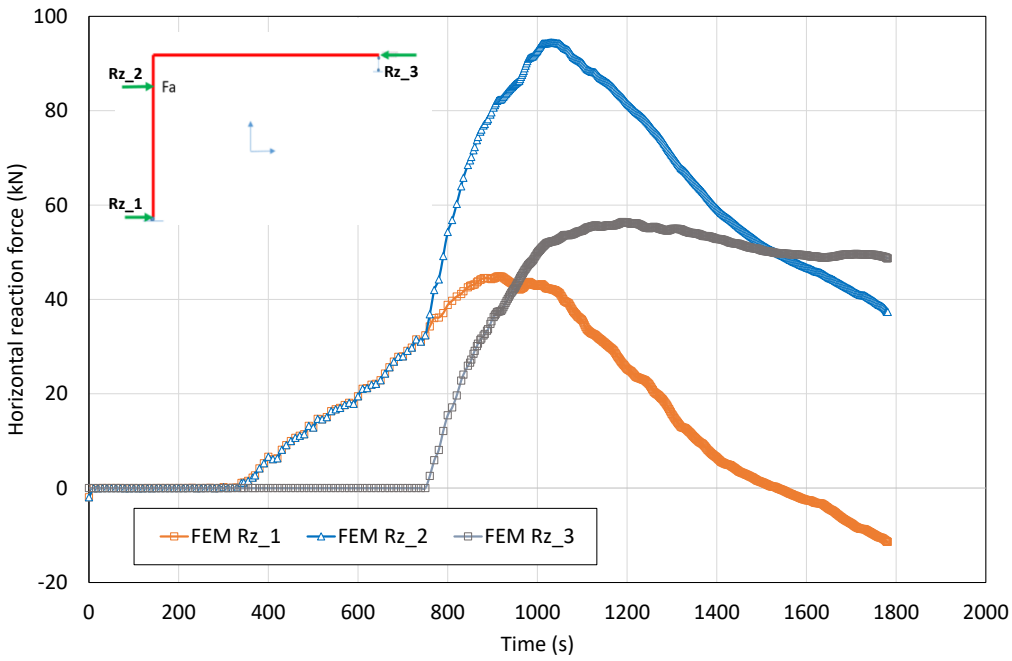

Figure 3.63: Horizontal reaction forces calculated for the portal frame n°1 where the lateral-torsional buckling of the beam is restrained

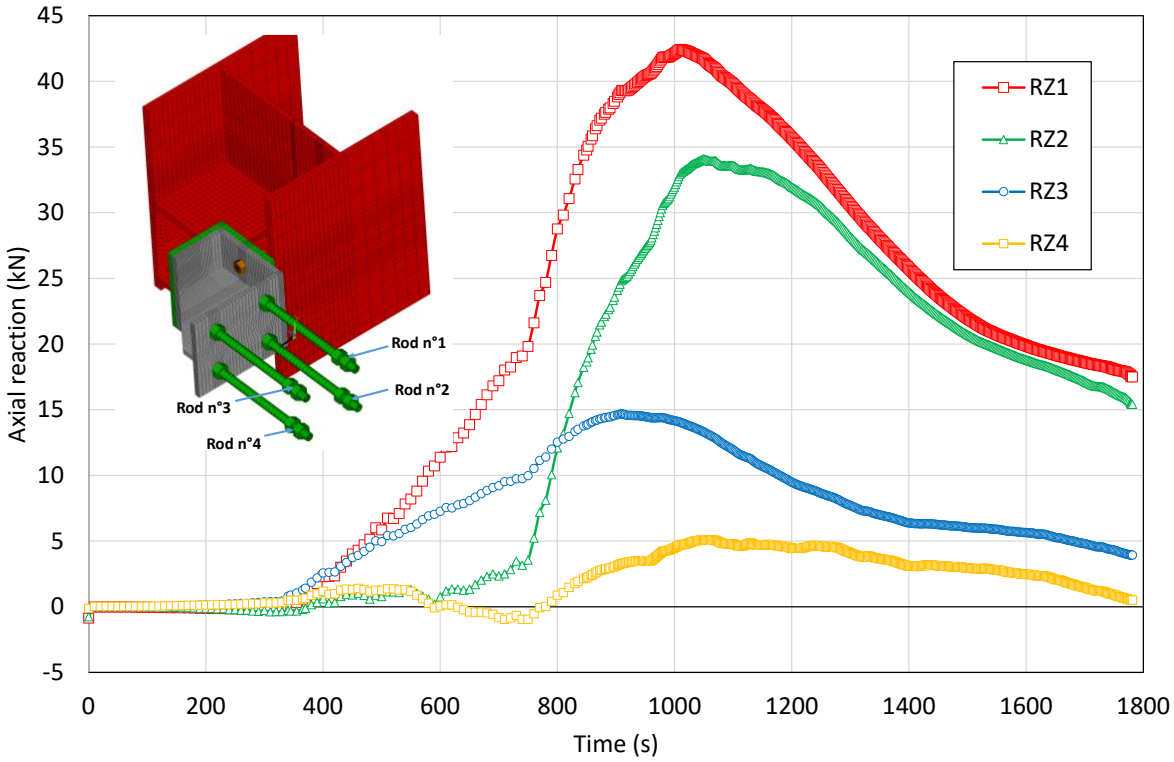

Figure 3.64: Time-axial reaction curves calculated at the restrained end of steel rods of fusible link n°1 where the lateral-torsional buckling of the beam is restrained

3.3 Conclusion

Comparison of the numerical results with experimental measurements indicates that the modelling assumptions adopted in the thermal analyses allow satisfactorily prediction of the heating of the tested specimen, when the measured hot-gas temperatures are used. However, the predicted heating of the fusible links is slightly higher than that measured during the test. This could be explained by the fact that the hot-gas temperatures at the level of the fusible links were probably slightly lower than those measured at level of the beams during the test. In addition, the shadow effects considered in the numerical model may be underestimated, leading to higher temperature rises.

Comparison results also indicate that the developed mechanical models correctly estimate the fire behaviour of steel portal frames and their failure mode. Unfortunately, during the test, it was no possible to measure displacements at the level of the fusible links exposed to the fire. Only their overall behaviour could be monitored visually. As observed experimentally, the developed FE models predict that both portal frames break away from the wall during the collapsing stage, with no noticeable damage or deformation of the fusible links during both the pushing and collapsing stages, except for the loss of aluminium bolts. However, the fire resistance rating obtained by modelling for both semi-portal frames is lower than that observed during the test, mainly due to the difficulty of accurately modelling the mechanical load applied to the portal frames, which evolved at the end of the test with the lateral torsional bulking of beams. The fire resistance of the steel portal frames also depends on material properties and heating conditions. In simulations, there are uncertainties in the values of the mechanical properties considered for the steel (yield and ultimate strengths) and in the thermal gradients introduced in the models along the steel members. Finally, the actual clearance at the free end of the beams could be slightly greater than the theoretical value considered, i.e. 50 mm. Furthermore, the value of the spring stiffness assigned to take account of the stop system could also be also overestimated.

4 VALIDATION OF THE NUMERICAL MODELS DEVELOPPED FOR STEEL PURLINS CROSSING THROUGHT A FIRE WALL

Numerical analyses of the test performed in task 3.2 were carried out in order to better understand the behaviour of the tested specimen [9], to provide a scientific interpretation of the test and to explain the observed behaviour. Analyses allowed also to validate the ability of the 3D detailed numerical models developed in task 3.4 to simulate the thermo-mechanical behaviour of steel purlins passing through a fire wall made of sandwich panels.

The comparison of the FE model results with the outputs of the test is presented hereafter.

4.1 Brief description of the fire test

A short description of the test specimen and the test setup is given hereafter.

4.1.1 Tested specimen

Figure 4.1 shows a schematic of the test arrangement. The test specimen consisted of two IPE200 steel purlins intersecting a fire wall made up of 175 mm thick lightweight sandwich panels providing 120 minutes of fire resistance (EI 120). The purlins were cantilevered single-span members. They were simply supported on the fire-exposed side by a fork support, allowing free axial thermal expansion of over 60 mm. On the fire-unexposed side, the purlins were bolted to a beam that formed part of a horizontal support frame placed around the furnace and running along the wall. The continuity effects of the purlin were accounted for by a steel beam, which also prevented the potential uplift of the free end of the purlins on the fire-unexposed side. The purlins spanned approximately 6.25 metres, with cantilever lengths of approximately 1m. The purlins were spaced 1.5m apart and supported a 1.5m wide and 1 mm thick continuous steel roof deck (type JI 40-190-950 roof steel sheeting), covered with a 100mm thick layer of mineral wool insulation.

The wall was 3.2 metres high and 3 metres wide and was constructed using Euroclad's Eurobond Rockspan Extra panels. The wall was erected according to standard practice. The sandwich panels were installed vertically, with the first purlin crossing the wall at the junction between two panels, and the secondpurlin crossing at the mid-width of a panel. On the fire-exposed side, the purlins were fire-protectedby an encasement system extending 50 cm from the fire wall, leaving the voids formed between the ribs of the trapezoidal steel sheeting and the top flange of the steel purlins unfilled. The encasement systems were also made from 175 mm thick sandwich panels.

For one of the purlins, the voids within the encasement system (between the purlin flanges) were filled with mineral wool. In addition, wall openings at the level of the purlins were also filled with mineral wool. The same type of mineral wool used in the core of the sandwich panels was applied throughout. Figure 4.3 shows photographs taken at various stages in the erection of the test specimen. Dead weights of 15kN, applied at mid-span, were used to load the purlins in addition to the self- weight of the test specimen (steel profiles, trapezoidal steel sheeting, and mineral wool insulation), as illustrated in Figure 4.3. One side of the wall and the roof system,from below, were exposed to fire. The temperature rise in the furnace was controlled to closely follow the ISO-834 standard fire curve. Temperatures were recorded in the furnace, at various locations along the steel purlins, and on the unexposed side of the wall. As the high furnace temperatures did not permit the installation of displacement sensors inside the furnace, draw-wire displacement sensors were installed above the steel roof decking (outside the furnace) and attached to the test specimen by stainless steel rods to measure the vertical displacement at various locations along the heated purlins, specifically at the encasement systems and at the purlin mid-span. Unfortunately,it was not possible to record the inclination of the purlin.

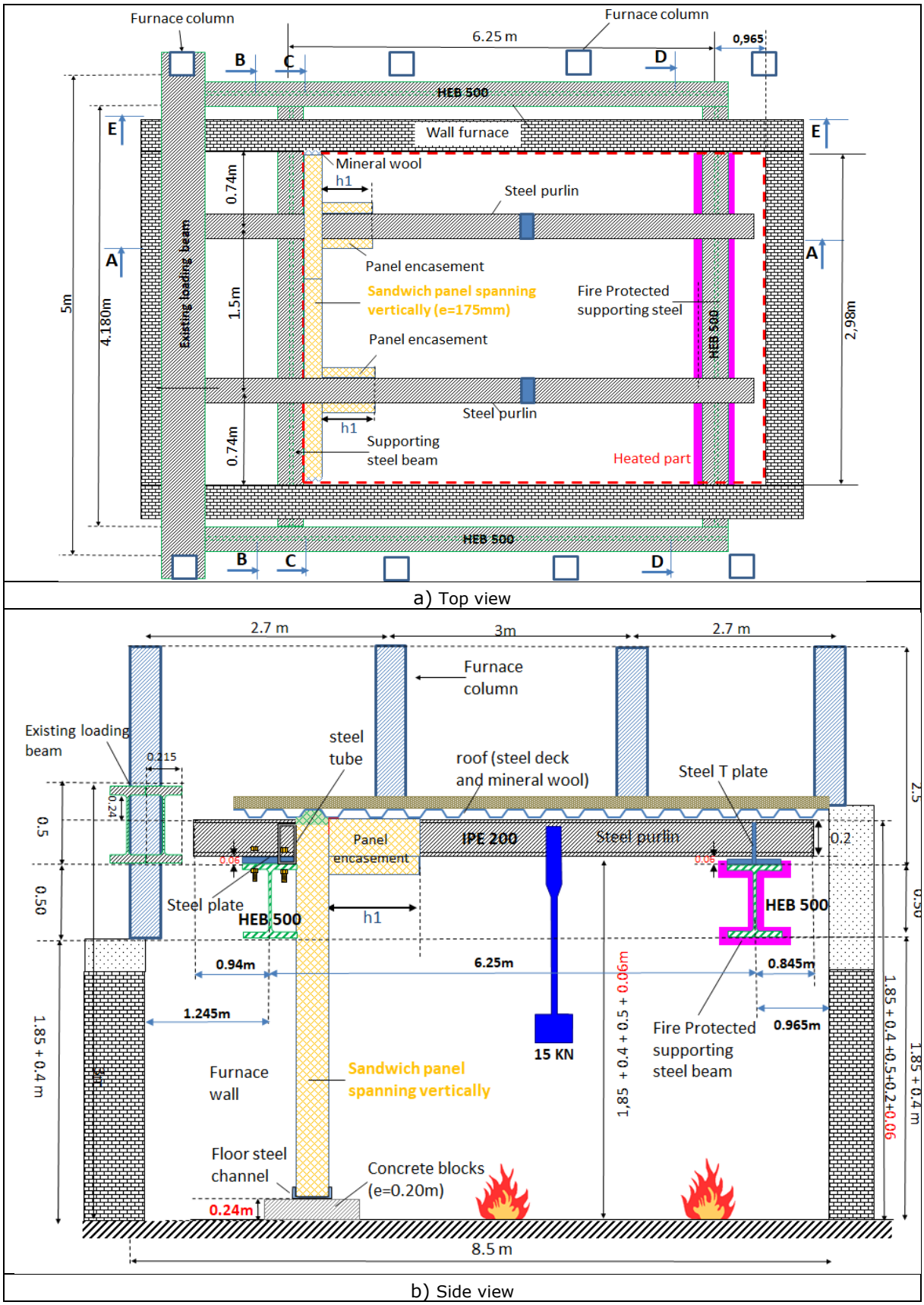

Figure 4.1 : Schematic of the test arrangement

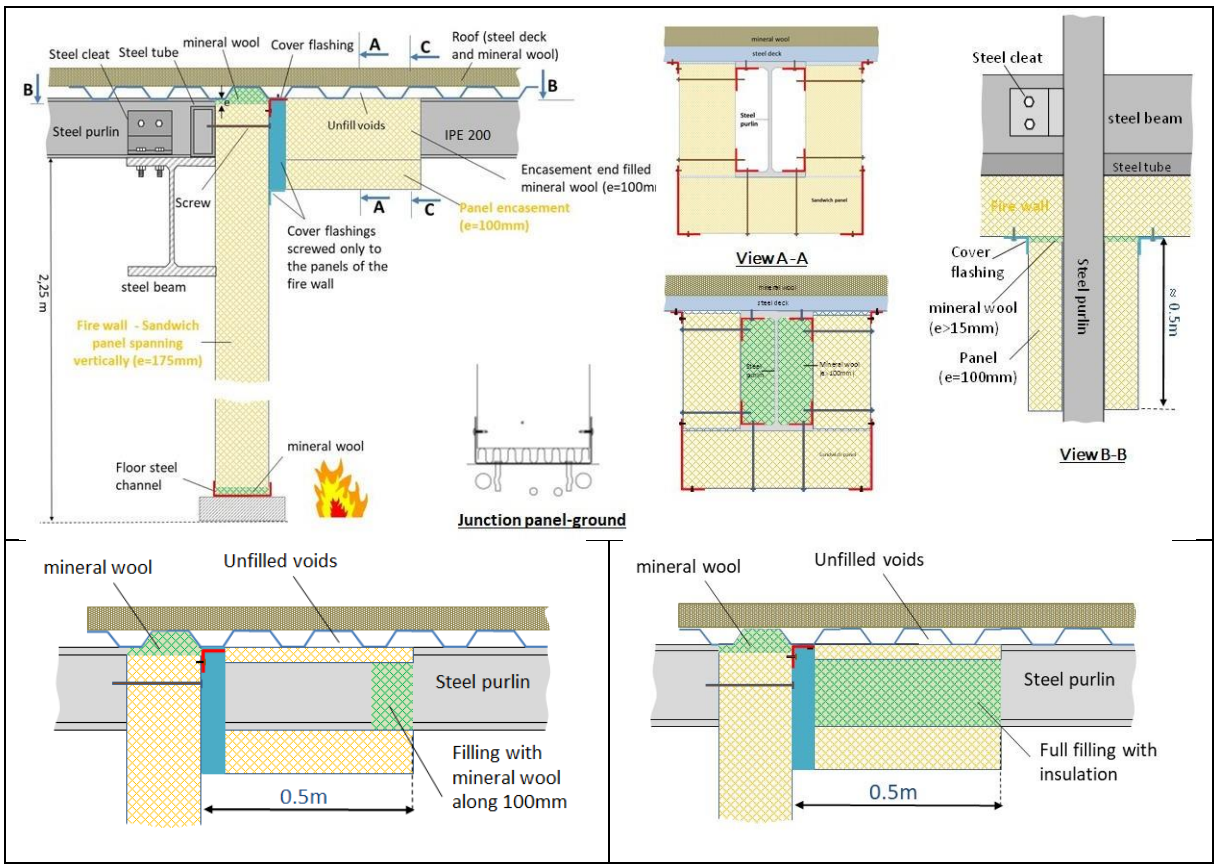

Figure 4.2 : Geometrical details of the test specimen

Figure 4.3: view of the test specimen after assembly (outside and inside the furnace)

Figure 4.4: view of constructional details of the tested specimen

4.1.2 Main test results

In this section, only the temperatures of the test specimen measured at key locations considered to be most significant are presented and discussed. These include temperatures at the bottom flange, mid-height of the web and top flange of the purlins, distinguishing the purlin parts directly exposed to the fire from those enclosed by the sandwich panels. In addition, the temperature evolution of the hot gases measured inside the furnace is also presented.

For information purpose, Figure 4.5 shows the location of the measuring cross-sections placed along the purlins while Figure 4.6 shows the location of plate-thermometers used to control the hot gases temperatures during the test.

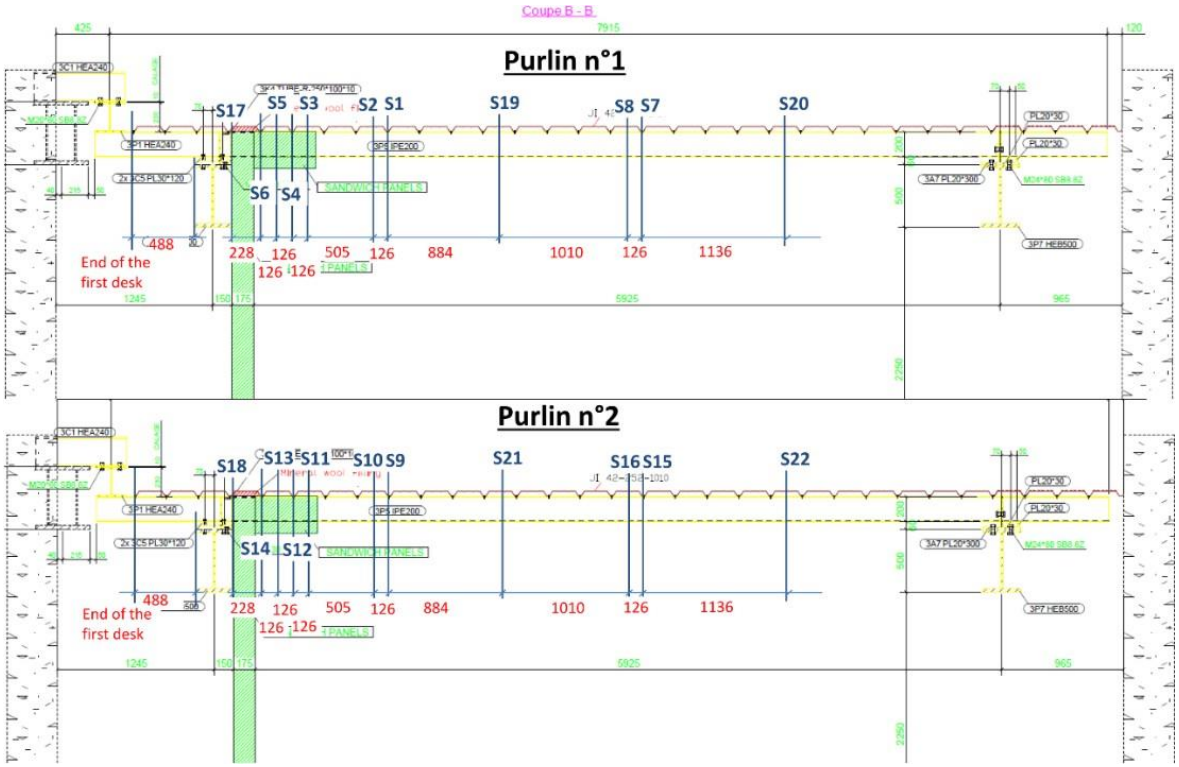

Figure 4.5: location of the measuring cross-sections placed along the purlins during the test

Figure 4.6: Location of plate-thermometers used to control hot gases temperatures during the test

4.1.2.1 Hot gases temperatures inside the furnace

Figure 4.7 shows the evolution of the hot gas temperatures measured in the furnace during the test. It can be seen that from the beginning of the heating process until about 500 seconds, the average temperature curve of the 12 plate-thermometers (T-four) rises more quickly than the ISO standard fire curve. The two curves then overlap until the end of the test. However, it should be noted that the temperature distribution in the furnace was not homogeneous. In fact, after about 500 seconds, the temperatures recorded by the plate-thermometers P1, P4, P7, P8, P10 and P11 are higher than the ISO standard fire curve (with a maximum difference of approximately 100°C at 3500 seconds). The temperatures at other positions (P2, P3, P5, P6, P9, P12) are lower.

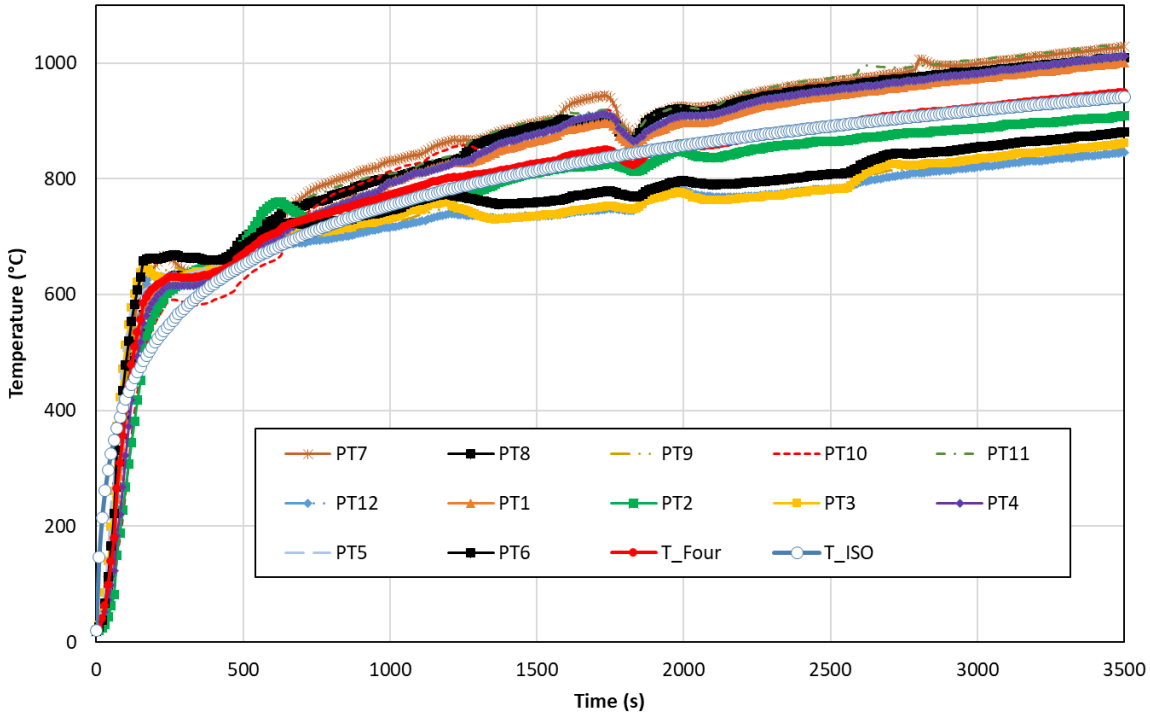

Figure 4.7: hot gas temperature-time curves recorded during the test

4.1.2.2 Heating of the purlin n°1

In this section, the following figures show the experimental temperatures recorded along the purlin n°1. Regarding the heating of the purlin, we are primarily interested in that of the upper flange and that of different part of the purlins, directly exposed to fire or not. To this end, the measured temperatures of the upper flange of the purlins are provided by distinguishing the purlin section at the level of the cavities from those in direct contact with the steel sheet.

Figure 4.8 and Figure 4.9 show the temperature curves measured at various points on purlin section S1 (in direct contact with the steel sheeting) and section S2 (at the level of a cavity) located along the part of the purlin directly exposed to the fire. As expected, the temperature rises of the web and the lower flange of the purlin are very similar over the duration of the test. They heat up faster than the upper flange, at least up to 1800 seconds. Comparing the temperature rise in the upper flange between sections S1 and S2 (see Figure 3.14), there is no significant difference in the temperature rises recorded, which is due to the heat conduction through the flange and the width of the cavity being greater than the width of the steel sheeting part in contact with the purlin.

The Figure 4.10 and Figure 4.11 shows the temperature rises in the purlin section S4 (in direct contact with the steel sheeting) and section S5 (at the level of a cavity), located on the encasement system. It should be noted that there is a significant temperature gradient appears within the section, with the upper flange heating up more than the web, which heats up faster than the lower flange. Whilst the top flange of the purlin is directly exposed to the fire in the cavities formed between the steel purlin and the trapezoidal steel sheet, the other parts of the purlin which are fire protected by the sandwich panels heat up mainly due to the heat conduction through the panels and the radiation heat exchange which occurs between the surfaces within the cavity formed by the encasement. Comparing the temperature rise in the upper flange between sections S4 and S5 (see Figure 4.13), there is some difference in the temperature rises recorded. Unlike the part of the purlin directly exposed to the fire, the top flange parts in the cavities formed between the steel purlin and the trapezoidal steel sheet heats up slightly more than the parts in direct contact with the steel sheet.

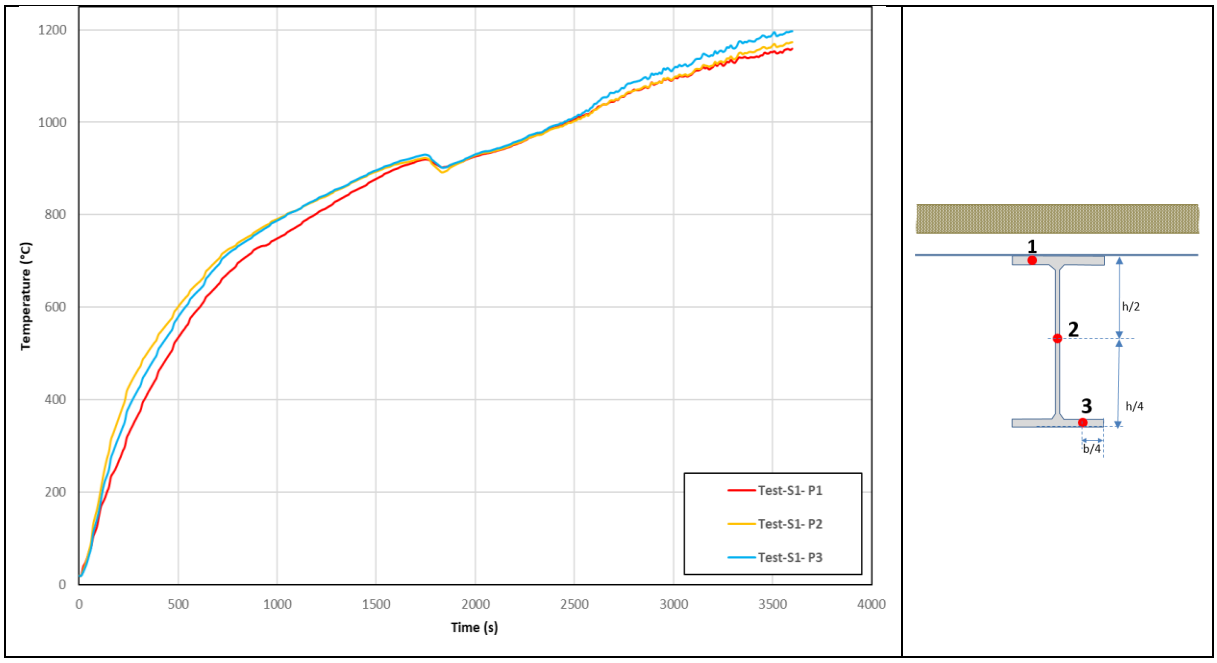

Figure 4.8: Temperature rises recorded on section S1 of purlin n°1

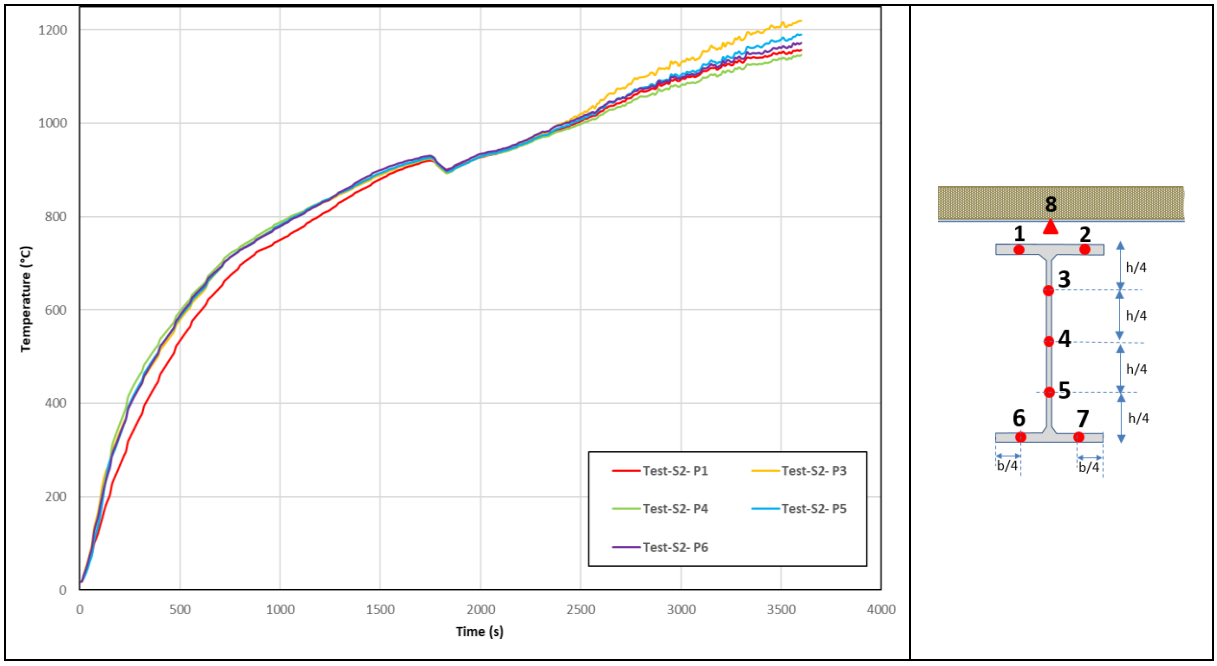

Figure 4.9: Temperature rises recorded on section S2 of purlin n°1

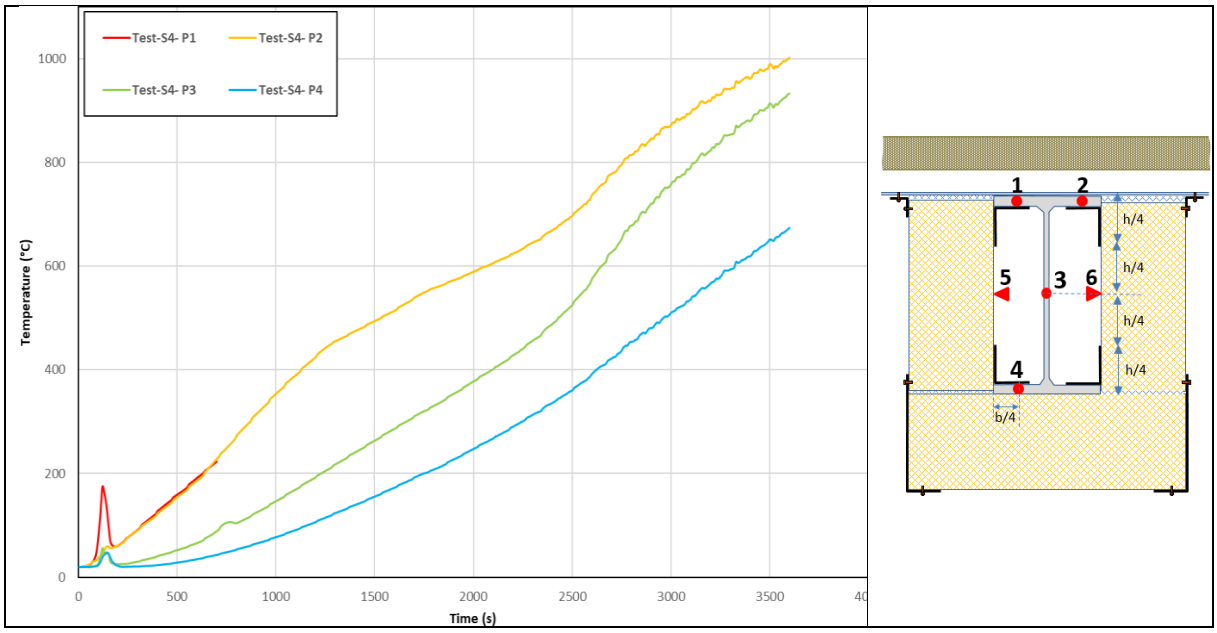

Figure 4.10: Temperature rises recorded on section S4 of purlin n°1

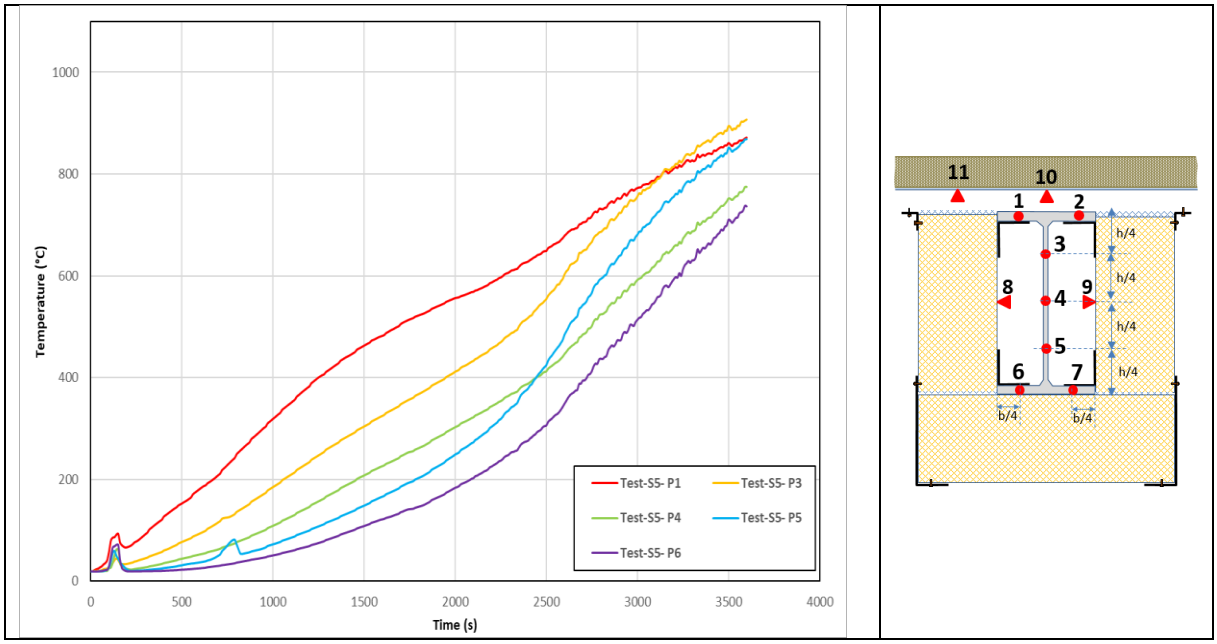

Figure 4.11: Temperature rises recorded on section S5 of purlin n°1

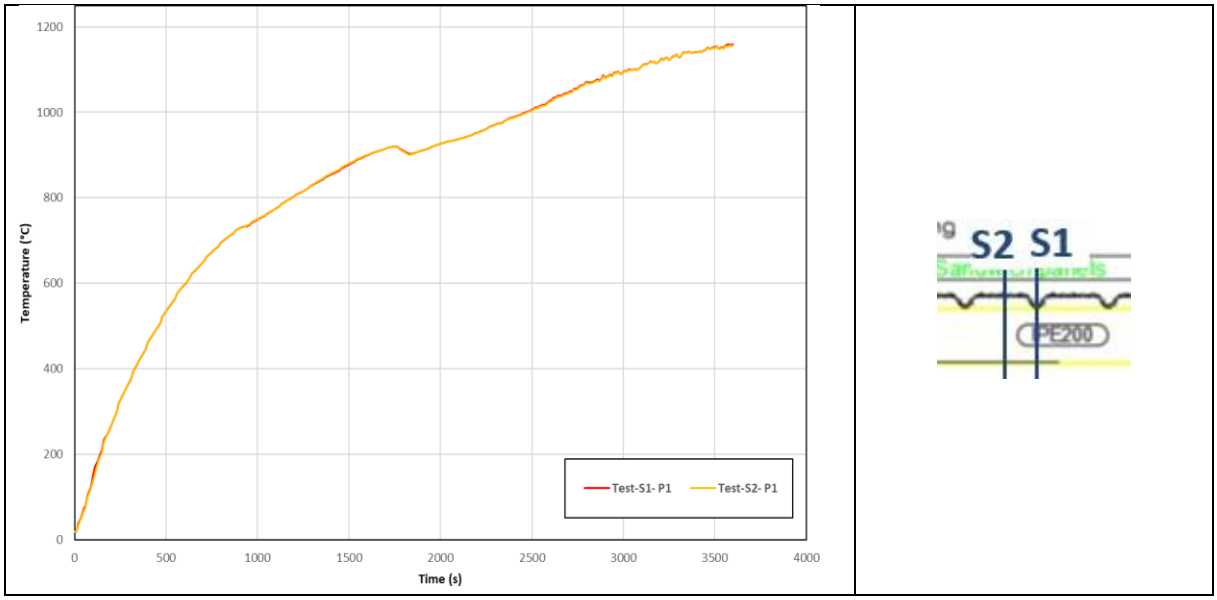

Figure 4.12: Temperature rises recorded on the top flange of sections S1 and S2 of purlin n°1

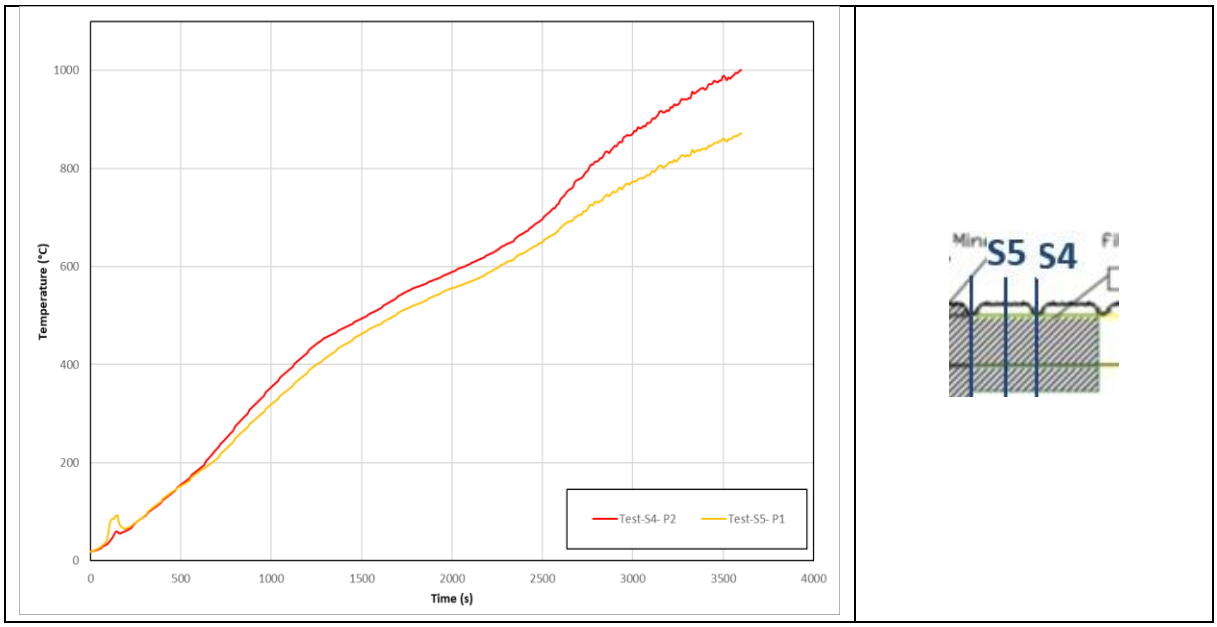

Figure 4.13: Temperature rises recorded on the top flange of sections S4 and S5 of purlin n°1

4.1.2.3 Heating of the purlin n°2

In this section, the following figures show the experimental temperatures recorded along purlin n°2, in cross-sections considered to be representative. The same observations can be made as for the first purlin. It should be noted that the parts of the purlin inside the sheathing (web and lower flange) heat up more slowly than for purlin No. 1, because the filling of the voids within the encasement system (between the purlin flanges) with mineral wool prevents any heat exchange by radiation inside the encasement.

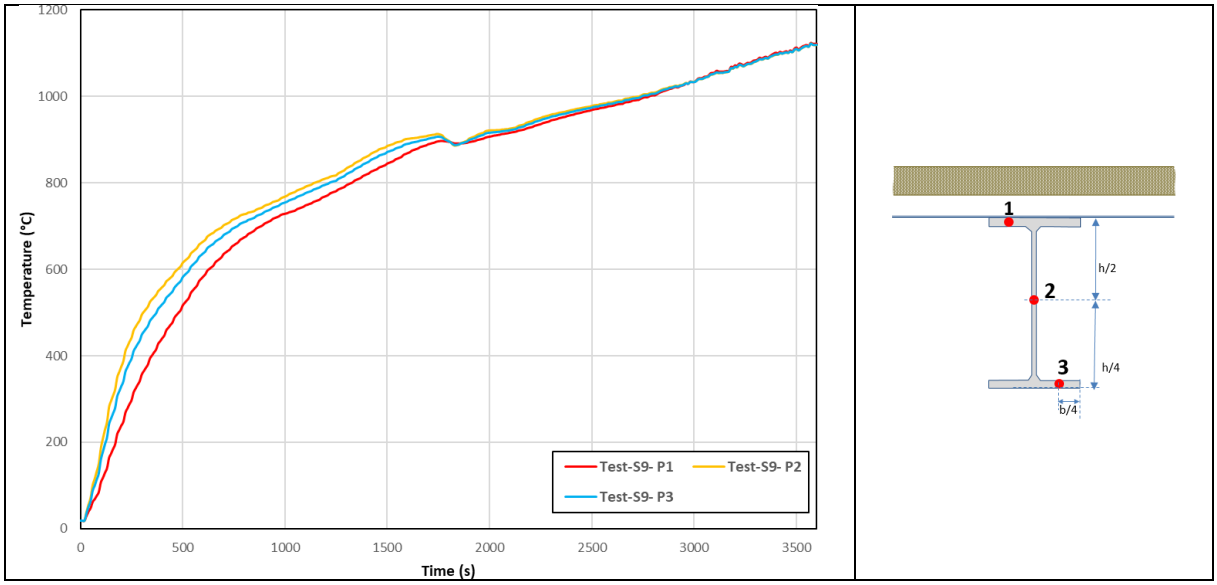

Figure 4.14: Temperature rises recorded on section S9 of the purlin n°2

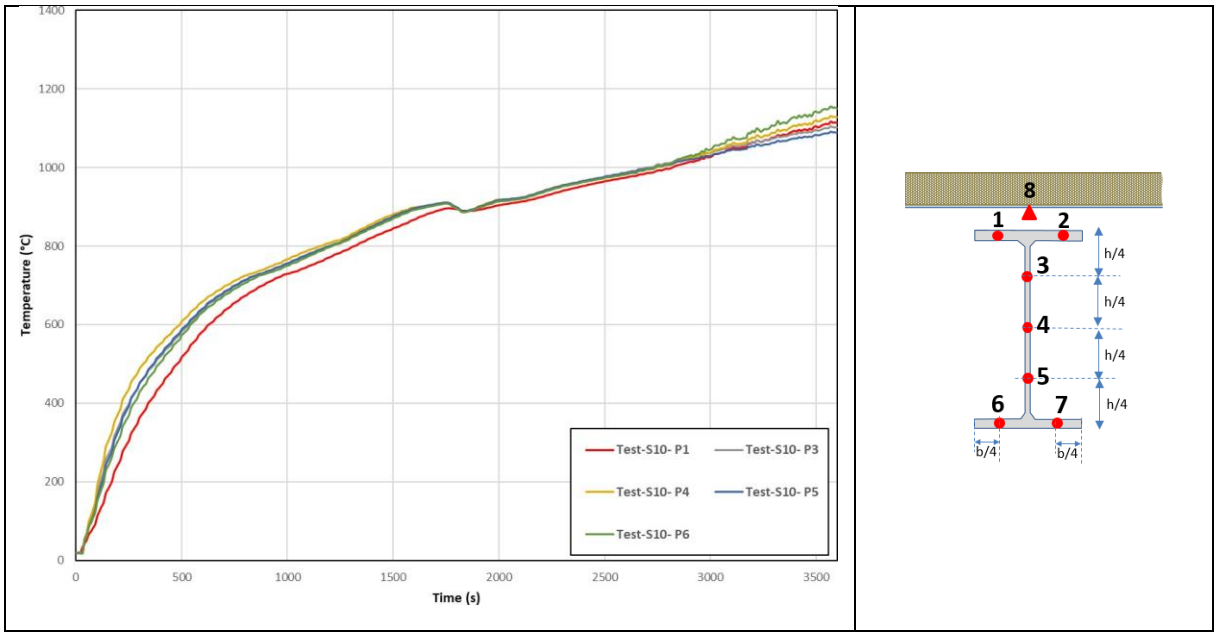

Figure 4.15: Temperature rises recorded on section S10 of the purlin n°2

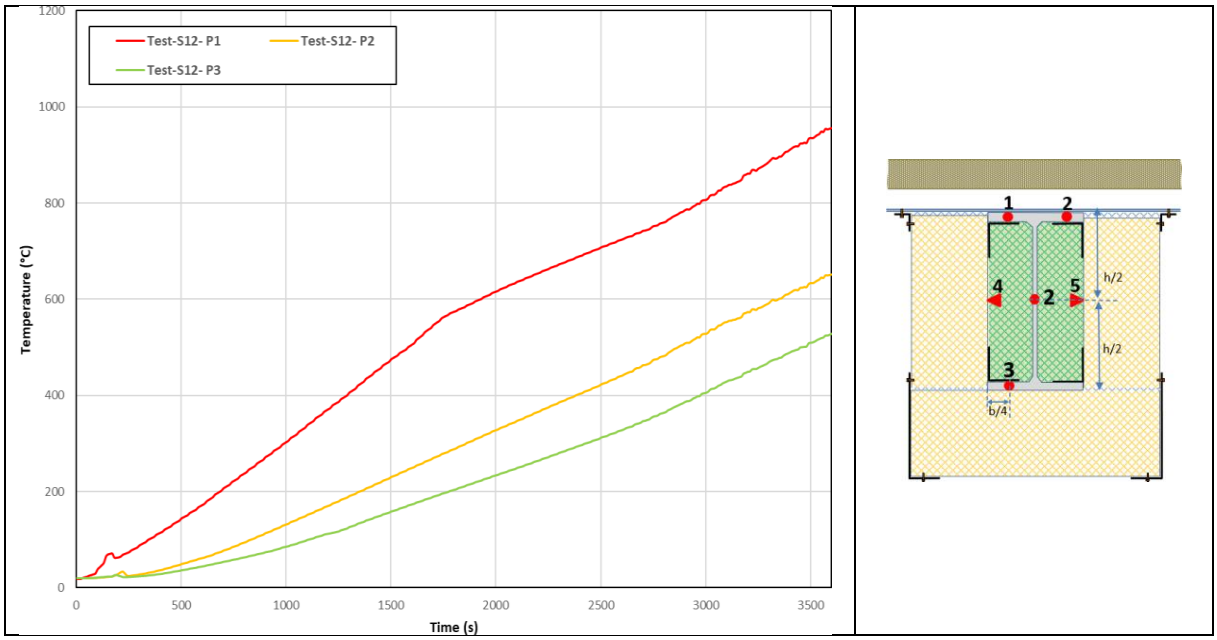

Figure 4.16: Temperature rises recorded on section 12 of the purlin n°2

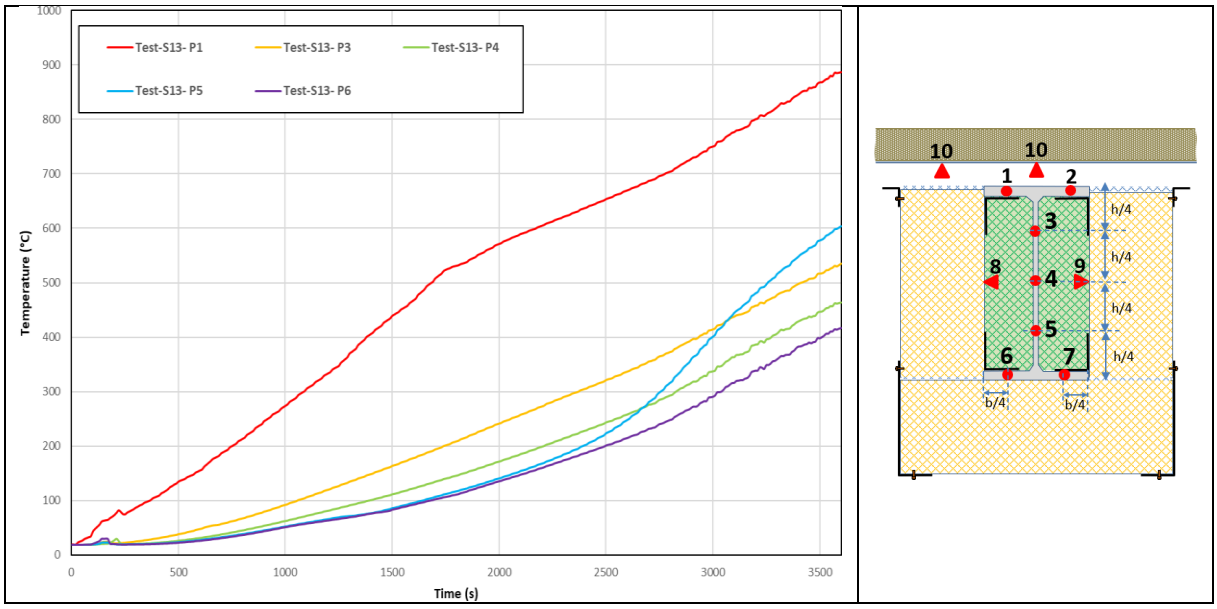

Figure 4.17: Temperature rises recorded on section S13 of the purlin n°2

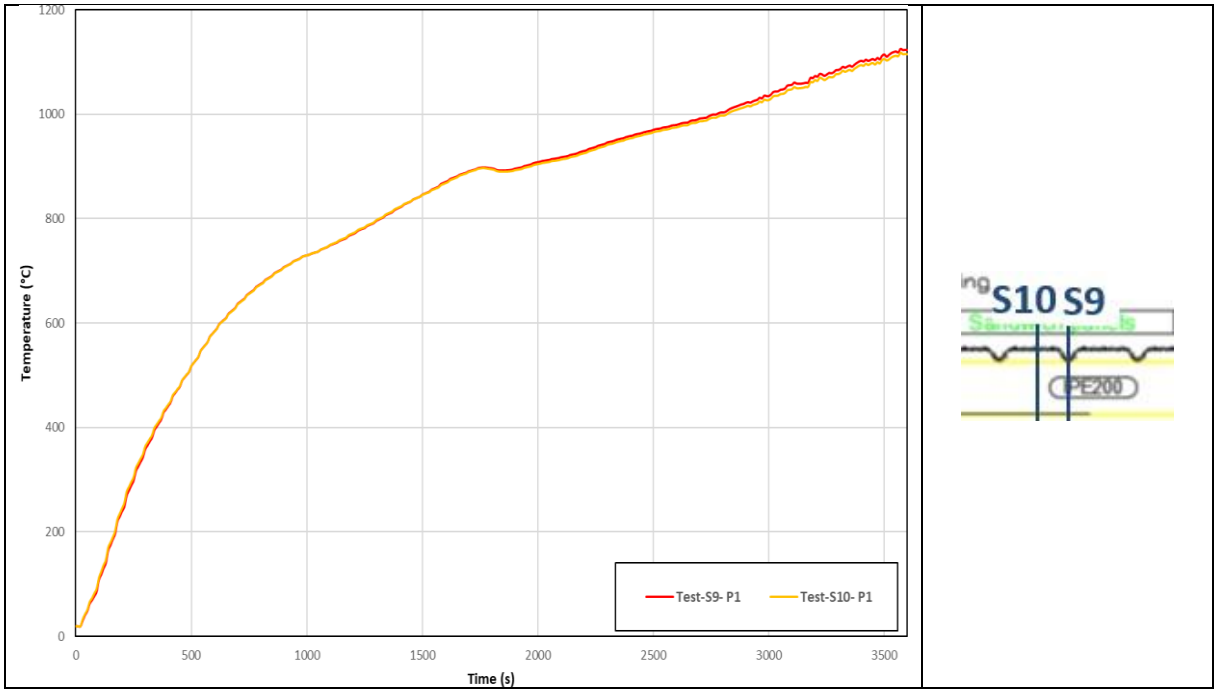

Figure 4.18: Temperature rises recorded on the top flange of sections S9 and S10 of purlin n°2

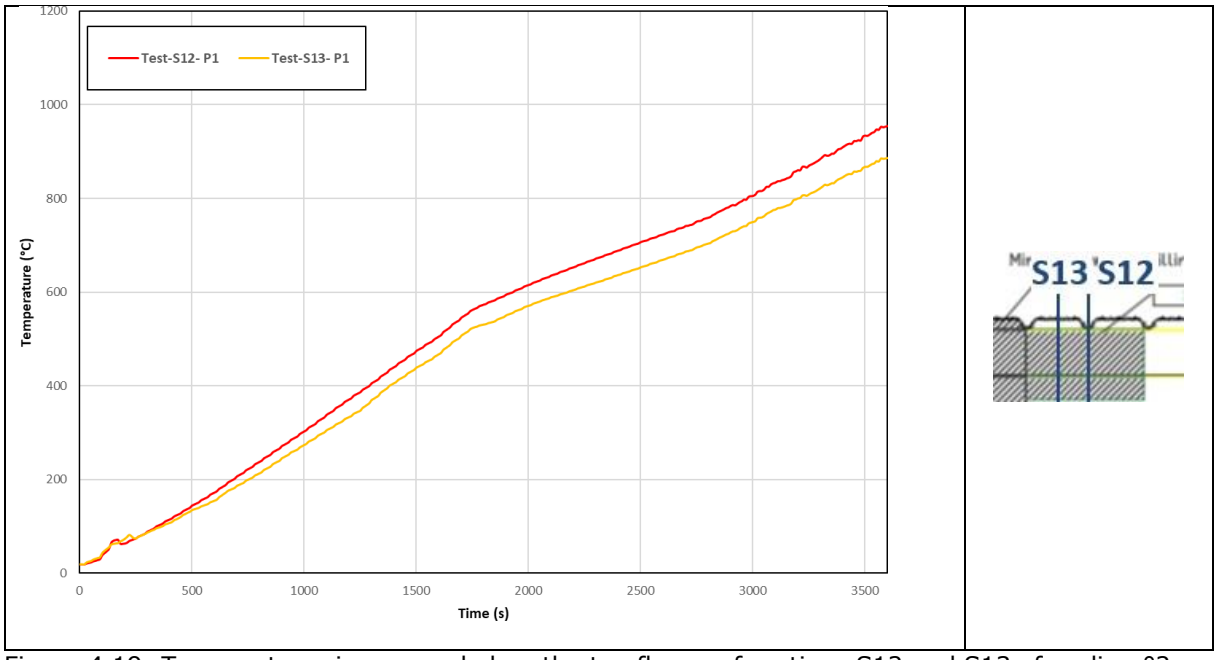

Figure 4.19: Temperature rises recorded on the top flange of sections S12 and S13 of purlin n°2

4.1.2.4 Mechanical behaviour

With regard to the structural behaviour of the purlins, it can be noted that no lateral torsional buckling was observed during the test, which leads to the conclusion that the purlins failed mainly by flexural bending (see Figure 4.20). The purlins were restrained in the lateral direction by the steel decks forming the roof, so that they could not move laterally. Some local buckling of purlin flanges in compression was observed at the end of encasement systems placed around the purlins. However, the deformation of the purlins at the wall level remained very limited and the purlin encasements made of sandwich panels were undamaged. In fact, observations after the test showed that the part of the purlins fire-protected by the panels still appeared to be straight, despite the large deflection of the heated parts of the purlins.

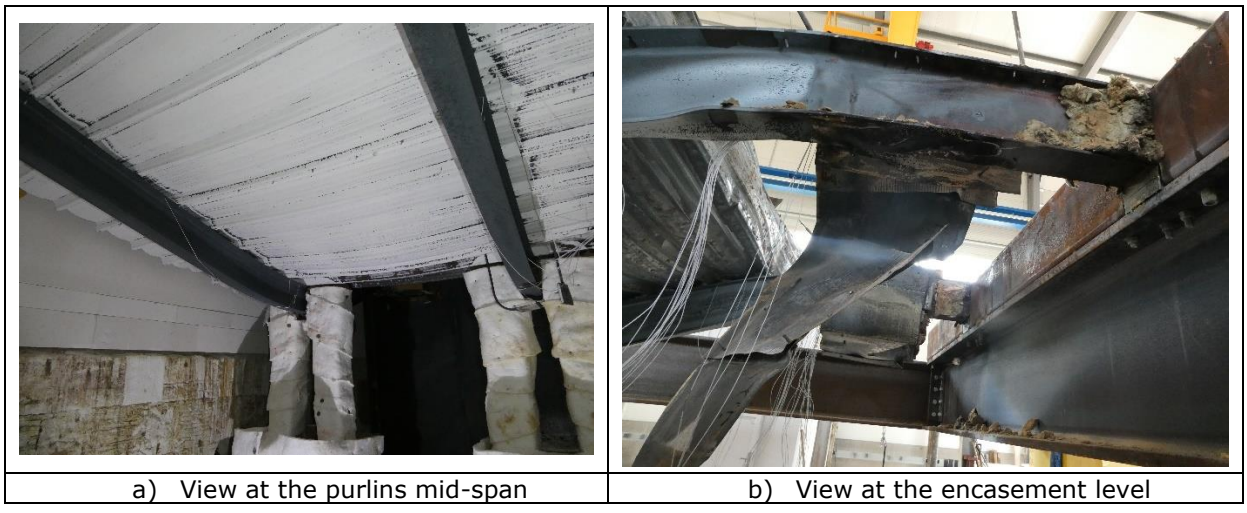

a) View at the purlins mid-span | b) View at the encasement level

Figure 4.20: View of purlins after the test

Figure 4.21 shows the vertical displacements of both purlins recorded during the test, with the mid-span displacement highlighted in Figure 3.26a ("V1" for purlin n°1 and "V4" for purlin n°2). Note that the positive displacements correspond to displacements of the purlins towards the inside of the furnace. During the first minutes of fire exposure, the displacement curve "V4" increases slightly faster than "V1". "V4" quickly overtakes "V1" and reaches a displacement of approximately 650 mm in just over 20 minutes, highlighting the failure of purlin n°2. Meanwhile, the displacement of purlin n°1 ("V1") reaches the same level a little later. After that, both curves continue to progressively increase and reach a displacement of about 700 mm. Looking at the vertical displacement at the end of the purlin sheathing (see Figure 4.21*b*) and at the wall-purlin junction (see Figure 4.21*c)*, it is easy to see that the vertical displacements remain very limited throughout the test. They are less than 20 mm.

It can also be seen that the purlin displacements are slightly different. These differences can mainly be explained by a slightly different heating of the two purlins (one purlin heats up slightly faster than the other) due to the uneven distribution of hot gases in the furnace.

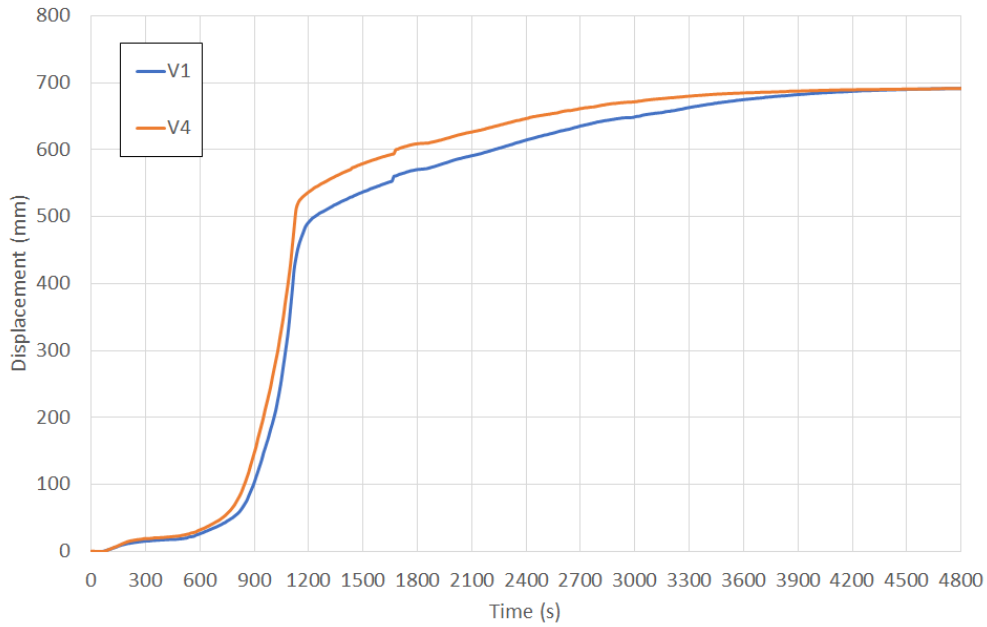

a) At mid-span of purlins

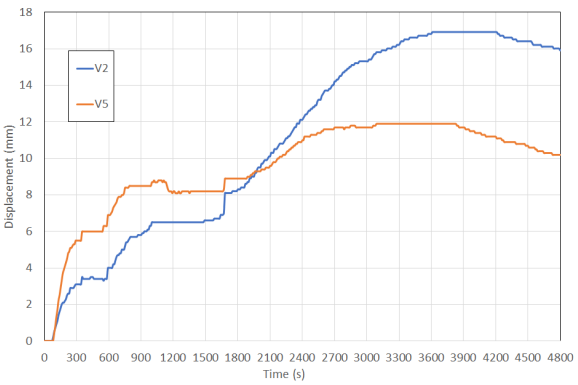

b) At the end of purlins encasement

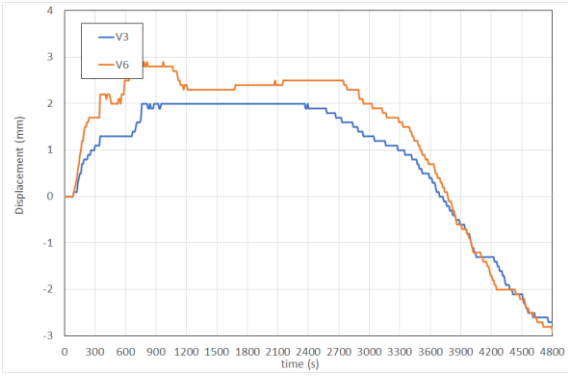

c) at the wall to purlins junction

Figure 4.21: Time-displacement curves recorded along the purlins during the test

4.2 Numerical analyses

A sequentially coupled three-dimensional thermal-mechanical analysis procedure has been adopted to simulate the fire behaviour of the test specimen, consisting of first performing a heat transfer analysis to obtain the temperature fields over the whole test specimen, and then performing a mechanical analysis using the previously calculated temperature fields to assess the fire behaviour of steel purlins. A static-dynamic procedure is used to simulate the progressive failure mechanism of the purlins. Moreover, the same meshing is used for both thermal and mechanical models, but appropriate finite element formulations are used for each type of analysis.

4.2.1 Thermal analyses

In order to analyse the heating of steel purlins in more detail and to consider the thermal loads acting in the cavities formed between the trapezoidal steel sheeting and the upper flange of the steel purlins, a specific three-dimensional finite element model has been developed using the ANSYS code. In this model, the boundary conditions are those recommended by EN 1991-1-2 [4] and the material properties are those recommended by EN 1993-1-2 [6].

4.2.1.1 Modelling considerations

The main assumptions are the following:

- The test specimen (including steel purlins, trapezoidal steel sheeting, sandwich panels, and insulation material) for both purlins is meshed with eight node brick elements (SOLID70) and four node surface elements (SURF152) are used to apply both convective and radiative exchanges to the outer surfaces.
- The steel faces of the sandwich panels, which are thought to have an insignificant effect on the thermal behaviour of the panels, have been omitted.
- Heat exchange between the test specimen and its surroundings is by convection and radiation. The radiative and convective exchange coefficients for the parts of the steel section and trapezoidal steel sheeting directly exposed to the fire are in accordance with EN 1991-1-2. The emissivity of the fire is set to 1, the surface emissivity of all materials (steel, mineral wool) is 0.7 and the convective heat transfer coefficient is 25 W/m²-K. For the parts not exposed to fire, the surface emissivity of the materials is also 0.7 and the convective heat transfer coefficient is 4 W/m²-K according to EN 1991-1-2. The ambient temperature is assumed to be 20°C.
- Perfect thermal continuity is assumed between all contact surfaces (wall, purlin, encasement, trapezoidal steel sheeting insulation, etc.).
- The shadow effect for radiation at the cavities formed between the steel purlin and the trapezoidal steel sheeting was explicitly considered. To do this, a special feature of the Ansys code was used in the model. Specifically, all the surfaces exposed to fire, including the surfaces inside the cavities, were grouped together, and the view factor was calculated for all parts of these surfaces. Then, the heat exchange by radiation between the parts with different temperatures within this group is considered in the temperature field in the model.
- On the fire exposed side, each purlin is fire protected by an encasement system extending 50 cm from the fire wall. The cavities formed between the ribs of the trapezoidal steel sheeting and the top flange of the steel purlins are left unfilled, while the cavities within the encasement system (between the purlin flanges) are either fully or partially filled (along 100 mm from the end of the encasement) with mineral wool.
- Heat exchanges by radiation between the surfaces in cavities inside the panel encasement (between the purlin flanges) are considered. The surface emissivity of all materials is 0.7.
- The thermo-physical properties (thermal conductivity, specific heat, density) of the steel are those given in the EN 1993-1-2.
- The thermo-physical properties of the sandwich panels (mineral wool) were the same as those considered in the thermal model developed to investigate the fire behaviour of steel portal frames associated with fusible links (see §3.2.1).
- The thermal properties of the rock wool used to fill the encasement system are as follows:
    - Density = 120 kg/m³,
    - Specific heat= 1000 J/kg·K,
    - Thermal conductivity:

Temperature (°C)	0	100	250	350	500	800	900	1000	1300
Thermal conductivity (W/mK)	0.2	0.2	0.2	0.2	0.35	0.8	4	10	100

- Since the temperature of the hot gases in the furnace differed slightly to the standard fire curve, in order to calculate more accurately the temperature distribution in the modelled members, in particular near the encasement system placed around the purlin, an ambient temperature of 20°C is applied for the heat exchanges on the fire unexposed surfaces of the test specimen, while the fire temperature curves shown in Figure 4.23 are applied for the heat exchanges on the fire exposed surfaces. These curves correspond to the average of the hot gas temperatures recorded by the plate thermometers PT1 and PT4 for the first purlin and the average temperatures of PT7 and PT10 for the second purlin.

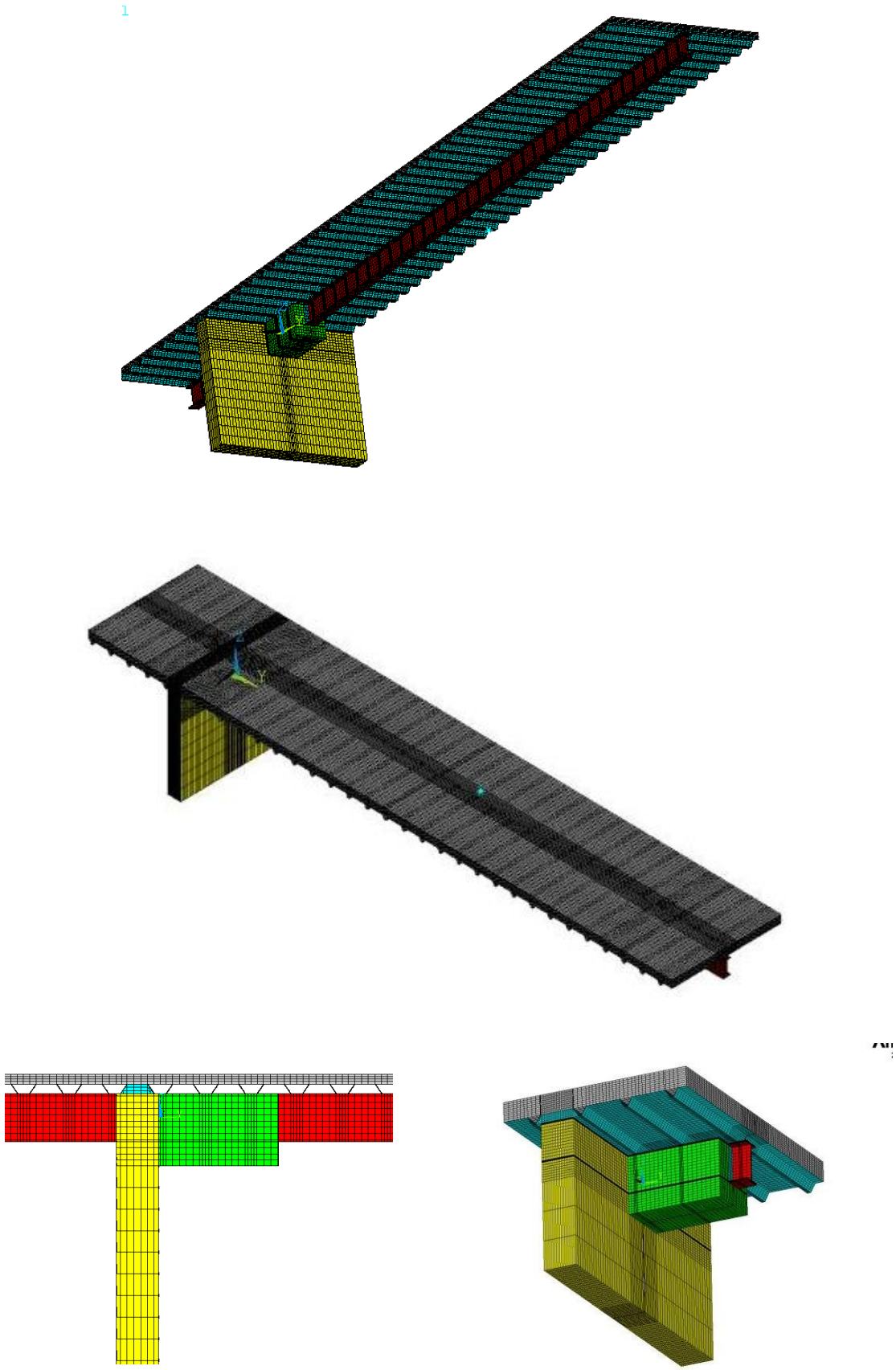

Figure 4.22: Thermal model developed for the studied test specimen

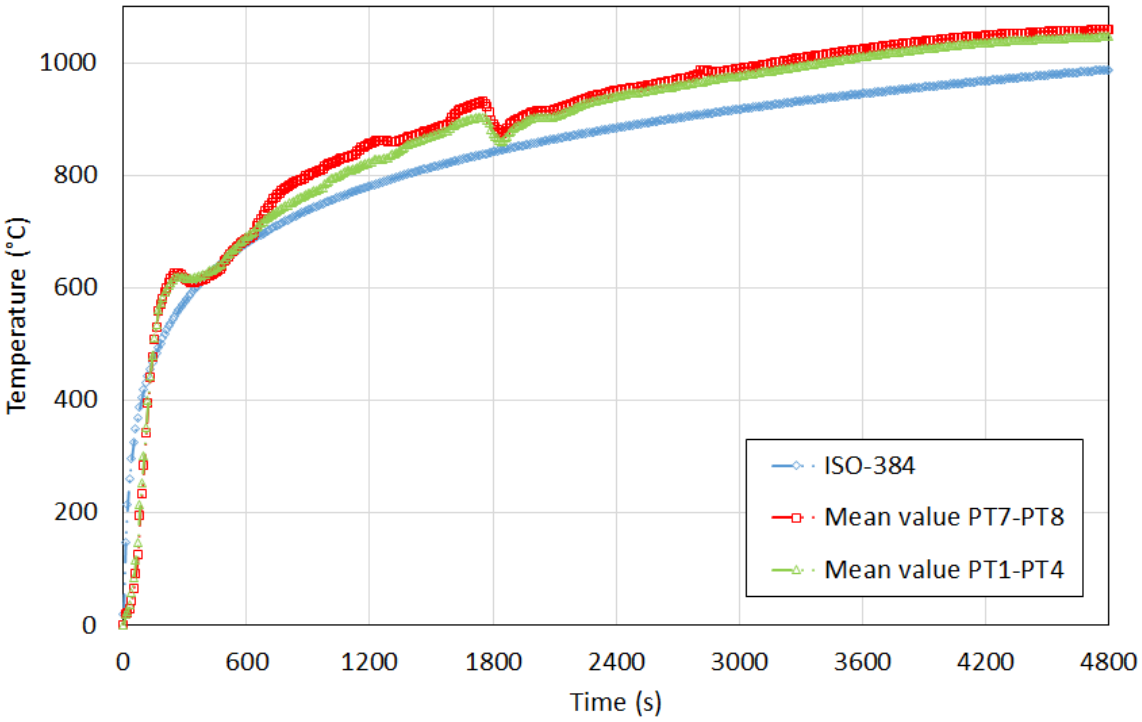

Figure 4.23: Temperature-times curves of hot gas considered in numerical modelling

4.2.1.2 Analysis results

4.2.1.2.1 Purlin n°1

This section is concerned with a comparison of the predicted temperature rises in Purlin n°1 with those measured during the test at several temperature measurement positions that are regarded as representative. The results of the comparisons are displayed in the following figures.

The following sections are considered: S1 (at the level where the trapezoidal steel sheeting is in contact with the purlin) and S2 (at the level of a cavity formed between the purlin top flange and the trapezoidal steel sheeting) located immediately after the purlin encasement; S4 (at the level where the trapezoidal steel sheeting is in contact with the purlin) and S5 (at the level of a cavity formed between the purlin top flange and the trapezoidal steel sheeting) located at the centre of the purlin encasement; and S7 (at the level where the trapezoidal steel sheeting is in contact with the purlin) and S8 (at the level of a cavity formed between the purlin top flange and the trapezoidal steel sheeting) located at the centre of the purlin span under consideration. Detailed results for other cross sections along the purlin are given in Appendix A.

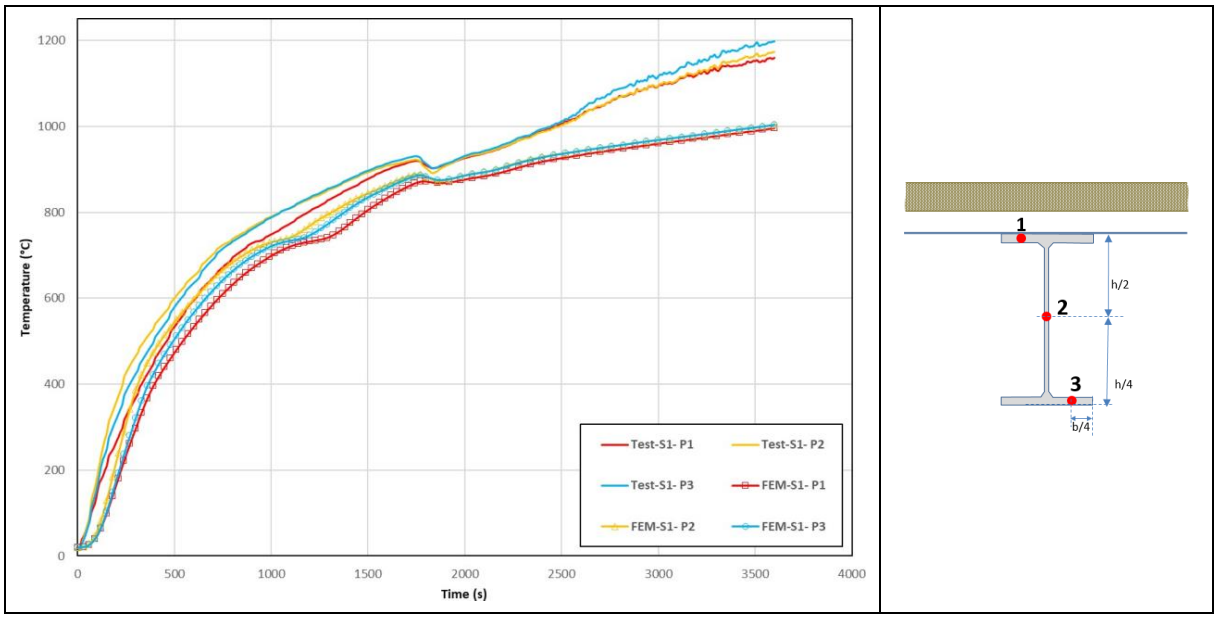

Figure 4.24: Comparison between numerical and experimental temperatures for the cross-section S1 along the purlin n°1

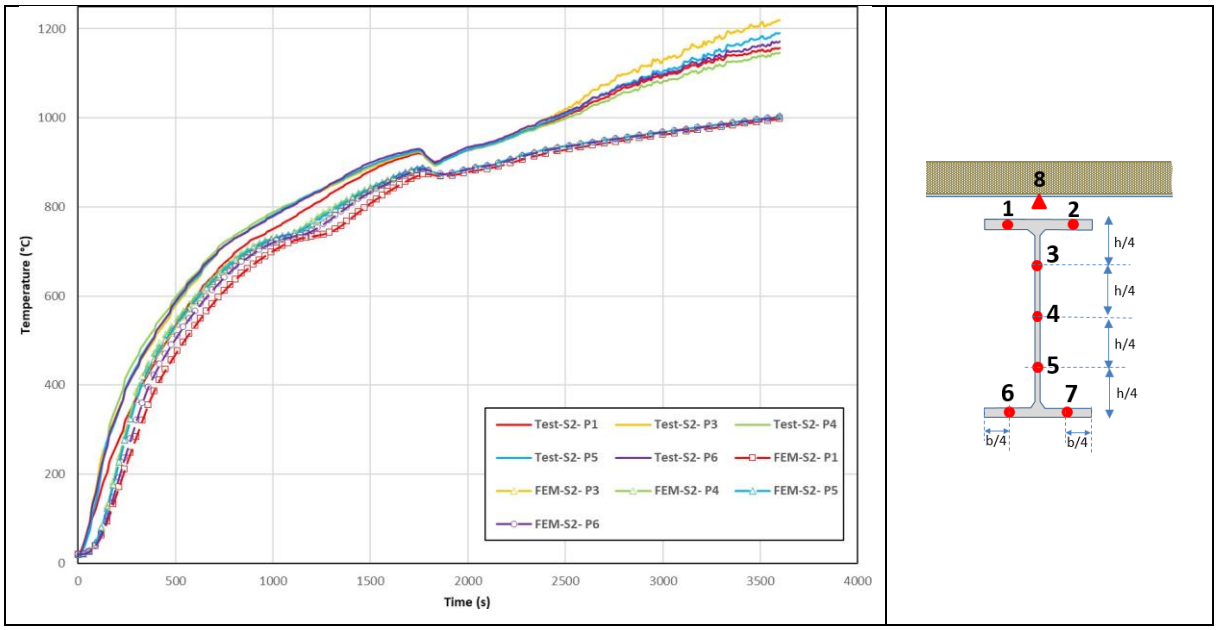

Figure 4.25: Comparison between numerical and experimental temperatures for the cross-section S2 along the purlin n°1

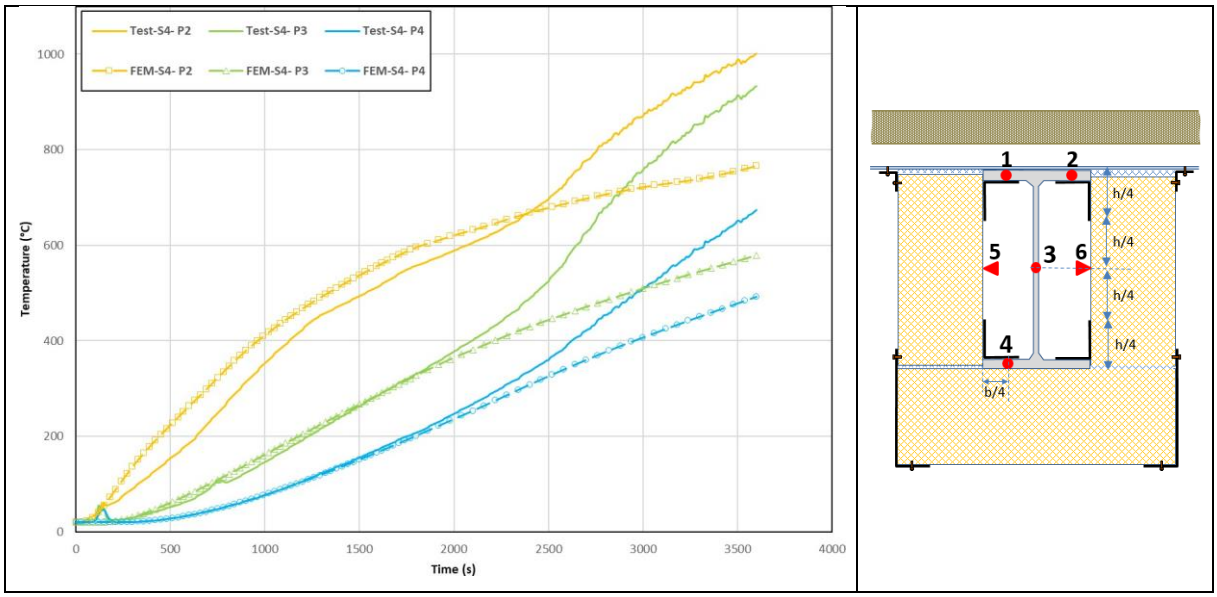

Figure 4.26: Comparison between numerical and experimental temperatures for the cross-section S4 along the purlin n°1

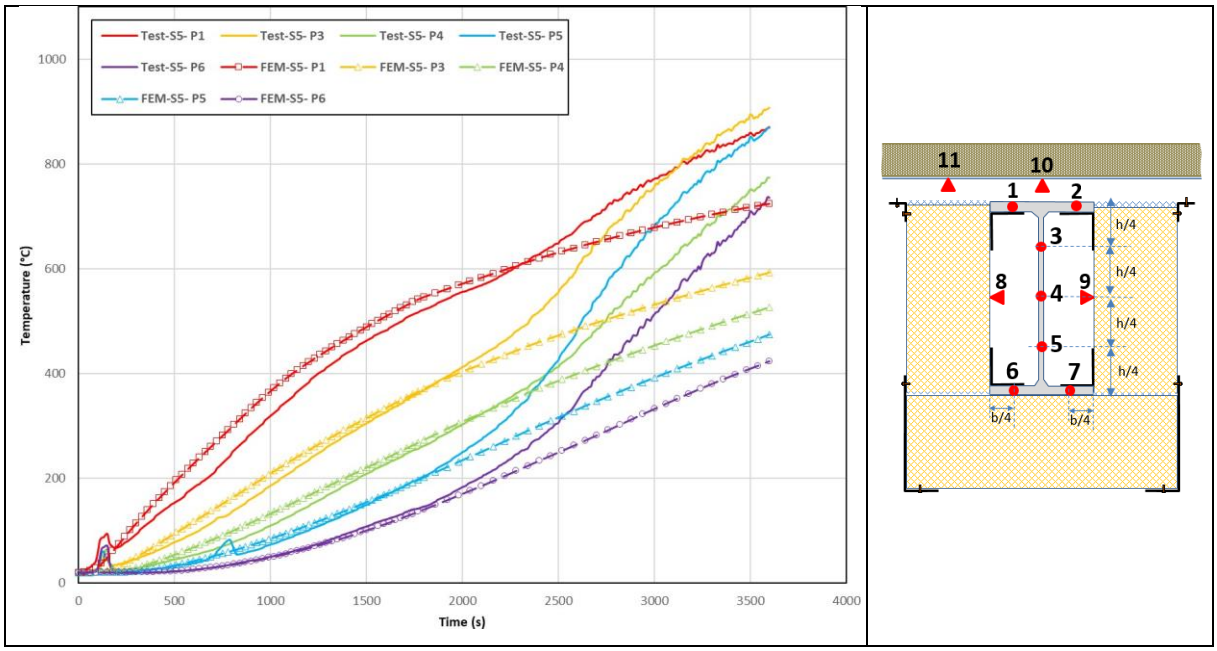

Figure 4.27: Comparison between numerical and experimental temperatures for the cross-section S5 along the purlin n°1

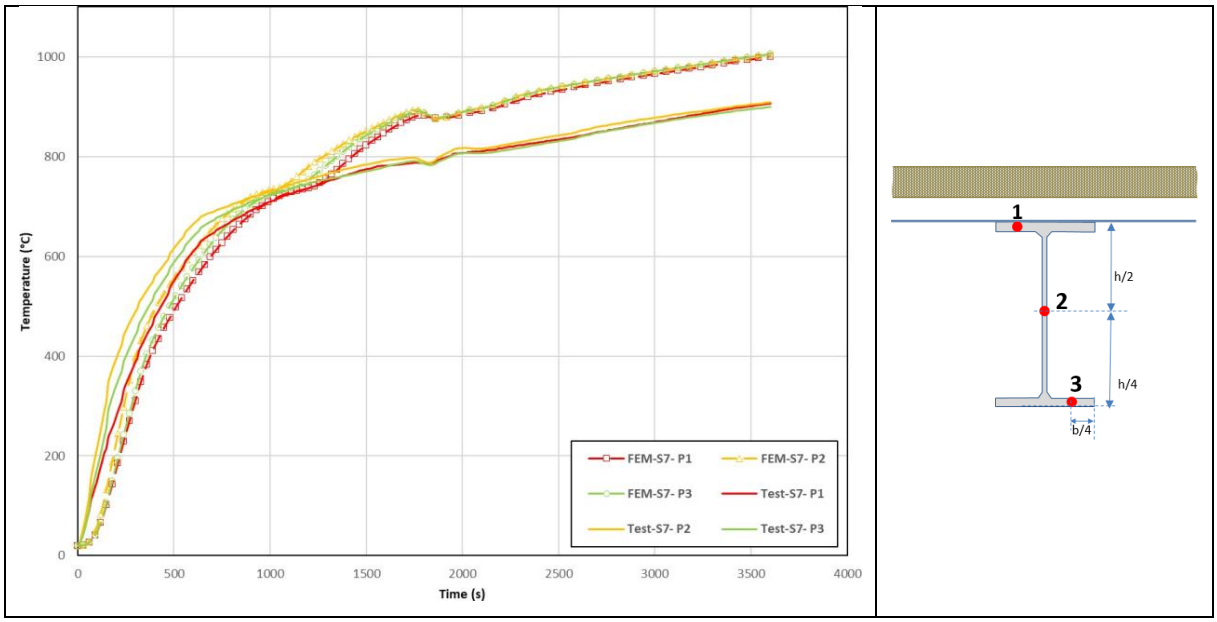

Figure 4.28: Comparison between numerical and experimental temperatures for the cross-section S7 along the purlin n°1

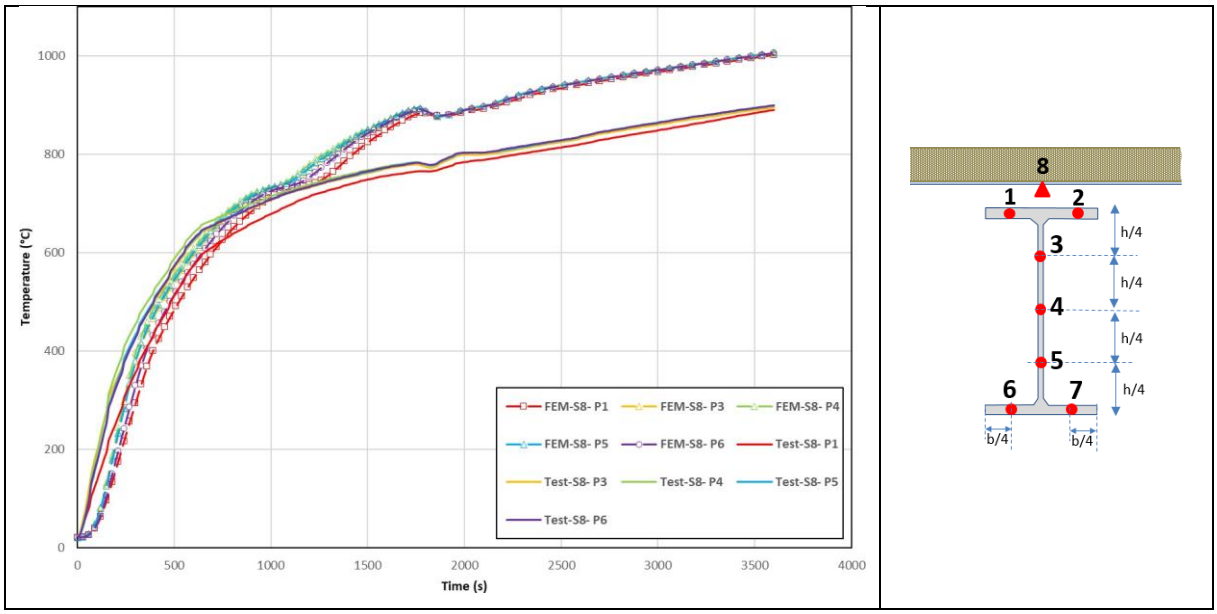

Figure 4.29: Comparison between numerical and experimental temperatures for the cross-section S8 along the purlin n°1

After a careful analysis of these figures, it can be noted that:

- Overall, the predicted curves have the same general shape as the experimental ones, at least for the first stage of the test (up to 1800 seconds of fire exposure), although they are slightly shifted in time. For the purlin parts directly exposed to fire, the temperature increase in the purlin web is higher than that in the flanges, and the temperature increase in the upper flange is the lowest. However, the temperature differences in the steel purlin in the experimental test are more pronounced than those predicted by the numerical model.
- For cross-section S1 (see Figure 4.24*)*, where the trapezoidal steel sheeting is in contact with the purlin, the predicted temperature curve for the top flange (P1) is in satisfactory agreement with the experimental curves during the first 1800 seconds. The temperature rise is sightly underestimated by the numerical model, with differences not exceeding 50°C. After 1800 seconds, the temperature differences become increasingly significant, up to 180°C. It should be noted that the temperatures measured for the purlin are higher than those measured for the hot gases inside the furnace. The reliability of such measurements after 1800 seconds can therefore be questioned. A similar trend is observed for the web (P2) and the lower flange (P3) of the steel purlin.

- For cross-section S2 (see Figure 4.25*)*, located at the level of a cavity formed between the top flange of the purlin and the trapezoidal steel sheeting, the comparison between the numerical model and the experimental test shows discrepancies similar to those observed for section S1, but with some variations depending on the parts of the purlin considered.
- For cross-section S4 *(*see Figure 4.26*)*, located along the encasement system and at the level where the trapezoidal steel sheeting is in contact with the purlin, the comparison between the numerical model and the test shows varying discrepancies depending on the purlin parts and the fire exposure time considered. For the top flange (P2), For the top flange (P2), the temperatures predicted by the FE model are satisfactory up to 2500 seconds of fire exposure, although the numerical model tends to slightly overestimate the temperature rise. However, after 2500 seconds, there is a more marked divergence, with differences reaching around 200°C at the end of the period analysed. For the web (P3) and the lower flange (P4), the test and numerical temperatures are very close up to about 2000 seconds. Beyond this time, an increasing divergence is observed, indicating an underestimation of the heating predicted by the numerical model, with differences reaching around 200°C to 400°C towards the end of the test. In summary, up to 2000 seconds, the heating of the purlin is satisfactorily predicted by the model: the top flange temperature (P2) shows the most significant discrepancies between the numerical model and the experimental results, followed by the web temperature (P3) and the bottom flange temperature (P4). These differences could be explained by the large flexural deformations that the purlins underwent during the test, after 1500 seconds, which could lead to both integrity and insulation losses of the encasement system with the emergence of openings at the level of the panel junctions, although no significant damage to the encasement system was observed during the test. Such potential damage is difficult to model accurately and is therefore not considered in the FE model. It is also possible that the thermal properties of both the sandwich panels and the mineral wool used to fill the end of the encasement system may deteriorate more rapidly at elevated temperature than assumed in the numerical model.
- For cross-section S5 *(*see Figure 4.27*)*, located along the encasement system at the level of a cavity formed between the purlin top flange and the trapezoidal steel sheeting, the temperatures predicted by the numerical model closely follow the experimental results up to 2000 seconds of fire exposure. After this period, the numerical model underestimates the temperature increases, with differences of around 100°C to 300°C at the end of the numerical simulation (3600 seconds).
- For cross-sections S7 and S8 *(*see Figure 4.28 and Figure 4.29 *)*, located along the purlin part directly exposed to the fire (at the level where the trapezoidal steel sheeting is in contact with the purlin and at the level of a cavity formed between the purlin top flange and the trapezoidal steel sheeting), the comparison between the numerical model and the test shows differences similar to those observed for cross-sections S1 and S2. Overall, the temperatures predicted by the numerical model closely follow the experimental curves up to 1200 s, with a slight underestimation. After this time there are larger differences, with a slight overestimation of the temperatures predicted by the numerical model compared to the temperatures recorded in the test. These differences are mainly due to the hot gas temperatures applied along the purlin in the numerical model, which represent an average of the hot gas temperatures measured only at the level of the casing system (plate thermometers PT1 and PT4). In fact, the hot gas temperatures measured during the test closest to sections S7 and S8 are lower than the average temperature considered.

For information purpose, Figure 4.30 and Figure 4.31 show the predicted temperature fields in the meshed members at 900 and 1800 seconds of fire exposure.

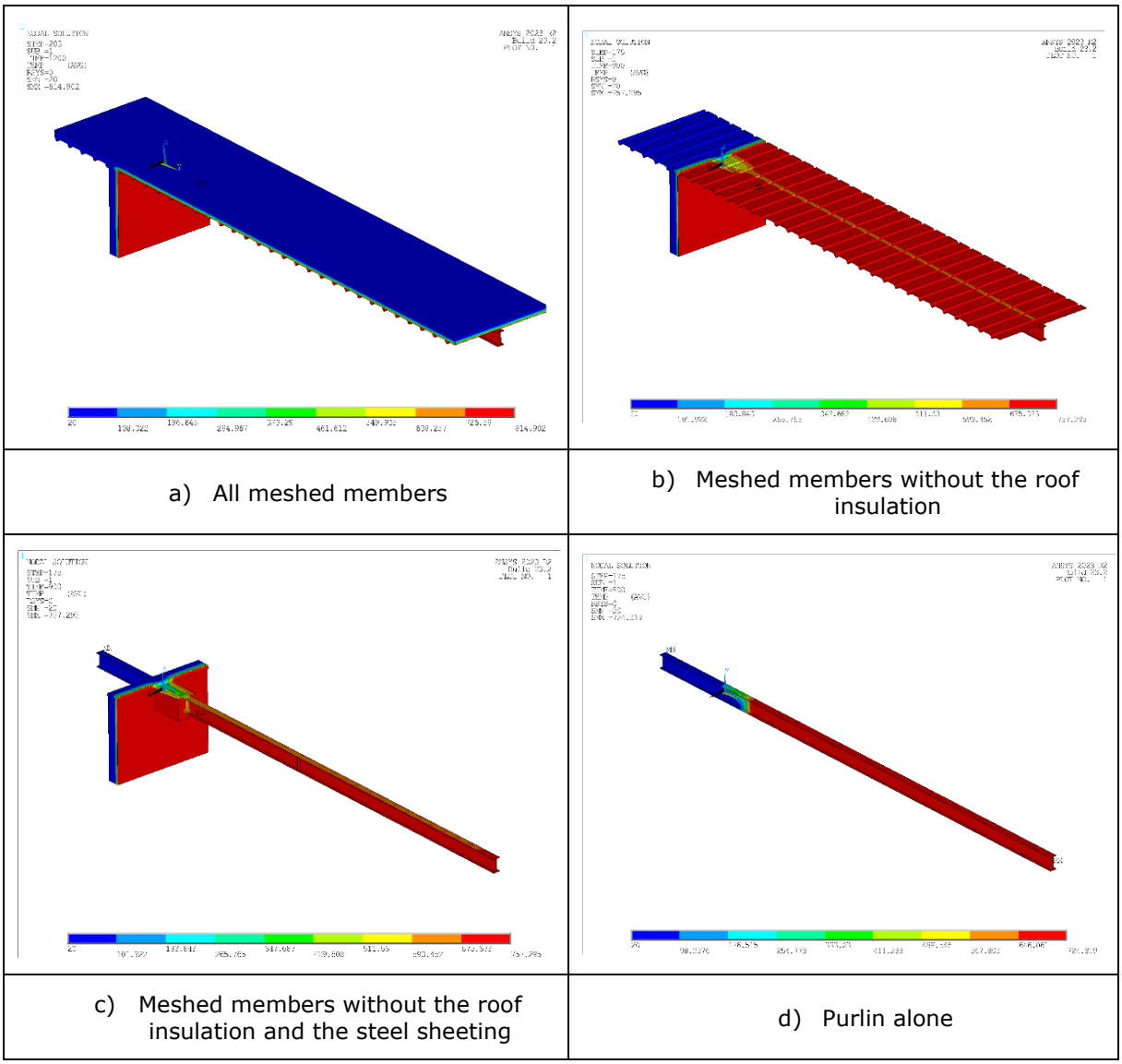

a) All meshed members

b) Meshed members without the roof insulation

c) Meshed members without the roof insulation and the steel sheeting

d) Purlin alone

Figure 4.30: Temperature fields calculated on meshed members of the test specimen at 900s of fire exposure

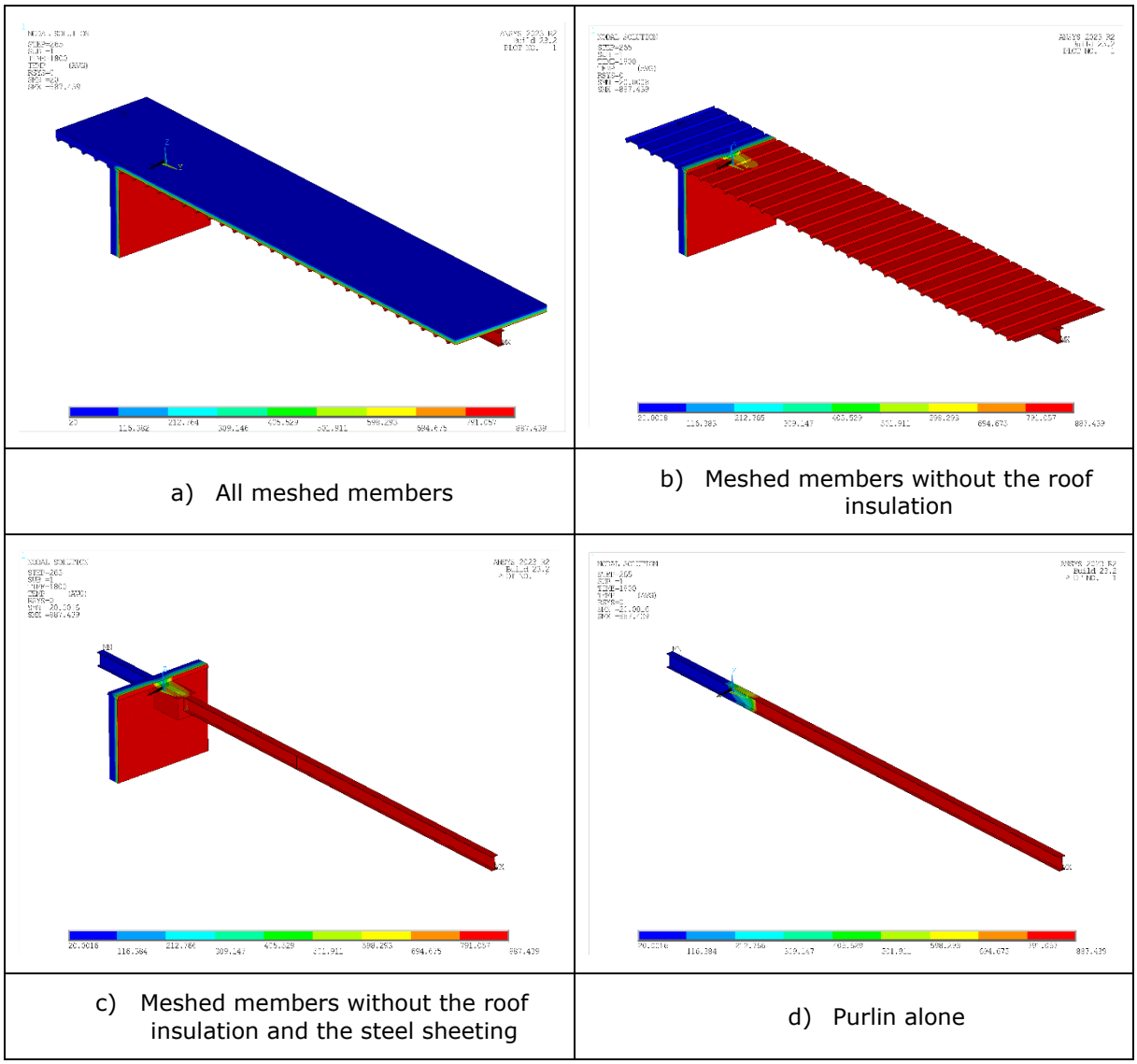

a) All meshed members

b) Meshed members without the roof insulation

c) Meshed members without the roof insulation and the steel sheeting

d) Purlin alone

Figure 4.31: Temperature fields calculated on meshed members of the test specimen at 1800s of fire exposure

4.2.1.2.2 Purlin n°2

This section compares the predicted temperature rises in purlin n°2 with those measured during the test at various temperature measurement positions considered to be representative. The results of these comparisons are shown in the following figures.

The following sections are considered: S9 (at the level where the trapezoidal steel sheeting is in contact with the purlin) and S10 (at the level of a cavity formed between the purlin top flange and the trapezoidal steel sheeting) located immediately after the purlin encasement; S12 (at the level where the trapezoidal steel sheeting is in contact with the purlin) and S13 (at the level of a cavity formed between the purlin top flange and the trapezoidal steel sheeting) located at the centre of the purlin encasement; and S15 (at the level where the trapezoidal steel sheeting is in contact with the purlin) and S16 (at the level of a cavity formed between the purlin top flange and the trapezoidal steel sheeting) located at the centre of the purlin span under consideration. Detailed results for other cross sections along the purlin are given in Appendix A.

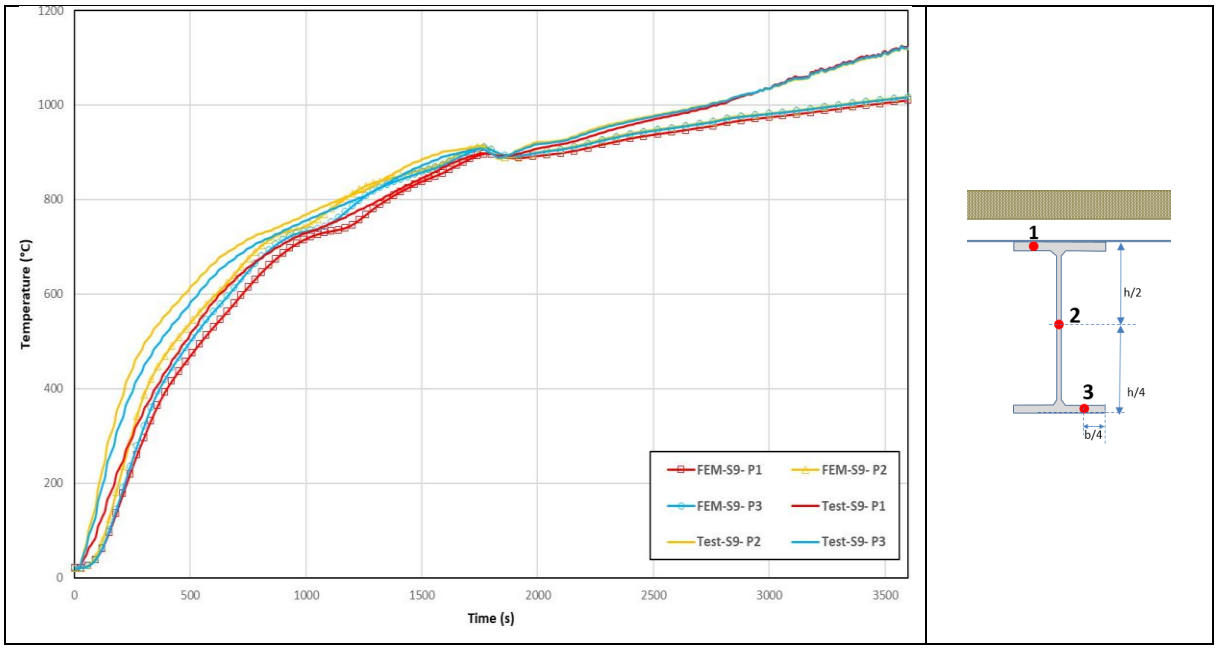

Figure 4.32: Comparison of temperatures between test and numerical calculation for section S9 of the purlin n°2

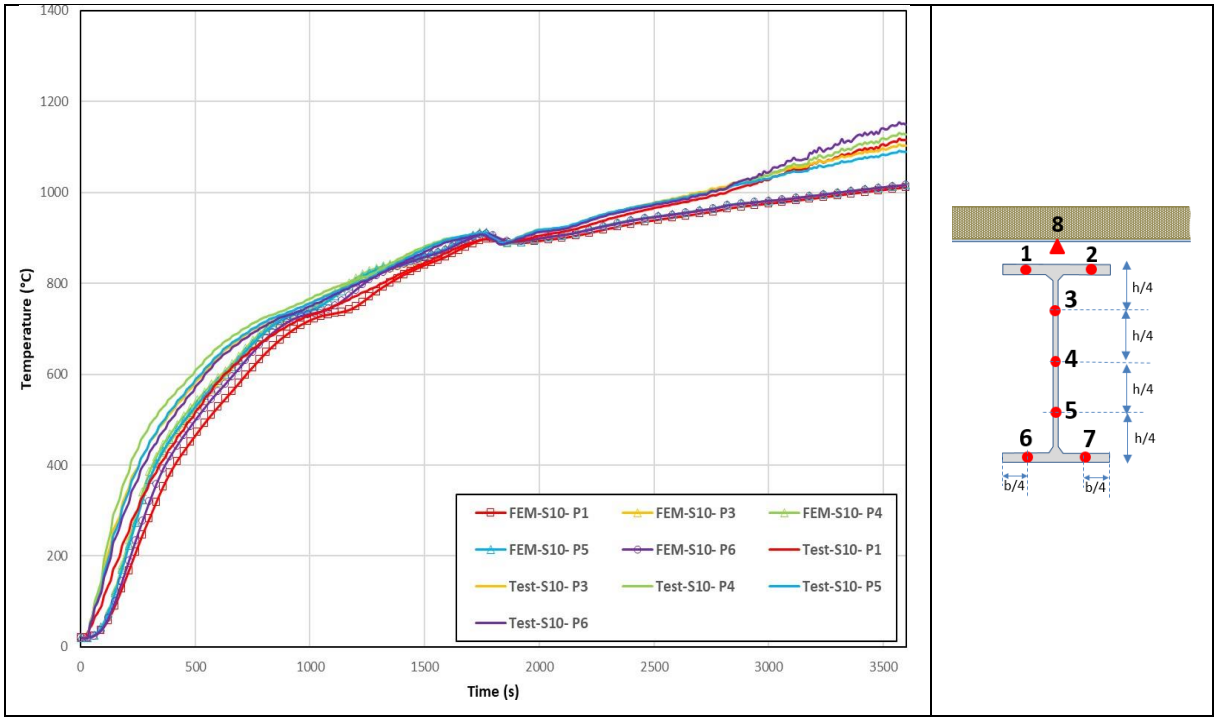

Figure 4.33: Comparison between numerical and experimental temperatures for the cross-section S10 along the purlin n°2

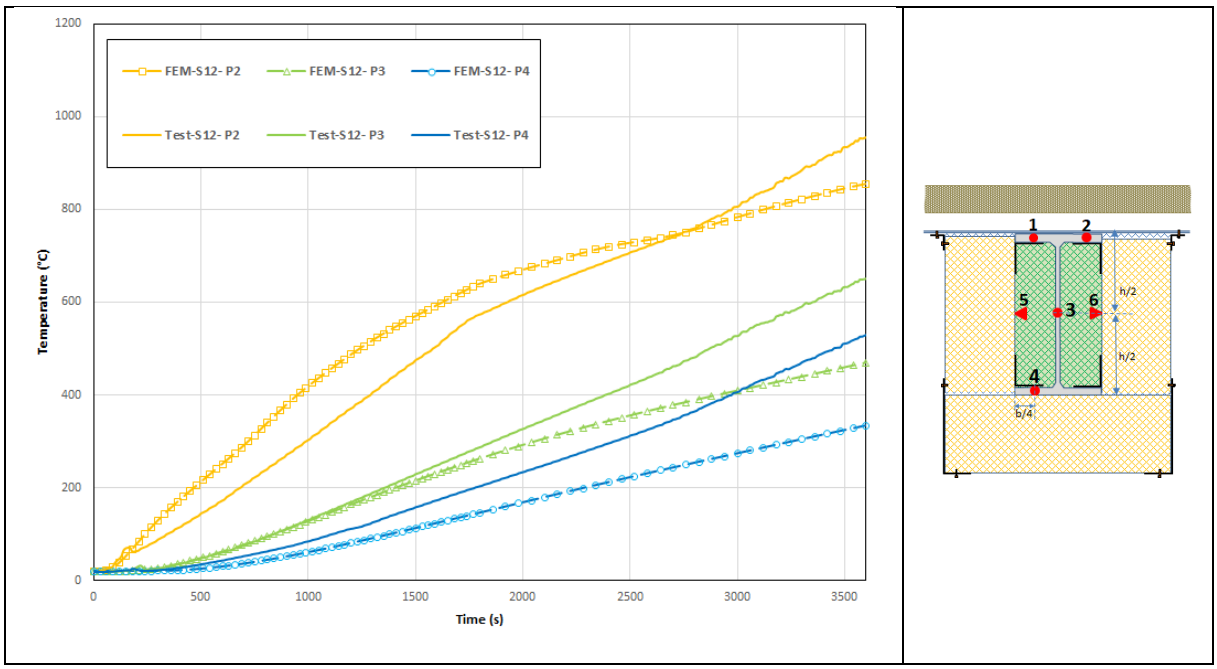

Figure 4.34: Comparison between numerical and experimental temperatures for the cross-section S12 along the purlin n°2

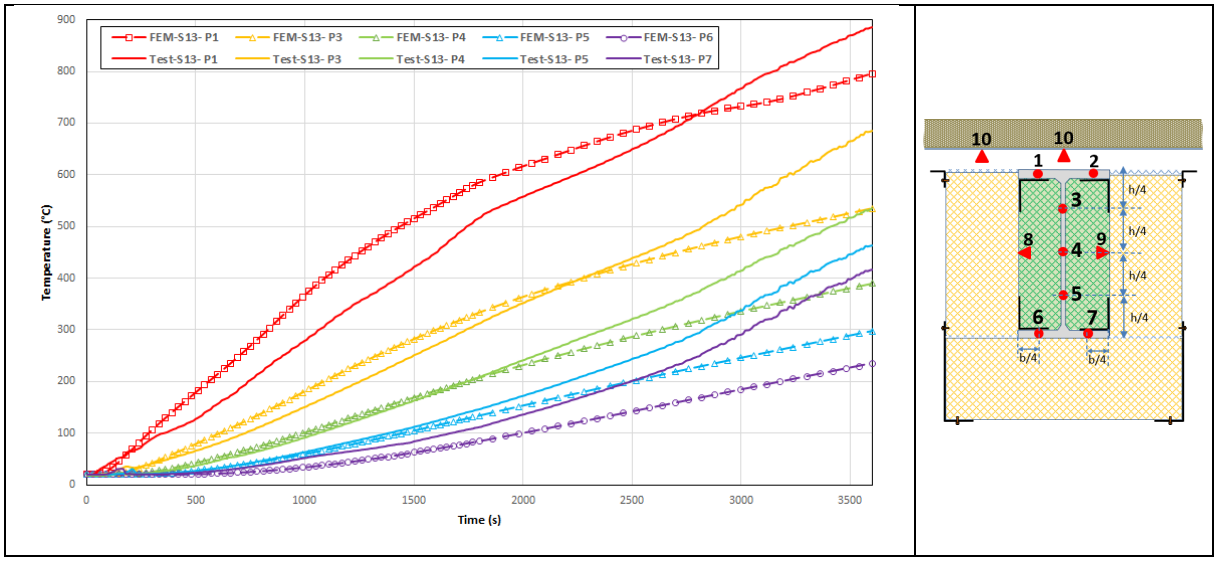

Figure 4.35: Comparison between numerical and experimental temperatures for the cross-section S13 along the purlin n°2

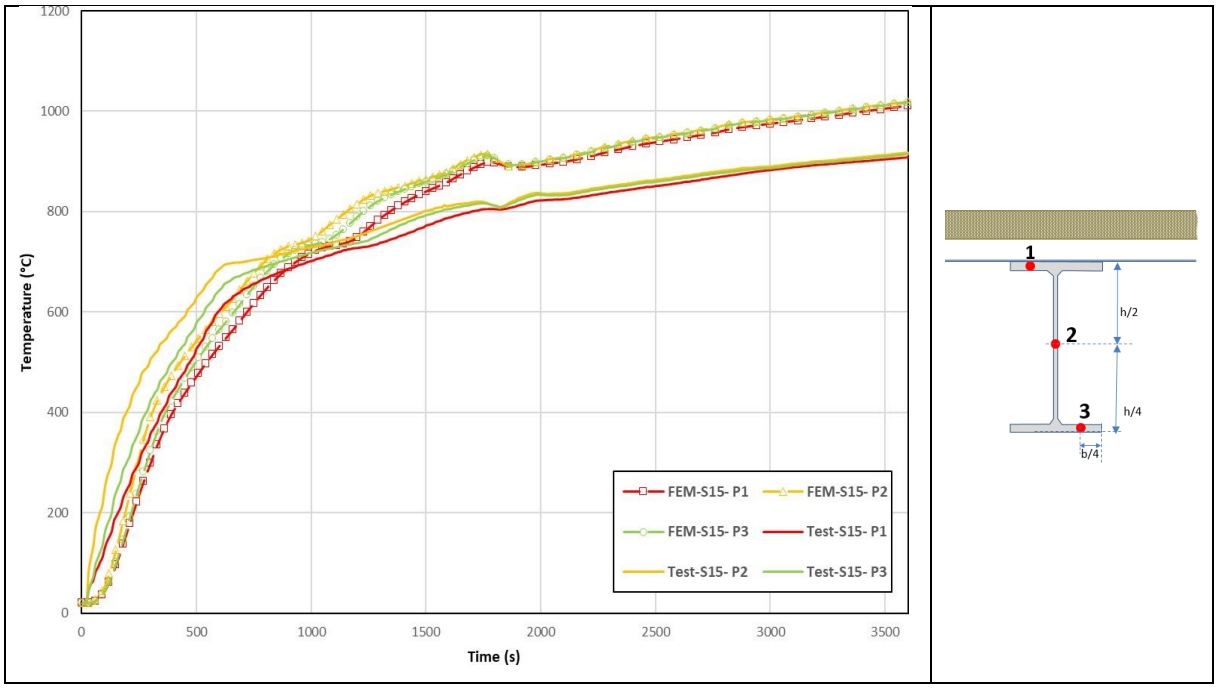

Figure 4.36: Comparison between numerical and experimental temperatures for the cross-section S15 along the purlin n°2

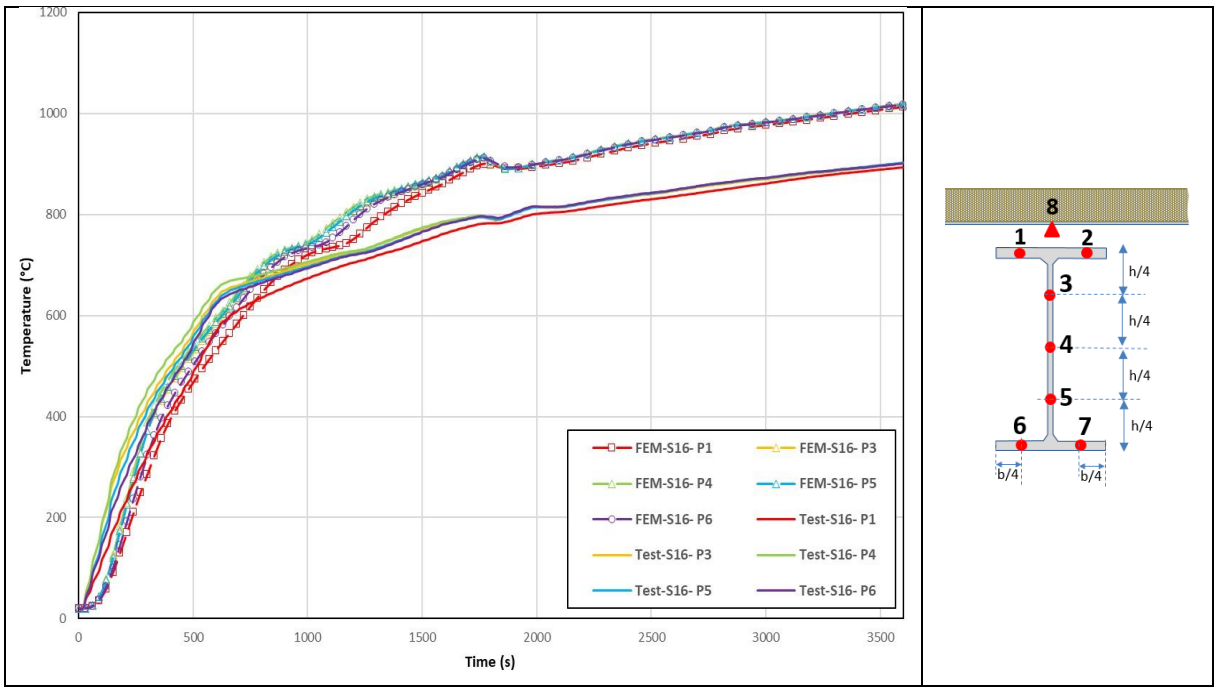

Figure 4.37: Comparison between numerical and experimental temperatures for the cross-section S16 along the purlin n°2

A careful analysis of these figures shows that:

- Overall, the predicted curves have the same general shape as the experimental ones, at least during the first phase of the test, although they are slightly shifted in time. For the purlin parts directly exposed to the fire, the temperature increase in the web of the steel purlin is higher than that in the flanges, and the temperature increase in the upper flange is the lowest. However, the temperature differences in the steel purlin are more pronounced in the experimental test than those predicted by the numerical model.
- For cross-section S9 (see Figure 4.32), here the trapezoidal steel sheeting is in contact with the purlin, the predicted temperature curve for the upper flange (P1) is in satisfactory agreement with the experimental curves during the first 1800 seconds. The temperature rise is significantly underestimated by the numerical model, with differences not exceeding 50°C. After 1800 seconds, the temperature differences become increasingly significant, up to

100°C. Once again, the temperatures measured for the purlin are higher than those measured for the hot gases inside the furnace. The reliability of such measurements after 1800 seconds can therefore be questioned. A similar trend is observed for the web (P2) and the lower flange (P3).

- In section S10, (see Figure 4.33) located at the level of a cavity formed between the top flange of the purlin and the trapezoidal steel sheeting, the comparison between the numerical model and the experimental test shows discrepancies similar to those observed for section S9, but with some variations depending on the purlin parts.
- For the section S12 *(*see Figure 4.34*)*, located along the encasement system and at the level where the trapezoidal steel sheeting is in contact with the purlin, the comparison between the numerical model and the experimental test shows noticeable differences. The predicted temperature curve in the upper flange (P2) shows a marked overestimation up to 2800 seconds of fire exposure, with differences of up to 120°C. The predicted temperatures are then slightly underestimated towards the end of the test. For the web (P3), although the correlation is good during the early part of the fire exposure, a gradual divergence appears after 1500 seconds, with the numerical model underestimating the temperatures up to 200°C. For the lower flange (P4), the temperature predicted by the numerical model is also underestimated up to 200°C throughout the test. These differences could be explained by the large flexural deformations that the purlins underwent during the test, after 1500 seconds, which could lead to both integrity and insulation losses of the encasement system with the emergence of openings at the level of the panel joints, even though no significant damage to the encasement system was observed during the test. Such potential damage is difficult to model accurately and is therefore not considered in the FE model. It is also possible that the thermal properties of both the sandwich panels and the mineral wool used to fill the end of the encasement may deteriorate more rapidly at elevated temperatures than assumed in the numerical model.
- In section S13 (see Figure 4.35*)*, located along the encasement system at the level of a cavity formed between the purlin top flange and the trapezoidal steel sheeting, the predicted temperature in the top flange (P1) is overestimated compared to the experimental test for most of the test duration, with gaps reaching up to 150°C at the end of the test. For the web (P3, P4, P5), the predicted temperatures are in good agreement with the experimental ones up to 2000 seconds of fire exposure. Then the experimental temperatures increase more rapidly. Finally, the predicted temperature in the bottom flange (P6) is underestimated throughout the test, with the discrepancies increasing as the end of the test is approached. Comparing the temperature increases in sections S12 and S13, it appears that the further away from the end of the purlin encasement system, the lower the temperatures in the purlin and the better the numerical results. The discrepancies between the experimental and FE results are believed to be mainly due to the high temperature degradation of the mineral wool used to fill the encasement system, which will degrade more rapidly than assumed in the numerical model.
- For section S15 and section S16 *(*see Figure 4.36 and Figure 4.37*)*, located along the purlin part directly exposed to the fire (at the level where the trapezoidal steel sheeting is in contact with the purlin and at the level of a cavity formed between the purlin top flange and the trapezoidal steel sheeting), the comparison between the numerical model and the test shows differences similar to those observed for sections S1 and S2. Overall, the temperatures predicted by the numerical model follow the experimental curves closely, with a slight underestimation, up to 1200 seconds. Beyond this time, there are larger deviations. The temperatures predicted by the numerical model are then overestimated compared to the temperatures recorded in the test, with differences remaining below 120°C. These differences are mainly due to the hot gas temperatures applied along the purlin in the numerical model, which represent an average of the hot gas temperatures measured only at the encasement level (plate thermometers PT1 and PT4). In fact, the hot gas temperatures recorded during the test closest to sections S15 and S16 are lower than the average temperature considered.

4.2.1.3 Conclusion

The comparison of the results shows a satisfactory correlation between the numerical model and the experimental test, at least up to the failure of the purlins (characterised by large flexural deformations). The discrepancies between the experimental and FE results are thought to be due to the hot gas temperature curves applied along the purlins in the numerical model, which correspond to an average of the hot gas temperatures measured only at the level of the encasement systems. In fact, the hot gas temperature distribution in the furnace was not uniform, with temperatures lower than the average temperature considered when moving away from the encasement systems. These differences could also be explained by the large flexural deformations that the purlins underwent

during the test, after 1500 seconds, which could lead to a loss of integrity and insulation of the cladding systems with the creation of openings at the level of the panel joints, although no significant damage to the encasement systems was observed during the test. Such potential damage is very difficult to model accurately and is therefore not considered in the FE model. It is also possible that the thermal properties of both the mineral wool of the sandwich panels and the insulation placed in the casing systems deteriorate more rapidly at elevated temperatures than assumed in the numerical model.

4.2.2 Mechanical analyses

A three-dimensional finite element model developed using the ANSYS code [8] was used for the mechanical analyses.

4.2.2.1 Modelling considerations

With regard to the model developed, only one purlin of the test specimen is considered and meshed. The following assumptions were also made to allow the development of a relatively simple model that would enable the simulation of the structural response to fire of the purlins under consideration:

- The purlin is meshed with a 20-node brick FEs (SOLID186), using the same meshes as those used in the thermal models.
- The purlin is continuous over three supports and made from S275 steel grade. Following steel properties are adopted at normal temperature:
    - Yield strength: f_y=275 (nominal value) or 334 MPa (value taken from the steel certificate)
    - Young's modulus: E = 210,000 MPa
- The mechanical properties of steel at elevated temperatures (reduction factors for characteristic strengths, stress-strain laws, and thermal expansion coefficient) are those specified in EN 1993-1-2. The partial safety factor for steel in fire conditions is $\gamma_{M,fi}$ =1.0.
- The purlin at the connection to the trapezoidal steel sheeting is assumed to be laterally restrained by preventing lateral displacement at the connection points. This connection is also assumed to provide partial torsional restraint to the purlin. This partial torsional restraint given to the purlin by the sheet connected to its top flange is represented by rotational springs acting on the top flange of the purlin, with spring stiffness calculated according to EN 1993-1-3. The purlin is also laterally restrained at support points.
- The support system (stop systems) on the fire exposed side has been modelled using uniaxial spring elements allowing free axial displacements of the purlin, over 50 mm or 40 mm depending on the direction considered (zero stiffness), after which the stiffness of the springs becomes equal to the flexural stiffness of the beam supporting the purlin.
- An initial geometric imperfection associated with the first mode at which the purlin may undergo a lateral torsional buckling is introduced into the model. For this purpose, a linear bifurcation (eigenvalue) analysis was performed beforehand. An amplification factor of L/1000 was used according to EN1993-1-2.
- In addition to the self-weight of the purlin, a concentrated vertical load of 15 kN is applied to the top flange, at the mid-span of the purlin to represent the suspended mass attached to each purlin in the test. The purlin also carries a uniformly distributed load equal to the self-weight of the steel sheets and the insulation above. These loads remain constant throughout the duration of the fire exposure.

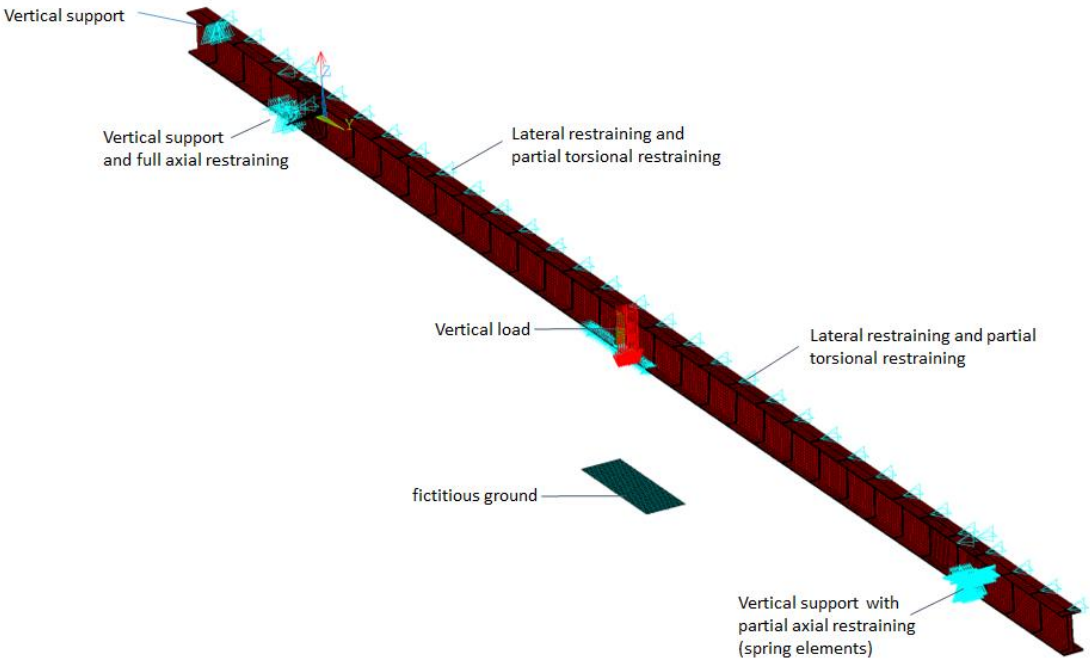

Figure 4.38: Mechanical model developed for the studied purlins

- Regarding the thermal loading, following cases have been considered:
  - "FEM 1" case: The temperature field applied to the purlin is derived directly from experimental data (using different thermocouples). The temperature curves collected during the test on different purlin sections are applied directly to the purlin by considering the temperature distributions along the purlin length, as shown in Figure 4.39, and an average temperature for the different parts of the purlin section, distinguishing the lower flange, the upper flange and the web.
  - "FEM 2" case: The temperature field applied to the purlin is that predicted by the FE thermal model where the hot gas temperature applied for heat exchange on the faces exposed to fire is represented by the average of temperatures recorded by plate-thermometers PT1 to PT4 (see Figure 4.40).
  - "FEM 3" case: The temperature field applied to the purlin is that predicted by the FE thermal model, where the hot gas temperatures applied for heat exchange on the faces exposed to fire is represented by the average of the temperatures recorded by plate-thermometers PT1 to PT4 at the encasement level, the average of the temperatures recorded by plate-thermometers PT2 to PT5 at the purlin mid-span, and the average of the temperatures recorded by plate-thermometers PT3 to PT6 at the purlin's end support (see Figure 4.41).

The averages of the temperatures recorded by the considered plate-thermometers are reported on Figure 4.42.

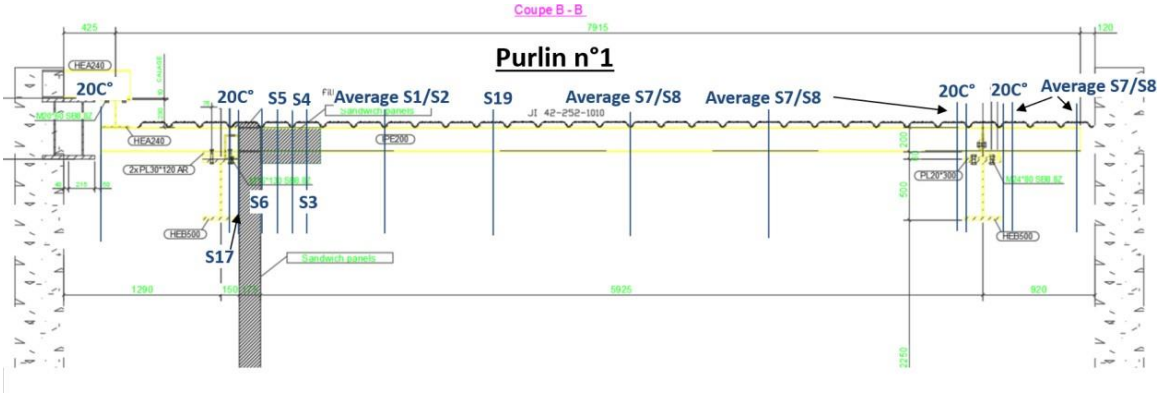

Figure 4.39: Temperature field based on test data considered in "FEM 1" modelling case

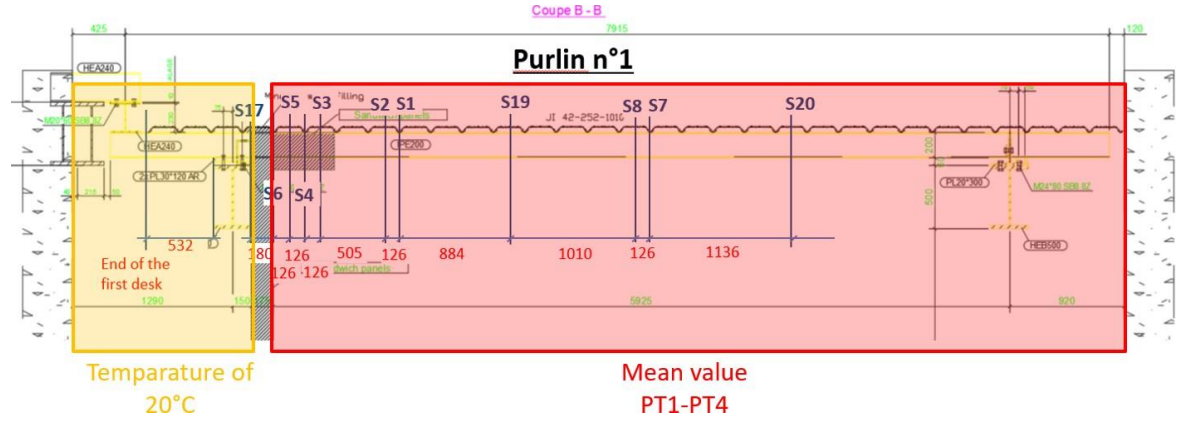

Figure 4.40: Distribution of hot gas temperatures considered in "FEM 2" modelling case

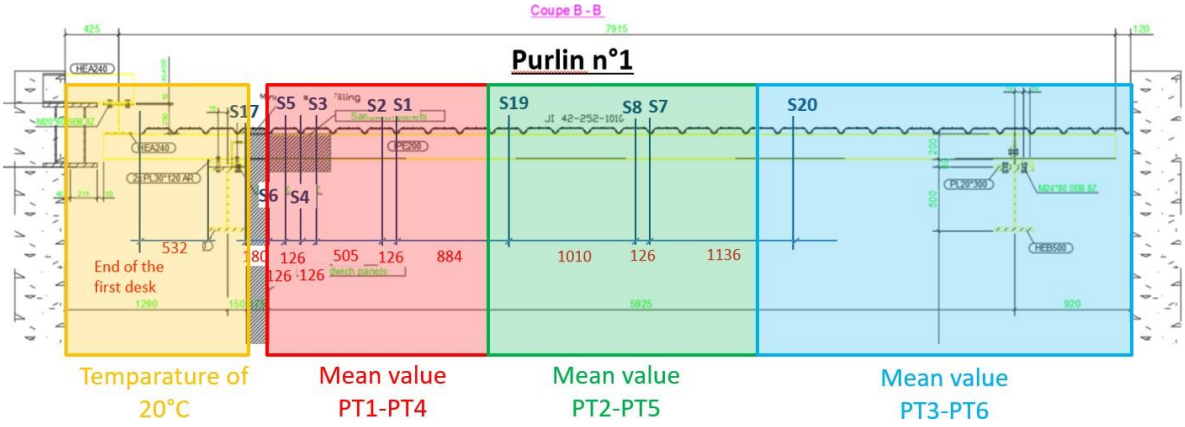

Figure 4.41: Distribution of hot gas temperatures considered in "FEM 3" modelling case

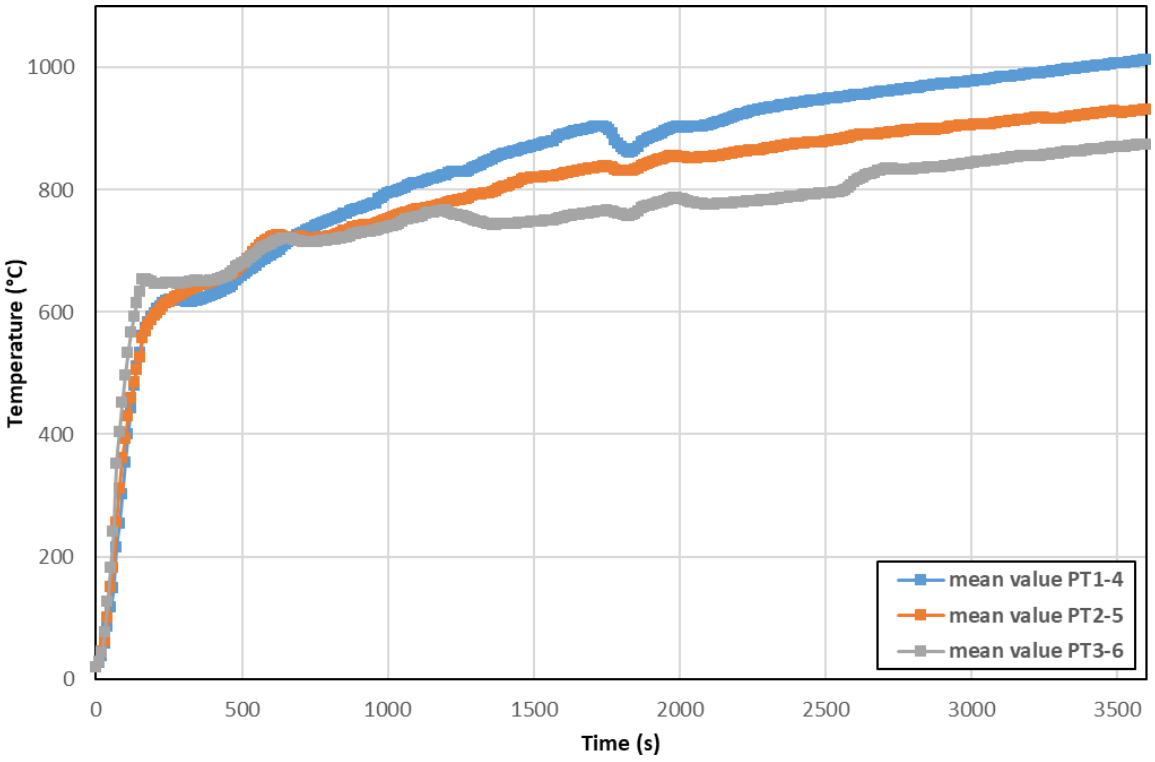

Figure 4.42: Hot gas temperature-time curves recorded around the purlin N°1 during the test

4.2.2.2 Analysis results

4.2.2.2.1 Global behavior of the purlin

Figure 4.43 and Figure 4.44 show the time vertical displacement curves calculated at the purlin mid-span, according to the thermal loading assumption (FEM 1, FEM 2 or FEM 3).

From these figures, the following comments can be made:

- The predicted behaviour of the purlin can be divided into four successive phases. In the first phase, the displacement increases gradually up to 860 s, the time at which the purlin comes into contact with the stop. Then the displacement increases more rapidly due to the combined effect of the compressive force resulting from the restraint on the purlin, the thermal expansion of the purlin, the applied load and the reduction in steel strength as the temperature rises. This is followed by a sudden increase in displacement, ranging from 1000 to 1300 seconds depending on the modelling assumptions, indicating the failure of the purlin. Finally, in the final stage, the vertical displacement increases more slowly and stabilises, reaching a maximum value of approximately 700 mm when the purlin is in direct contact with the ground.
- The experimental displacement curve is characterised by a gradual increase in displacement until 850s, followed by a faster increase until 1150s, corresponding to the failure phase of the purlin, and then a progressive increase in displacement, showing the ductile behaviour of the purlin until the end of the test.
- There is good agreement between the predicted displacements and the measurement when the yield strength of the steel is equal to the nominal value. In this case, the predicted failure time is about 1000 seconds, which is close to the observed one. If a higher yield strength based on the steel certificate is used, the failure time is slightly overestimated, increasing from 1000 to 1200 seconds.

Figure 4.45 and Figure 4.46 show the calculated vertical displacement curves at the end of the purlin encasement and at wall level, respectively. These are compared with experimental measurements. The purlin displacements are very small and that the predicted displacements are generally underestimated. These discrepancies are believed to be primarily due to the location of the measurement point and the straightforward method used to measure displacement, which is likely to be imprecise. For example, a better agreement between the displacement values is obtained when the measured displacement is compared with the vertical displacement calculated at 1 cm from the end of the purlin encasement. Additionally, the location of the plastic hinge predicted by the FE model at the end of the purlin encasement could be slightly different from the purlin zone with the largest residual deformations observed after the test.

The failure mode of the purlin is assessed by monitoring the strain states. By way of illustration, Figure 4.47 shows the distribution of the total Von Mises mechanical strain predicted in the purlin at different times of fire exposure, considering the thermal loading FEM 1 and a steel yield strength of 275 MPa. Strain values greater than 2% in steel are highlighted. The strain distribution in the components clearly shows the plastic hinges that progressively develop in the purlin, first at mid-span and at the level of the encasement end, and then at free support.

The differences with the test results could be explained by several assumptions adopted in the purlin modelling, that may not fully capture the test conditions:

- The fire resistance of the purlin depends on the material properties. In simulations, there are uncertainties in the values of the mechanical properties considered for the steel (both yield strength and ultimate strength). In fact, the material properties of the steel considered at ambient temperature are derived from the values indicated in the steel certificates supplied, which are not necessarily the actual values for the purlins tested.
- temperature gradient across the purlin cross-section considered in the modelling may not be sufficiently accurate.
- With regard to the support conditions at the free end of the purlin, the actual clearance provided by the support system could be slightly less than the designed value, i.e. 50 mm. In addition, the value of the spring stiffness assigned to take account of the stop system could be overestimated.

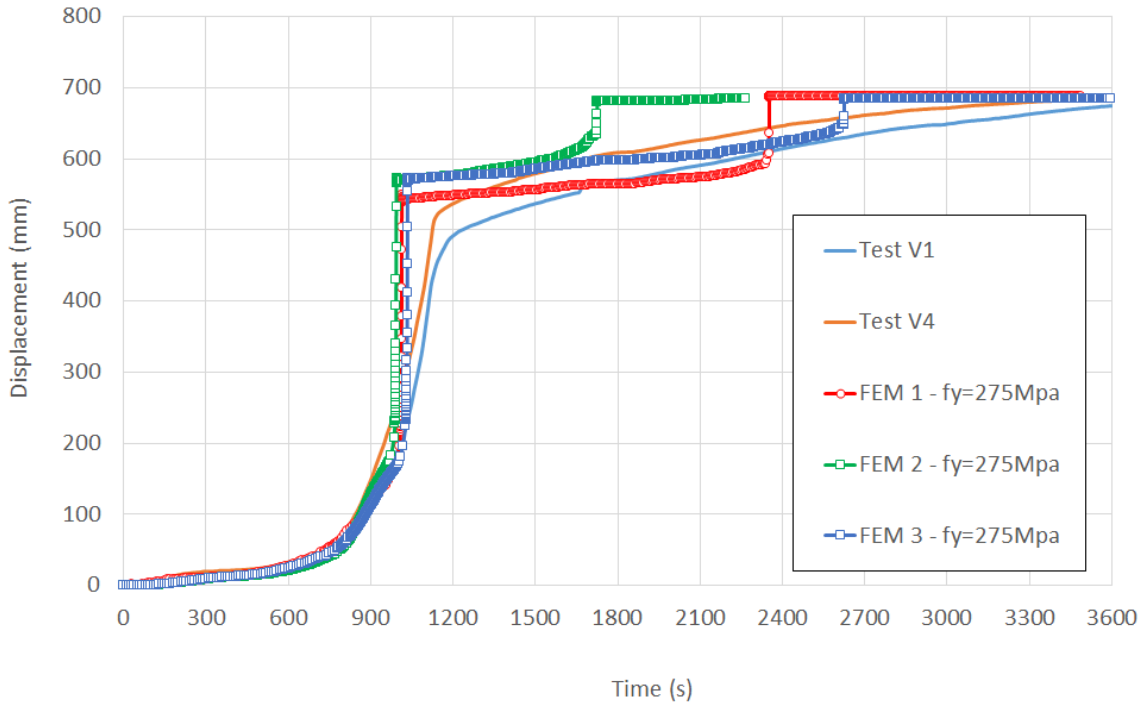

Figure 4.43: Time-vertical displacement curves of the purlin predicted at the purlin mid-span with a steel yield strength of 275 MPa

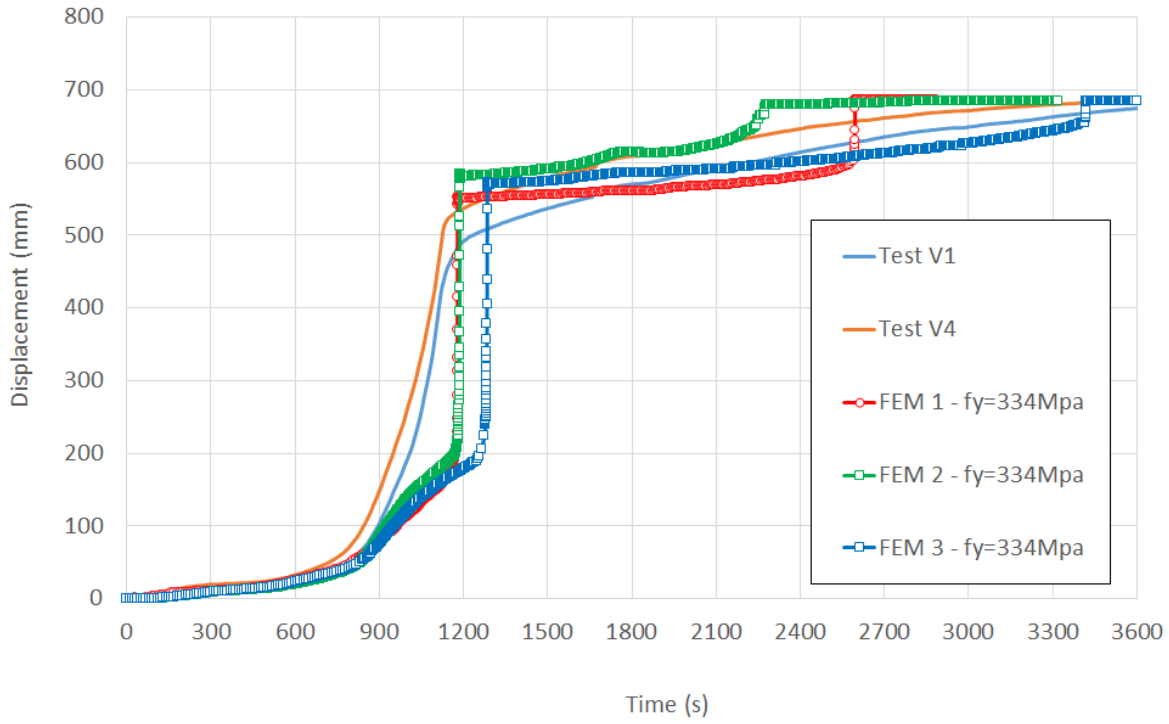

Figure 4.44: Time-vertical displacement curves of the purlin predicted at the purlin mid-span with a steel yield strength of 334 MPa

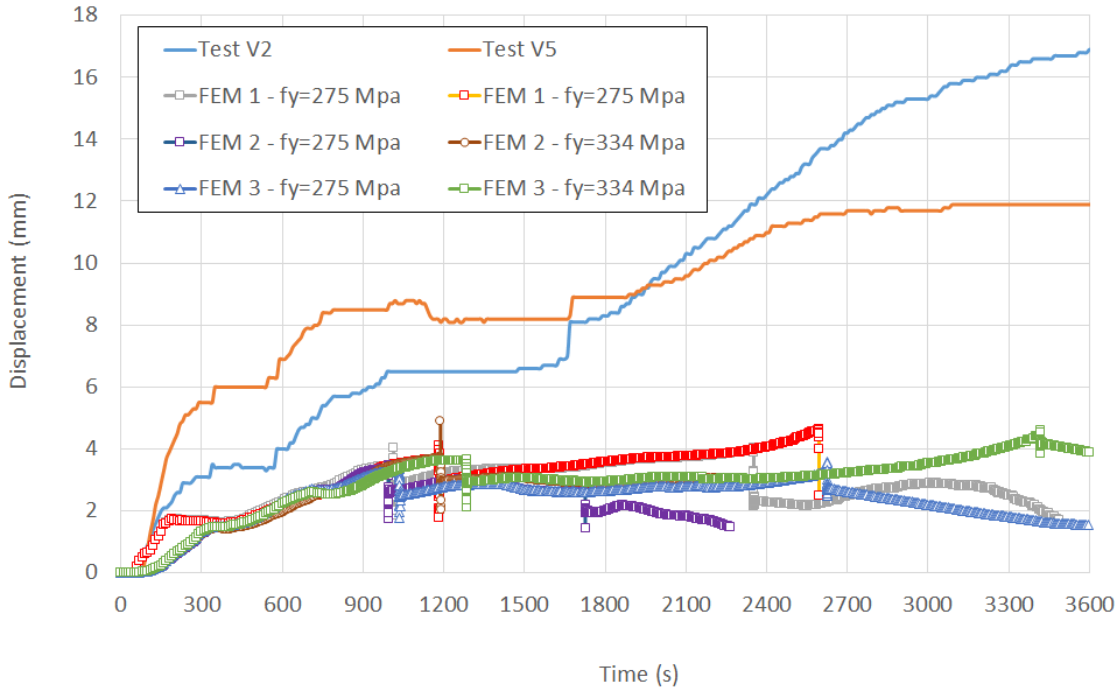

Figure 4.45: Time-vertical displacement curves of the purlin predicted at the encasement end

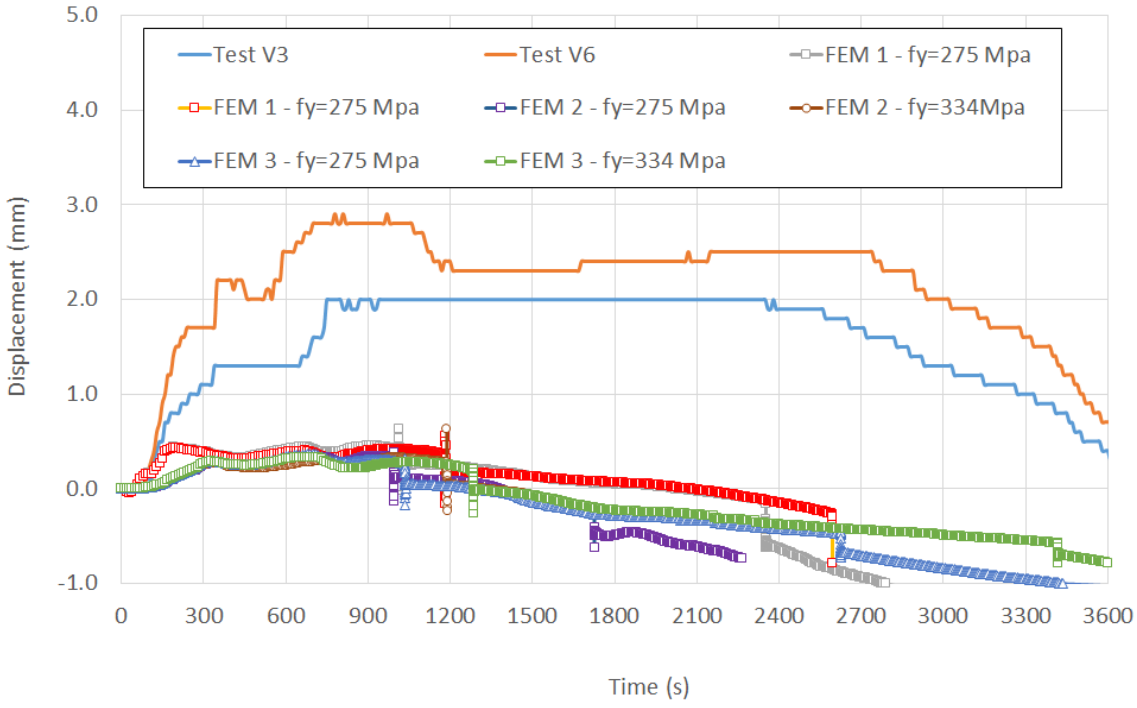

Figure 4.46: Time-vertical displacement curves of the purlin predicted at the wall level

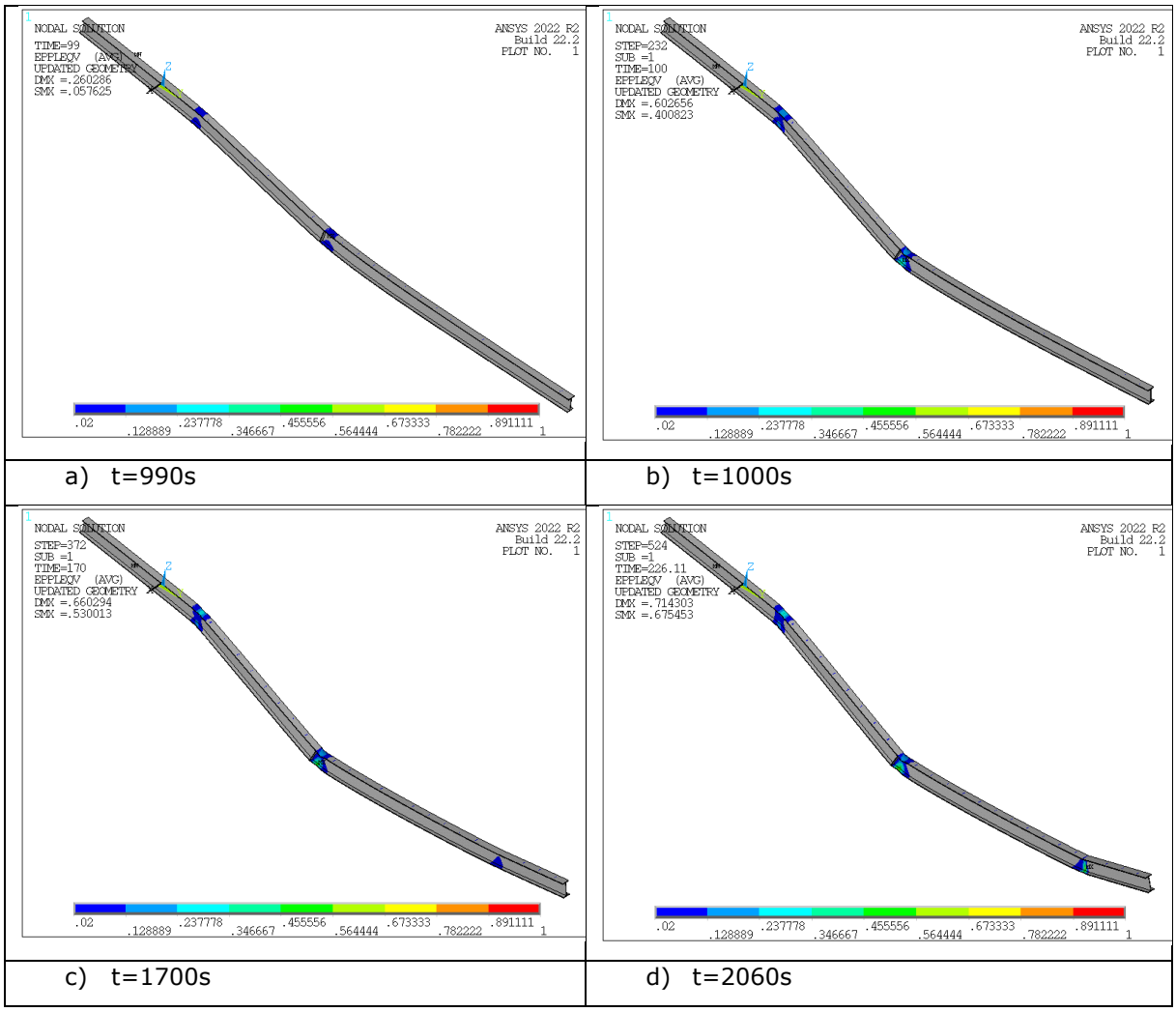

Figure 4.47: Predicted total von Mises mechanical strain in the purlin as a function of fire exposure time - thermal loading condition FEM 1 and 275 Mpa steel yield strength

4.2.2.2.2 Local behaviour of the purlin

The Figure 4.48 and the Figure 4.49 illustrate the predicted torsional rotation of the purlin section at the junction with the wall on the fire exposed side and at the end of the encasement protecting the purlin. The rotations are accompanied by out-of-plane displacements. By way of illustration, the rotations are accompanied by the out-of-plane displacements Ux and Uz predicted at the end of the encasement (see Figure 4.50), considering the thermal loading FEM 1 and a steel yield strength of 275 MPa. Unfortunately, comparisons with test measurements cannot be made, as these are very difficult, if not impossible, to perform in the furnace environment.

From these figures, as expected, the torsional rotation and displacement of the purlin remain very limited, since the lateral torsional buckling of the purlin is restrained by the steel sheeting connected to its upper flange.

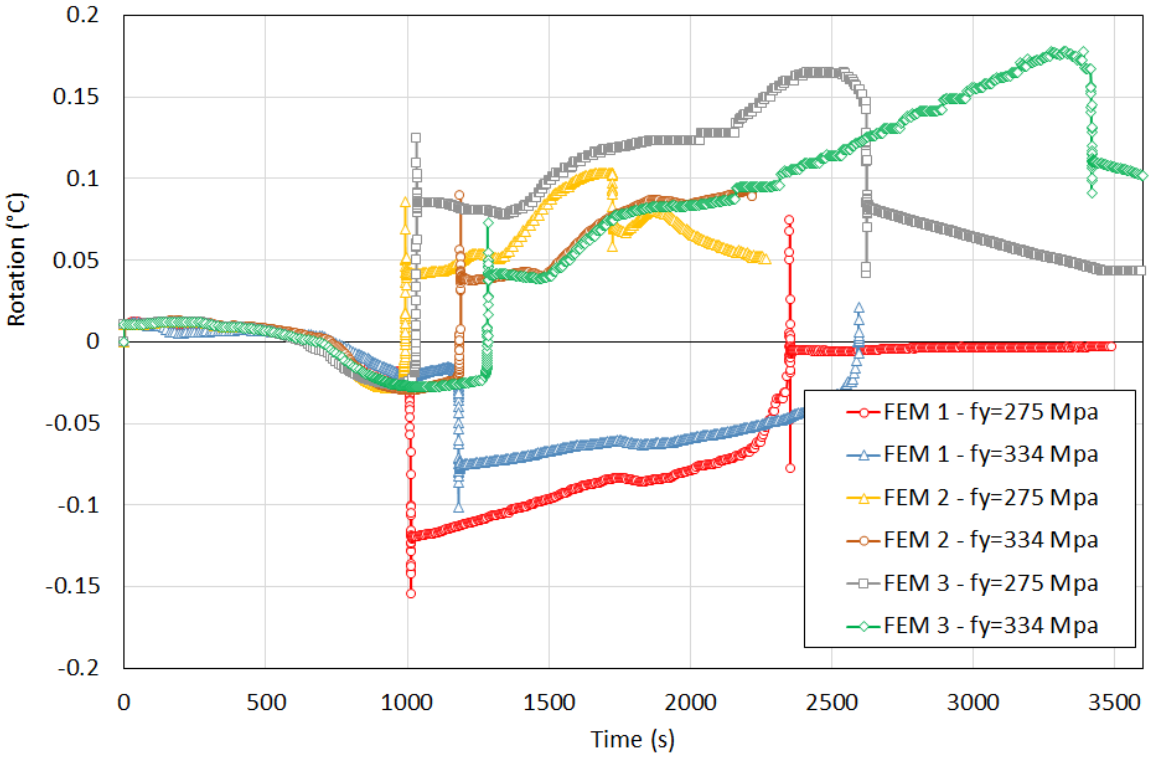

Figure 4.48: Time-rotation curves of the purlin predicted at the encasement end

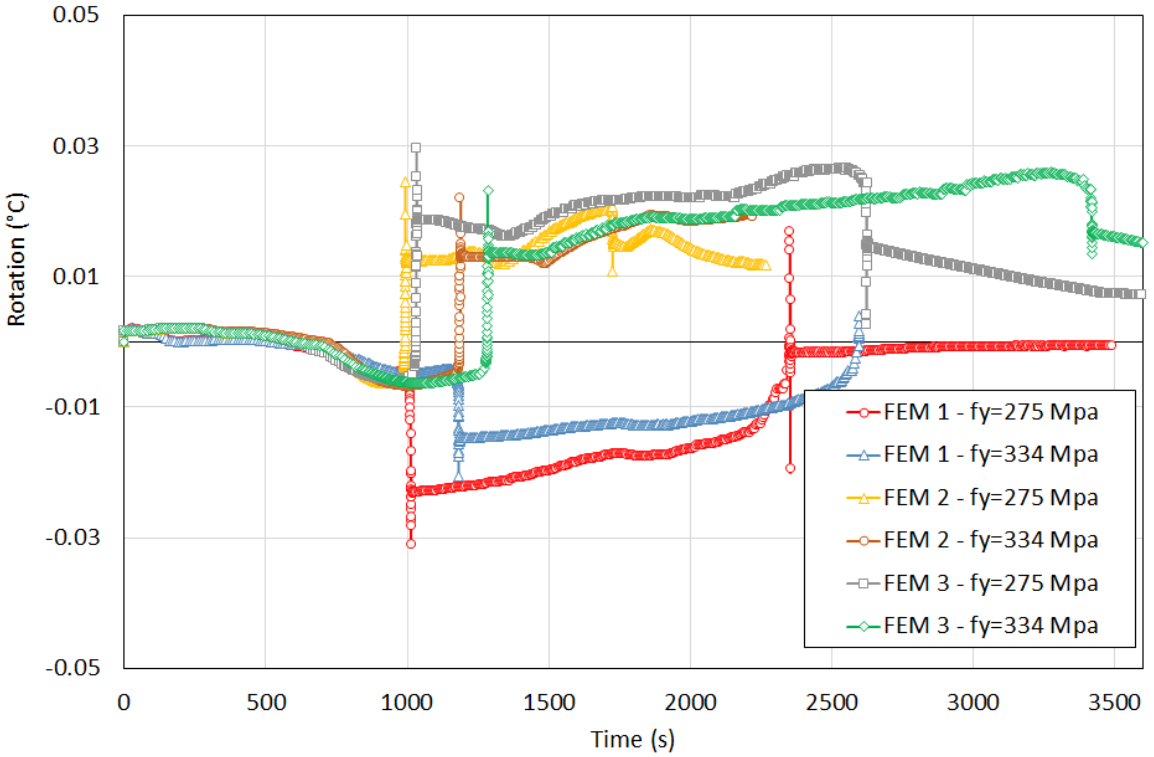

Figure 4.49: Time-rotation curves of the purlin predicted at the wall level

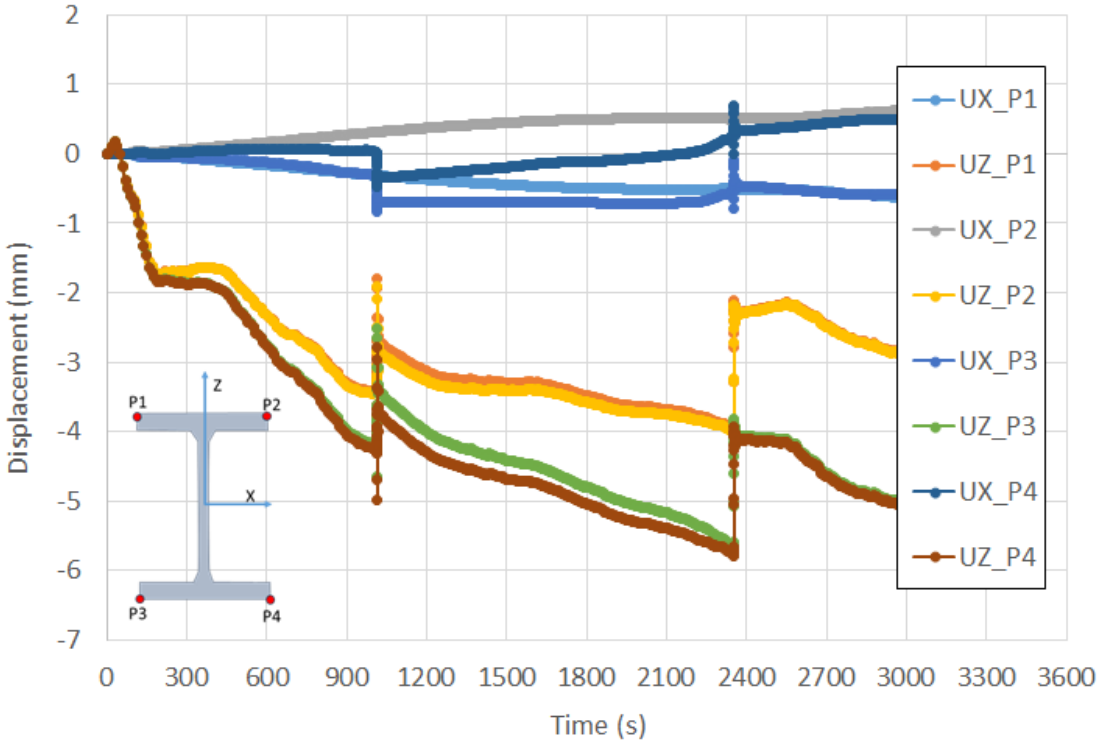

Figure 4.50: Predicted purlin displacements at the end of the encasement - thermal loading condition FEM 1 and 275 Mpa steel yield strength

4.2.3 Conclusion

The results of the thermal analyses carried out confirmed a satisfactory correlation between the experimental data and the purlin heating predicted by the developed FE model, despite some differences explained by several simplifying assumptions and uncertainties. Firstly, the numerical model applied the same fire exposure conditions to all fire-exposed surfaces of the specimen, using an average of the temperatures measured by some plate thermometers, whereas the temperature of the hot gas in the furnace was not homogeneous. In addition, the temperature of the hot gas in the cavities formed between the steel sheet and the upper flange of the purlins was probably lower than that of the fire in the common part of the furnace. The higher the voids, the easier it is for the hot gas to pass through. Secondly, an important requirement for accurate numerical heat transfer modelling is the accuracy of the thermal properties of the input material. While the material properties of steel are well known, the thermal properties of insulation materials at high temperatures are unfortunately difficult to measure. Consequently, the thermal properties considered in the modelling for the rock wool are 'apparent' values derived from a preliminary calibration study rather than 'real' physically based material properties.

The mechanical model satisfactorily predicts the test results in terms of global deformation and failure mode. According to the model assumptions, the predicted failure time is also close to that observed during the test. The differences between the numerical and experimental results are mainly due to the simplifying assumptions made in the numerical model in terms of the thermal loading (temperatures) applied to the purlins, the steel strength and the boundary conditions. The purlins were initially designed to be free to expand thermally during the test, but the flexural deformations of the heated part of the purlins, associated with the support systems used, could result in some limitation of the purlin expansion. There is also some uncertainty about the real value of the steel yield strength of the purlin. With regard to the numerical results, it can be noted that the numerical model predicts very low purlin deformations near the wall, with low torsional rotation and displacement values, sufficiently low to not damage the encasement system, as observed during the test.

5 CONCLUSIONS

The present report summarises the results of the numerical FE simulations of the two fire resistance tests carried out in the PAVUS testing laboratory as part of the WP3 and presented in the project reports D3.2 [2] and D3.3 [1]. The first test involved a fire wall made of sandwich panels connected to an unprotected steel structure by two fusible link solutions based on conventional steel connections with aluminium bolts as the fusible component. The second test involved a fire wall made of steel-faced sandwich panels attached to an unprotected steel structure and penetrated by two steel purlins supporting an insulated steel roof. All the simulations were conducted from 3D FE models, allowing to perform detailed analyses and providing a better understanding of the structural behaviour and the failure mechanisms of the studied test specimens. The purpose of these simulations was to check the ability of the 3D FE models developed in a pre-modelling work to simulate as accurately as possible the structural behaviour of the tested elements.

The results of the numerical simulations performed on the considered fire tests underlined the satisfactory agreement between the developed FE models and the experimental results in terms of heating of the members, failure time and failure mode of the tested elements.

For the fire wall connected to an unprotected steel structure by two fusible link solutions, the comparison of the numerical results with experimental measurements indicates that the modelling assumptions adopted in the thermal analyses allow a satisfactory prediction of the heating of the elements when using the measured hot gas temperatures, even if the predicted heating of the fusible links is slightly higher than that measured during the test. The comparison results also indicate that the developed mechanical models correctly estimate the fire behaviour of the steel portal frames and their failure mode. Unfortunately, during the test it was not possible to measure displacements at the level of the fusible links exposed to the fire. Only their overall behaviour could be observed visually. As observed experimentally, the developed FE models predict that both portal frames break away from the wall during the collapsing phase, with no significant damage or deformation of the fusible links during both the pushing and collapsing phases, except for the loss of aluminium bolts. However, the fire resistance obtained from modelling for both semi-portal frames is lower than that observed during the test, mainly due to the difficulty of accurately modelling the mechanical load applied to the portal frames, which developed at the end of the test with the lateral torsional buckling of the beams.

Regarding the fire wall penetrated by purlins, the comparison results demonstrate a satisfactory correlation between the temperature rises recorded in the tested purlins and the heating predicted by the developed finite element (FE) thermal model. However, there are some differences, which are explained by several simplifying assumptions and uncertainties related to the test data. The results also indicate that the mechanical model accurately predicts the global deformation and failure mode of the tested purlins. The numerical model predicts very low purlin deformations near the wall, with torsional rotation and displacement values sufficiently low to avoid damaging the encasement system, as was observed during the test.

The developed FE models will be used through parametric studies to

- Investigate the fire resistance of the studied fusible link solutions by varying their geometric characteristics, to develop simplified design rules to easily and quickly calculate the load bearing capacity of fusible links under standard fire conditions.
- To study the fire behaviour of purlins penetrating a fire wall made of sandwich panels by considering purlin spans and sheeting different from those tested.

This deliverable also aimed to report the results of a comparative study carried out to compare several 3D numerical models developed with different FE codes (ANSYS, LS-DYNA and ABAQUS) that could be used to study the fire resistance of fusible links. The results of this comparative study highlighted a satisfactory agreement between the different models developed.

6 REFERENCES

[1] Vaněk J., FISHWALL project, RFSC-2020, GAN 101034083, Work Package 3, Deliverable 3.3, Fire test report on fire wall connected to an unprotected steel structure by means of fusible links, 2023.

[2] Vaněk J., FISHWALL project, RFSC-2020, GAN 101034083, Work Package 3, Deliverable 3.2, Fire test reports on partition fire walls made of sandwich panels with large spans, 2023

[3] Vijayakumar M., Kozich M. and Wald F. FISHWALL project, RFSC-2020, GAN 101034083, Work Package 3, Deliverable 3.1, Experimental analysis of mechanical behaviour of aluminium bolts at ambient and elevated temperature, 2022

[4] EN 1991-1-2: Eurocode 1: Actions on structures - Part 1-2: General actions - Actions on structures exposed to fire, Brussels, Belgium, CEN, 2002.

[5] EN 1993-1-1: Eurocode 3: Design of steel structures. Part 1-1: General rules and rules for buildings, CEN, 2005.

[6] EN 1993-1-2: Eurocode 3: Design of steel structures – Part 1-2: General rules – Structural fire design, Brussels, Belgium, CEN, 2005.

[7] EN 1999-1-2, Eurocode 9: Design of aluminium structures - Part 1-2: Calculation of fire behaviour, Brussels, Belgium, CEN, 2007.

[8] ANSYS, ANSYS User's Manual for Revision 8.0 – Volume IV – Theory, Swanson Analysis LINK, INC., Houston USA, 1992.

[9] Vaněk J., FISHWALL project, RFSC-2020, GAN 101034083, Work Package 3, Deliverable 3.2, Fire test report on a fire wall solidly attached to an unprotected steel structure and penetrated by steel purlins, 2024.

APPPENDIX A. COMPARISON OF THE PURLIN HEATING PREDICTED BY THE THERMAL FE MODEL WITH THE TEST DATA

A.1. Purlin n°1

This section compares the predicted temperature rises in purlin n°1 with those measured during the test. Here the thermal analyses have been carried out assuming that the fire exposed part of test specimen is uniformly exposed to hot gas temperatures equal to the average of the hot gas temperatures recorded by plate thermometers PT1 and PT4 during the test.

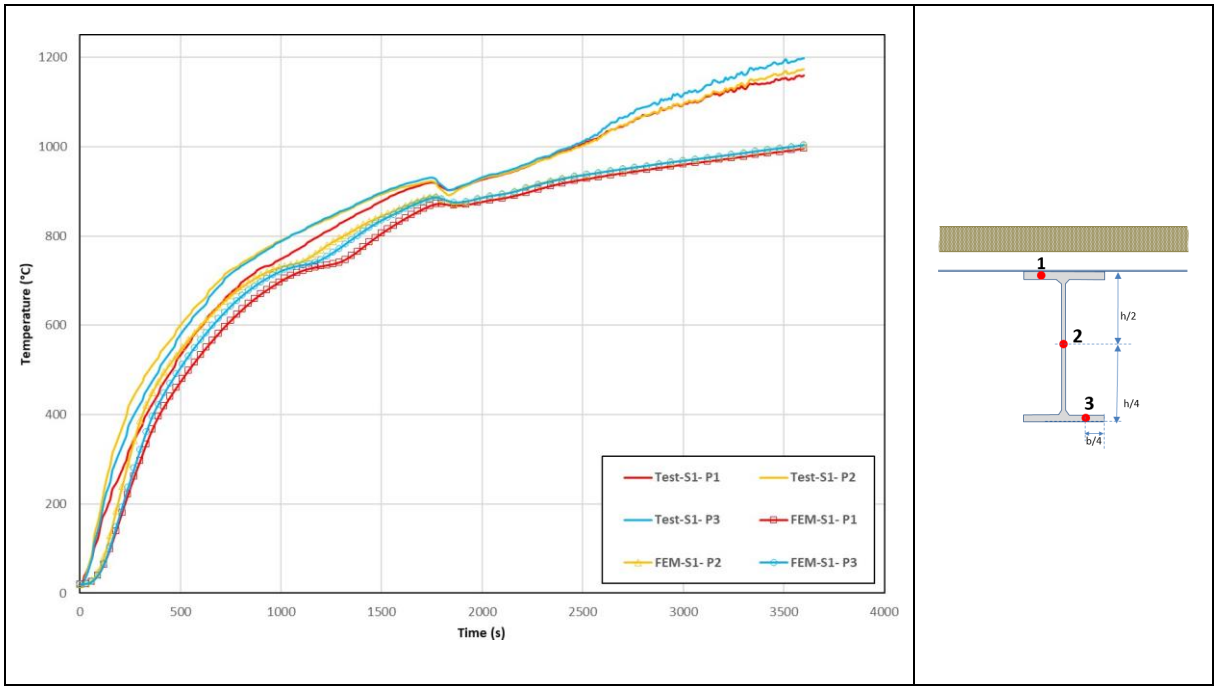

Figure A.1: Comparison between numerical and experimental temperatures for the cross-section S1 along the purlin n°1

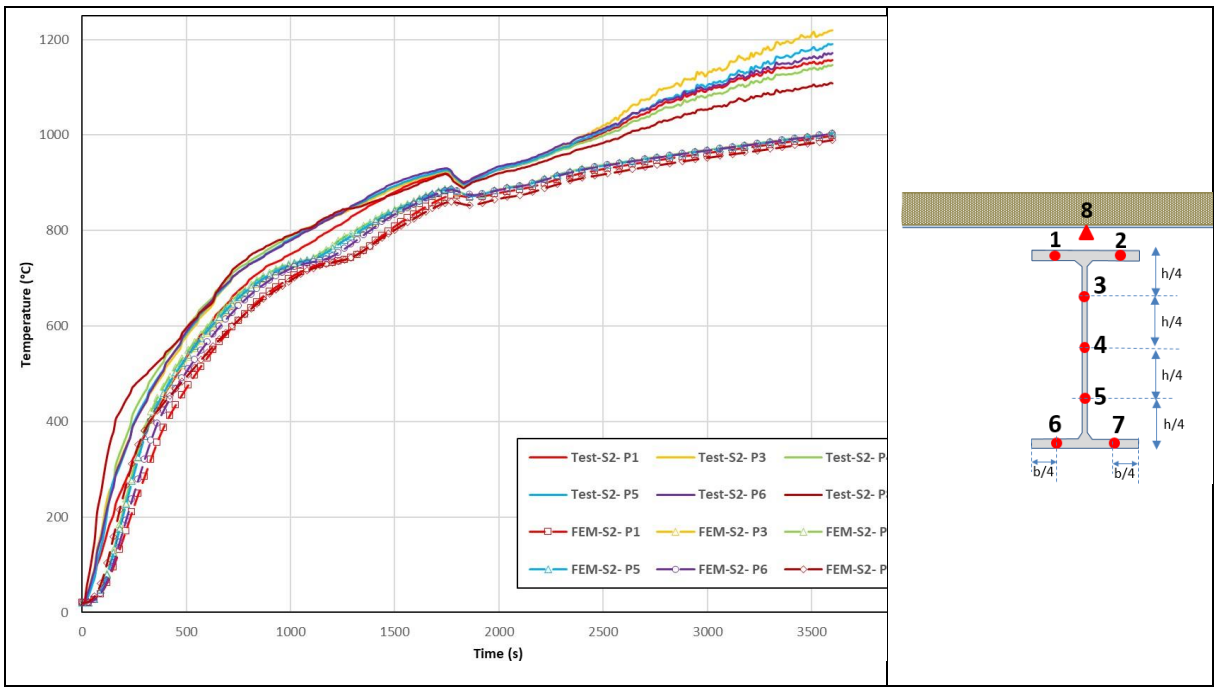

Figure A.2: Comparison between numerical and experimental temperatures for the cross-section S2 along the purlin n°1

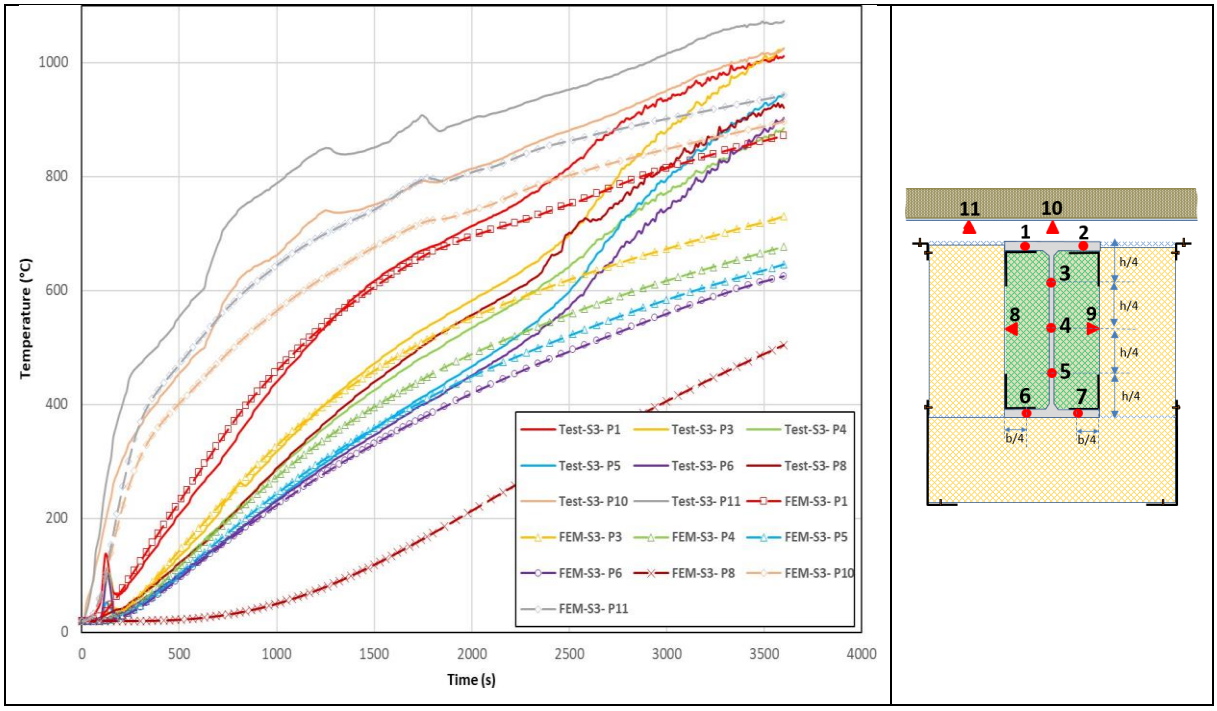

Figure A.3: Comparison between numerical and experimental temperatures for the cross-section S3 along the purlin n°1

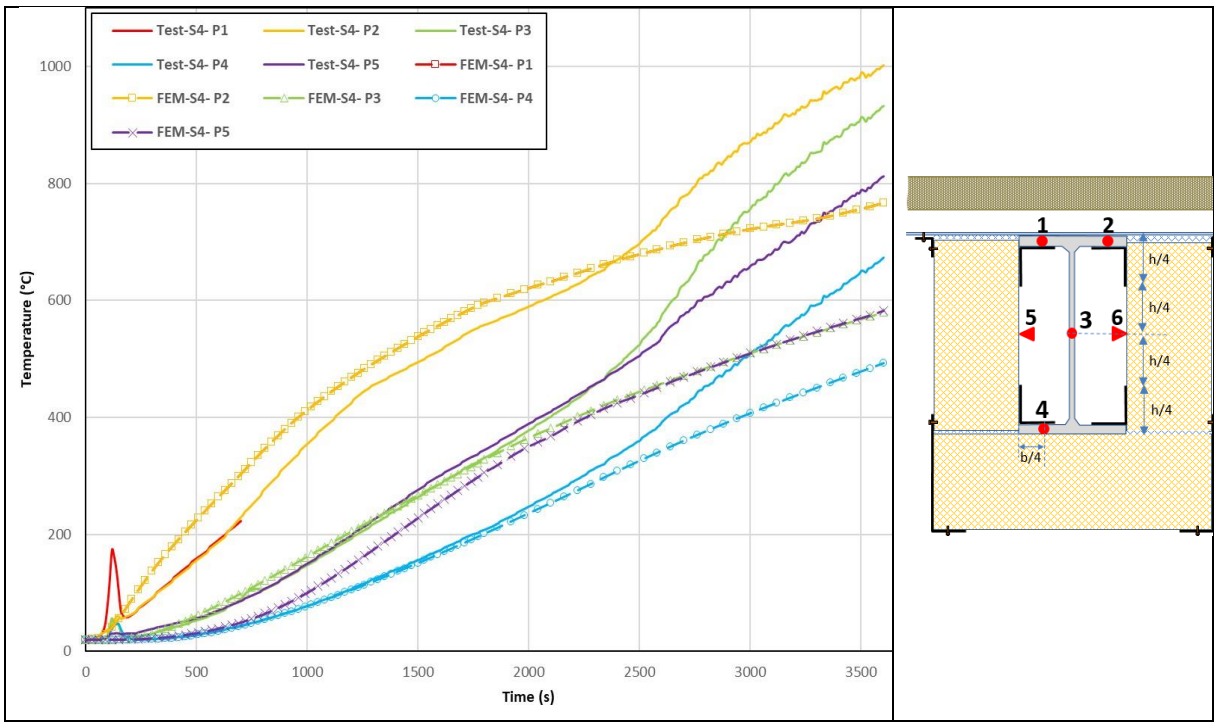

Figure A.4: Comparison between numerical and experimental temperatures for the cross-section S4 along the purlin n°1

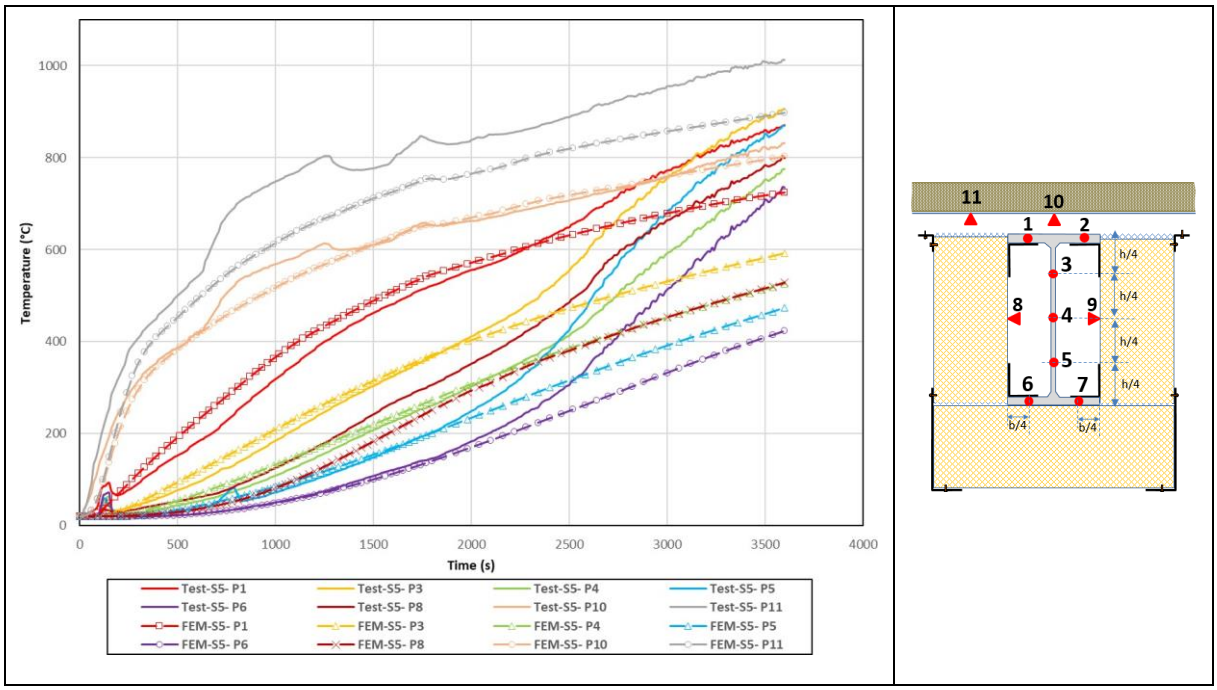

Figure A.5: Comparison between numerical and experimental temperatures for the cross-section S5 along the purlin n°1

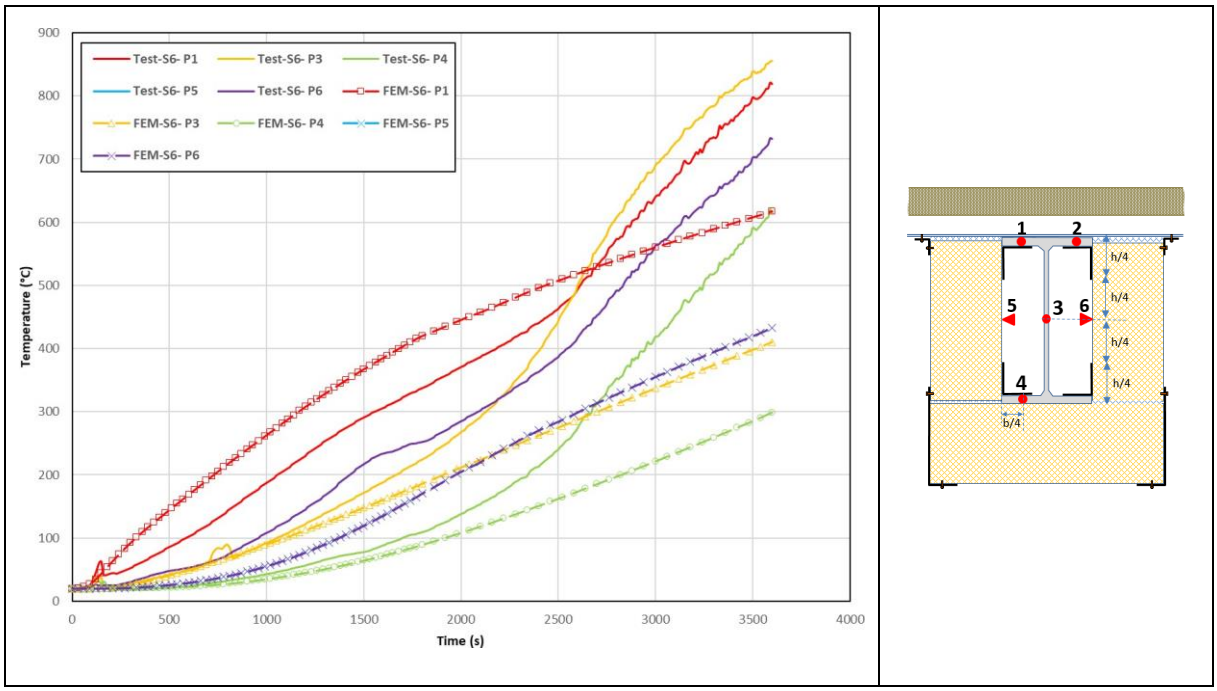

Figure A.6: Comparison between numerical and experimental temperatures for the cross-section S6 along the purlin n°1

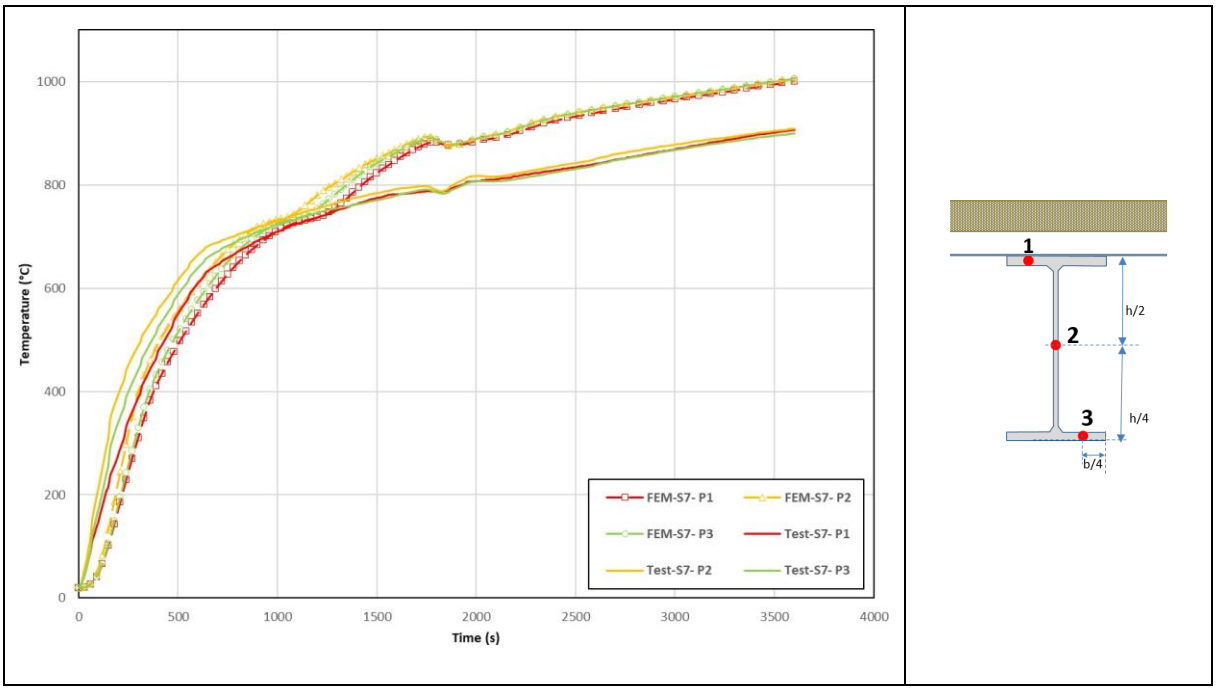

Figure A.7: Comparison between numerical and experimental temperatures for the cross-section S7 along the purlin n°1

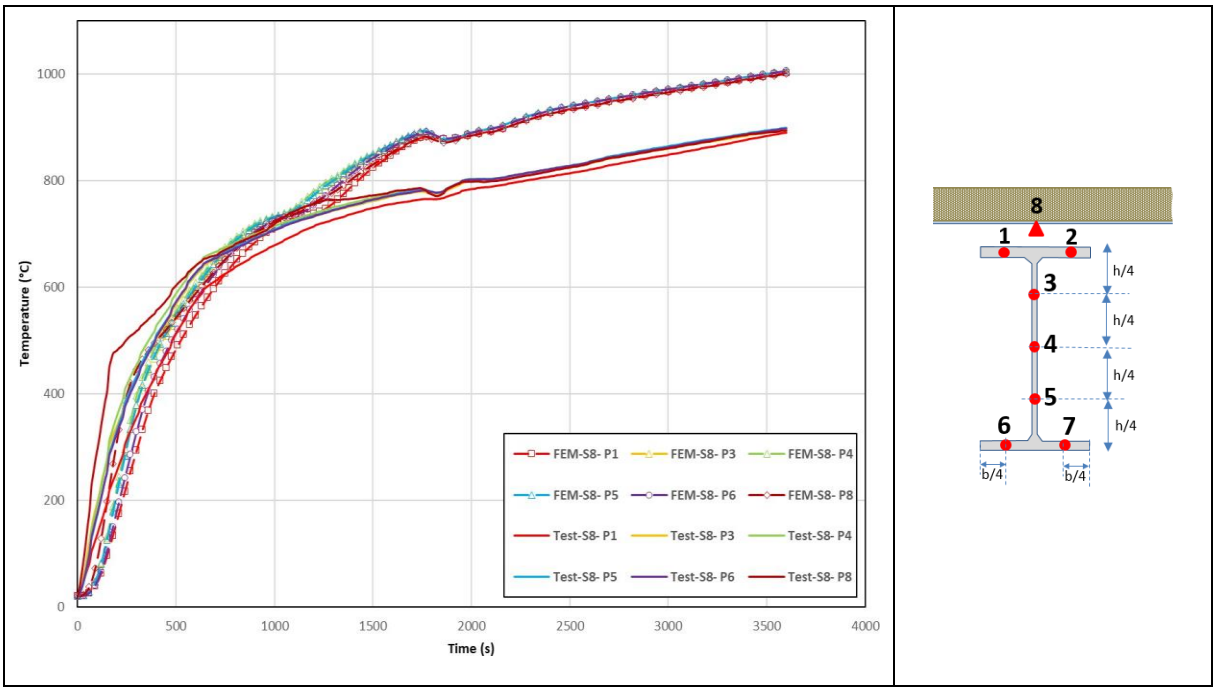

Figure A.8: Comparison between numerical and experimental temperatures for the cross-section S8 along the purlin n°1

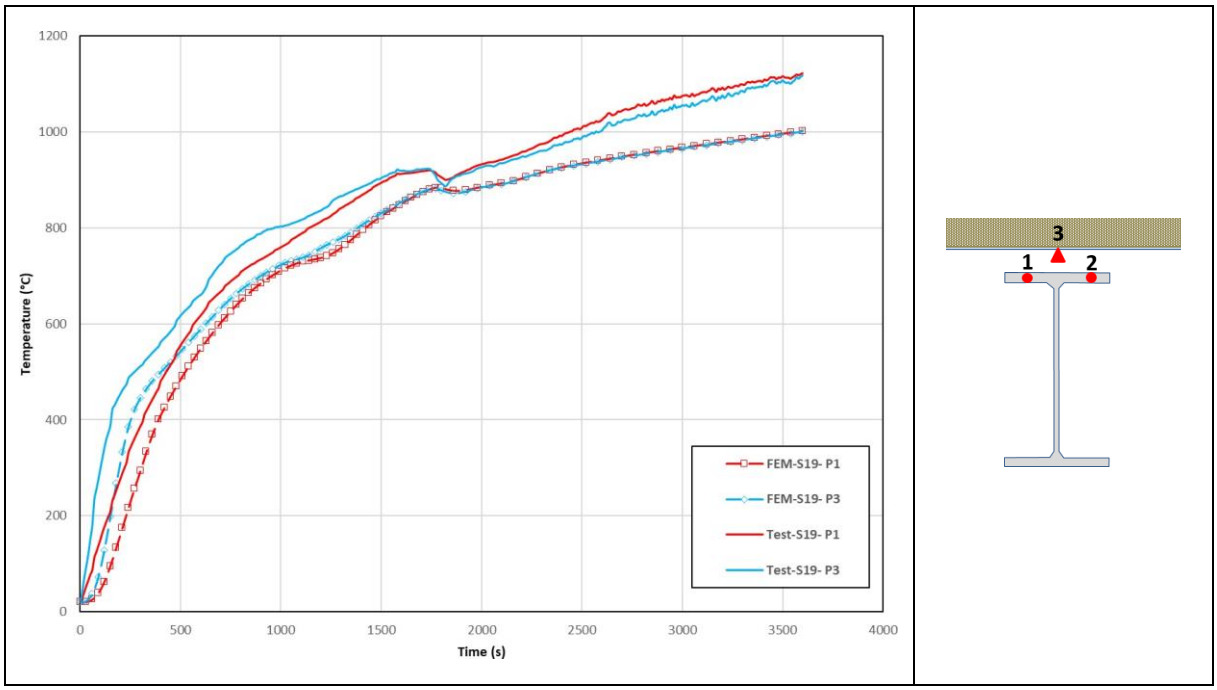

Figure A.9: Comparison between numerical and experimental temperatures for the cross-section S19 along the purlin n°1

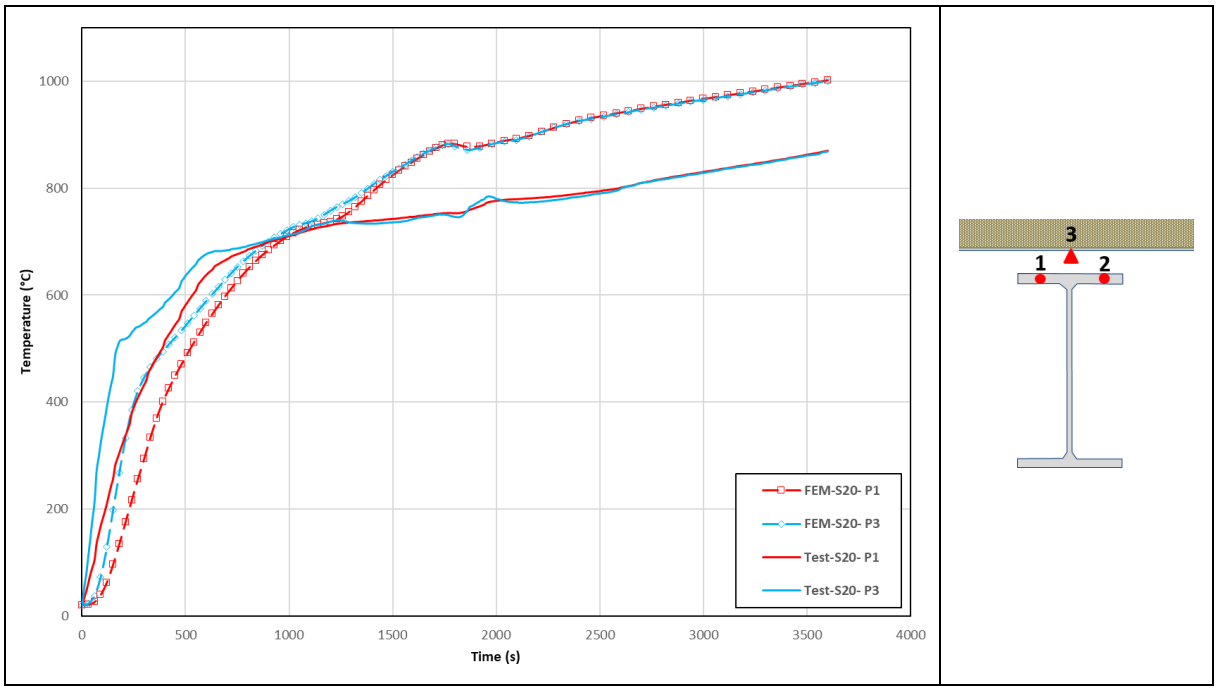

Figure A.10: Comparison between numerical and experimental temperatures for the cross-section S20 along the purlin n°1

A.2. Purlin n°2

This section compares the predicted temperature rises in purlin n°2 with those measured during the test. Here the thermal analyses have been carried out assuming that the fire exposed part of test specimen is uniformly exposed to hot gas temperatures equal to the average of the hot gas temperatures recorded by plate thermometers PT7 and PT10 during the test.

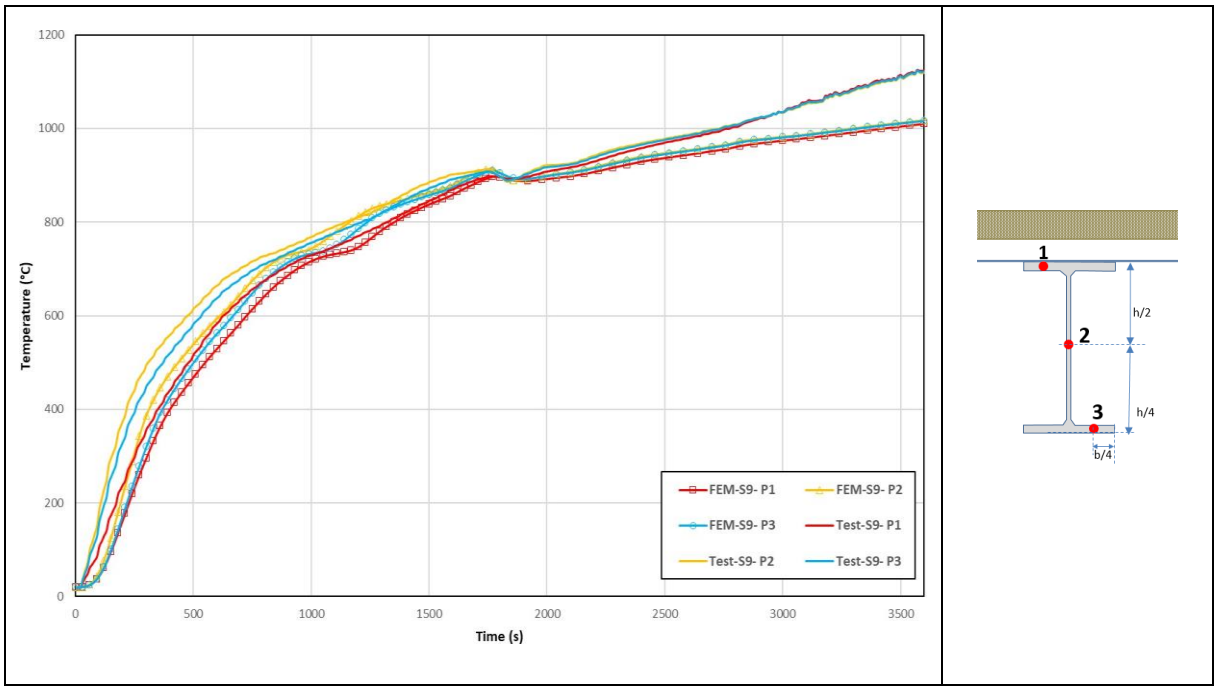

Figure A.11: Comparison between numerical and experimental temperatures for the cross-section S9 along the purlin n°2

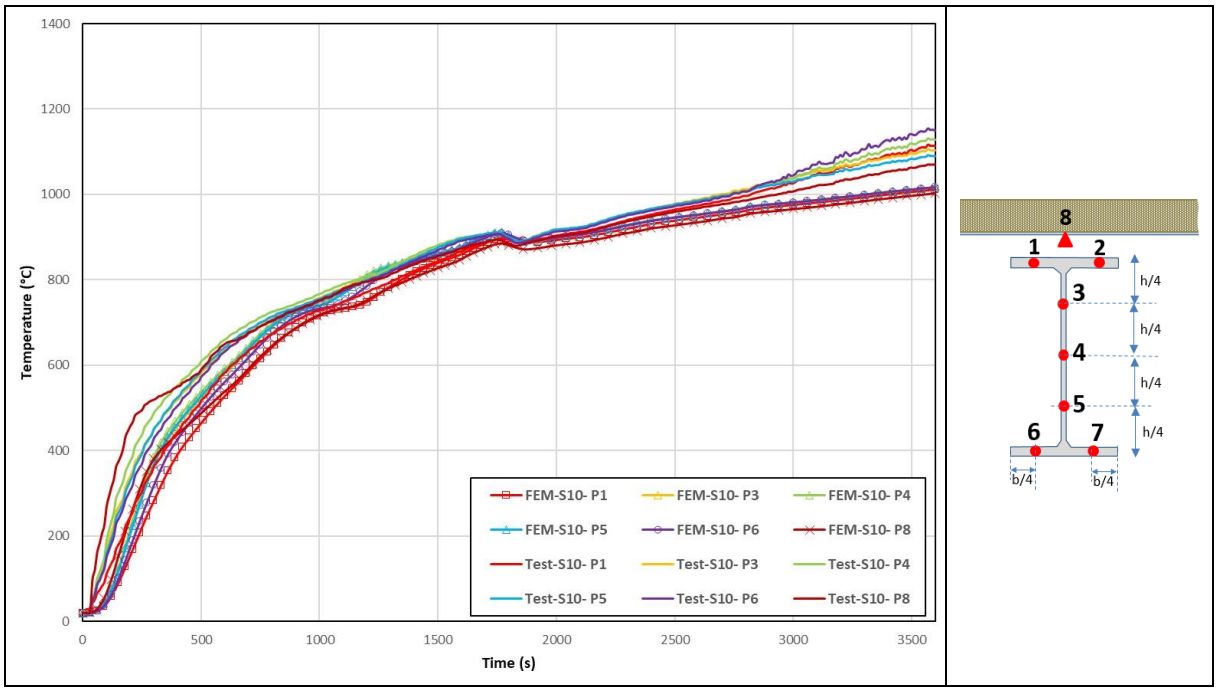

Figure A.12: Comparison between numerical and experimental temperatures for the cross-section S10 along the purlin n°2

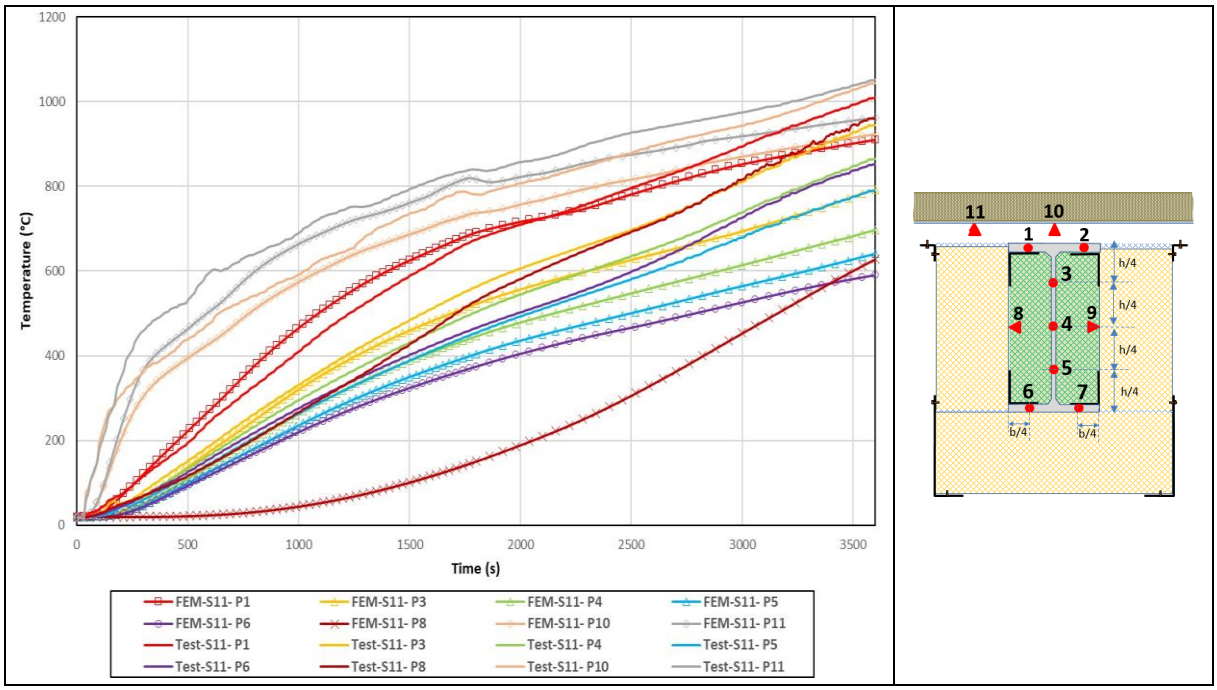

Figure A.13: Comparison between numerical and experimental temperatures for the cross-section S11 along the purlin n°2

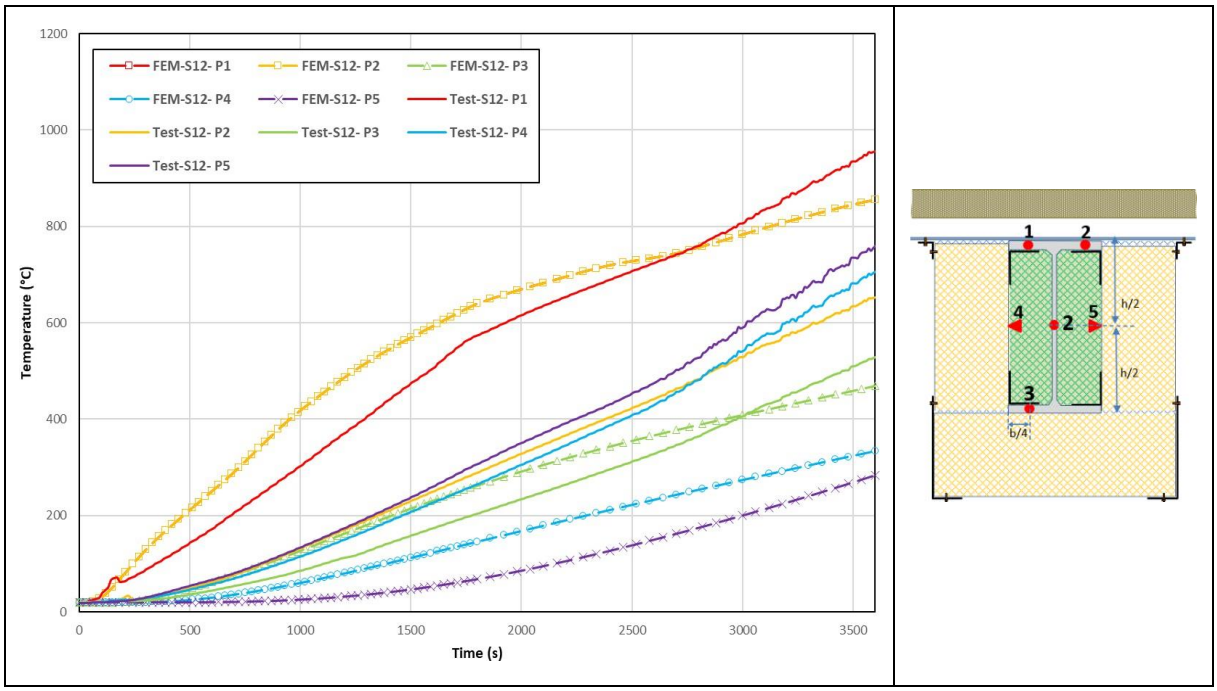

Figure A.14: Comparison between numerical and experimental temperatures for the cross-section S12 along the purlin n°2

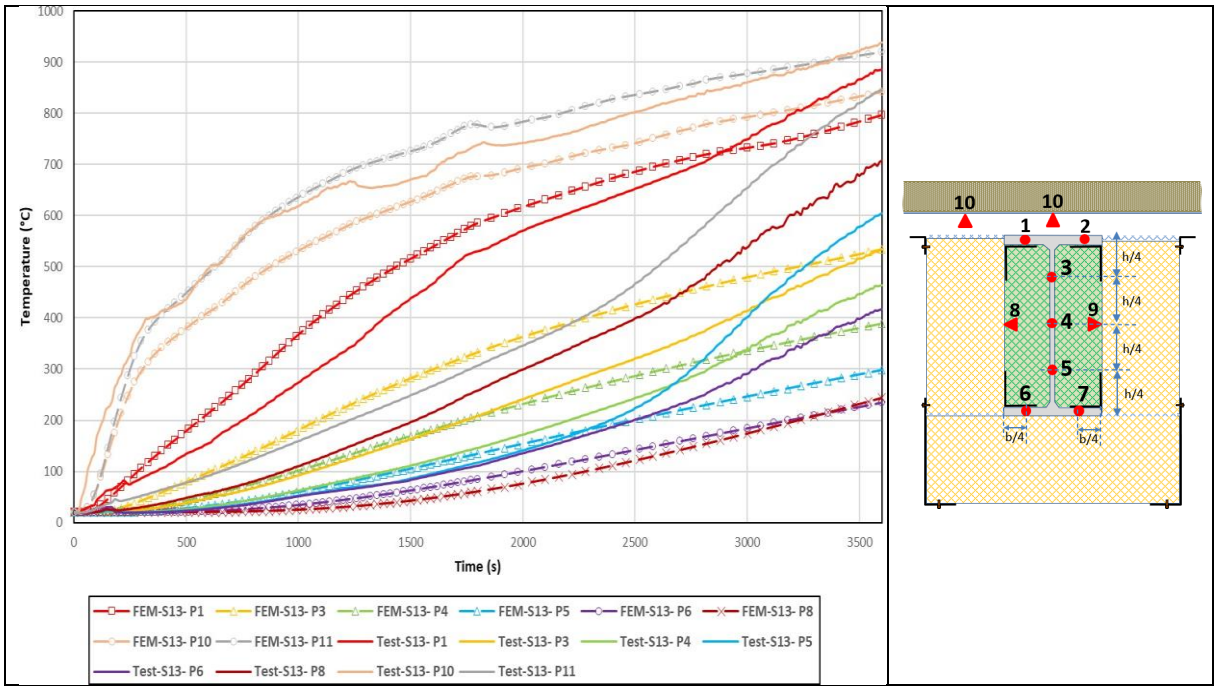

Figure A.15: Comparison between numerical and experimental temperatures for the cross-section S13 along the purlin n°2

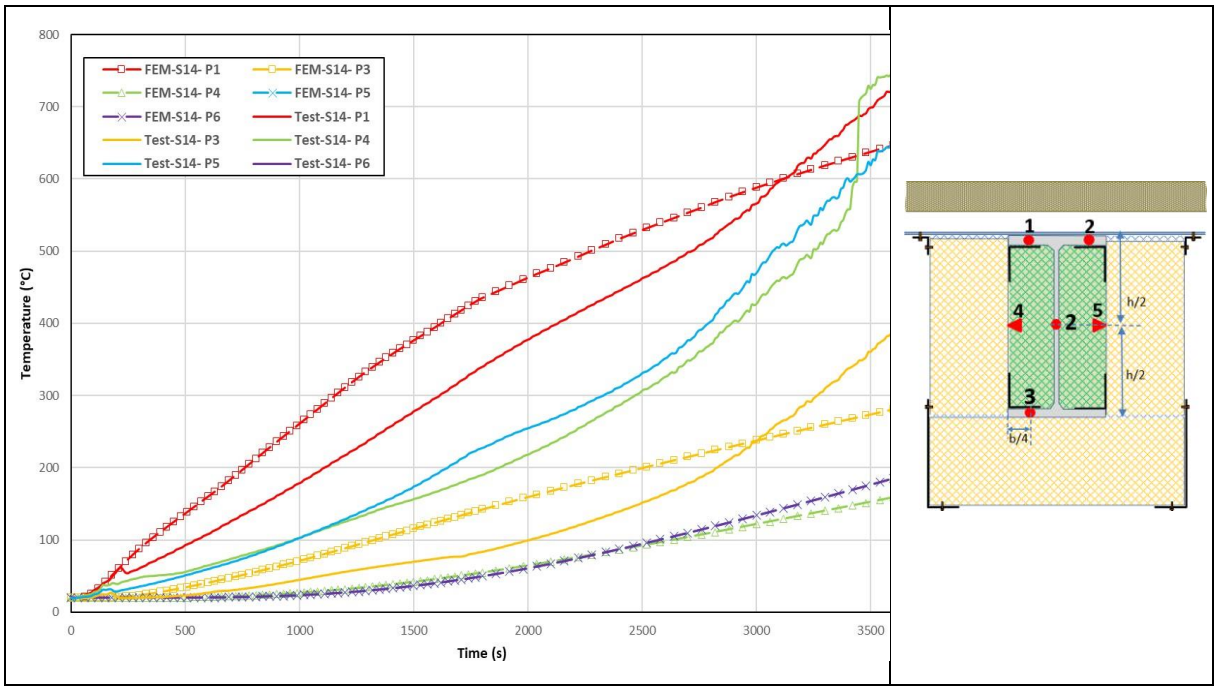

Figure A.16: Comparison between numerical and experimental temperatures for the cross-section S14 along the purlin n°2

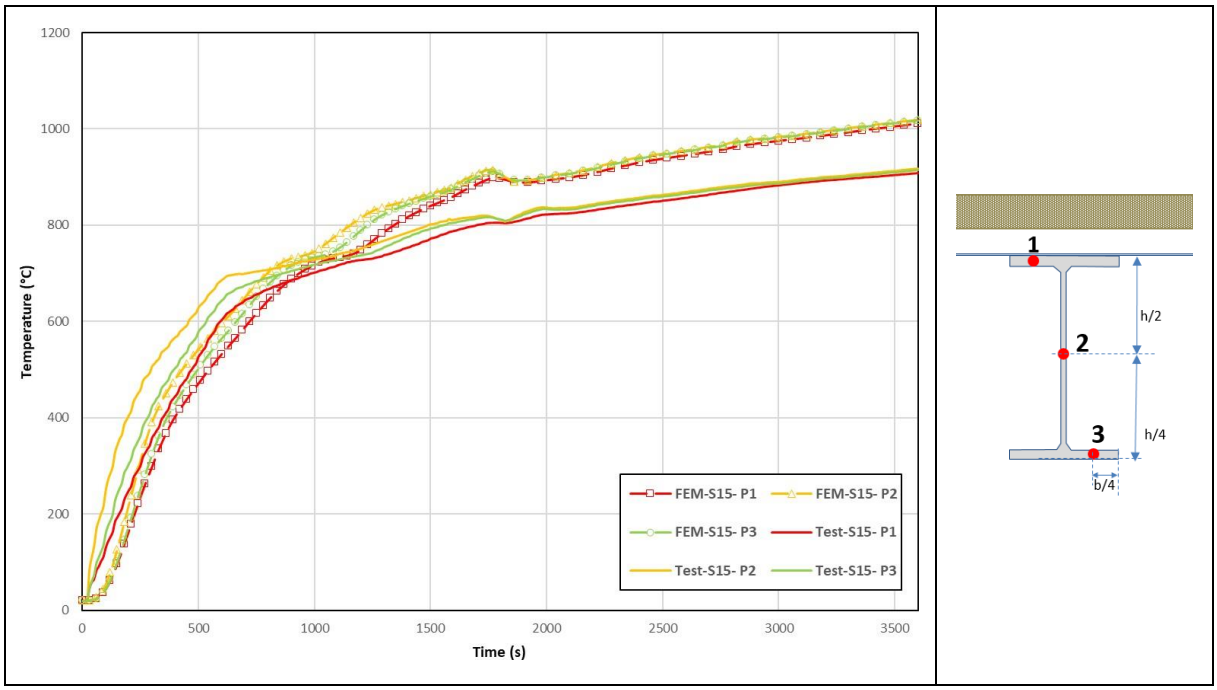

Figure A.17: Comparison between numerical and experimental temperatures for the cross-section S15 along the purlin n°2

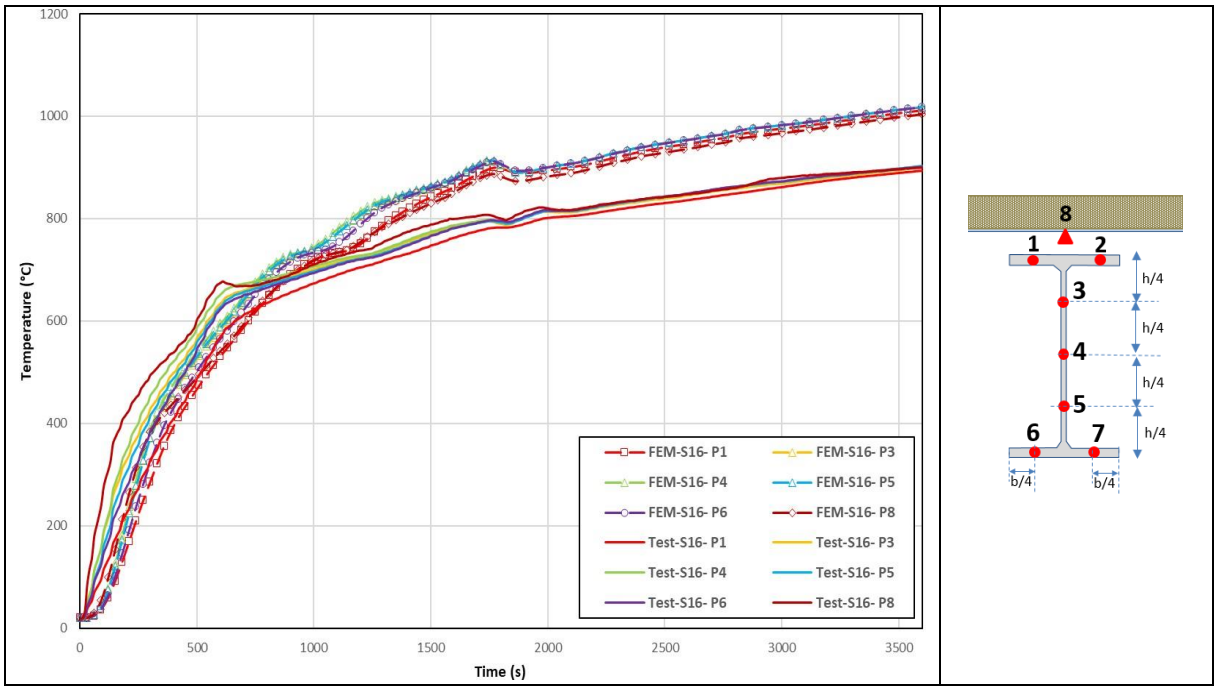

Figure A.18: Comparison between numerical and experimental temperatures for the cross-section S16 along the purlin n°2

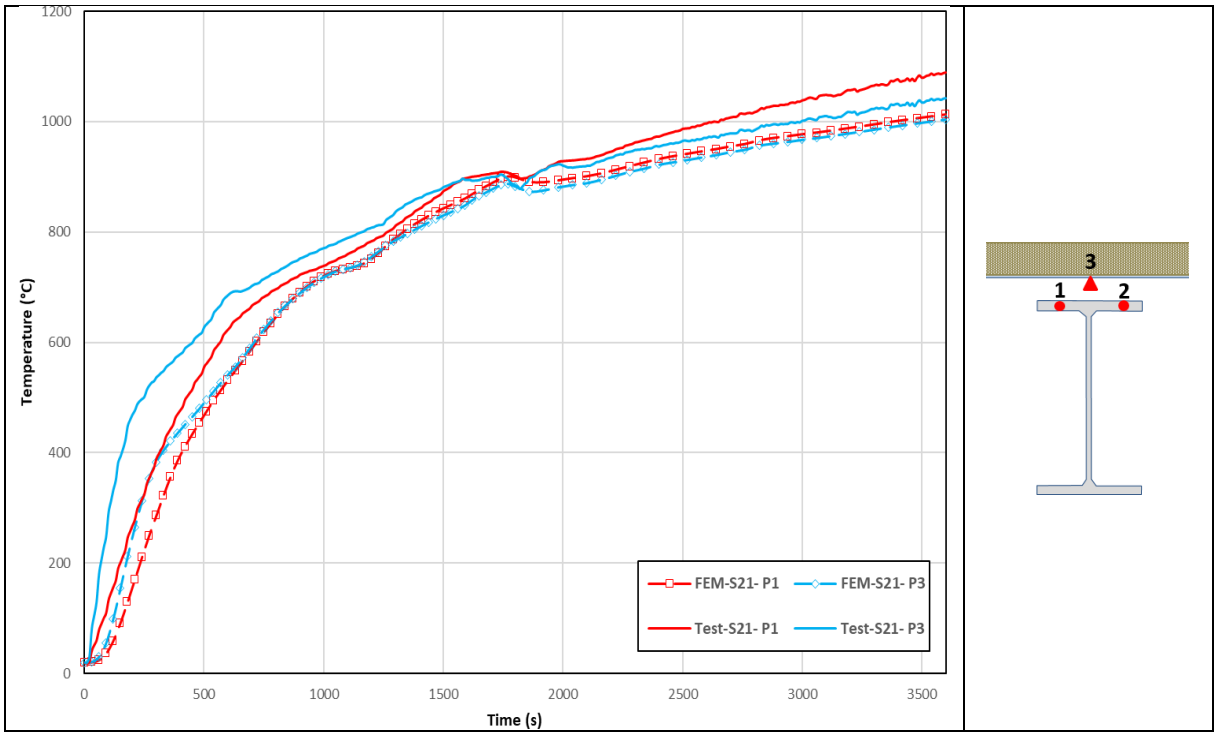

Figure A.19: Comparison between numerical and experimental temperatures for the cross-section S21 along the purlin n°2

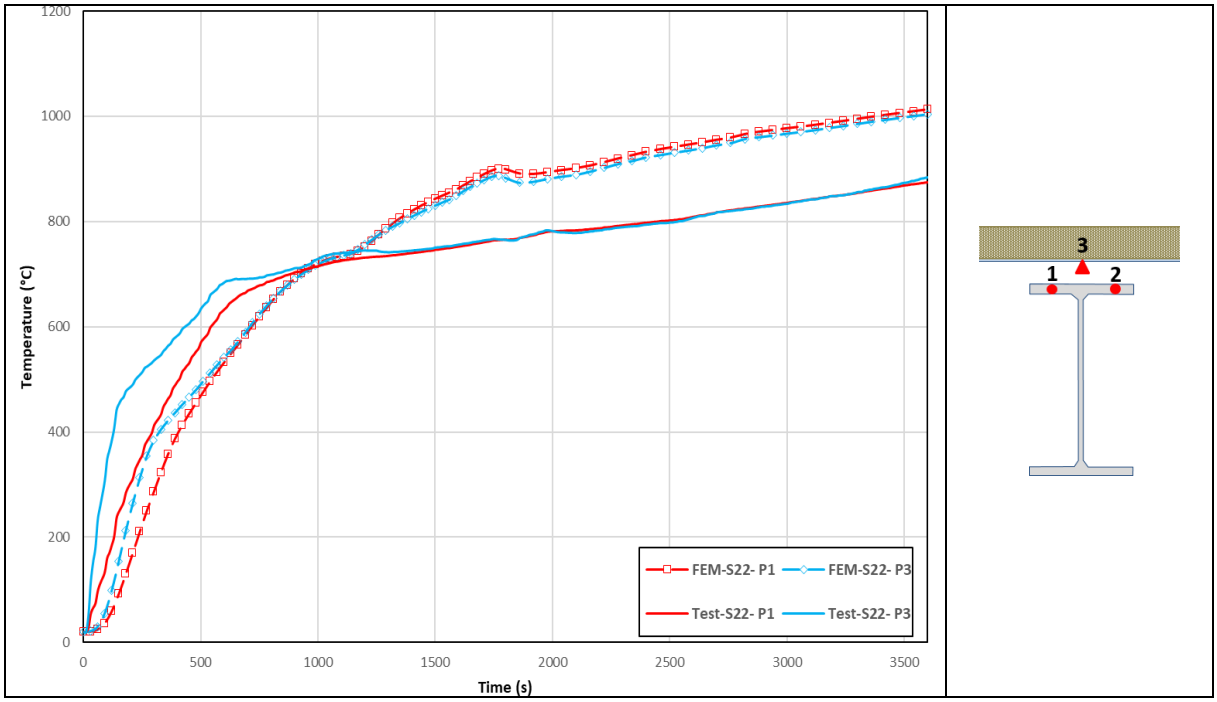

Figure A.20: Comparison between numerical and experimental temperatures for the cross-section S22 along the purlin n°2